Techniques d'inversion pour la diagraphie différée et l'imagerie électromagnétique

Amelie Litman

Université de Provence N° ordre :

Mémoire d'habilitation à diriger des Recherches

Techniques d'inversion pour la diagraphie différée et l'imagerie électromagnétique

par

Amélie LITMAN

Institut Fresnel

Soutenance le 27 novembre 2009 , devant le jury constitué de :

Mr	Marc	Bonnet	Rapporteur
Mr	Jean-Marc	Layet	Rapporteur
Mr	Dominique	Lesselier	Rapporteur
Mr	Hugues	Giovannini	Examinateur
Mr	Laurent	Jammes	Examinateur
Mr	Jean-Pierre	Lefebvre	Examinateur
Mr	Frédéric	Zolla	Examinateur

Introduction

Les travaux présentés dans ce mémoire ne sont pas présentés forcément de manière chronologique. Il faut néanmoins en distinguer deux étapes importantes dans ma carrière scientifique, une étape dans le monde industriel suivie et précédée d'une étape dans le monde académique. Il se trouve que j'ai eu la chance de pouvoir néanmoins conserver une thématique commune lors de ces différentes expériences professionnelles, à savoir les problèmes inverses. Seuls les phénomènes physiques sous-jacents ont variés au cours des ans. Ce manuscrit essaie donc de retracer au mieux les différentes thématiques, en mettant l'accent sur les difficultés inhérentes à chacune des configurations étudiées. Venant d'une formation plutôt orientée vers les mathématiques appliquées, en particulier les équations aux dérivées partielles, et l'informatique, je me suis intéressée de plus en plus à des problématiques relevant du domaine de la physique, et particulièrement l'électromagnétisme.

Ce manuscrit est divisée en quatre parties :

- La première partie (les chapitres 1 et 2) décrit mon parcours professionnel, les encadrements, les enseignements, les projets et les collaborations dans lesquelles je me suis impliquée.
- La deuxième partie (chapitre 3) présente les travaux que j'ai effectué lorsque j'étais ingénieur à Schlumberger. J'ai essayé de fournir une vue globale du métier que j'exerçais à cette époque, ainsi que de la problématique spécifique associée à la prospection pétrolière et plus particulièrement à la diagraphie différée.
- La troisième partie (les chapitres 4, 5, 6 et 7) correspond à la thématique de recherche que je poursuis à l'Institut Fresnel et que j'ai commencé lors de ma thèse. Elle concerne plus particulièrement les problèmes inverses de diffraction en électromagnétisme. Mon but est d'intervenir au mieux dans la conception et l'exploitation d'instruments d'imagerie par diffraction, pour obtenir des images quantitatives avec une haute résolution spatiale.
- La dernière partie (chapitre 8) présente une sélection d'articles illustrant plus en détail les différents aspects évoqués dans les deux parties précédentes.

Table des matières

Chapitre 1

Curriculum Vitae

Coordonnées professionnelles

Institut Fresnel - UMR CNRS 6133
Groupe HIPE
Domaine Universitaire de St Jérôme
13397 Marseille Cedex 20
Tél : 04 91 28 80 04
Mel : amelie.litman@fresnel.fr

Polytech'Marseille
Département MT
Technopôle de Chateau-Gombert
13451 Marseille Cedex 20

Mel : amelie.litman@polytech.univ-mrs.fr

Renseignements personnels

Née le 06 Mai 1972
Nationalité française

Mariée
Deux enfants

Expérience professionnelle

Depuis Nov. 2002 — **Maître de Conférences à l'Université de Provence**
Enseignement à l'Ecole Polytechnique Universitaire de Marseille, filière MicroElectronique et Télécommunications.
Recherche à l'Institut Fresnel, sur des problèmes de diffraction inverse et méthodes de minimisations non-linéaires.

Sept. 2001 - Oct. 2002 — **Chef de groupe, Schlumberger, Service Interprétation, Clamart**
Coordination et encadrement d'un groupe de deux ingénieurs, spécialisé dans les développements algorithmiques nécessaires à l'interprétation de mesures de résistivité, utilisées en prospection pétrolière.

Juil. 1998 - Sept. 2001 — **Ingénieur, Schlumberger, Service Interprétation, Clamart**
Elaboration de méthodes d'inversions utilisées pour l'interprétation de mesures de résistivité et de mesures nucléaires, en prospection pétrolière.

Nov. 1997 - Juil. 1998 — **Post-Doct au Laboratoire d'Electromagnétisme Université d'Eindhoven, Pays-Bas**
Post-Doctorat dirigé par le Prof. A.G. Tijhuis, portant sur le développement d'algorithmes de minimisation non-linéaires pour des problèmes de diffraction inverse.

Formation

Oct. 1994 - Oct. 1997 — **Thèse en Mathématiques Appliquées, Université Paris Sud, Orsay**
Titre : "Deux méthodes d'inversion pour la caractérisation électromagnétique ou acoustique d'objets enfouis : transformée de Fourier-Laplace inverse et déformation d'ensembles de niveaux"
Directeur de thèse : D. Lesselier, Directeur de Recherches CNRS
Laboratoire d'accueil : Lab. des Signaux et Systèmes, Gif-sur-Yvette
Membres du jury : M. Bertero, G. Chavent, C. De Mol, G. Lebeau, D. Lesselier, F. Santosa, J.P. Zolésio

Juin 1994 — **D.E.A en Mathématiques Appliquées**
Université Joseph Fourier, Grenoble

Juin 1994 — **Diplôme d'Ingénieur de l'ENSIMAG**
Ecole Nationale Supérieure d'Informatique et de Mathématiques Appliquées de Grenoble

1.1 Activités d'encadrement

1.1.1 Responsable de groupe à Schlumberger

De 2001 à 2002, j'ai travaillé chez Schlumberger où j'étais responsable des activités d'un groupe de trois jeunes mathématiciens spécialisés dans le traitement de mesures électromagnétique : P. Belik maintenant assistant professeur à l'Université de St Paul, Minnesota, USA ; J.M. Donadille qui est parti ensuite en tant qu'ingénieur à Schlumberger Pékin, Chine ; et M. Hamdi-Cherif, étudiante de DESS qui a ensuite poursuivi par une thèse au CIRED.

Les mesures que nous avions à traiter étaient acquises dans des puits de forage et servent à estimer la teneur en pétrole des couches géologiques traversées. Les algorithmes que nous avons développés en lien étroit avec les pétrophysiciens étaient toujours validés de façon intensive sur des données terrain avant d'être commercialisés (logiciels PrePlus et Invasion2). Mon travail a donc consisté à former, encadrer, définir les objectifs de l'équipe, effectuer le suivi des travaux et coordonner nos activités avec celles des autres groupes de travail de Schlumberger tant en France qu'à l'étranger ou avec les clients.

1.1.2 Responsable du groupe HIPE à l'Institut Fresnel

Depuis Septembre 2008, j'ai pris en charge la responsabilité du groupe HIPE, Hyperfréquences, Instrumentations, Processing et Expérimentations, nouvellement créé au sein de l'Institut Fresnel. Ce groupe est constitué à l'heure actuelle de 4,5 permanents, à savoir quatre maîtres de conférences,un ingénieur de recherches CNRS, et trois thésards. Ses activités s'organisent autour de la conception, du développement, de la mise en place et de l'exploitation d'outils d'instrumentation dans le domaine spectral des micro-ondes. Ces instruments ont plusieurs finalités :
– améliorer la compréhension des phénomènes de propagation des ondes,
– caractériser le comportement électromagnétique de composants actifs ou passifs,
– explorer la faisabilité d'instruments de sondage microonde dans/avec des environnements complexes (diffraction inverse, imagerie microonde, ...).

La réalisation de tels instruments hyperfréquences nécessite un couplage étroit entre des avancées à la fois expérimentales et théoriques. Ceci s'organise au sein du groupe selon différents axes de recherches :
– le design et la conception d'appareils de mesure dédiés,
– la mesure de champs électromagnétiques,
– la modélisation des phénomènes de propagation et de diffraction,
– la calibration des champs mesurés,
– le développement de méthodes d'inversion et d'imagerie,
– la détermination de caractéristiques électromagnétiques de matériaux.

1.1.3 Encadrement de stages

Depuis ma venue à l'Université de Provence, j'ai encadré chaque année plusieurs étudiants de niveaux très variables, allant de l'après-baccalauréat au stage de Master.

Stage TIPE
– P. Trouve, en 2005, portant sur la dualité en sciences.

– R. Robert, en 2009, portant sur les radars.

Stage en L1 (1 mois)
– L. Grouès, en 2008, portant sur la détermination de la permittivité de l'eau à partir de mesures de diffraction.

Stage en M1 (1 mois)
– F. Ballestra, en 2007, portant sur l'optimisation de configurations expérimentales.
– O. Diop, en 2009, portant sur l'imagerie micro-onde pour des applications en biomédical.

Projets tutorés d'étudiants en dernière année de Polytech (100h)
– F. Devaux et S. Renaud, en 2004, portant sur la mise en place d'un code de modélisation électromagnétique en configuration 2D H// par éléments finis, en collaboration avec H. Tortel, Maître de Conférences à l'Université de Provence,
– S. Teixier et M. Guichon, en 2005, portant sur l'incorporation d'information a-priori dans la détection d'objets diffractants,
– J. Ghilini et O. Laaroussi, en 2006, encadré en collaboration avec H. Tortel, portant sur la mise en place d'un code de modélisation électromagnétique par éléments finis en utilisant un formalisme en champ diffracté,
– F. Ballestra et O. Blanc, en 2007, portant sur l'optimisation de la configuration expérimentale que nous utilisons pour le contrôle non-destructif de l'eau dans des colonnes de sols reconstitués,
– S. Cheniour et K. Boutafza, en 2008, portant sur l'amélioration du protocole de calibration du scanner microonde circulaire utilisé pour le contrôle non-destructif de l'eau dans des colonnes de sols reconstitués.

Stage de Master 2 (4 mois min)
– G. Sautron, en 2004, venant du DEA Optique et Photonique de Marseille et qui a travaillé sur la détection de contours dans des images issues d'algorithmes de diffraction inverse, en collaboration avec H. Tortel et P. Vincent, Professeur à l'Université Paul Cézanne,
– J. Mondragon, en 2005, venant du DEA Optique et Photonique et qui s'intéressait à la prise en compte d'information a-priori dans les algorithmes de diffraction inverse,
– F. Dresk, en 2005, du DEA Physique Fondamentale et Appliquée de l'Ecole Centrale de Paris, en collaboration avec A. Sentenac, Chercheur CNRS, pour travailler sur la méthode des fonctions de niveaux pour des applications en imagerie optique haute-résolution,
– S. Wang, en 2009, du DEA Optique et Photonique de Marseille et qui travaille sur l'utilisation de la décomposition en valeurs singulières dans les méthodes d'imagerie micro-onde, en collaboration avec M. Guillaume, Maître de Conférences à l'Ecole Centrale de Marseille,
– O. Caratozzolo, en 2009, de l'Université de Regio Calabria, en Italie, et qui travaille sur l'influence des résonances d'une cavité dans les images issues d'algorithmes de diffraction inverse, en collaboration avec L. Crocco, Chercheur IREA-CNR, en Italie.

1.1.4 Encadrement de thèse

D'Octobre 2005 à Octobre 2008, j'ai co-encadré à hauteur de 95% avec H. Giovannini, Professeur à l'Université Paul Cézanne, la thèse de R. Lencrerot. R. Lencrerot avait suivi auparavant une formation d'ingénieur à l'Ecole Nationale Supérieure de Physique de Marseille. Il travaille actuellement comme ingénieur en recherche et développement dans le domaine de la géophysique chez Total, à Pau.

Sa thèse s'intitule "Outils de modélisation et d'imagerie pour un scanner micro-onde : Application au contrôle de la teneur en eau d'une colonne de sol." La soutenance s'est effectuée devant un jury constitué de D. Lesselier, L. Crocco, J.P. Lefevbre, S. Ruy, H. Giovannini et moi-même, avec l'obtention de la mention Très Honorable.

L'objectif des travaux de la thèse était d'exploiter les couplages qui existent entre la teneur en eau d'un milieu et sa permittivité diélectrique, afin de définir un protocole d'imagerie micro-onde pour caractériser la variation en eau dans des colonnes de sols reconstitués. R. Lencrerot a mis au point des outils numériques de modélisation et d'imagerie permettant de décrire le phénomène de diffraction dans le prototype de scanner circulaire micro-onde développé à l'Institut Fresnel. Il a en particulier mis au point un algorithme itératif avec ajout d'informations a priori basé sur une décomposition en polynômes de Zernike pour stabiliser le problème inverse. Il a également pris en compte les propriétés de l'opérateur de radiation pour comprendre la quantité de données accessibles et les informations a priori qu'il est légitime de considérer dans la configuration de mesure étudiée.

1.2 Activités nationales et internationales

1.2.1 Activités locales

J'ai été membre de la Commission de Spécialistes 61-63ème section à l'Université de Provence de 2004 à 2008.

J'anime les "cafés scientifiques" de l'Institut Fresnel depuis Septembre 2007. Ce sont des séminaires scientifiques informels d'une vingtaine de minutes qui ont lieu de façon mensuelle, permettant aux chercheurs de l'Institut Fresnel d'exposer leurs plus récents travaux.

1.2.2 Activités nationales

Je suis porteur d'un projet ANR Jeunes Chercheurs pour la période 2006-2009 et intitulé CESAR : Contrôle radiofréquence de l'écoulement de l'eau dans le sol et de l'absorption racinaire". Ce projet s'effectue en collaboration avec l'Unité, Climat, Sol et Environnement de l'INRA d'Avignon, l'Université de Gand en Belgique et le CEREGE à Marseille. Un budget total de 142 000 euros nous a été attribué pour ce projet.

Le but du projet CESAR est de démontrer le potentiel d'une approche non destructive d'imagerie radiofréquence pour caractériser l'écoulement de l'eau dans le sol. Pour cela, nous développons des dispositifs expérimentaux d'imagerie micro-onde, ayant chacun des dispositions géométriques des antennes d'émission et de réception différentes (circulaire, plane, ...). Ces dispositifs servent à mesurer le champ électromagnétique diffracté par la zone éclairée et des algorithmes d'inversion permettent ensuite de remonter à la cartographie en coupe de la permittivité diélectrique qui est directement liée à la teneur en eau des sols. C'est dans ce cadre que s'est inscrit la thèse de R. Lencrerot. Le groupe HIPE a également recruté un post-doctorant, M. Serhir, pendant un an pour travailler à la mise en place expérimentale de la configuration à géométrie plane.

1.2.3 Activités internationales

Projets d'Action Intégré

– J'ai participé au Projet d'Action Intégré Tournesol pour les années 2004 et 2005 entre l'Institut Fresnel et l'Université de Gand en Belgique et qui s'intitulait « Techniques micro-ondes de caractérisation d'objets enfouis. Application à l'évaluation non destructive du béton armé et à la détection de canalisation ».
– J'ai participé au Projet d'Action Intégré Galiléo pour l'année 2006-2007 entre l'Institut Fresnel et le Laboratoire DIMET de l'Università Mediterranea di Reggio Calabria en Italie et qui s'intitulait :« Microscopie optique à haute résolution sans lentilles ».

Collaborations internationales
– J'ai été responsable à l'Institut Fresnel en 2008-2009 pour le projet INTAS Nr. 06-1000017-8909 qui portait sur le « Development of a unified approach and software for numerically solving inverse and optimization problems for distributed systems » en collaboration avec l'Université de Kocaeli en Turquie, avec le Cybernetics Institute en Azerbaijan, l'Institute of Cybernetics en Ukraine et le North Caucasus State Technical University en Russie. Un budget de 7 500 euros nous a été attribué pour cela.
– J'ai obtenu une bourse de chercheur invité par l'Ecole Centrale de Marseille pour L. Crocco, Chercheur CNR-IREA, Italie, qui est venu passer deux mois à l'automne 2008 pour travailler à l'Institut Fresnel sur, entre autres, l'optimisation de systèmes d'imagerie microonde.

Rapporteur

Je suis rapporteur pour les revues "Inverse Problems","Inverse Problems in Science and Engineering", "Journal of Inverse and Ill-Posed Problems", "Optics Express", "IEEE Trans Geoscience and Remote Sensing", "IEEE Trans Microwave Theory and Techniques", "IEEE Trans Antennas and Propagation".

Symposiums
– J'ai été co-chairman, avec T. Mannseth de l'Université de Bergen, Norvège, pour un Mini-Symposium sur les "Level-set Methods", lors de la conférence "Inverse Problems : Modeling and Simulation" en Turquie en Mai 2008.
– J'ai été co-chairman et co-organisatrice, avec L. Crocco de l'IREA-CNR de Naples, Italie, pour la session invitée « Near sub-surface electromagnetic imaging : methods and applications » à la conférence IGARSS à Boston, USA, en Juillet 2008.

Session spéciale
J'ai pris en charge, en collaboration au départ avec K. Belkebir puis ensuite avec L. Crocco, la mise en place d'une session spéciale dans la revue Inverse Problems. Cette session est la troisième du genre, après celles de 2001 et 2005. Elle est parue en février 2009 et s'intitule "Testing inversion algorithms against experimental data : 3D targets". L'Institut Fresnel a mesuré les champs diffractés par cinq cibles tridimensionnelles en configuration multi-statique et multifréquence. Il a ensuite proposé ces mesures à la communauté scientifique des problèmes inverses de diffraction. Six contributions venant de différentes équipes de recherche (France, Italie, Etats-Unis, Belgique) ont présenté les images reconstruites de ces cinq objets, obtenus à partir des différents algorithmes qu'ils avaient développés.

1.3 Activités pédagogiques

Depuis Novembre 2002, j'effectue la totalité de mon service d'enseignement à Polytech' Marseille, dans le département MicroElectronique et Télécommunications. J'interviens en 1ère et 2ème Années avec des enseignements qui ont varié au cours des ans.

1.3.1 Service d'enseignement au cours des années

En 2002-2003 (156h équivalent TD)
– TP (128h) en Electromagnétisme et physique des semi-conducteurs en 1ère année
– Cours (20h) et TD (20h) en Signaux aléatoires en 1ère année
– TD (20h) en Ondes électromagnétiques en 1ère année
N'ayant pris mes fonctions qu'au 1er novembre 2002, mon service horaire a été calculé au prorata.

En 2003-2004 (139h équivalent TD)
– TP (40h) en Signaux, Systèmes, Electronique, Automatique en 1ère année
– TD (12h) en Analyse numérique en 1ère année
– Cours (20h) et TD (20h) en Signaux aléatoires en 1ère année
– Cours (20h) et TD (20h) en Ondes électromagnétiques en 1ère année
Cette année-là, mon service était réduit suite à mon congé maternité.

En 2004-2005 (197h équivalent TD)
– TP (40h) en Signaux, Systèmes, Electronique, Automatique en 1ère année
– Cours (20h) et TD (20h) en Analyse numérique en 1ère année
– Cours (20h) et TD (20h) en Signaux aléatoires en 1ère année
– Cours (20h) et TD (20h) en Ondes électromagnétiques en 1ère année
– Projet tutoré en 3ème année (20h)

En 2005-2006 (157h équivalent TD)
– Projet (24h) d'Informatique - Langage C
– TP (64h) en Signaux, Systèmes, Electronique, Automatique en 1ère année
– Cours (20h) et TD (48h) en Analyse numérique en 1ère année
– Projet tutoré en 3ème année (20h)
Cette année-là, certains cours de 1ère année sont passés en 2ème année et on a donc une année de transition qui a changé l'organisation des cours. Le volume horaire non effectué a été reporté sur l'année suivante.

En 2006-2007 (230h équivalent TD)
– TP (32h) et Projet (16h) d'Informatique - Langage C
– Cours (20h) et TD (48h) en Analyse numérique en 1ère année
– Cours (20h) et TD (20h) en Signaux aléatoires en 2ème année
– Cours (20h) et TD (20h) en Ondes électromagnétiques en 2ème année
– Projet tutoré en 3ème année (20h)

En 2007-2008 (210h équivalent TD)
– TP (32h) et Projet (16h) d'Informatique - Langage C
– Cours (20h) et TD (48h) en Analyse numérique en 1ère année
– Cours (20h) en Signaux aléatoires en 2ème année
– Cours (20h) et TD (20h) en Ondes électromagnétiques en 2ème année
– Projet tutoré en 3ème année (20h)

En 2008-2009 (210h équivalent TD)
– TP (32h) et Projet (16h) d'Informatique - Langage C
– Cours (20h) et TD (48h) en Analyse numérique en 1ère année
– Cours (20h) en Signaux aléatoires en 2ème année
– Cours (20h) et TD (20h) en Ondes électromagnétiques en 2ème année
– Projet tutoré en 3ème année (20h)

1.3.2 Contenu des enseignements

Je n'évoquerais ici que les enseignements dont je suis responsable, à savoir par le choix du contenu des cours magistraux et des travaux dirigés, ainsi que des sujets d'examen et leurs corrections.

Signaux aléatoires

Ce cours, que j'ai entièrement construit à mon arrivée et que je continue à améliorer aux cours des années, permet à l'étudiant de se familiariser avec des situations aléatoires où le temps intervient. Il doit assimiler le vocabulaire associé aux phénomènes aléatoires (corrélation, stationnarité, ergodisme, densité spectrale de puissance, ...). Il doit comprendre les notions de bruit et de filtrage associé (théorème de Wiener-Kintchine, formule des interférences, bande passante équivalent de bruit, ...).

Il suppose des pré-requis en probabilités, filtrage linéaire, transformée de Fourier et de Laplace. Au départ en 1ère année, il a été déplacé fort heureusement en 2ème année pour laisser aux étudiants le temps d'assimiler les matières prérequises.

Ondes électromagnétiques

Pour ce cours, je me suis fortement inspirée des notes de mon prédécesseur, M. Saillard, Professeur à l'Université de Toulon. Au départ en 1ère année, il est passé en 2ème année afin d'avoir une continuité sur la formation en électromagnétisme dans toutes les années de la formation d'ingénieur.

Il permet d'étudier la propagation des ondes électromagnétiques en présence d'interfaces, en régime harmonique. On y parle de coefficients de réflexion et transmission sur une interface plane, de métal infiniment conducteur, de guides d'ondes métalliques, de cavités métalliques et si le temps le permet de guides d'ondes diélectriques.

Il suppose des prérequis sur la propagation des ondes dans un milieu infini, sur la transformée de Fourier, le produit de convolution et des notions sur les distributions.

Analyse numérique

J'ai adapté ce cours à partir des notes de mon prédécesseur, L. Raymond, Maître de Conférences à l'Université de Provence. Le but de ce cours est de rendre l'étudiant apte à sélectionner une méthode de résolution numérique adaptée à un problème donné. On y parle d'arithmétique des calculateurs, d'algèbre linéaire, de résolution numérique d'équations linéaires et non-linéaires, d'interpolation numérique, d'intégration et dérivation numérique, ainsi que de schémas simples pour les équations différentielles ordinaires. Les prérequis concernent simplement des notions d'algèbre linéaire élémentaire, ainsi que des notions sur la continuité, dérivabilité, convergence des fonctions.

J'ai également bâti des séances de travaux dirigés sur ordinateur, en me basant sur l'utilisation du logiciel Matlab, afin de sensibiliser les étudiants à une mise en oeuvre pratique des algorithmes numériques étudiés.

Chapitre 2

Articles publiés dans des revues internationales à comité de lecture

Ne sont donnés ici que les articles publiés dans des revues internationales à comité de lecture. Les conférences que j'ai pu faire depuis de nombreuses années ne sont pas citées.

1. L Crocco and **A Litman**. On embedded microwave imaging systems : retrievable information and design guidelines. *Inverse Problems*, 25 :065001, 2009.
2. J-M Geffrin, C Eyraud, **A Litman**, and P Sabouroux. Optimization of a bistatic microwave scattering measurement setup : from high to low scattering targets. *Radio Science*, 44 :RS2007, 2009.
3. R Lencrerot, **A Litman**, H Tortel, and J-M Geffrin. Imposing Zernike representation for two-dimensional targets imaging. *Inverse Problems*, 25 :035012, 2009.
4. R Lencrerot, **A Litman**, H Tortel, and J-M Geffrin. Measurement strategies for a confined microwave circular scanner. *Inverse Problems in Science and Engineering*, 357869, 2009.
5. **A Litman** and L Crocco. Testing inversion algorithms against experimental data : 3D targets. *Inverse Problems*, 25 :020201, 2009.
6. C Eyraud, **A Litman**, A Herique, and W Kofman. Microwave imaging from experimental data within a bayesian framework with realistic random noise. *Inverse Problems*, 25 :024005, 2009.
7. C Eyraud, J-M Geffrin, P Sabouroux, P Chaumet, H Tortel, H Giovannini, and **A Litman**. Validation of a 3D bistatic microwave scattering measurement setup. *Radio Science*, 43 :RS4018, 2008.
8. M D'Urso, K Belkebir, L Crocco, T Isernia, and **A Litman**. Phaseless imaging with experimental data : facts and challenges. *J. Opt. Soc. A.-A*, 25(1) :271–281, 2008.
9. O Cmielewski, H Tortel, **A Litman**, and M Saillard. A two-step procedure for characterizing obstacles under a rough surface from bistatic measurements. *IEEE Trans. Geosci. Remote Sens.*, 45(9) :2850–2858, 2007.
10. C Eyraud, J-M Geffrin, **A Litman**, P Sabouroux, and H Giovannini. Drift correction for scattering measurements. *Applied Physics Letters*, 89(244104), 2006.
11. **A Litman** and K Belkebir. Inverse profiling using phaseless data. *J. Opt. Soc. A-A*, 23(11) :2737–2746, 2006.
12. **A Litman**. Reconstruction by level sets of n-ary scattering obstacles. *Inverse Problems*, 21(6) :S131–S152, 2005.
13. M T Galli, M Gonfalini, M Mele, P Belik, O Faivre, L Jammes, and **A Litman**. Resistivity modeling of array laterolog tools : an application in an offshore norway clastic reservoir. *SPE Reservoir Evaluation Engineering*, 8(1) :77–87, 2005.
14. A G Tijhuis, K Belkebir, **A Litman**, and B P de Hon. Multiple-frequency distorted-wave born approach to 2D inverse profiling. *Inverse Problems*, 17(6) :1635–1644, 2001.
15. A G Tijhuis, K Belkebir, **A Litman**, and B P de Hon. Theoretical and computational aspects of 2d inverse profiling. *IEEE Trans. GeoSci. Remote Sens.*, 39(6) :1316–1330, 2001.
16. **A Litman** and D Lesselier. On attenuation-matched inversion methods of diffusive wavefields. *Inverse Problems*, 15(1) :99–111, 1999.
17. **A Litman**, D Lesselier, and F Santosa. Inversion of a two-dimensional binary obstacle by controlled evolution of a level-set. *Inverse Problems*, 14(3) :685–706, 1998.

Chapitre 3

Diagraphie différée

3.1 Prospection pétrolière

Lorsque les géologues ont établi qu'une zone pouvait s'avérer renfermer des hydrocarbures, il est alors important d'aller en explorer localement le sous-sol afin de s'assurer des possibilités d'exploitation et de leurs rentabilités financières. Ceci passe par une étape de forage suivie d'une campagne de mesures, les mesures pouvant même être effectuées en même temps que le forage. Cette campagne de mesure permettra d'obtenir des diagraphies, à savoir un enregistrement selon la profondeur des grandeurs physiques représentatives des formations traversées par les sondes. En fonction des valeurs obtenues, la zone explorée devient financièrement exploitable ou non, d'où l'importance de telles diagraphies.

L'entreprise Schlumberger s'est spécialisée dans la création d'outils de mesure, qu'elle ne vend pas. Elle vend uniquement du service associé à l'exploration, à savoir l'obtention des diagraphies (données brutes) mesurées dans le puits d'exploration et si le client le souhaite, elle peut effectuer des traitements numériques supplémentaires afin de proposer également des diagraphies interprétées.

Parmi les diagraphies classiques qui se rencontrent en exploration, on peut distinguer [13]
- des mesures passives qui correspondent à l'enregistrement de phénomènes naturels engendrés spontanément : potentiel spontané, radioactivité naturelle, température, diamètre du trou, déviation du trou de forage, ...
- des mesures actives qui correspondent à l'enregistrement de paramètres physiques obtenus par excitation : résistivité, conductivité, indice d'hydrogène neutron, densité de formation, section efficace photoélectrique, vitesse du son, ...

Toutes ces informations sont ensuite transmises au pétrophysicien qui peut ainsi évaluer le potentiel en hydrocarbure de la zone.

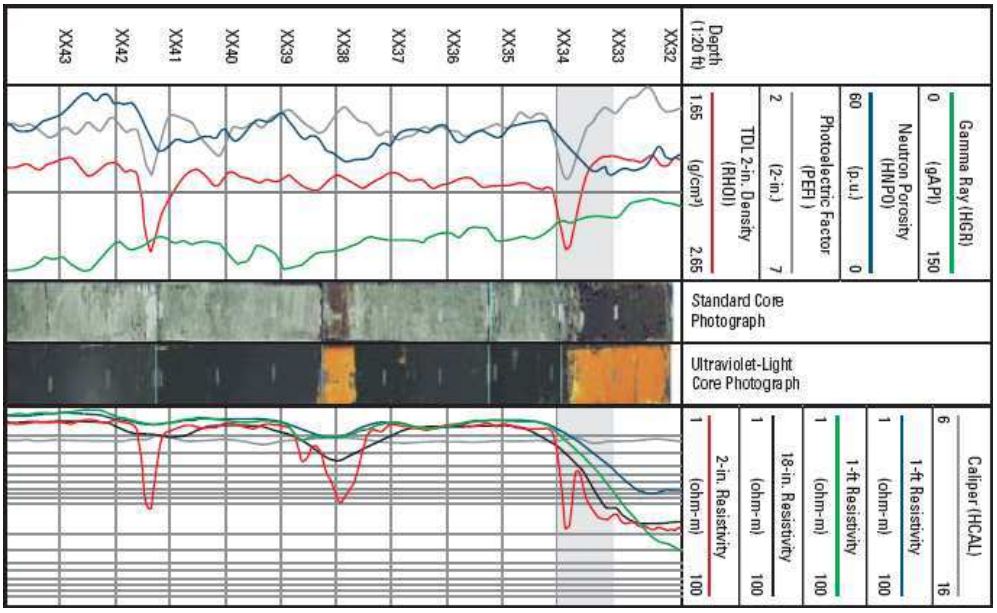

FIG. 3.1 – Un exemple de diagraphie différée qui regroupe des mesures passives et actives. Les profondeurs sont volontairement cachées afin de garder confidentiel les zones susceptibles de contenir une forte proportion d'hydrocarbures.

Lors de ma période à Schlumberger, je suis intervenue dans la partie qui concerne le traitement des mesures actives, permettant de passer de la mesure brute à la diagraphie

vendue au client, tout d'abord à l'aide d'outils de mesure nucléaire puis d'outils de mesure de résistivité.

3.2 Le forage

Avant d'arriver aux principes des diagraphies étudiées, il est nécessaire de comprendre la façon dont se passe le forage. Celui-ci s'effectue à l'aide d'un trépan qui s'enfonce progressivement dans la roche, poussé par un train de tiges creuses. Une boue spéciale y circule en même temps. Elle sert à remonter les déblais, à maintenir les parois du trou, à refroidir l'outil, ... La pression de la colonne de boue est maintenue plus forte que celle de la roche environnante pour éviter tout effondrement. Malheureusement, là où la roche est perméable, la partie fluide de la boue va avoir tendance à rentrer (phénomène d'invasion), tandis que les particules solides de la boue vont rester collées à la paroi. Le forage modifie donc localement les propriétés de la roche et vont grandement perturber les mesures qui seront faites ensuite à l'aide des différents outils de diagraphies.

3.3 Diagraphie de densité

Les outils de densité sont basés sur le principe de l'interaction des rayons gamma avec la matière, qui sont principalement gouvernés par la densité et le numéro atomique de la roche traversée. Ces deux informations permettent ensuite de remonter à la lithologie et à la porosité de la zone traversée, qui font partie des informations indispensables au pétrophysicien pour son interprétation.

Malheureusement dans un trou de forage, les parois du trou sont souvent couvertes d'une couche de boue (gâteau de boue) qui empêche de mesurer les caractéristiques de la roche directement. Afin de pouvoir contrôler ces effets dûs à l'environnement de mesure, les sondes comportent plusieurs capteurs, avec plusieurs profondeurs d'investigation. Il est alors nécessaire de construire des algorithmes pour combiner ces différentes mesures et en extraire des informations pertinentes sur la roche.

Traditionnellement, les pétrophysiciens utilisaient les différences entre les densités apparentes vues par les différents capteurs et à l'aide d'abaques, tel l'abaque du Spine and Ribs, ils remontaient aux informations qui les intéressent [1]. La mise en place d'algorithmes d'inversion a progressivement remplacé ces techniques d'abaques [3], mais les contraintes associées à ce type d'algorithmes sont très fortes. Il faut en effet que l'algorithme d'inversion

- fournisse une solution en temps réel,
- fournisse une solution physiquement acceptable et robuste au bruit même dans de mauvaises conditions de mesure,
- reproduise les solutions des anciens outils, voire même améliorer les résultats tant au niveau de la précision que de la prise en compte du gâteau de boue,
- fournisse des solutions avec une meilleure résolution spatiale.

Parmi les outils de mesures de densité, le Platform Express est très souvent employé, car il a l'avantage de combiner à la fois des mesures de densité, de résistivité, de diamètre de trou, ... C'est sur cet outil de mesure que je suis donc intervenue.

Ma première tâche a été de me familiariser avec la physique sous-jacente et les algorithmes d'inversions déjà mis en place, d'aider les pétrophysiciens à comprendre les résultats qu'ils

obtenaient dans les différents puits d'exploration en cours, modifier si besoin le logiciel en fonction des nouvelles conditions de mesures. Le Platform Express est largement commercialisé par Schlumberger et la chaîne de traitement numérique associé appelé GeoFrame/PrePlus fait partie des logiciels de base de Schlumberger en ce qui concerne l'interprétation pétrophysique.

3.3.1 Principe

Le Platform Express contient une source de rayons gamma (Cesium-137) et trois détecteurs (backscatter, short-spacing et long-spacing) (figure 3.2), le tout monté sur un patin. Le patin reste en contact constant avec la paroi du trou de forage.

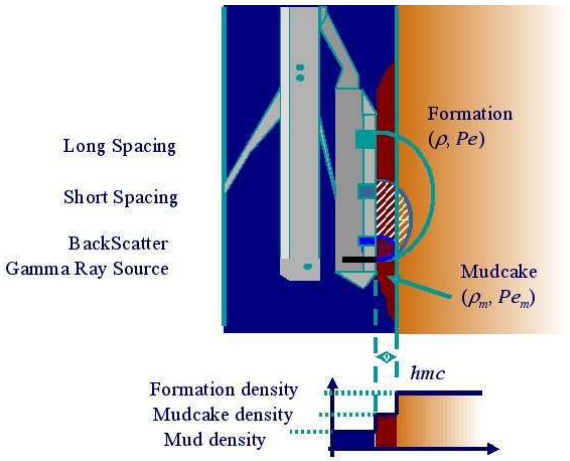

FIG. 3.2 – Position du patin et des capteurs - Modélisation du profil de la zone sondée.

Les photons sont émis dans la roche et trois types d'interaction peuvent se produire, suivant l'énergie du photon incident :
- la production de paire électron-positron, dont l'influence est négligée pour les sources utilisées dans les outils de diagraphie gamma-gamma,
- l'effet compton, qui va permettre de fournir principalement des informations sur la densité électronique de la roche,
- l'effet photo-électrique, qui est d'autant plus grand que l'énergie du rayonnement gamma est faible et le numéro atomique des éléments élevé.

Ces deux derniers effets sont captés par les trois détecteurs. Les spectres en énergie mesurés par les trois détecteurs sont alors combinés en fenêtres d'énergie pour être ensuite analysées (figure 3.3).

3.3.2 Le problème direct

Le problème direct sert à prédire le taux de comptage associé à chaque fenêtre en énergie en fonction des différents paramètres de la roche et du trou de forage. Due à la très faible zone de sensibilité de la source, une modélisation simplifiée est employée en supposant un profil radial en forme de marche d'escalier (figure 3.2) et ce, profondeur par profondeur. La réponse du détecteur devient alors

$$W_{i,j} = f_{i,j}(p) \quad \text{avec} \quad p = (\rho, Pe, \rho_m, Pe_m, hmc)$$

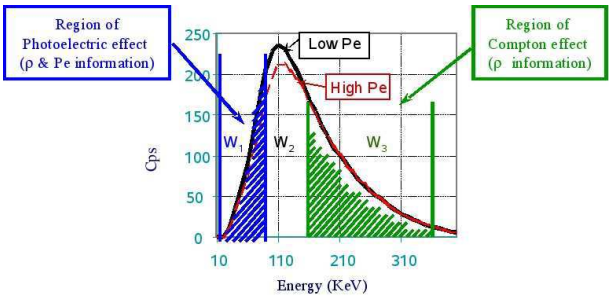

FIG. 3.3 – Fenêtres en énergie

pour chaque fenêtre en énergie i de chaque détecteur j, avec ρ la densité de la roche, Pe son facteur photoélectrique, ρ_m la densité de la boue, Pe_m son facteur photoélectrique et hmc l'épaisseur du gâteau de boue qui se trouve en face du patin. Les valeurs classiques rencontrées sont de l'ordre de

Roche	Boue sans barite	Boue avec barite
$1.70 < \rho < 3.03$ g/cc	$1.25 < \rho_m < 2.35$ g/cc	$1.48 < \rho_m < 1.98$ g/cc
$1.2 < Pe < 6.0$	$1.57 < Pe_m < 1.91$	$10 < Pe_m < 100$
	$0 < hmc < 1.5$ in	$O < hmc < 0.5$ in

sachant que la barite est un additif qui est rajouté dans certains cas à la boue de forage pour faciliter les conditions de forage.

Un modèle idéal consisterait à résoudre l'équation de transport de Boltzmann, qui n'a pas de solution analytique simple pour un environnement complexe comme celui du capteur. Le problème direct a été alors défini comme un modèle non-linéaire paramétrique, dont les coefficients ont été déterminés à partir d'une base de données de mesures de références effectuées avec des roches parfaitement tabulées.

3.3.3 L'algorithme d'inversion

L'algorithme d'inversion intervient après une étape de correction de vitesse, de calibration, de correction de température, de remise en profondeur, de correction de trou, ... Il fonctionne sur un principe classique de maximum de vraisemblance, appliqué à chaque profondeur [15]. Le bruit est supposé blanc, additif et gaussien. Le critère à minimiser à chaque profondeur est donc de la forme

$$c_1(p) = (W - f(p))^t R_1^{-1} (W - f(p))$$

Les coefficients de la matrice de covariance R_1 ont été estimés expérimentalement et varient en fonction des conditions de mesure et des amplitudes des fenêtres en énergie mesurées.

Il faut à cela rajouter un certain nombre d'informations a priori et de contraintes. La première contrainte consiste à restreindre le domaine de solutions possibles à des solutions physiquement réalisables

$$1.05 < \rho < 4.5 \text{ g/cc}, \quad 0.9 < Pe < 10, \quad 0 < hmc$$

Plusieurs termes de pénalisation sont ensuite rajoutés dans la fonction coût, qui devient alors

$$F(p) = c_1(p) + c_2(p) + c_3(p) + c_4(p)$$

Le terme c_2 est un terme qui impose au profil de p de garder une certaine régularité selon la profondeur, il est donc de la forme

$$c_2(p) = (p - p_{prev})^t R_2^{-1} (p - p_{prev})$$

où p_{prev} est la valeur estimée à la profondeur précédente. Ce n'est donc rien d'autre qu'un terme de Tikhonov de type L_2.

Le terme c_3 est un terme dit de stabilité qui empêche à la solution de converger vers des valeurs qui sont en dehors de la base de données ayant servi à la mise au point du problème direct, en particulier lorsque l'épaisseur de gâteau de boue est trop importante

$$c_3(p) = \alpha_3(hmc)(hmc - hmc_{avg})^2$$

où hmc_{avg} est une épaisseur de boue moyenne et le coefficient α_3 est dessiné de manière à augmenter lorsque hmc augmente.

Le dernier terme c_4 est un terme qui impose à la solution d'être proche de la solution Spine and Ribs, qui est considérée comme "la solution de référence" et qui est calculée à chaque profondeur en fonction de la différence entre les densités apparentes mesurées par chacun des capteurs séparément,

$$c_4(p) = \alpha_4(\rho)(\rho - \rho_{SR})^2$$

A nouveau, le paramètre α_4 varie en fonction des conditions de mesure. Ce dernier terme permet en plus de contrôler la solution dans le cas où l'étape de calibration s'est mal passée ou lorsque le patin du capteur présente des traces d'usure.

Toute cette algorithmique est faite de manière à être non-supervisée. Il est en effet impensable que le pétrophysicien soit amené à modifier ces paramètres, il ne doit avoir qu'à appuyer sur un bouton pour obtenir le résultat. Pour cela, les paramètres α_i sont définis et ajustés sur un nombre très important de mesures afin de satisfaire à la plupart des conditions rencontrées sur le terrain. Ils sont donc modifiés si jamais une nouvelle configuration apparaît mais sans devoir remettre en cause tous les résultats obtenus jusqu'alors.

Outre le paramètre p qui contient les informations nécessaires, il y a également tout un ensemble d'indicateurs qui permettent de valider le résultat obtenu : est-ce que l'algorithme a convergé, est-ce que les valeurs obtenues sont en dehors des limites de la base de données, est-ce qu'il y a des soucis de calibration, ... Ces indicateurs sont donnés conjointement à p, en plus des barres d'erreur (figure 3.4).

3.3.4 La barite

A mon arrivée, l'algorithme d'inversion était en fait scindé en deux, suivant la présence ou non de barite dans la boue. La barite permet d'alourdir la boue et évite ainsi l'effondrement des parois du trou. Par contre, c'est un très fort absorbant pour les photons qui reviennent au détecteur. Il était alors nécessaire à l'utilisateur de signaler en lançant le programme si il y avait de la barite ou non. En raison du nombre très important de fois où l'ingénieur terrain se trompait dans sa sélection et obtenait alors de mauvais indicateurs de qualité en fin de traitement et remettait en cause la qualité des mesures, il a été décidé de supprimer ce critère dans l'interface utilisateur. Cette tâche m'a ainsi été confiée.

En premier lieu, il a fallu trouver comment détecter la présence de barite en se servant uniquement de la mesure. Pour cela, F. Allioli, un des ingénieurs qui a participé à la

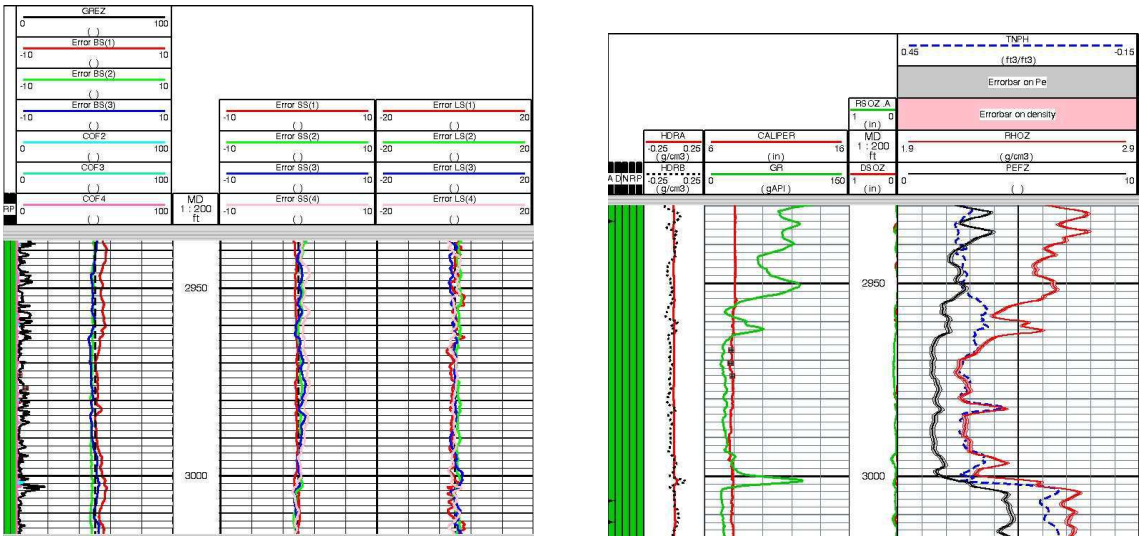

FIG. 3.4 – Paramètres de contrôle de la qualité de l'inversion : drapeaux (en vert si ok), erreur des termes de la fonction coût, barres d'erreur sur les paramètres reconstruits.

conception du PlatformExpress, a mis au point un indicateur de barite (val_{bar}), en utilisant des rapports entre les différentes fenêtres en énergie du Backscatter. Malheureusement cet indicateur ne fournit pas une réponse binaire et il n'était donc pas possible de garder l'algorithme d'inversion en l'état.

La deuxième étape a été de définir un modèle direct unique. Ceci a été effectué en se basant le même principe que les deux modèles précédents (avec et sans barite) mais en utilisant une base de données encore plus étendue, couvrant en particulier les cas où il y avait peu de barite [5].

Finalement, il a fallu revoir l'algorithme d'inversion dans son ensemble. Les termes de pénalisation sont restés identiques, mais les hyper-paramètres α_i ont été adaptés pour fonctionner correctement en fonction de l'indicateur de barite. De plus, un cinquième terme a été rajouté dans la fonction coût

$$c_5(p) = \alpha_5^{nonbar}(val_{bar})(Pe_m - Pe_m^{nonbar})^2 + \alpha_5^{bar}(val_{bar})(Pe_m - Pe_m^{bar})^2$$

où Pe_m^{bar} et Pe_m^{nonbar} sont les valeurs typiques que peut pendre le facteur photoélectrique de la boue, avec ou sans barite. Le paramètre α_5 varie en fonction de l'indicateur de barite val_{bar} et fait tendre la solution vers l'une ou l'autre situation.

Ce nouvel algorithme a été testé sur toutes les diagraphies disponibles au centre de Clamart. Il a également été validé par plusieurs pétrophysiciens [10] avant d'être ensuite commercialisé au sein de GeoFrame/PrePlus.

3.4 Diagraphie de résistivité

La mesure de résistivité est la première diagraphie différée effectuée par les frères Schlumberger en 1927. Son succès en tant que détecteur d'hydrocarbures est dû au fait que la résistivité électrique de la zone sondée dépend fortement de la concentration en hydrocarbures, ces derniers étant des isolants électriques. La conduction électrique a lieu grâce à l'eau présente entre les pores de la roche. Schématiquement, lorsque la résistivité mesurée

est haute, ceci peut indiquer la présence d'huile ou de gaz dans les pores. Par contre, une résistivité faible peut signaler la présence d'eau dans les pores.

3.4.1 Porosité et saturation en eau

La fraction (ou pourcentage) du volume de la roche qui est occupée par les pores est appelée sa porosité (ϕ). Une vue idéalisée de la roche est donnée dans la figure 3.5. La matrice est constituée de grains de sable, limon ou dolomite. L'espace intersticiel est rempli d'eau, d'huile ou de gaz. L'eau constitue également un film tout autour des grains et occupe toutes les fines crevasses. L'huile occupe les pores de taille moyenne, tandis que le gaz se trouve dans les plus larges pores.

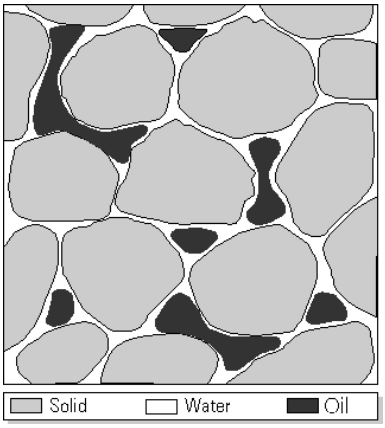

FIG. 3.5 – Représentation schématique des vides dans une roche.

La porosité et la saturation en eau (S_w) sont utilisées pour déterminer la quantité d'hydrocarbures présentes dans la roche. La porosité est mesurée à l'aide d'outils nucléaires ou acoustiques. Les outils de résistivités permettent de mesurer la saturation en eau (S_w) grâce à des lois empiriques liant la résistivité de la roche (R_t) à S_w. Parmi de telles lois, on peut citer la loi d'Archie, qui peut se mettre sous la forme simplifiée suivante :

$$S_w^n = \frac{a}{\phi^m}\frac{R_w}{R_t}$$

où R_w est la résistivité de l'eau présente dans les pores, n est l'exposant de saturation et m l'exposant de cémentation. En général, l'eau "fraiche" est plutôt résistive. L'eau salée, qui est souvent rencontrée dans les fortes profondeurs, là où se trouvent les hydrocarbures, est plutôt conductrice. La valeur de R_w est obtenue en mesurant la résistivité d'un banc de sable se trouvant à proximité de la zone d'intérêt.

En présence d'argiles, la relation d'Archie est modifiée car les argiles possèdent une conductivité propre non négligeable. En conséquence, cette argile va influencer la mesure de résistivité en fonction de son pourcentage. D'autres relations, par exemple de type Waxman-Smits, permettront de déterminer S_w connaissant en plus la proportion d'argiles dans la roche.

La fraction de la roche qui correspond effectivement à des hydrocarbures est alors donnée par $\phi(1 - S_w)$.

3.4.2 Principe physique

Il existe de nombreux outils de résistivité qui permettent une mesure locale (les outils à patins à faible profondeur d'investigation mais à grande résolution verticale) ou une mesure plus globale (les outils à "mandrel" à large profondeur d'investigation, mais à faible résolution verticale). Dans la suite, je n'évoquerai que ces derniers types d'outils.

Le principe physique est simple : une source (électrode ou solénoïde) envoie un signal (courant électrique, champ électromagnétique) dans la formation ; un récepteur situé à une certaine distance de la source enregistre les réactions du terrain à ce signal. On distingue deux grandes familles d'outils : les outils dits à induction et les outils latérologs.

- Les outils à induction, tels que l'AIT, utilisent des bobines de courants basses fréquences (quelques kHz) qui génèrent un champ primaire dans la formation. Ce champ induit un courant dans la formation qui génère à son tour un champ électromagnétique secondaire mesuré par la bobine réceptrice. Les outils à induction sont principalement utilisés dans des puits forés avec des boues à huile, qui ont des résistivités de l'ordre de 1000 ohm-m.
- Les outils latérologs, tels que le HALS ou le HRLA [14], injectent un courant basse fréquence (quelques Hz) dans la roche grâce à des électrodes métalliques directement en contact avec la boue du trou. La différence de potentiel mesurée en retour est directement liée à la résistivité de la roche. Ces outils sont surtout utilisés dans des boues à eau, qui ont des résistivités allant de 0.005 à 0.1 ohm-m.

Le but est de remonter, à partir des quantités mesurées, à la résistivité de la roche.

3.4.3 Les perturbations dans la mesure

Malheureusement, aucun des outils de résistivité n'est capable de mesurer directement R_t. Il existe plusieurs raisons à cela :

- l'outil n'est pas positionné directement dans la roche mais dans le trou de forage, le diamètre du trou ainsi que la résistivité de la boue (R_m) sont donc à prendre en compte,
- le gâteau de boue peut également influencer la mesure,
- il peut y avoir des phénomènes d'invasion, donc une perturbation des fluides présents dans les pores de la matrice, avec des zones de transition plus ou moins continues,
- la roche peut être anisotrope, voire même largement anisotrope,
- le trou de forage n'est pas forcément vertical et les effets tridimensionnels ne peuvent pas être négligés. En particulier, les outils de mesure sont sensibles à des zones bien plus grandes que les outils de densité, les valeurs des résistivités des couches se trouvant au-dessus ou au-dessous de la zone sondée vont également intervenir (effet d'épontes, effet Groningen, ...).

3.4.4 Traitement de la mesure

Malheureusement, tous ces paramètres ne peuvent pas être pris en compte simultanément. Il est alors nécessaire de procéder par petites étapes simplificatrices. Traditionnellement, la séquence de traitement utilisée est la suivante : on suppose que les différents effets cités ci-dessus sont dissociés et on corrige successivement pour l'effet de trou, l'effet d'épontes et l'effet d'invasion, en se plaçant dans une géométrie mono-dimensionnelle (Figure 3.6). La correction se traduit généralement par la multiplication de la mesure par un coefficient choisi dans des abaques. L'effet d'invasion est éventuellement corrigé en utilisant un algorithme d'inversion, où le vecteur des paramètres inconnus contient la résistivité de la

zone dite lavée R_{xo}, d'une zone de transition R_i, avant d'avoir la zone non contaminée ou formation vierge de résistivité R_t (figure 3.7).

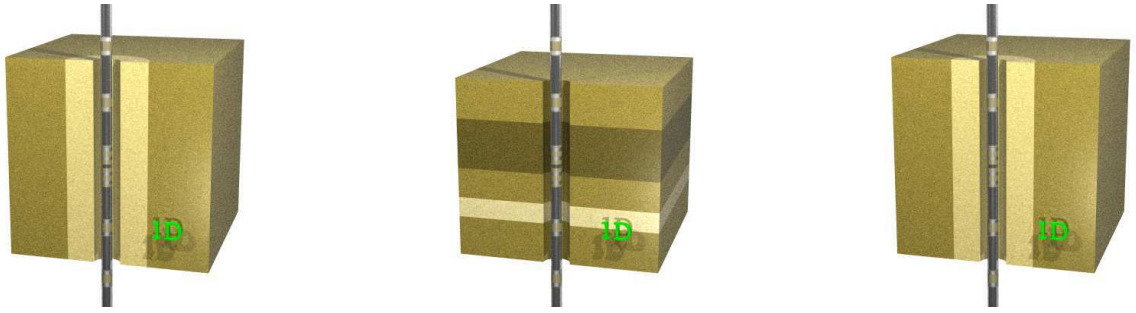

(a) (b) (c)

FIG. 3.6 – Traitement séquentiel 1D : Correction pour (a) l'effet de trou seul, (b) pour l'effet d'éponte seul, (c) pour l'effet d'invasion seul.

Dans les années 95, des algorithmes bidimensionnels (avec une symétrie radiale) (Figure 3.8), basés sur des techniques d'inversion, sont apparus [11]. On suppose maintenant couplés les effets d'invasion et les effets d'épontes tout en prenant en compte l'effet de trou dans la modélisation (l'hypothèse de symétrie radiale est toujours présente). Ceci nécessite donc de disposer de codes de modélisation directs permettant d'estimer la réponse des outils à des configurations données. Les codes employés étaient basés sur une résolution des équations par éléments finis, différences finies ou par des combinaisons de solutions analytiques et numériques [4]. Ces dernières années sont apparus des algorithmes d'inversion basés sur des modélisation 2.5D voire 3D (Figure 3.8) [2, 16].

3.4.5 Invasion 2

Le projet "Invasion 2" sur lequel je suis intervenue visait à rendre commercial un algorithme d'inversion utilisant une représentation bidimensionnelle de la configuration de mesure. Il se voulait adapté à la fois aux outils latérologs et inductifs et était basé sur un prototype développé en interne appelé Rt2D. Son but était de fournir un traitement plus fin de la mesure qui venait en complément d'une approche 1D+1D+1D telle que celle présentée Figure 3.6. J'ai donc participé à la fois au niveau de la définition du cahier des charges, à la mise en place de la version commerciale, au alpha-test et beta-test de la première version mais j'ai quitté Schlumberger avant sa commercialisation définitive.

Ce progiciel était pensé selon différents modules, qui pouvaient être sélectionnés de manière séquentielle si nécessaire :
- Traitement 1D multi-outils :
  - BestRt : Interface de traitement multi-outils permettant de sélectionner la réponse la mieux adaptée en fonction du domaine de validité des outils de résistivité qui avaient analysé la même zone,
  - TimeLapse : Interface de traitement multi-outils permettant de suivre le processus d'invasion entre deux passages d'outils de diagraphie, la première diagraphie ayant été effectuée pendant le forage, la deuxième diagraphie lors de la campagne d'exploration. Ce traitement multiphysique est basé sur une modélisation de l'écoulement des fluides dans une zone poreuse et de l'influence de tels écoulements sur les mesures de résistivité [12].

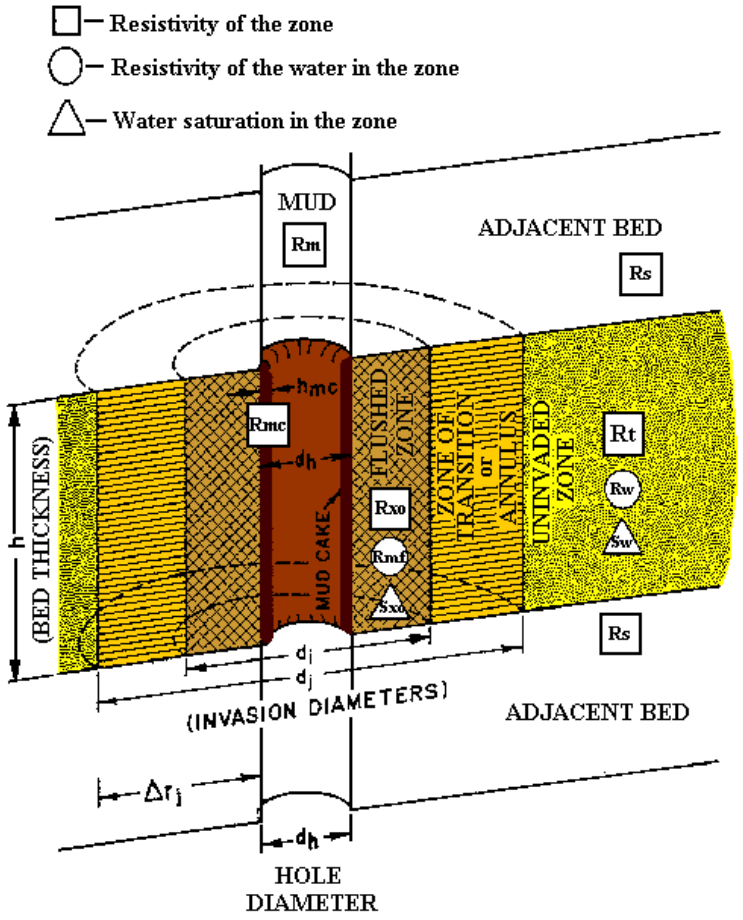

FIG. 3.7 – Modélisation radiale d'une couche, séparée en plusieurs zones de transition avant d'atteindre la formation vierge.

(a) (b)

FIG. 3.8 – Complexification de la modélisation de l'environnement entourant l'outil de résistivité, allant (a) d'une modélisation 2D à (b) une prise en compte du pendage du trou de forage (2.5D), avant d'aborder une configuration complète 3D anisotrope.

- Traitement 2D et 2.5D :
  - Automated Processing : Interface de traitement automatisé pour traiter une diagraphie de résistivité l'une après l'autre. Ce traitement est mis en place après qu'un traitement 1D+1D+1D classique a été effectué. A partir de la courbe 1D, une étape de sélection des couches horizontales est automatiquement effectuée pour définir la géométrie verticale. La géométrie radiale est définie comme un profil en forme de marche d'escalier, sans zone d'invasion. Une inversion 2D est alors effectuée, les seuls paramètres à rechercher sont les valeurs des résistivités de la zone vierge et de la zone envahie, et ce dans chaque couche, ainsi que le rayon de la zone envahie [7]. Tout le traitement est effectué de manière non supervisée.
  - Expert Processing : Interface de traitement supervisée. A partir des courbes 1D, une géométrie verticale est proposée. L'utilisateur peut faire évoluer la taille de chaque couche manuellement. Il peut ensuite adopter pour chaque couche un profil de résistivité plus ou moins complexe, profil radial avec une seule marche, avec plusieurs zones d'invasion, avec un profil d'invasion provenant de phénomènes d'écoulement des fluides, ... [9]. Les paramètres d'inversion vont donc changer d'une couche à l'autre en fonction des choix effectués par le pétrophysicien.
- Tool response simulation : Outil de simulation permettant d'obtenir la réponse d'un outil de résistivité dans une configuration de mesure donnée, afin de vérifier la validité d'un modèle pétrophysique mis au point par un pétrophysicien expert.

Des résultats obtenus avec un tel environnement logiciel sont visibles dans l'article inséré à la page 69 en fin de manuscrit, cet article a été écrit conjointement avec des clients où ils exposent les résultats obtenus ainsi que l'analyse pétrophysique qu'ils en ont fait spécifique de la zone sondée.

Outre le développement de ce progiciel, j'ai mené également des études prospectives afin d'améliorer les temps de calcul des algorithmes d'inversion utilisés, ainsi que leur robustesse au bruit. Un moyen simple d'accélérer le temps de traitement de la mesure était de calculer différemment les gradients qui interviennent dans les algorithmes itératifs, sachant qu'à l'époque, une différenciation numérique était employée. J'ai donc proposé et suivi tout un travail basé sur l'utilisation des états adjoints provenant d'une formulation lagrangienne du problème d'optimisation [6] afin d'obtenir une expression analytique rapide pour le calcul des gradients [8].

Bibliographie

[1] Highly integrated logging tool - HILT-B - Field engineer manual. Technical report, Schlumberger, 1995. 13

[2] A. Abubakar, T. Habashy, V. Druskin, L. Knizhnerman, and S. Davydycheva. A 3D parametric inversion algorithm for triaxial induction data. *Geophysics*, 71 :G1–G9, 2006. 20

[3] F. Allioli, O. Faivre, L. Jammes, and M. Evans. A new approach to computing formation density and Pe free of mudcake effects. *SPWLA Annual Logging Symposium*, 1997. 13

[4] B. Anderson. *Modeling and inversion methods for the interpretation of resistivity logging tool response*. PhD thesis, Delft University, 2001. 20

[5] F. Attale. On a switchless forward model. Technical report, Schlumberger - SRPC, 1998. 17

[6] D. Bertsekas. *Constrained optimization and lagrange multiplier methods*. Academic Press, 1982. 22

[7] M-T. Galli, M. Gonfalini, M. Mele, P. Belik, O. Faivre, L. Jammes, and A. Litman. Resistivity modeling of array laterolog tools : an application in an offshore norway clastic reservoir. *SPE Reservoir Evaluation Engineering*, 8 :77–87, 2005. 22

[8] M. Hamdi-Cherif. Calcul de sensibilité dans un code de différences finies 3D. Technical report, DESS, Univ. Pierre et Marie Curie, 2002. 22

[9] L. Jammes, O. Faivre, E. Legendre, P. Rothnemer, J-C Trouiller, M-T Galli, M. Gonfalini, and P. Gossenberg. Improved saturation determination in thin bed environments using 2D parametric inversion. *SPE Annual conference*, page 62907, 2000. 22

[10] A. Litman, S. Farag, and F. Allioli. Switchless density algorithm for the PEx. Technical report, Schlumberger - SRPC, 1999. 17

[11] A.G. Mezzatesta, M. Eckard, and K. Strack. Integrated interpretation of galvanic and induction measurements by inversion methods. *SPWLA Annual Logging Symposium*, 1995. 20

[12] T. Ramakrishnan and D. Wilkinson. Water cut and fractional flow logs from array induction measurements. *SPE Annual Conference*, pages 36503–MS, 1996. 20

[13] O. Serra. *Diagraphies différées. Bases de l'interprétation*. Bull. Cent. Rech. Explor. Prod. Elf-Aquitaine, 1979. 12

[14] J. Smits, D. Benimeli, I. Dubourg, O. Faivre, D. Hoyle, V. Tourillon, J-C Trouiller, and B. Anderson. High resolution from a new laterolog with azimuthal imaging. *SPE Annual Conference*, page 30584, 1995. 19

[15] A. Tarantola. *Inverse problem theory : Methods for data fitting and model parameter estimation*. Elsevier, 1987. 15

[16] M. Zhdanov and E. Tartaras. Three-dimensional inversion of multitransmitter electromagnetic data based on the localized quasi-linear approximation. *Geophysical journal international*, 148 :506–519, 2002. 20

Chapitre 4

Diffraction inverse - Généralités

4.1 Introduction

Lorsqu'une onde électromagnétique interagit avec un ou plusieurs obstacles, elle génère un champ appelé champ diffracté, qui est directement lié à la présence de ces obstacles et de leurs caractéristiques électromagnétiques. On parle de problème direct lorsque toutes les conditions expérimentales sont parfaitement maîtrisées : on connaît exactement les propriétés électromagnétiques de la source primaire (fréquence d'émission ou largeur d'impulsion, diagramme de rayonnement, position, ...) ainsi que toutes les propriétés électromagnétiques de l'environnement entourant la source (permittivité diélectrique, géométrie, ...). Le but est alors d'étudier le champ résultant de l'interaction de l'onde émise par la source et l'obstacle. Lorsque les dimensions des obstacles sont de l'ordre de la longueur d'onde, des phénomènes de diffraction apparaissent. La difficulté réside ici dans le fait de pouvoir fournir une description précise de l'environnement afin de modéliser correctement l'interaction des ondes.

On parle ensuite de problème inverse de diffraction lorsqu'on ne connaît que les propriétés électromagnétiques de la source primaire ainsi qu'une idée des caractéristiques électromagnétiques de l'environnement dans lequel l'onde se propage. Le but est ici de déterminer les propriétés géométriques (forme, position) ou physique (caractéristiques diélectriques) des objets présents. La plus grande majorité de mes travaux de recherche porte sur cette problématique, avec la mise au point théorique de nouveaux algorithmes numériques permettant de remonter aux caractéristiques des diffracteurs à partir de la mesure du champ électromagnétique en un certain nombre de capteurs. Avant d'aller plus avant dans le sujet, un bref rappel des notations et des principes physiques mis en jeu s'avère nécessaire.

4.2 Principe physique

Les obstacles ont des formes géométriques complexes Ω et sont supposés être contenus dans un domaine borné D. Le milieu extérieur entourant ces objets Ω_b est supposé de permittivité connue $\varepsilon_b = \varepsilon_0 \varepsilon_{br}$ et de perméabilité connue $\mu = \mu_0$ (ε_0 et μ_0 correspondent à la permittivité et perméabilité du vide). Les obstacles ont une permittivité diélectrique complexe différente de celle de l'environnement $\varepsilon(\mathbf{r}) = \varepsilon_0 \varepsilon_r(\mathbf{r})$. La configuration d'étude est supposée non-magnétique $\mu = \mu_0$. Les sources qui génèrent l'excitation électromagnétique sont localisées sur certains points de l'espace $(\mathbf{r}_l)_{1 \leq l \leq L}$ et fonctionnent en régime harmonique (Figure 4.1).

L'équation de Lippman-Schwinger suivante [2, 4] traduit un phénomène de diffraction général pour un objet pénétrable quelconque

$$E_l(\mathbf{r} \in D) \quad = \quad E_l^{\mathrm{i}} + k_0^2 \int_D \chi(\mathbf{r}')\, E_l(\mathbf{r}')\, G(\mathbf{r}, \mathbf{r}')\, \mathrm{d}\mathbf{r}'. \tag{4.1}$$

La fonction $\chi(\mathbf{r}) = \varepsilon_r(\mathbf{r}) - \varepsilon_{br}$ est appelée contraste de permittivité et devient nulle en dehors du domaine $D \supset \Omega$. $G(\mathbf{r}, \mathbf{r}')$ correspond à la fonction de Green associée à la configuration d'étude et k_0 représente le nombre d'onde du vide. Le champ E_l est traditionnellement appelé champ total. De part la linéarité des équations de Maxwell, il correspond à la superposition du champ incident E_l^{i} qui est mesuré lorsqu'il n'y pas de diffracteurs et du champ diffracté E_l^{s}, qui correspond au champ rayonné par les courants induits à l'intérieur des diffracteurs Ω.

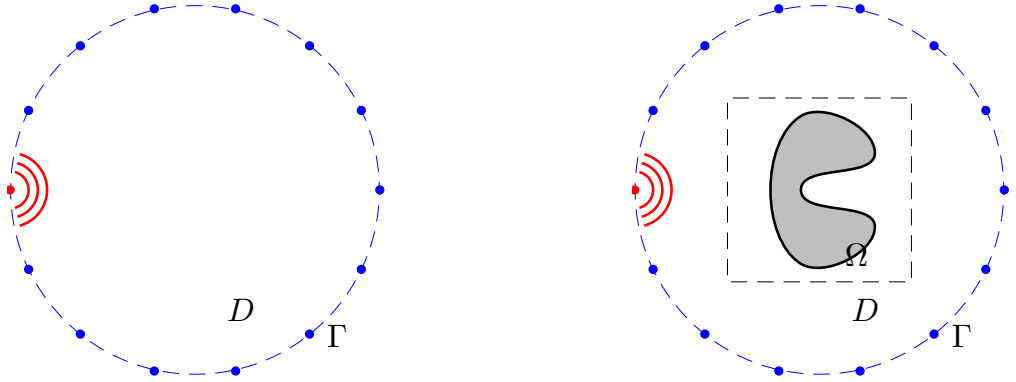

(a) Champ incident (b) Champ total

FIG. 4.1 – Configuration associée à la mesure du champ incident et du champ total avec le positionnement des antennes en émission et réception sur une ligne Γ. D désigne la zone où se trouve l'objet.

Lorsque le point d'observation se trouve en dehors de la zone test D, l'équation précédente se transforme en une équation de Fredholm de première espèce

$$E_l^{\mathrm{s}}(\mathbf{r} \in \Gamma) \quad = \quad k_0^2 \int_D \chi(\mathbf{r}')\, E_l(\mathbf{r}')\, G(\mathbf{r}, \mathbf{r}')\, \mathrm{d}\mathbf{r}' = k_0^2 \int_D J(\mathbf{r}')\, G(\mathbf{r}, \mathbf{r}')\, \mathrm{d}\mathbf{r}', \tag{4.2}$$

où $J(\mathbf{r}')$ correspond aux courants induits à l'intérieur des diffracteurs.

Les phénomènes de diffraction sont présentés ici avec un formalisme intégral car celui-ci correspond au formalisme le plus souvent employé par la communauté des problèmes inverses de diffraction. C'est d'ailleurs sous ce formalisme que j'ai abordé jusqu'en 2005 ces problèmes en utilisant la méthode des moments [5]. Depuis, en collaboration avec H. Tortel, je me suis plus particulièrement attachée à prendre en compte un formalisme basé sur une formulation faible des équations de Helmholtz [6] en utilisant des outils de résolution basés sur la méthode des éléments finis [3, 8]. L'avantage d'un formalisme par éléments finis est de pouvoir bénéficier d'un maillage conforme et donc d'une meilleure prise en compte de l'information a priori disponible sur la géométrie de la configuration de mesure.

4.3 Problème inverse

Le problème inverse consiste à retrouver les cartes de permittivité $\chi(\mathbf{r})$ à partir de la mesure du champ diffracté sur un certain nombre de récepteurs $(\mathbf{r}_r)_{1 \leq r \leq N}$ positionnés sur une ligne de mesure Γ (Figure 4.2).

Ce problème inverse peut être reformulé en terme de problème d'optimisation. Dans ce cas, les paramètres inconnus, à savoir le contraste χ, le champ total E dans la zone d'investigation et le champ diffracté E^{s} sur les récepteurs sont progressivement ajustés de manière à minimiser une fonctionnelle $\mathcal{J}(\chi)$ correctement choisie. Traditionnellement, cette fonctionnelle est définie de manière à représenter la différence qui existe entre les champs mesurés et les champs simulés sur les récepteurs

$$\mathcal{J}(\chi) = \frac{1}{2} \sum_{l=1}^{L} \| E_l^{\mathrm{obs}} - E_l^{\mathrm{s}}(\chi) \|_{W,\Gamma}^2 \tag{4.3}$$

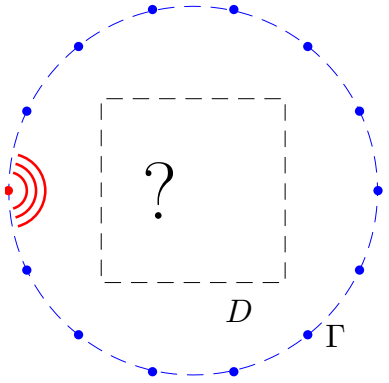

FIG. 4.2 – Configuration associée au problème inverse. On mesure le rayonnement sur les différentes antennes et on cherche les variations de permittivité se trouvant dans la zone inconnue D.

où E^{obs} correspond aux champs mesurés disponibles pour chaque incidence l. La norme $\| \|^2_{W,\Gamma}$ correspond à une norme pondérée, la pondération variant d'un émetteur à un autre et d'un récepteur à un autre.

Il faut alors minimiser cette fonctionnelle sous les contraintes imposées par les équations (Eq. 4.1) et (Eq. 4.2). Sous certaines approximations (approximation de Born par exemple) ou si on ne s'intéresse qu'aux géométries, la contrainte imposée par (Eq. 4.1) est oubliée et le problème d'optimisation devient un problème linéaire. La solution s'obtient alors en calculant l'inverse de Moore-Penrose [1] de l'opérateur linéaire associé. Si par contre les deux équations sont prises en compte, le problème est non-linéaire et il n'existe pas de solutions explicites. Dans ce cas, une suite d'approximations successives $\chi^{(n)}$ est construite en utilisant des relations de récurrence

$$\chi^{(n)} = \chi^{(n-1)} + \alpha^{(n)} d^{(n)} \tag{4.4}$$

et tout l'art réside alors dans le choix de la direction de descente $d^{(n)}$ et du pas $\alpha^{(n)}$ [9].

Il existe un nombre grandissant de méthodes d'inversion et une large littérature associée [1, 4, 7]. Ceci s'explique par le fait que les relations liant les paramètres inconnus aux données diffèrent d'une configuration expérimentale à une autre, rendant parfois impossible l'utilisation de techniques précédemment développées. De plus, comme on ne dispose que d'un nombre réduit de données, il est nécessaire de compenser cette sous-détermination par de l'information a priori. Mais cette information a priori doit être judicieusement choisie en fonction de la configuration expérimentale étudiée. Chaque nouveau type d'information a priori correspondra alors à un nouveau problème et débouchera éventuellement sur une nouvelle méthode d'inversion.

Dans un premier temps, je m'attacherai à décrire les différentes configurations expérimentales que j'ai eu à étudier aux cours de ces dernières années. Je m'efforcerai de mettre en avant les spécificités de traitement qui ont été mis en place pour chaque cas d'étude. Dans un deuxième temps, je décrirai comment j'ai introduis différents types d'informations a priori dans des algorithmes d'inversion, sachant que ces nouvelles méthodes d'inversion ne sont pas forcément spécifiques à une configuration expérimentale donnée.

Bibliographie

[1] M. Bertero, P. Boccaci, and P. Boccaci. *Introduction to inverse problems in imaging*. Institute of Physics, 1998. 28

[2] W.C. Chew. *Waves and fields in inhomogeneous media*. IEEE Press, 1995. 26

[3] O. Cmielewski, H. Tortel, A. Litman, and M. Saillard. A two-step procedure for characterizing obstacles under a rough surface from bistatic measurements. *IEEE Trans. Geosci. Remote Sens.*, 45 :2850–2858, 2007. 27

[4] D. Colton and R. Kress. *Inverse acoustics and electromagnetic scattering theory*. Springer-Verlag, 1997. 26, 28

[5] R. Harrington. The method of moments in electromagnetics. *J. Electromagn. Waves Applic.*, 1 :181–200, 1987. 27

[6] J. Jin. *The finite element method in electromagnetics*. Willey-Interscience, 2002. 27

[7] A. Kirsch. *An introduction to the mathematical theory of inverse problems*. Springer-Verlag, 1996. 28

[8] R. Lencrerot, A. Litman, H. Tortel, and J-M. Geffrin. Measurement strategies for a confined microwave circular scanner. *Inverse Problems in Science and Engineering*, page 357869, 2009. 27

[9] J. Nocedal and S. Wright. *Numerical optimization*. Springer-Verlag, 2006. 28

Chapitre 5

Diffraction inverse - Configurations expérimentales

Dans ce chapitre sont présentées les trois configurations de mesure que j'ai eu à étudier durant ces dernières années. La première est la plus simple en terme de modélisation car elle correspond à une configuration dite en espace libre, la seconde a l'avantage d'avoir un domaine de définition limité de part la présence de parois métalliques, la dernière configuration, celle d'un demi-espace, est beaucoup plus complexe à gérer de part le fait que les antennes ne capturent pas toute la signature électromagnétique des objets diffractants.

5.1 Espace libre

5.1.1 Géométrie

La grande chambre anéchoique à laquelle a accès l'Institut Fresnel se situe au sein du Centre Commun de Ressources Microondes (CCRM) (figure 5.1) [14]. Elle consiste en une grande chambre faradisée et anéchoique de 14.50 m de long, 6.50 m de large, et 6.50 m de haut. Sa spécificité réside dans une arche semi-circulaire sur laquelle sont montés deux chariots servant à positionner des antennes. Elle permet de faire des mesures de diagrammes de diffraction dans une configuration à géométrie sphérique, les émetteurs et les récepteurs étant disposés sur une sphère autour de l'objet.

Fig. 5.1 – Grande chambre anéchoique de l'Institut Fresnel

De nombreuses configurations expérimentales peuvent être étudiées grâce à cinq positionneurs mécaniques. Le premier permet d'ajuster l'orientation de l'objet sous test qui est placée au centre du dispositif sur un mat en polystyrène. Le second positionneur contrôle le bras mécanique sur lequel est positionné une antenne, ce bras bougeant dans un plan horizontal radialement autour du mat. Les troisième et quatrième positionneurs servent à déplacer les antennes qui sont fixées sur les deux wagons de l'arche. Le bras azimutal

et l'arche ont un rayon de 2 m. Finalement, le cinquième positionneur, placé à 10.5 m de l'objet sert pour les mesures de SER.

De part son anéchoicité, sa modélisation électromagnétique en est très simple car elle est directement comparable à une configuration en espace libre (condition de radiation de Sommerfeld à l'infini). Le seul élément perturbateur dans la configuration expérimentale provient de l'obstacle qui est placé au centre du dispositif.

5.1.2 Diffraction par des objets 2D

Cette chambre a d'abord servi à mesurer les champs diffractés par des objets bidimensionnels, ces champs ont ensuite été proposés à la communauté internationale "Problèmes inverses" lors de deux sessions spéciales [1, 2] publiées dans la revue "Inverse Problems" en 2001 et 2005. Ma contribution lors de ces deux sessions spéciales a principalement été axée sur le développement de nouvelles méthodes d'inversion.

En 2001, lors de mon post-doctorat effectué sous la direction de A.G. Tijhuis à l'Université d'Eindhoven, je me suis attachée à démontrer l'intérêt d'algorithmes de minimisation de type Distorted wave-Born ou de type quasi-Newton pour améliorer la résolution des reconstructions obtenues [24], c'est-à-dire à proposer de nouvelles techniques de sélection de la direction de descente $d^{(n)}$ intervenant dans (Eq. 4.4). L'utilisation conjointe d'une approche multi-fréquence, par une technique dite de saut en fréquence ("frequency-hopping"), a d'ailleurs été employée avec succès. La justification théorique de ce "frequency-hopping" a été décrite en détail dans [25].

En 2005, comme les objets diffractants inconnus étaient donnés comme étant des objets homogènes de matériaux connus, je me suis plus particulièrement attachée à introduire cette information a-priori à l'intérieur d'un algorithme d'inversion [19] grâce à l'utilisation d'un formalisme par fonctions de niveau qui sera repris dans la Section 6.3.

5.1.3 Diffraction par des objets 3D

Au vu de l'essor des méthodes numériques prenant en compte les effets tridimensionnels et la polarisation des ondes, il a alors été décidé de poursuivre l'expérience des sessions spéciales en proposant cette fois-ci des champs diffractés par des objets tridimensionnels. Malheureusement, comme les dimensions des objets sont de l'ordre de la longueur d'onde, l'amplitude des champs diffractés associés sont très faibles et proches du niveau de bruit de l'appareillage électronique de la chambre. Il a donc fallu revoir le protocole de mesure afin d'obtenir des sensibilités de mesure suffisantes. J'ai participé à ce travail en collaboration avec C. Eyraud, J-M. Geffrin et P. Sabouroux, avec un intérêt porté plus particulièrement sur le bruit de mesure et son influence sur le spectre du champ diffracté mesuré.

Ceci a donné lieu à plusieurs résultats intéressants :
– la définition d'une correction de dérive basée sur la largeur spectrale du champ diffracté. En effet, il est montré théoriquement qu'un champ diffracté par un objet à support spatial borné est forcément à bande limité [3]. Les hautes composantes spectrales que nous retrouvions expérimentalement ne pouvaient donc pas provenir du diffracteur mais du bruit de mesure, que nous avons modélisé comme un coefficient de dérive traduisant les variations expérimentales survenant entre l'instant où le champ incident était mesuré et celui où le champ total était à son tour mesuré (Figure 5.2). Au lieu d'effectuer un filtrage passe-bas, nous avons préféré mettre au point une procédure de minimisation

de spectre qui a pour avantage de ne pas nécessiter d'information supplémentaire sur la largeur de bande du champ diffracté, donc d'information supplémentaire sur le rayon de la sphère minimale entourant les diffracteurs [9]. De plus amples détails sur la méthode sont disponibles dans l'article correspondant qui a été inséré à la page 79 en fin de manuscrit.

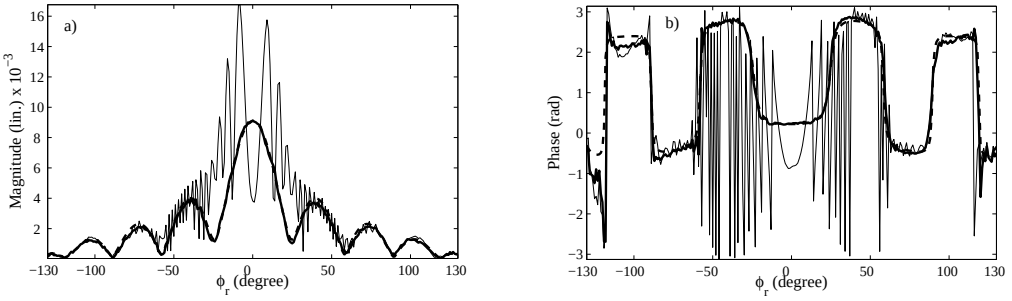

(a) (b)

FIG. 5.2 – (a) Amplitude et (b) phase du champ diffracté par une sphère diélectrique de diamètre 50 mm, mesuré à 11 GHz dans la chambre anéchoique. (Trait plein fin) Champ mesuré sans correction de dérive, (Trait plein épais) champ mesuré avec correction de dérive, (Trait en pointillé) champ simulé.

- l'optimisation du protocole de mesure, avec la mise en place d'une procédure de calibration très simplifiée, basée sur la détermination d'un coefficient complexe de correction en amplitude et phase, en n'utilisant que la mesure dans une seule polarisation de la diffraction par une sphère métallique prise comme objet de référence [13],
- la validation de la chaîne complète de mesure, en comparant les champs mesurés à des champs simulés pour des objets diffractants parfaitement connus et maîtrisés expérimentalement [10],
- la prise en compte du bruit de mesure dans les algorithmes d'inversion, en adaptant la forme de la matrice de pondération W qui intervient dans la fonctionnelle coût à minimiser (Eq. 4.3). Les analyses de bruit qui ont été menées [13] ont permis de caractériser le bruit associé à la grande chambre anéchoique comme étant du bruit additif blanc gaussien, dont la variance est directement proportionnelle à l'amplitude des champs mesurés, à savoir le champ total et le champ incident, et non pas à l'amplitude du champ diffracté comme cela était traditionnellement utilisé en problèmes inverses de diffraction. La variance varie de plus en fonction de la fréquence et de la position des antennes d'émission et de réception. Dans [11], nous avons montré qu'il est important de déterminer correctement le bruit de mesure pour améliorer les cartes de permittivité reconstruites lorsqu'on l'introduit dans un algorithme d'inversion (Figure 5.3).
- la mise en place de la troisième base de données pour la session spéciale dans Inverse Problems qui est parue en 2009 et dont j'ai été la co-éditrice avec L. Crocco [21]. Cette session spéciale a regroupé 6 contributions venant d'équipes de recherche internationales spécialisée en problèmes inverses de diffraction (Figure 5.4).

5.1.4 Mesures sans phase

Lorsqu'on s'intéresse à des montages dans le régime des longueurs d'onde de l'optique ou lorsqu'on simplifie l'appareillage de mesure, il devient alors parfois impossible voire difficile de mesurer la phase du champ électromagnétique. La problématique est alors de pouvoir

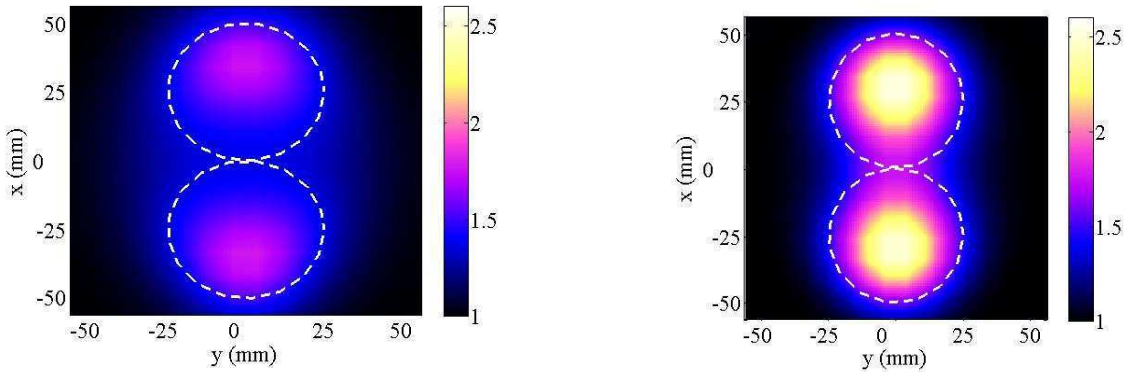

(a) (b)

FIG. 5.3 – Cartes de permittivité reconstruites à partir des champs mesurés à 3 GHz dans la grande chambre anéchoique, lorsque l'information sur la nature du bruit est introduite à l'intérieur de la fonctionnelle (Eq. 4.3). La matrice de pondération est (a) prise égale à la matrice identité , ou (b) elle tient compte de la nature exacte du bruit de mesure. L'objet est constitué de deux sphères diélectriques de permittivité relative 2.6, collées l'une à l'autre et leur contour est représenté en pointillé sur la figure.

Inverse
Problems

Volume 25 Number 2 February 2009

SPECIAL SECTION ON TESTING INVERSION ALGORITHMS AGAINST EXPERIMENTAL DATA: 3D TARGETS

GUEST EDITORS' INTRODUCTION

020201 **Testing inversion algorithms against experimental data: 3D targets**
Amélie Litman, Lorenzo Crocco and Guest Editors

SPECIAL SECTION PAPERS

024001 **Continuing with the Fresnel database: experimental setup and improvements in 3D scattering measurements**
J M Geffrin and P Sabouroux

024002 **3D microwave imaging via preliminary support reconstruction: testing on the Fresnel 2008 database**
Ilaria Catapano, Lorenzo Crocco, Michele D'Urso and Tommaso Isernia

024003 **Three-dimensional reconstruction from real data using a conjugate gradient-coupled dipole method**
Patrick C Chaumet and Kamal Belkebir

024004 **Three-dimensional quantitative microwave imaging from measured data with multiplicative smoothing and value picking regularization**
Jürgen De Zaeytijd and Ann Franchois

024005 **Microwave imaging from experimental data within a Bayesian framework with realistic random noise**
C Eyraud, A Litman, A Hérique and W Kofman

024006 **Application of the multiplicative regularized contrast source inversion method on 3D experimental Fresnel data**
Maokun Li, Aria Abubakar and Peter M van den Berg

024007 **Reconstruction of 3D objects from multi-frequency experimental data with a fast DBIM-BCGS method**
Chun Yu, Mengqing Yuan and Qing Huo Liu

FIG. 5.4 – Troisième session spéciale dans la revue Inverse Problems, traitant d'algorithmes d'inversion pour des objets diffractants tridimensionnels.

remonter aux cartes de permittivité à partir de la mesure de l'amplitude du champ seul. Ce travail a été effectué conjointement avec K. Belkebir et l'Instituto per il Rilevamento Elettromagnetico dell'Ambiante (IREA) en Italie.

Dans un premier temps, nous avons supposé que nous pouvions mesurer toutes les phases hormis celle du champ diffracté. Dans ce cas, la fonctionnelle coût à minimiser devient

$$\mathcal{J}(\chi) = \frac{1}{2}\sum_{l=1}^{L} \| I_l^{obs} - |E_l^s(\chi)|^2 \|_{W,\Gamma}^2 \tag{5.1}$$

où I_l^{obs} correspond aux intensités des champs diffractés mesurés disponibles pour chaque incidence l. Ce problème est toujours non-linéaire et le calcul de la direction de descente $d^{(n)}$ est un peu plus complexe à obtenir. Nous avons alors montré qu'il pouvait se calculer facilement en utilisant la notion d'état adjoint [20]. Cet état adjoint n'est rien d'autre qu'un autre problème de diffraction où les récepteurs deviennent sources et renvoient conjointement la différence qui existe à ces endroits précis entre le champ mesuré et le champ simulé (cf Section 6.1). Nous avons montré en utilisant des approximations de Born dans le calcul des champs totaux et des champs adjoints qu'on retombait sur des expressions simplifiées de direction de descente que l'on rencontre classiquement dans la littérature. De plus, les techniques de rétropropagation classique [15] ne fonctionnant pas sans phase, j'ai mis au point une autre façon de déterminer l'estimation initiale $\chi^{(0)}$ en utilisant des notions issues des dérivées topologiques [22] (Figure 5.5. Tous les résultats et les détails associés à cette approche sont visibles dans l'article inséré à la page 82 en fin de manuscrit.

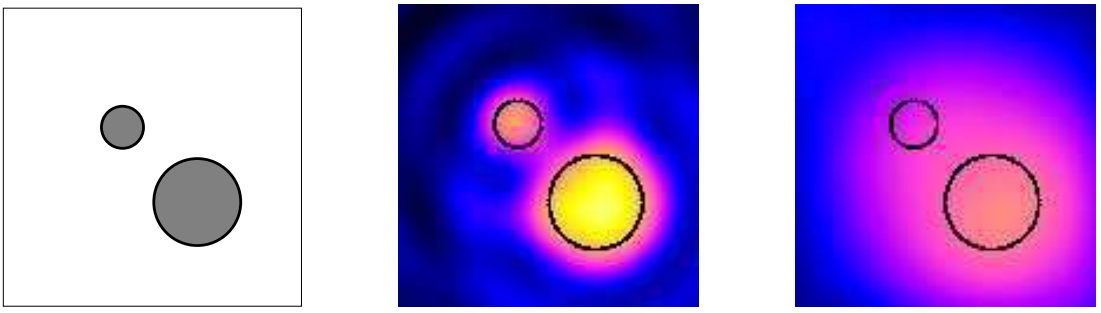

(a) (b) (c)

FIG. 5.5 – (a) Image exacte, (b) Image obtenue par dérivées topologiques en utilisant le module et la phase, (c) Image obtenue par dérivées topologiques en n'utilisant que le module.

Dans un deuxième temps, afin de se rapprocher au mieux d'une réalité expérimentale, nous avons supposé que nous ne pouvions mesurer ni l'amplitude ni la phase des champs incidents et totaux. La phase du champ incident peut être retrouvée, connaissant son amplitude et le diagramme de rayonnement de la source, à condition qu'un nombre suffisant de mesures du champ incident soit effectué [5]. Reste alors à retrouver la phase du champ total, et donc par déduction celle du champ diffracté. Nous avons alors comparé deux approches :

– soit nous changeons le critère de minimisation (Eq. 5.1) en ne travaillant plus que sur le champ total,

$$\mathcal{J}(\chi) = \frac{1}{2}\sum_{l=1}^{L} \| I_l^{obs} - |E_l(\chi)|^2 \|_{W,\Gamma}^2, \tag{5.2}$$

avec I_l^{obs} étant cette fois-ci l'intensité du champ total mesuré sur la ligne de mesure. Ceci implique à nouveau de calculer les nouveaux gradients associés à cette fonctionnelle coût.

– soit nous passons par une première étape de récupération de la phase du champ diffracté. En effet, la phase du champ total fait apparaître un terme d'interférences entre la phase du champ incident et la phase du champ diffracté,

$$|E_l|^2 = |E_l^{\mathrm{i}}|^2 + |E_l^{\mathrm{s}}|^2 + 2\Re e(E_l^{\mathrm{s}} E_l^{\mathrm{i}*}).$$

A partir de ce terme d'interférence et avec suffisamment de points de mesure, il est possible d'extraire la phase du champ diffracté. L'algorithme redevient alors un algorithme classique avec minimisation de la fonctionnelle (Eq. 4.3).

Les deux approches ont été testées en utilisant les données de la chambre anéchoique pour des objets bidimensionnels en polarisation $E//$ [8].

5.2 Scanner circulaire

5.2.1 Géométrie

La configuration du scanner circulaire (Figure 5.6) s'appuie sur le prototype expérimental mis au point par J-M. Geffrin il y a une dizaine d'années lors de travaux de recherche dans le domaine biomédical [12] et qui a été transféré du Laboratoire des Signaux et Systèmes à l'Institut Fresnel en 2002.

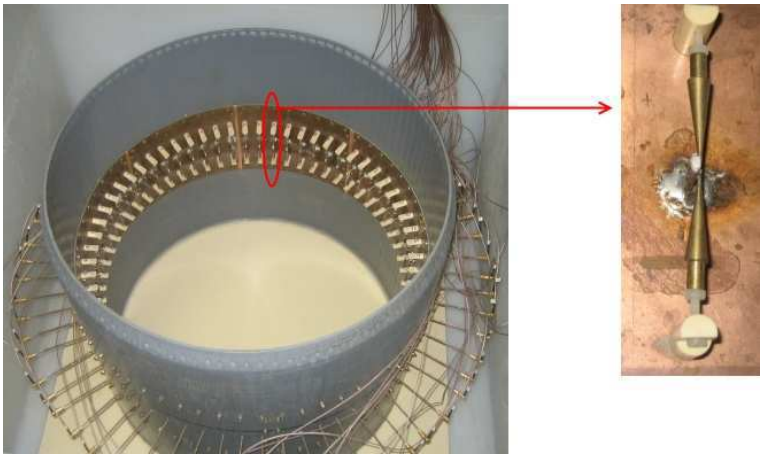

FIG. 5.6 – Photo du scanner circulaire et antenne biconique

Ce système de mesure est constitué d'une cavité circulaire métallique, afin de s'affranchir des perturbations électromagnétiques provenant de l'environnement extérieur. Il dispose de 64 antennes biconiques pouvant émettre et recevoir un champ électromagnétique, placée sur une couronne à l'intérieur du cylindre métallique. Ces antennes sont adaptées pour rayonner dans l'eau ($\varepsilon_{br} \approx 80 + 3i$) à 434 MHz. A cette fréquence, la longueur d'onde dans l'eau est de l'ordre de 7.7 cm. Un multiplexeur/démultiplexeur permet d'effectuer un balayage électronique des antennes, sachant que lorsqu'une antenne émet, les autres deviennent réceptrices. Le tout est relié à un analyseur de réseau et est commandé par un ordinateur.

Ce système a été largement exploité dans le cadre du projet CESAR où le but ultime est de positionner une colonne de terre (monolithe) à l'intérieur d'une telle structure afin de pouvoir visualiser et contrôler l'évolution de la teneur en eau à l'intérieur du monolithe. En effet, la permittivité des matériaux varie suivant plusieurs paramètres (température, fréquence, humidité, ...). Il existe en particulier des relations empiriques liant la teneur eau à la permittivité des roches [26]. En mesurant les perturbations des champs électromagnétiques introduites par une variation de la permittivité, et en utilisant des algorithmes d'inversion, on peut remonter aux cartes de permittivité associées et ainsi, aux cartes de teneur en eau de la zone illuminée.

Sa modélisation électromagnétique est un peu plus complexe car il faut tenir compte de la paroi métallique. Plusieurs méthodes de modélisation ont été mises en place dans le cadre d'une configuration supposée bidimensionnelle en polarisation $E//$, basées soit sur une formulation intégrale avec la fonction de Green de la cavité ou la fonction de Green de l'espace libre associée à des techniques de de-embedding, soit sur une formulation faible avec l'utilisation des éléments finis (Figure 5.7). C'est vers cette dernière voie que l'accent s'est porté ces dernières années, en particulier lors de la thèse de R. Lencrerot [16] que j'ai co-encadrée.

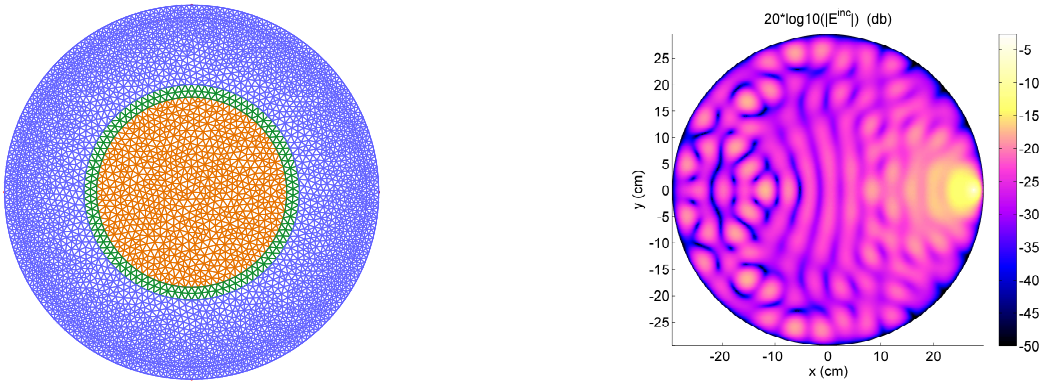

(a) Maillage (b) Champ incident

FIG. 5.7 – (a) Maillage par éléments finis de la cavité circulaire. Dans la modélisation, la paroi en PVC qui entoure la colonne de sol est également prise en compte. La colonne est supposée positionnée dans la zone centrale de la cavité. (b) Module du champ incident rayonnée par une antenne placée seule à l'intérieur de la cavité.

.

5.2.2 Diffraction par des objets 2D

Les premières mesures effectuées à l'aide de ce scanner circulaire l'ont été sur des objets parfaitement contrôlés, à savoir des fantômes constitués d'assemblage de cylindres remplis de liquides de différentes permittivités. Ces cylindres étant suffisamment longs, une approximation bidimensionnelle a donc été possible. Un protocole de mesure a ainsi été mis au point, en collaboration avec J-M. Geffrin et H. Tortel. Il consiste à effectuer trois mesures successives :

– une mesure à vide, la cuve étant simplement remplie d'eau, afin de mesurer le champ incident. Nous nous sommes d'ailleurs aperçus qu'il était nécessaire de faire chauffer au préalable l'eau afin d'en éliminer les bulles d'air qui se collent sur les antennes et en perturbent le rayonnement électromagnétique,

– une mesure avec un obstacle de référence, pris ici comme étant un cylindre métallique,
– une mesure avec l'objet inconnu à imager.

Un protocole de calibration a ensuite été mis en place, similaire à celui utilisé dans la grande chambre anéchoique (Figure 5.8). Certaines subtilités propres à la configuration ont été introduites, en particulier le fait de calibrer en se basant sur la forme du champ des antennes voisines, en éliminant les antennes qui ne fonctionnent pas lors de l'expérience dû à des problèmes de soudures défaillantes (phénomènes de corrosion), ...

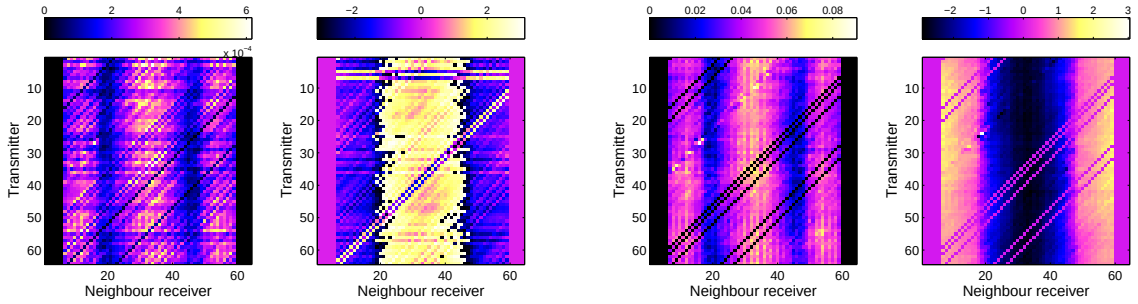

(a) Amplitude et phase brutes (b) Amplitude et phase calibrées

FIG. 5.8 – (a) Matrice de diffraction brute, (b) Matrice de diffraction après calibration et détection/élimination des antennes défaillantes (ce qui correspond aux lignes en noir sur la matrice de diffraction). L'objet mesuré correspond à un cylindre centré métallique de diamètre 60cm.

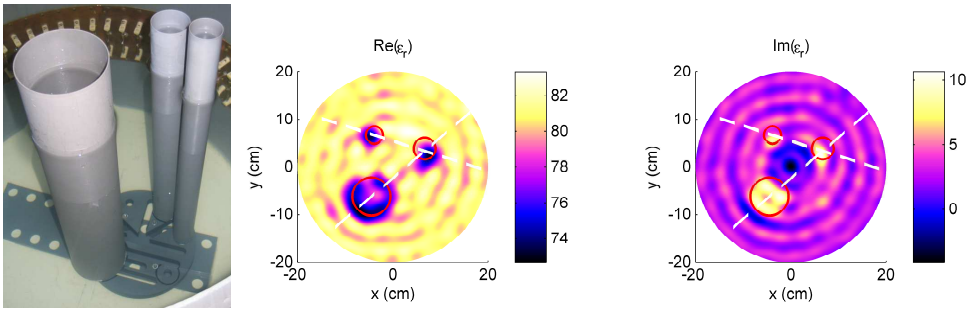

(a) Fantômes (b) Cartes reconstruites

FIG. 5.9 – (a) Fantôme constitué de trois tubes remplis de mélange d'éthanol et d'eau. (b) L'image reconstruite associée à cette expérience montre la partie réelle et imaginaire de la permittivité. Les cercles concentriques qui sont également visibles correspondent à un effet de cavité dû à une imprécision de mesure sur la permittivité de l'eau qui est utilisée comme information a-priori lors du calcul du problème de simulation électromagnétique associé.

L'algorithme d'inversion associé est un algorithme de type gradient-conjugué classique où la fonctionnelle coût est toujours celle explicitée en (Eq. 4.3). Le calcul du gradient se fait toujours en utilisant la notion d'état adjoint. L'avantage ici provient du fait que les émetteurs et les récepteurs sont positionnés au même endroit et donc que le calcul du champ adjoint est déjà fait lors du calcul du champ total. Les résultats obtenus ont été présentés dans [16, 18] et un exemple est illustré dans la figure 5.9. Les antennes qui sont détectées comme défectueuses sont automatiquement ignorées par l'algorithme d'inversion, grâce à des masques précisant les couples d'antennes valables. Une sophistication de cet

algorithme d'inversion a également été entreprise avec l'ajout d'information a priori (cf Section 6.2 et Section 6.3).

5.2.3 Optimisation de configuration

Au vu des performances du scanner existant par rapport à l'application visée, à savoir visualiser les variations de teneur en eau dans le sol, nous avons été amenés à réfléchir à la conception d'une nouvelle génération du scanner circulaire. Avant de se lancer dans la construction d'un nouveau prototype, une approche théorique a été mise en place afin de définir la notion d'optimalité et de déterminer les paramètres qui sont les plus critiques.

Deux approches ont été menées :
- Dans un premier temps, nous avons essayé de tirer partie au mieux de la configuration existante, en conservant la géométrie des antennes, la fréquence de fonctionnement, ... Nous avons donc joué sur la position de la colonne de sol à l'intérieur de la cuve, de la possibilité d'y adjoindre une couronne d'adaptation optimisée pour limiter les phénomènes de réflexion aux interfaces. Les résultats obtenus sont synthétisés dans [17].
- Dans un deuxième temps, nous avons joué sur tous les paramètres disponibles et avons défini des critères théoriques basés sur l'utilisation des spectres de l'opérateur de radiation qui régit le phénomène de diffraction à l'intérieur de la cavité (Figure 5.10. Cet opérateur est défini par l'équation (Eq. 4.2) en prenant en compte l'expression analytique de la fonction de Green adaptée à la configuration de mesure, i.e., tenant compte des réflexions multiples dûes à la paroi métallique. Ce travail, effectué conjointement avec L. Crocco de l'IREA, a montré l'influence des modes de la cavité dans la définition d'une configuration optimale ainsi que l'importance des positions des antennes vis-à-vis de la paroi métallique [6]. Cet article est repris en fin de document (page 92).

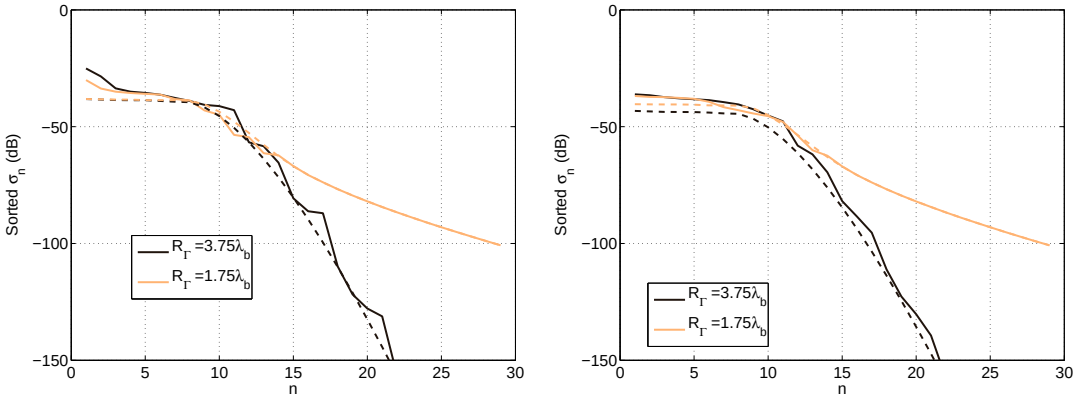

(a) Sans pertes (b) Avec pertes

FIG. 5.10 – Comparaisons du spectre de l'opérateur de diffraction dans le cas de l'espace libre (trait pointillé) ou du scanner circulaire (trait plein) pour deux positions de la ligne de mesure. L'objet est situé au centre du domaine, avec un rayon $R_\Omega = 1.5\lambda$ et la paroi métallique, si elle existe, est située à $R_\Sigma = 4\lambda$. Le milieu ambiant est soit (a) sans pertes, soit (b) avec pertes avec une tangente de pertes de $\tan(\delta) = 0.051$.

5.3 Milieu stratifié

5.3.1 Géométrie

La configuration d'étude est cette fois-ci à aspect limité (Figure 5.11). Deux milieux de permittivité différentes sont séparés par une interface, qui peut être plane ou rugueuse. Les antennes se trouvent dans l'un des milieux, les diffracteurs dans un autre. En mesurant les champs transmis et/ou réfléchis, on cherche à remonter aux caractéristiques de l'environnement. Ce genre de configuration se rencontre par exemple dans des applications de détection d'objets enfouis dans le sol (mines, canalisations, ...) ou dans des applications de microscopie optique où des échantillons sont positionnés sur un support.

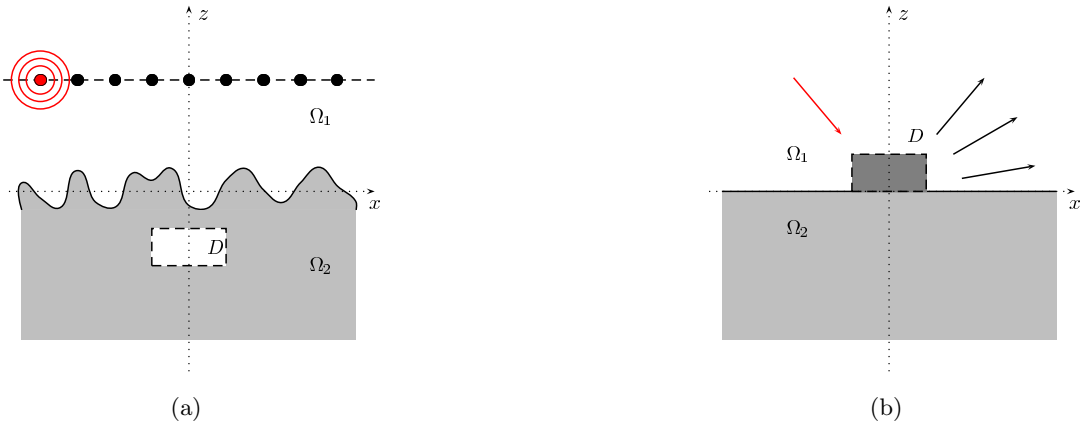

FIG. 5.11 – Configuration stratifiée (a) dans le cas d'un objet enfoui sous une interface rugueuse avec une ligne de mesure proche de la surface (b) dans le cas d'un objet posé sur une interface plane et éclairée par une onde plane incidente, par exemple dans le cas des applications en tomographie optique.

J'ai abordé la première configuration en collaboration avec O. Cmielewski, H. Tortel et M. Saillard [4] dans le cas où les objets à détecter étaient faiblement enfouis sous une interface rugueuse (Figure 5.11(a)). Nous avons mis au point une méthodologie de détection et caractérisation en deux étapes :

- Dans un premier temps, en se basant sur une approximation d'interface faiblement rugueuse, nous avons montré qu'il existait un lien direct entre la corrélation des champs mesurés sur une ligne de mesure au-dessus de l'interface et le profil de rugosité de la surface.
- Dans un deuxième temps, ce profil est introduit dans la modélisation, grâce à un maillage conforme qui n'est possible qu'avec un code de modélisation par éléments finis. Ceci permet alors de prendre en compte exactement la fonction de Green du milieu environnant et d'améliorer le processus de caractérisation de l'objet enfoui. Une méthode d'optimisation, basé sur un formalisme par fonction de niveau (cf Section 6.3) a alors été mis en place pour effectuer la caractérisation.

J'ai également abordé la deuxième configuration (Figure 5.11(b)) en collaboration avec A. Sentenac et F. Dresk dans le cadre d'un sujet de master [7]. Cette fois-ci, l'obstacle est directement posé sur une surface plane, dans le régime de longueur d'onde de l'optique, et le but est de pouvoir remonter à ses caractéristiques géométriques, connaissant sa permittivité. Un formalisme par fonction de niveaux spécifiques aux objets homogènes

a été mis en place. Le travail n'a pas été poursuivi, les difficultés que nous avons alors rencontrés venant du fait que nous trouvions des obstacles qui "lévitaient" au dessus de l'interface. Il aurait fallu alors imposer comme information a-priori le fait que les objets étaient forcément posés sur l'interface.

5.3.2 Chambre anéchoique plane

En liaison étroite avec les études menées dans la grande chambre anéchoique, un nouveau dispositif de mesures polyvalent est développé au sein de l'Institut Fresnel (Figure 5.12). Ce dispositif est constitué d'une enceinte anéchoique (un cube d'environ 3m de côté), de positionneurs d'antennes (exploration du plan horizontal avec une excursion de 2.5 m×2.5 m et des rotations pour l'orientation des antennes), d'un analyseur de réseau qui peut fonctionner jusqu'à 40 GHz.

FIG. 5.12 – Photo de la petite chambre anéchoique, où l'on voit les positionneurs mécaniques dédiés aux antennes d'émission et de réception.

Ce système de mesure est en cours de validation. Un post-doctorant, M. Serhir, a travaillé pendant un an à sa mise en route. Nous avons en particulier montré qu'il était possible de valider des mesures de diagrammes de rayonnement d'antennes effectués dans la grande chambre anéchoique avec des mesures de champs rayonnés par ces mêmes antennes, captés cette fois-ci sur une ligne à l'intérieur de la petite chambre anéchoique [23].

Cette chambre ouvre tout un aspect intéressant de recherches, particulièrement adaptée aux configurations stratifiées que nous rencontrons par exemple dans la problématique du projet CESAR liée au contrôle de la teneur en eau dans le proche sous-sol.

Bibliographie

[1] K. Belkebir and M. Saillard. Special section on testing inversion algorithms against experimental data. *Inverse Problems*, 17 :1565–1571, 2001. 33

[2] K. Belkebir and M. Saillard. Special section on testing inversion algorithms against experimental data : Inhomogeneous targets. *Inverse Problems*, 21 :S1–S3, 2005. 33

[3] O. Bucci and G. Franceschetti. On the spatial bandwidth of scattered fields. *IEEE Trans. Antennas Propagat.*, 35 :1445–1455, 1987. 33

[4] O. Cmielewski, H. Tortel, A. Litman, and M. Saillard. A two-step procedure for characterizing obstacles under a rough surface from bistatic measurements. *IEEE Trans. Geosci. Remote Sens.*, 45 :2850–2858, 2007. 41

[5] L. Crocco, M. D'Urso, and T. Isernia. Faithful non-linear imaging from only-amplitude measurements of incident and total fields. *Opt. Express*, 15 :3804–3815, 2007. 36

[6] L. Crocco and A. Litman. On embedded microwave imaging systems : Retrievable information and design guidelines. *Inverse Problems*, 25 :065001, 2009. 40

[7] F. Dresk. Imagerie optique haute résolution. Technical report, Master, Ecole Centrale de Paris, 2005. 41

[8] M. D'Urso, K. Belkebir, L. Crocco, T. Isernia, and A. Litman. Phaseless imaging with experimental data : Facts and challenges. *Journal of the Optical Society of America A*, 25 :271–281, 2008. 37

[9] C. Eyraud, J-M. Geffrin, A. Litman, P. Sabouroux, and H. Giovannini. Drift correction for scattering measurements. *Applied Physics Letters*, page 244104, 2006. 34

[10] C. Eyraud, J-M. Geffrin, P. Sabouroux, P.C. Chaumet, H. Tortel, H. Giovannini, and A. Litman. Validation of a 3d bistatic microwave scattering measurement setup. *Radio Science*, 2008. 34

[11] C. Eyraud, A. Litman, A. Herique, and W. Kofman. Microwave imaging from experimental data within a bayesian framework with realistic random noise. *Inverse Problems*, 25 :024005, 2009. 34

[12] J-M. Geffrin. *Imagerie microonde : Etude d'un scanner à 434 MHz pour applications biomédicales*. PhD thesis, Université Paris XI, Orsay, 1995. 37

[13] J-M. Geffrin, C. Eyraud, A. Litman, and P. Sabouroux. Optimization of a bistatic microwave scattering measurement setup : from high to low scattering targets. *Radio Science*, 44 :RS2007, 2009. 34

[14] J-M. Geffrin, P. Sabouroux, and C. Eyraud. Free space experimental scattering database continuation : experimental set-up and measurement precision. *Inverse Problems*, 21 :S117–S130, 2005. 32

[15] R. Kleinman and P.M. van den Berg. A modified gradient method for two-dimensional problems in tomography. *J. Comput. Appl. Math.*, 42 :17–35, 1992. 36

[16] R. Lencrerot. *Outils de modélisation et d'imagerie d'un scanner micro-onde : Application au contrôle de la teneur en eau d'une colonne de sol*. PhD thesis, Université Aix-Marseille III, 1998. 38, 39

[17] R. Lencrerot, A. Litman, H.Tortel, and J-M Geffrin. Measurement strategies for a confined microwave circular scanner. *Inverse Problems in Science and Engineering*, page 357869, 2009. 40

[18] R. Lencrerot, A. Litman, H. Tortel, and J-M. Geffrin. A microwave imaging circular setup for soil moisture information. *IGARSS Proc.*, pages 4394–4397, 2007. 39

[19] A. Litman. Reconstruction by level sets of n-ary scattering obstacles. *Inverse Problems*, 21 :S131–S152, 2005. 33

[20] A. Litman and K. Belkebir. Inverse profiling using phaseless data. *J. Optical Society of America A*, 23 :2737–2746, 2006. 36

[21] A. Litman and L. Crocco. Testing inversion algorithms against experimental data : 3D targets. *Inverse Problems*, 25 :020201, 2009. 34

[22] M. Masmoudi, J. Pommier, and B. Samet. The topological asymptotic expansion for the maxwell equations and some applications. *Inverse Problems*, 21 :547–564, 2005. 36

[23] M. Serhir, J-M. Geffrin, A. Litman, and P. Besnier. Aperture antenna modelling by a finite number of elemental dipoles from spherical field measurements. *IEEE Trans. Antennas Propagat.*, page submitted, 2009. 42

[24] A.G. Tijhuis, K. Belkebir, A. Litman, and B.P. de Hon. Multiple-frequency distorted-wave born approach to 2D inverse profiling. *Inverse Problems*, 21 :1635–1644, 2001. 33

[25] A.G. Tijhuis, K. Belkebir, A. Litman, and B.P. de Hon. Theoretical and computational aspects of two-dimensional inverse profiling. *IEEE Trans. Geosci. Remote Sens.*, 39 :1316–1330, 2001. 33

[26] G. Topp, J. Davis, and A. Annan. Electromagnetic determination of soil water content : Measurements in coaxial transmission lines. *Water Ressources Research*, 16 :574–582, 1980. 38

Chapitre 6

Diffraction inverse - Information a-priori

Il est bien connu que tout problème inverse mal-posé nécessite de contraindre les solutions afin d'éviter tous minima secondaires ou toutes solutions physiquement irréalisables. Cela conduit à l'introduction de toute forme d'information a-priori disponible, de la manière la plus élégante possible. Le caractère "élégant" mathématiquement parlant est indispensable pour bien conceptualiser les informations et amener à des algorithmes efficaces.

Une des façons de limiter le caractère mal-posé du problème est de rajouter des termes de pénalisation dans la fonctionnelle coût (Eq. 4.3), telle que cela a été fait par exemple dans l'approche adoptée pour traiter la diagraphie de densité (Section 3.1). Le problème est d'alors adapter les hyper-paramètres de régularisation en fonction du niveau de bruit, ou en fonction du résultat attendu. Cette étape est toujours très délicate et pas forcément robuste. J'ai préféré m'intéresser aux solutions qui étaient physiquement réalisables ou atteignables, en imposant ainsi à la solution de faire partie d'une "famille" particulière. Nous verrons ainsi le cas des "familles" polynomiales adaptées à la géométrie de la zone de recherche, ainsi que des "familles" de fonctions de niveau, adaptées à des objets homogènes par morceaux. Une combinaison au final des deux aspects sera alors abordé.

Tous ces algorithmes sont de type quantitatifs. Un algorithme de minimisation est alors traditionnellement mis en place et nécessite le calcul des dérivées directionnelles pour déterminer les différentes directions de descente. Je commencerai donc par rappeler brièvement le calcul des dérivées de Fréchet dans le cas classique d'une configuration bidimensionnelle.

6.1 Dérivée de Fréchet et état adjoint

Dans les algorithmes quantitatifs, on recherche le minimum de la fonctionnelle coût définie dans (Eq. 4.3). Ce minimum est obtenu en particulier lorsque le gradient de la fonctionnelle s'annule. Les dérivées secondes ne seront pas utilisées, car elles peuvent être remplacées par une approximation du Hessien en n'utilisant que les dérivées premières combinées avec un terme correctif, de type Quasi-Newton [23, 24].

Ce minimum se calcule en tenant compte des équations (Eq. 4.1) et (Eq. 4.2). Le problème est alors exprimé sous la forme d'une optimisation sous contrainte avec l'introduction d'une fonctionnelle Lagrangienne [2] sous la forme suivante

$$\mathcal{L}(\chi, E^{\mathrm{s}}, E) = \sum_{l=1}^{L} \mathcal{J}(\chi) + < U_l^{\mathrm{s}} \mid E_l^{\mathrm{s}} - \mathbf{K}\chi E_l >_{W,\Gamma} + < U_l \mid E_l - E_l^{\mathrm{i}} - \mathbf{G}\chi E_l >_D \quad (6.1)$$

où $< \mid >_D$ (resp. $< \mid >_{W,\Gamma}$) correspond aux produits scalaires sur le domaine D (resp. sur la ligne de mesure avec une pondération dépendant du bruit de mesure observé [9]).

Il est possible de montrer [11, 13, 14] que le gradient de la fonctionnelle $\mathcal{J}$ s'exprime sous la forme

$$\nabla_\chi \mathcal{J}(\chi) = k_0^2 \left[\sum_{l=1}^{L} E_l(\mathbf{r}) P_l(\mathbf{r}) \right]^* \mathbb{1}_\Omega(\mathbf{r}) \quad (6.2)$$

où P_l correspond à l'état adjoint du problème qui, grâce au principe de réciprocité que vérifient les équations de Maxwell, est équivalent à un problème de diffraction classique (Figure 6.1), la seule différence étant que les récepteurs deviennent sources avec une am-

plitude qui est liée à l'erreur mesurée en ce point

$$P_l(\mathbf{r} \in D) = P_l^{\mathrm{i}}(\mathbf{r}) + k_0^2 \int_D \chi(\mathbf{r}')\, P_l(\mathbf{r}')\, G(\mathbf{r}, \mathbf{r}')\, \mathrm{d}\mathbf{r}', \tag{6.3}$$

$$P_l^{\mathrm{i}}(\mathbf{r} \in D) = -\int_\Gamma G^\dagger(\mathbf{r}, \mathbf{r}')\, \overline{\nabla \mathcal{J}}(\mathbf{r}')\, \mathrm{d}\mathbf{r}'. \tag{6.4}$$

où $G^\dagger$ correspond au noyau de l'opérateur adjoint de (Eq. 4.2). Une fois le gradient calculé,

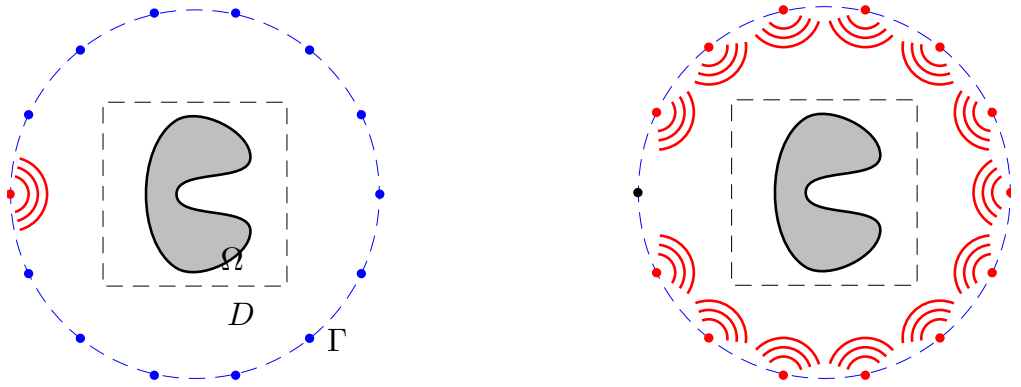

(a) Champ total (b) Champ adjoint

FIG. 6.1 – Illustration de l'expérience de rayonnement effectué dans le cas (a) du calcul du champ total et (b) du calcul du champ adjoint associé.

il est possible d'appliquer une large variété d'algorithmes de minimisation [18], de type steepest-descent, gradient conjugué, Levenberg-Marquardt, ...

6.2 Décomposition sur une base adaptée

Le nombre d'inconnues va dépendre ensuite de la façon dont la fonction inconnue χ est représentée numériquement. Le plus simple est d'associer une valeur à chaque cellule du maillage, en utilisant une interpolation constante par morceaux ou une interpolation linéaire par morceaux si on veut raffiner un peu les choses. Il est possible d'utiliser un maillage plus grossier pour représenter l'inconnue et rediscrétiser ensuite pour effectuer une simulation électromagnétique fiable, la discrétisation dépendant alors de la longueur d'onde. Le problème alors est de pouvoir contrôler la stratégie de maillage localement. Il apparaît plus judicieux d'utiliser une décomposition de la fonction inconnue en utilisant une base de fonctions dont le support recouvre toute la zone d'investigation. La fonction inconnue sera alors de la forme

$$\chi(\mathbf{r}) = \sum_n a_n f_n(\mathbf{r}) \tag{6.5}$$

où les fonctions $\{f_n\}$ représentent une famille complète sur la zone d'investigation. Le calcul du gradient se fait simplement par composition de fonction, en se basant sur (Eq. 6.2), sachant que les inconnues sont maintenant les coefficients $\{a_n\}$

$$\nabla_{a_n} \mathcal{J}(\{a_n\}) = k_0^2 < \left[\sum_{l=1}^{L} E_l P_l\right] \mathbf{1}_\Omega \mid f_n >_D \tag{6.6}$$

Ceci amène deux avantages :

– Il est possible de choisir judicieusement la base $\{f_n\}$ qui colle le mieux à la géométrie de la zone d'investigation,
– Il est possible ensuite de limiter le nombre de paramètres inconnues, ici les coefficients $\{a_n\}$ en fonction de la quantité d'information contenue dans le champ diffracté. Le lien existant entre le nombre de paramètres inconnus et les degrés de liberté présents dans le champ mesuré peut d'ailleurs même s'estimer théoriquement [4].

6.2.1 Domaine d'investigation circulaire

Les deux avantages ont été combinés dans le cas de la configuration du scanner circulaire [12] décrite dans la Section 5.2 dans le cadre de la thèse de R. Lencrerot. En effet, la forme de la zone d'investigation est connue par avance, étant forcément circulaire. La base des polynômes de Zernike est donc apparue comme étant la plus naturelle et la mieux adaptée à la configuration étudiée [3]. Ces polynômes sont définis par (Figure 6.2)

$$\chi(\rho,\theta) = \sum_{l,m} a_m^l Z_m^l(\rho,\theta) \quad \text{avec}$$

$$Z_m^l(\rho,\theta) = R_m^l(\frac{\rho}{R})\exp(il\theta), \qquad R_m^l(\rho) = \sum_{p=0}^{(m-l)/2} \frac{(-1)^p(m-p)!}{p!(\frac{m+l}{2}-p)!((\frac{m-l}{2}-p)!}\rho^{m-2p}$$

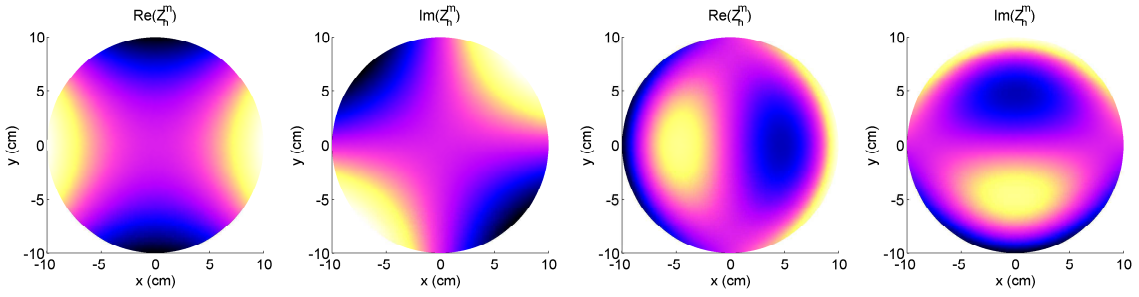

(a) (b)

FIG. 6.2 – Polynômes de Zernike. Les figures (a) et (b) représentent respectivement les parties réelles et imaginaires pour les polynômes Z_2^2 et Z_3^1.

Le nombre de coefficients inconnus a été déterminé en regardant le nombre de degrés de liberté présents dans le champ diffracté, et ceci a été obtenu en analysant le spectre de la matrice de diffraction. L'algorithme d'inversion a bien sûr été validé sur des champs diffractés mesurés avec des fantômes positionnés à l'intérieur du scanner circulaire de l'Institut Fresnel [12]. Tous les résultats numériques associés à cette approche sont visibles à la page 109 à la fin du manuscrit et un exemple en est visible dans les figures 6.3 et 6.4.

6.2.2 Demi-espace d'investigation

Dans le cadre d'une configuration enfouie similaire à la configuration décrite dans la Section 5.3, appropriée à une application de type contrôle non-destructif par courants de Foucault, une approche similaire avait déjà été entreprise [16] en utilisant une version

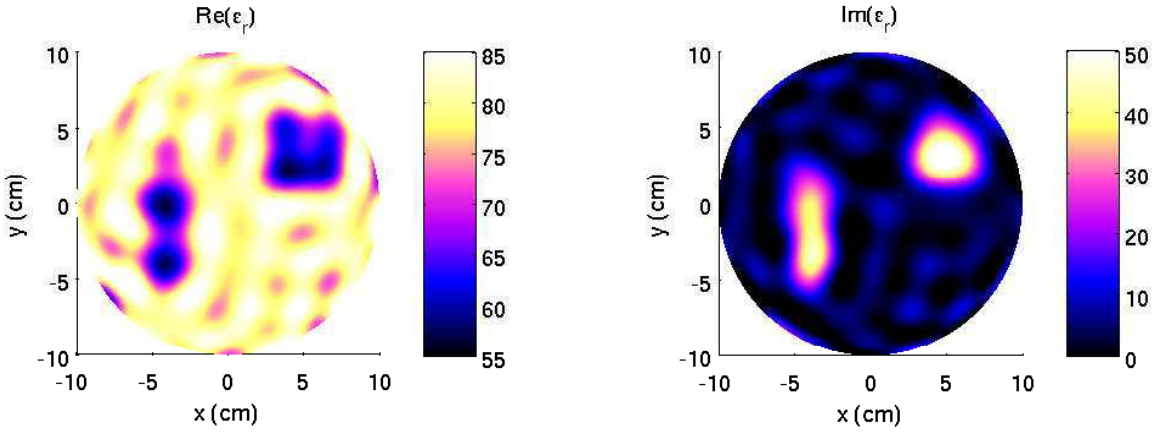

FIG. 6.3 – Partie réelle (gauche) et imaginaire (droite) de la carte de permittivité reconstruite après 100 itérations, dans la configuration du scanner circulaire. Le champ diffracté a été simulé et du bruit blanc gaussien a été rajouté avec un rapport signal à bruit de 10 dB. La valeur de la permittivité dans chaque triangle du maillage est recherché. Il y a donc autant d'inconnues que de cellules de discrétisation. L'estimation initiale est un fond homogène.

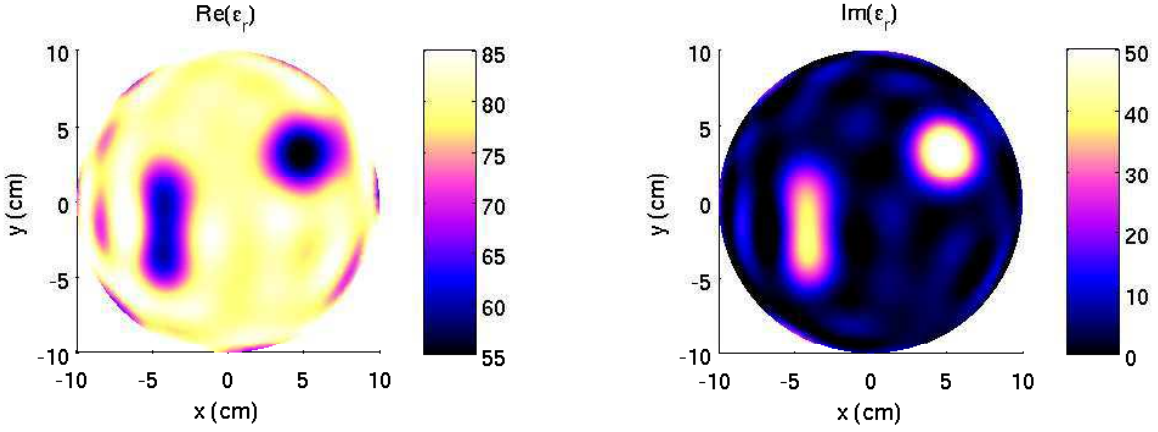

FIG. 6.4 – Partie réelle (gauche) et imaginaire (droite) de la carte de permittivité reconstruite après 100 itérations, dans la configuration du scanner circulaire. Le champ diffracté a été simulé et du bruit blanc gaussien a été rajouté avec un rapport signal à bruit de 10 dB. Le profil de permittivité a été projeté sur la base des polynômes de Zernike en utilisant des polynômes jusqu'à l'ordre 12. L'estimation initiale est un fond homogène.

linéarisée du problème de diffraction (approximation de Born). La fonction inconnue a été décomposée cette fois sur une base de famille de fonctions de type Fourier-Mellin, combinant une représentation de Fourier selon l'axe x (parallèle à l'interface) et une représentation sur une base de fonctions à bande de Mellin limitée selon l'axe z (selon la profondeur) [20]. Ceci amène à

$$\hat{\chi}(\kappa_x, z) = \sum_m a_m(\kappa_x) Z_B(z/z_m),$$

$$\text{avec} \quad z_n = \tau^n,\ \tau = \exp(\frac{\pi}{B}),\ Z_B(t) = \frac{\sin(B \ln t)}{B\sqrt{t} \ln t}$$

où $\hat{\chi}$ correspond à la transformée de Fourier de χ selon l'axe x avec κ_x la fréquence spatiale associée, et les $Z_B(z)$ correspondent aux fonctions qui interviennent dans le cadre du théorème d'échantillonnage exponentiel (Figure 6.2.2). L'avantage de ces fonctions est de traduire très simplement le caractère atténuant des ondes à l'intérieur du demi-espace inférieur, atténuation qui devient de plus en plus importante à mesure que l'onde pénètre à l'intérieur du matériau qui est forcément absorbant.

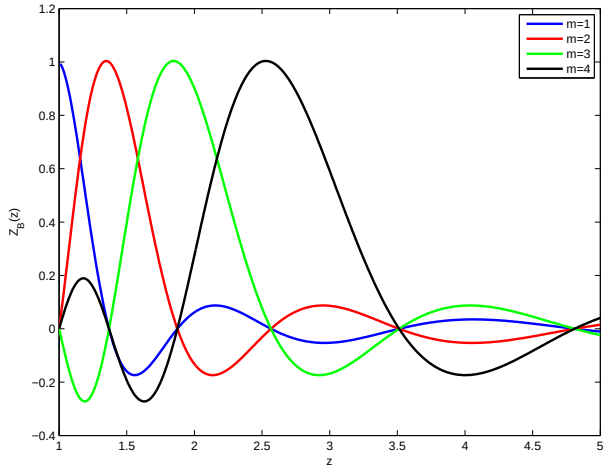

FIG. 6.5 – Fonctions de base $Z_B(z)$ intervenant dans le théorème d'échantillonnage exponentiel et adaptées à une configuration stratifiée plan.

La figure 6.6 démontre l'intérêt d'incorporer l'information disponible sur le support de recherche dans le cas d'une configuration de type objet enfoui, où une première méthode basée sur la tomographie par diffraction est utilisée et prend en compte la totalité de l'espace comme domaine de recherche alors que la deuxième méthode se restreint au demi-espace inférieur avec une décomposition des inconnues sur la base des fonctions Z_B.

6.3 Décomposition sur des fonctions de niveaux

Les fonctions $\{f_n\}$ définies précédemment sont des fonctions forcément continues. Elles ne permettent pas de retranscrire fidèlement des situations où on sait pertinemment que les objets inconnus sont fabriqués à partir de matériaux connus et homogènes. Il est donc intéressant d'essayer d'introduire ce type d'information a-priori à l'intérieur de l'algorithme d'inversion. On se ramène alors à des problèmes d'optimisation de forme, les valeurs de

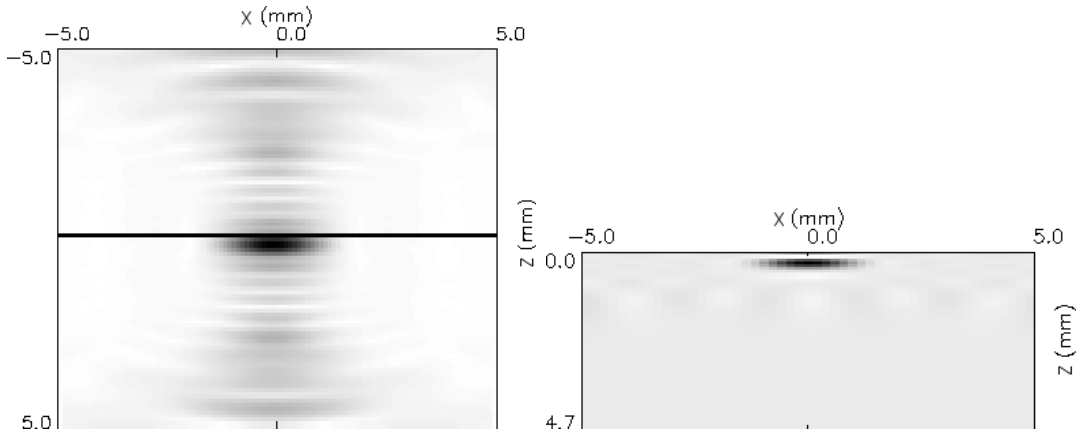

(a) (b)

FIG. 6.6 – L'objet est dans le demi-espace inférieur. Les antennes émettrices et réceptrices se trouvent au-dessus de la surface et effectuent un balayage le long d'une ligne à plusieurs fréquences (basse fréquence). (a) Le domaine de recherche n'est pas restreint et un algorithme de tomographie classique est appliqué, (b) le domaine de recherche est limité au demi-espace inférieur et les inconnues sont projetées sur la base des fonctions Z_B. Seul le problème linéarisé est considéré dans cette configuration issue du contrôle non-destructif par courants de Foucault.

permittivité des différents matériaux constituant la scène étant connues par avance. Il suffit donc de définir les contours des zones homogènes pour avoir une description complète de la zone sondée. Il existe de nombreuses façons de représenter des contours, soit par des approches explicites (coordonnées polaires, paramétrisation des courbes, ...) soit par des approches implicites. La représentation par fonctions de niveaux s'avère très puissante car elle constitue une approche implicite qui permet de gérer facilement tout changement topologique (fusion, scission, ...). Elle a largement été utilisée dans la littérature à la fois des problèmes inverses et du traitement des images. Pour les problèmes inverses de diffraction, les premiers travaux reposent sur l'article de F. Santosa [21], suivi de celui que j'ai écrit pendant ma thèse [17]. Je présenterai ici les améliorations que j'ai introduite, avec mes collègues, dans cette thématique de recherche. Des articles de synthèses reprenant les différentes avancées dans cette thématique sont également disponibles [6, 8].

6.3.1 Rappel sur les fonctions de niveaux

On s'intéresse à la représentation de la forme Ω de la fonction inconnue χ que l'on sait être à support borné. On introduit alors une fonction de niveau $\phi \in C^1(D)$ telle que

$$\partial\Omega = \{\mathbf{r} \in D \mid \phi(\mathbf{r}) = 0\} \tag{6.7}$$
$$\Omega = \{\mathbf{r} \in D \mid \phi(\mathbf{r}) < 0\} \tag{6.8}$$

Avec une telle représentation implicite, la définition du contour se fait grâce à la définition de la fonction ϕ qui peut présenter plusieurs passages de part et d'autre du plan $\{\phi(\mathbf{r}) = 0\}$ (Figure 6.7)

Connaissant la permittivité, il suffit alors de rechercher la forme de l'obstacle et la fonc-

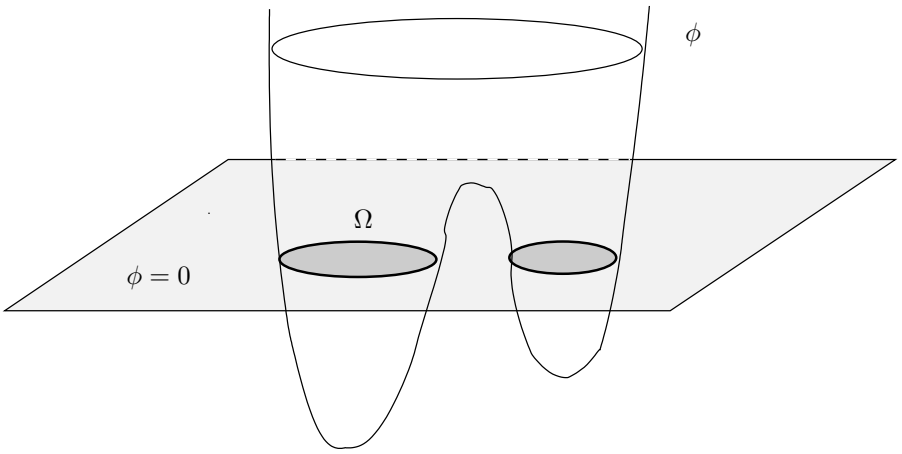

FIG. 6.7 – Fonction de niveau permettant de décrire un objet homogène.

tionnelle coût définie dans (Eq. 4.3) devient donc

$$\mathcal{J}(\Omega) = \frac{1}{2}\sum_{l=1}^{L} \| E_l^{\text{obs}} - E_l^{\text{s}}(\Omega) \|_{W,\Gamma}^2 \tag{6.9}$$

La difficulté réside alors à calculer correctement la dérivée de forme d'une telle fonctionnelle et toute une littérature existe également sur ce sujet [22]. Pour décrire le processus de déformation de la surface, il est possible d'introduire un temps fictif t qui correspond à l'évolution de l'algorithme itératif. Dans ce cadre, l'évolution du contour de niveau 0 de la fonction de niveau ϕ est régi par l'équation suivante :

$$\begin{aligned} \frac{\partial \phi}{\partial t}(\mathbf{r}) + \vec{V} \cdot \vec{n} \mid \nabla \phi \mid &= 0 \\ \text{avec} \quad \frac{\partial \mathbf{r}}{\partial t} = \vec{V}(\mathbf{r}, t),\ \vec{n} &= \frac{\nabla \phi}{\mid \nabla \phi \mid} \end{aligned} \tag{6.10}$$

Cette équation est une équation de type Hamilton-Jacobi [19], dans laquelle la vitesse de déformation $\vec{V}$ est directement liée à la dérivée de la fonctionnelle coût $\mathcal{J}(\Omega)$. En contrôlant cette vitesse, on contrôle le processus d'évolution de la fonction de niveau et donc le processus de l'algorithme itératif dans son ensemble. Le plus simple est ainsi d'utiliser un algorithme de steepest-descent en imposant $\mid \vec{V} \mid = -\nabla_\Omega \mathcal{J}(\Omega)$. Mais on peut également utiliser tout autre schéma de descente, de type gradient-conjugué ou Levenberg-Marquardt [5].

6.3.2 Maillage triangulaire

La difficulté de l'approche par fonctions de niveaux réside dans le fait que la résolution de l'équation de Hamilton-Jacobi (Eq. 6.10) est délicate. Il faut utiliser les bons schémas de différences finies pour éviter des problèmes de singularités aux interfaces. Cette équation intervient également pour définir la propagation des fronts de flammes et il est impensable d'avoir un schéma numérique qui fait revenir en arrière un front de flamme dans une zone où tout a déjà été brûlé.

Sur un maillage rectangulaire tel que celui utilisé avec une méthode des moments, Osher et Sethian [19] ont proposé un schéma numérique efficace, qui a permis de développer toute

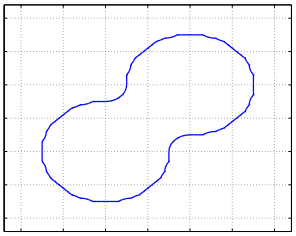

(a) Maillage pour la méthode des moments [17]

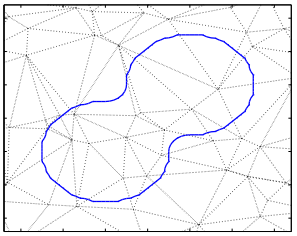

(b) Maillage pour les éléments finis [7]

FIG. 6.8 – Représentation du contour $\phi = 0$ dans le cas où (a) le maillage est rectangulaire, le schéma numérique employé étant alors celui de Osher et Sethian [19], (b) le maillage est triangulaire et conforme, le schéma numérique employé étant alors celui de Abgrall [1].

l'approche des problèmes inverses de diffraction par fonctions de niveau (Figure 6.8). Sur un maillage triangulaire tel que celui utilisé avec une méthode par éléments finis, le schéma devient beaucoup plus complexe à gérer. Abgrall a alors proposé un schéma efficace [1] que nous avons mis en place dans le cadre de la configuration objet faiblement enfoui sous une interface rugueuse (cf Section 5.3).

Dans cette application, la démarche s'est d'ailleurs effectuée en deux temps [7], l'article correspondant est d'ailleurs inséré à la page 127 en fin de manuscrit :

– la rugosité de l'interface h a été retrouvée en corrélant les champs diffractés mesurés pour différentes incidences x_l et le champ réfléchi E_{plan} par une interface plane se trouvant à la même position en moyenne que l'interface rugueuse (Figure 5.11(a)),

$$h(X) \approx \Im \iint E^{\mathrm{s}}(X + x; x_l) E_{plan}(X - x; x_l) dx dx_l \tag{6.11}$$

– une fois cette rugosité retrouvée, elle a été introduite dans la modélisation par éléments finis grâce au maillage conforme et la détection de l'objet faiblement enfoui a été mis en oeuvre en utilisant l'approche par fonction de niveau décrite précédemment.

6.3.3 Fonction de Heaviside "mollifiée"

La résolution de l'équation d'Hamilton-Jacobi restant néanmoins délicate, il apparaît plus intéressant de travailler avec des fonctions régulières. La notion de binarité a alors été amoindrie en utilisant une fonction de niveau combinée avec une fonction de Heaviside "mollifiée". En effet, la fonction inconnue peut s'écrire sous la forme suivante

$$\chi(\mathbf{r}) = (\varepsilon_r - \varepsilon_{br}) \mathbb{1}_\Omega(\mathbf{r}) = (\varepsilon_r - \varepsilon_{br}) H_\eta(-\phi(\mathbf{r})) \tag{6.12}$$

où H_η est la fonction de Heaviside classique, ainsi que sa dérivée, qui a été "mollifiée" (Figure 6.9) grâce à une expression de la forme [25]

$$H_\eta(x) = \frac{1}{2}(1 + \frac{2}{\pi} \arctan(\frac{x}{\eta})), \quad \delta_\eta(s) = \frac{1}{\pi} \frac{\eta^2}{\eta^2 + x^2} \tag{6.13}$$

Dans ce cas, tout redevient à nouveau facilement dérivable et en utilisant la composition de fonctions, on obtient la dérivée de la fonctionnelle coût par rapport à la fonction de

(a) $H_{-\infty}(\phi)$ (b) $H_{\eta}(\phi)$

FIG. 6.9 – Représentation de la fonction inconnue χ lorsque (a) la fonction Heaviside présente une vraie discontinuité et (b) lorsqu'elle est rendue continue.

niveau

$$\nabla_{\phi}\mathcal{J}(\phi) = k_0^2 \left[\sum_{l=1}^{L} E_l(\mathbf{r})P_l(\mathbf{r})\right]^* (\varepsilon_r - \varepsilon_{br})\delta_{\eta}(-\phi(\mathbf{r})) \tag{6.14}$$

Cet algorithme a ainsi été appliqué à la fois dans le cadre d'une configuration en espace libre [14] et dans le cadre de la configuration du scanner circulaire [15], sur des données synthétiques et sur des champs mesurés expérimentalement dans les deux configurations.

6.3.4 Fonction de Heaviside "mollifiée" et projection sur une base adaptée

Il est ensuite possible de combiner l'approche de régularisation proposée dans la Section 6.2 avec une représentation par fonctions de niveau pour s'adapter à des cas où les objets inconnus sont homogènes. La régularisation se fait sur la fonction de niveau en la projetant sur une famille adaptée à la configuration géométrique de mesure. Ceci permet de régulariser la fonction de niveau en limitant le nombre d'inconnue représentant la fonction de niveau au nombre de projections choisis dans la base, et en même temps d'utiliser l'information de binarité. Ceci se fait alors en projetant ϕ sur la base des $\{f_n\}$

$$\phi(\mathbf{r}) = \sum_n b_n f_n(\mathbf{r}), \quad \chi(\mathbf{r}) = (\varepsilon_r - \varepsilon_{br})\, H_{\eta}(\sum_n a_n f_n(\mathbf{r})) \tag{6.15}$$

La dérivée de la fonctionnelle coût se fait à nouveau par composition de fonctions, les paramètres inconnus étant maintenant les coefficients $\{b_n\}$. Cette approche a été mise en place dans le cadre de la configuration du scanner circulaire, en utilisant des données à la fois simulées et mesurées (Figure 6.10). Toute la simulation est faite par éléments finis, l'algorithme de descente est de type gradient conjugué, la seule différence provient du choix de l'inconnue qui dépend de l'information a-priori que l'on introduit dans l'algorithme. La base de projection $\{f_n\}$ correspond ici à la base des polynômes de Zernike adaptée à cette configuration circulaire.

6.3.5 Objets homogènes par morceaux

Dans la nature, il est quand même rare de ne rencontrer que deux types de matériaux. Il parait plus intéressant de considérer des cas où les objets sont à valeurs de permittivité constantes par morceaux. Ceci correspond en particulier aux objets qui ont été mesurés

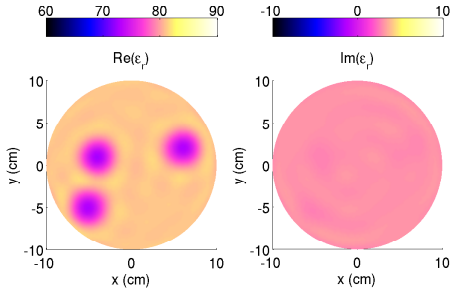

(a) L'inconnue est χ

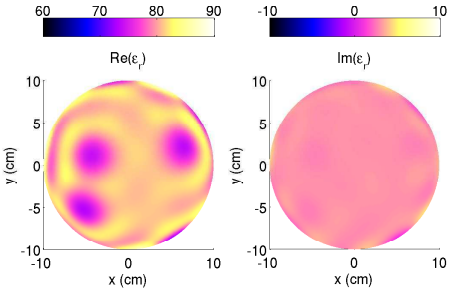

(b) L'inconnue est $\{a_m^l\}$

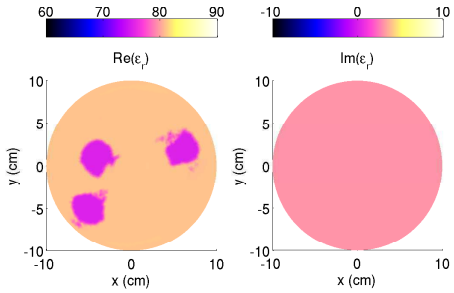

(c) L'inconnue est ϕ

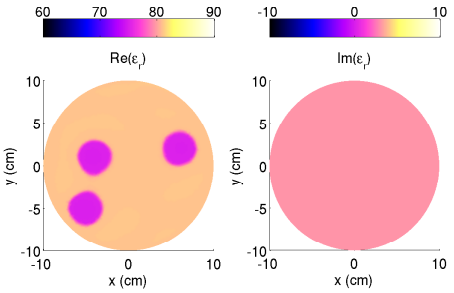

(d) L'inconnue est $\{b_m^l\}$

FIG. 6.10 – Parties réelles et imaginaires des profils de permittivité reconstruits en utilisant quatre algorithmes itératifs différents, en utilisant la même configuration du scanner circulaire. La différence entre les algorithmes provient des informations a-priori qui sont introduites dans chaque algorithme.

lors de la seconde base de données de l'Institut Fresnel [10]. On dispose ainsi d'un ensemble Θ d'obstacles définis par

$$\Theta = \bigcup_{i=1}^{n} \Omega_i \quad \text{and} \quad \Omega_i \bigcap_{i \neq j} \Omega_j = \emptyset \tag{6.16}$$

Les permittivités de chacun des milieux sont supposées connues. Afin de prendre en compte cette multiplicité de matériaux, j'ai introduit deux approches par décomposition par fonctions de niveaux [13].

6.3.5.1 Une seule fonction de niveau

Dans la première approche, une seule fonction de niveau sert à représenter tous les types de matériaux possibles (Figure 6.11),

$$\partial\Omega_i = \{\mathbf{r} \in D \mid \phi(\mathbf{r}) = c_i\} \tag{6.17}$$

$$\Omega_i = \{\mathbf{r} \in D \mid c_{i+1} < \phi(\mathbf{r}) < c_i\} \tag{6.18}$$

et dans ce cas, la fonction inconnue associée à l'obstacle Ω_i s'écrit sous la forme

$$\mathbb{1}_{\Omega_i}(\mathbf{r}) = H(\phi(\mathbf{r}), c_{i+1}) - H(\phi(\mathbf{r}), c_i) \tag{6.19}$$

où la fonction de Heaviside est remplacée par

$$H(x,c) = \begin{cases} 1 & \text{if } x < c \\ 0 & \text{if } x > c \end{cases}$$

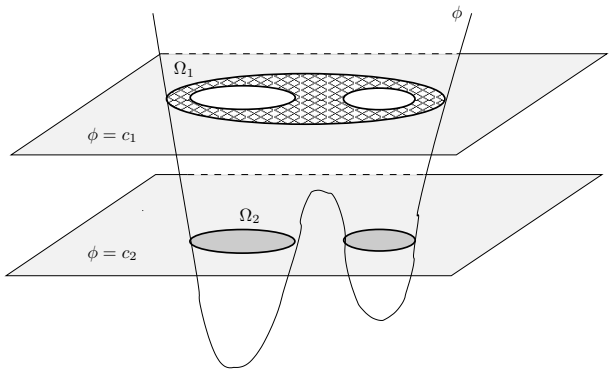

FIG. 6.11 – Une seule fonction de niveau permettant de décrire plusieurs objets homogènes.

6.3.5.2 Plusieurs fonctions de niveaux

Dans la deuxième approche, j'ai utilisé plusieurs fonctions de niveaux. Mais pour éviter tout problème de recouvrement d'une fonction de niveaux à une autre, j'ai effectué un codage binaire du nombre de matériaux disponibles et j'ai associé un bit de codage à une des fonctions de niveau. Pour n phases, il y a donc m fonctions de niveau, sachant que $(n+1) = 2^m$ (Figure 6.12). Un obstacle Ω_i est donc représenté par sa fonction caractéristique

$$\mathbb{1}_{\Omega_i}(\mathbf{r}) = \prod_{b=1}^{m} R_i(\phi_b(\mathbf{r})) \tag{6.20}$$

où B_i^j est une fonction qui renvoie le $j^{\text{ième}}$ bit du matériau i et la fonction R_i vaut

$$R_i(\phi_b) \quad = \quad \begin{cases} H(\phi_b, 0) & \text{if } B_i^b = 1 \\ 1 - H(\phi_b, 0) & \text{if } B_i^b = 0 \end{cases}$$

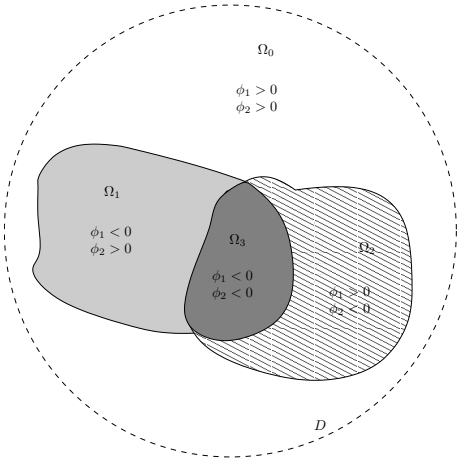

FIG. 6.12 – Plusieurs fonctions de niveau permettant de représenter plusieurs objets homogènes

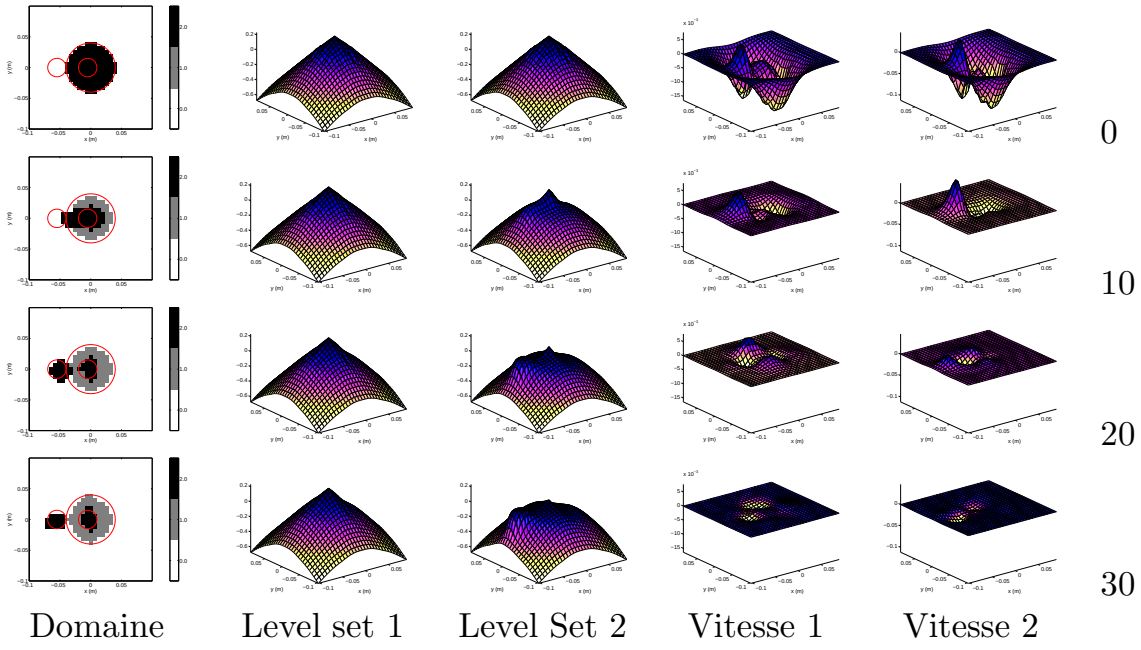

FIG. 6.13 – Evolution des fonctions de niveaux et des vitesses associés dans le cas de la reconstruction d'un objet homogène par morceau. Les champs ont été mesurés dans la chambre anéchoique de l'Institut Fresnel et cet objet, appelé FoamTwinDiel, fait partie de la seconde base de données publiée dans la revue Inverse Problems.

Les résultats des deux approches ont été à nouveau testés sur des données simulées puis sur des champs mesurés dans la grande chambre anéchoique de l'Institut Fresnel [13] (figure 6.13). L'article correspondant est inséré à la page 136 en fin de manuscrit. Il contient en particulier l'expression analytique de tous les gradients qui interviennent dans les différentes formulations.

Bibliographie

[1] R. Abgrall. Numerical discretization of the first-order hamilton-jacobi equations on triangular meshes. *Comm. Pure Appl. Math.*, 49 :1339–1373, 1996. 53

[2] D. Bertsekas. *Constrained optimization and lagrange multiplier methods.* Academic Press, 1982. 46

[3] M. Born and E. Wolf. *Principles of Optics.* Pergamon Press, 1959. 48

[4] O. Bucci and T. Isernia. Electromagnetic inverse scattering : retrievable information and measurement strategies. *Radio Science*, 32 :2123–2138, 1997. 48

[5] M Burger. Levenberg-marquardt level set methods for inverse obstacle problems. *Inverse Problems*, 20 :259–282, 2004. 52

[6] M. Burger and S.J. Osher. A survey on level set methods for inverse problems and optimal design. *Eur. J. Appl. Math.*, 16 :263–301, 2005. 51

[7] O. Cmielewski, H. Tortel, A. Litman, and M. Saillard. A two-step procedure for characterizing obstacles under a rough surface from bistatic measurements. *IEEE Trans. Geosci. Remote Sens.*, 45 :2850–2858, 2007. 53

[8] O. Dorn and D. Lesselier. Level set methods for inverse scattering. *Inverse Problems*, 22 :R67–R131, 2006. 51

[9] C. Eyraud, A. Litman, A. Herique, and W. Kofman. Microwave imaging from experimental data within a bayesian framework with realistic random noise. *Inverse Problems*, 25 :024005, 2009. 46

[10] J-M. Geffrin, P. Sabouroux, and C. Eyraud. Free space experimental scattering database continuation : experimental set-up and measurement precision. *Inverse Problems*, 21 :S117–S130, 2005. 55

[11] R. Lencrerot, A. Litman, H.Tortel, and J-M Geffrin. Measurement strategies for a confined microwave circular scanner. *Inverse Problems in Science and Engineering*, page 357869, 2009. 46

[12] R. Lencrerot, A. Litman, H. Tortel, and J-M. Geffrin. Imposing zernike representation for two-dimensional targets imaging. *Inverse Problems*, 25 :035012, 2009. 48

[13] A. Litman. Reconstruction by level sets of n-ary scattering obstacles. *Inverse Problems*, 21 :S131–S152, 2005. 46, 55, 57

[14] A. Litman and K. Belkebir. Inverse profiling using phaseless data. *J. Optical Society of America A*, 23 :2737–2746, 2006. 46, 54

[15] A. Litman, R. Lencrerot, and J-M. Geffrin. Combining spatial support information and shape-based method for tomographic imaging inside a microwave cylindrical scanner. *Inverse Problems in Science and Engineering*, page accepted, 2009. 54

[16] A. Litman and D. Lesselier. On attenuation-matched inversion methods of diffusive wavefields. *Inverse Problems*, 15 :99–111, 1999. 48

[17] A. Litman, D. Lesselier, and F. Santosa. Reconstruction of a two-dimensional binary obstacles by controlled evolution of a level-set. *Inverse Problems*, 14 :685–706, 1998. 51, 53

[18] J. Nocedal and S. Wright. *Numerical optimization*. Springer-Verlag, 2006. 47

[19] S. Osher and J.A. Sethian. Fronts propagating with curvature-dependent speed : Algorithms based on hamilton-jacobi formulations. *J. Comput. Phys.*, 79 :2–49, 1988. 52, 53

[20] N. Ostrowsky, D. Sornette, P. Parker, and E.R. Pike. Exponential-sampling method for light scattering polydispersity analysis. *Optica Acta*, 28 :1059–1070, 1981. 50

[21] F. Santosa. A level-set approach for inverse problems involving obstacles. *ESAIM : Control, Optimisation and Calculus of Variations*, 1 :17–33, 1996. 51

[22] J Sokolowski and J P Zolésio. *Introduction to Shape Optimization. Shape Sensitivity Analysis*, volume 16 of *Springer Series in Computational Mathematics*. Springer Verlag, Heidelberg, 1992. 52

[23] A.G. Tijhuis, K. Belkebir, A. Litman, and B.P. de Hon. Multiple-frequency distorted-wave born approach to 2D inverse profiling. *Inverse Problems*, 21 :1635–1644, 2001. 46

[24] A.G. Tijhuis, K. Belkebir, A. Litman, and B.P. de Hon. Theoretical and computational aspects of two-dimensional inverse profiling. *IEEE Trans. Geosci. Remote Sens.*, 39 :1316–1330, 2001. 46

[25] L. Vese and T. Chan. A multiphase level-set framework for image segmentation using the mumford and shah model. *Int. J. Comp. Vision*, 50 :271–293, 2002. 53

Chapitre 7

Conclusion - Perspectives

Conclusion

Ce manuscrit retrace les différents développements que j'ai pu effectuer depuis ma thèse dans des thématiques de recherche associées aux problèmes inverses. Ces thématiques sont devenues maintenant très vastes car elles interviennent dans tous les domaines de la physique, il suffit d'avoir une configuration dans laquelle il est possible de mesurer une grandeur physique qui possède une sensibilité aux paramètres spécifiques de son environnement. De cette mesure, tout l'art est ensuite de remonter aux informations intrinsèques à cet environnement.

J'ai ainsi pu aborder différents domaines de la physique, passant du nucléaire, aux mesures électromagnétiques très basse fréquence pour finir par le sondage par des signaux électromagnétiques en régime harmonique. Chacun de ces phénomènes physiques m'a amené à proposer des solutions particulières, tirant partie des spécificités propres à chaque configuration de mesure. On retrouve néanmoins certaines méthodologies communes, que j'ai employées dans la plupart des algorithmes que j'ai pu mettre en oeuvre, à savoir :

- une définition exacte du problème direct, qui est essentiel afin de pouvoir aborder n'importe quel problème inverse. J'ai ainsi utilisé des modèles simplifiés paramétrisés pour éviter de faire des simulations de type Monte-Carlo coûteuses en temps de calcul (diagraphie différée nucléaire), des schémas par différences finies (diagraphie différée de résistivité), des équations intégrales de domaine (diffraction électromagnétique) ou des schémas de type éléments finis (diagraphie différée de résistivité et phénomènes de diffraction électromagnétique).
- une étape importante de traitement du signal mesuré est de limiter les effets d'instabilité des solutions dûs aux bruits de mesure et au caractère mal-posé des problèmes inverses étudiés. J'ai ainsi participé à la mise au point de procédure de calibrages et de filtrages intelligents des données, tirant profit des propriétés mathématiques des signaux mesurés, en particulier la connaissance de leurs propriétés spectrales.
- une définition fine du critère d'erreur qui permet de valider si les paramètres retrouvés correspondent ou non aux valeurs mesurées. Dans ce critère d'erreur, qui peut être basé sur la recherche du maximum de vraisemblance ou être une estimation de distance au sens des moindres carrés, il est indispensable d'incorporer toute l'information disponible sur le type de bruit de mesure rencontré et sa dépendance aux conditions expérimentales. Ce critère permet également d'estimer la sensibilité que l'on attend du système d'imagerie dans son ensemble.
- un paramétrage adéquat de l'algorithme de minimisation mis en jeu. En effet, la plupart des techniques d'inversion passent à un moment ou à un autre par une étape d'optimisation sous contraintes. Le formalisme Lagrangien, que j'ai abordé pendant ma thèse, puis largement exploré depuis, s'avère être un outil essentiel pour toute technique d'optimisation. Il permet ainsi de définir et de calculer avec élégance les gradients qui interviennent dans ces algorithmes de minimisation. La notion d'état adjoint s'avère également très performante, d'autant que dans le cadre des équations de Maxwell harmoniques, il existe des propriétés de réciprocité qui rendent cet état adjoint très facile à calculer numériquement.
- une prise en compte des informations a-priori disponibles, et ce, à toutes les étapes de l'algorithme d'inversion. La prise en compte du caractère homogène des obstacles présents dans les configurations de mesure a occupé une grande partie de mes recherches jusqu'à présent, avec l'utilisation du formalisme par fonctions de niveaux qui s'avère être un outil puissant et qui garde encore un fort potentiel de recherche.

Tous ces aspects ne sont malheureusement pas suffisants pour construire un bon système

d'imagerie. Il faudrait en effet coupler encore plus finement les phénomènes physiques avec les méthodes et intervenir plus en amont dès de la conception du système de mesure pour pouvoir espérer en extraire les meilleures performances. Il faut ainsi :

- une prise en compte fidèle du rayonnement des capteurs, qui est également essentiel pour affiner le problème direct, et qui s'avère d'autant plus problématique que les sources se rapprochent des objets à imager,
- un positionnement des antennes en émission et en réception, qui tiennent compte des spécificités de l'environnement de mesure (cavité, anéchoicité, ...). Pour cela, il faut définir des outils théoriques permettant de quantifier la performance d'une configuration de mesure par rapport à une autre et c'est dans cette direction que mes recherches se portent actuellement.
- un couplage étroit entre expérimentateur, numéricien, théoricien et utilisateur final. Ce genre d'approche est d'ailleurs celle retenue à Schlumberger où l'équipe qui développait un nouveau système d'imagerie possédait toutes ces compétences. Nous avons la chance de bénéficier de ce même vivier au sein du groupe Hipe de l'Institut Fresnel. De plus, la confrontation mesure-simulation s'avère nécessaire pour proposer des solutions innovantes, issues de la prise en compte des contraintes imposées par les conditions expérimentales.

Perspectives

Chaque thème abordé dans ce manuscrit suscite une volonté de poursuite. Il y a ainsi une multiplicité de thèmes de recherche possibles pour les années futures, qui risquent d'être plus orientés par les opportunités de financement que par l'intérêt que j'y porte personnellement. Ces axes de recherche sont des axes collectifs, car la conception et l'amélioration d'un instrument d'imagerie nécessite obligatoirement de multiples compétences.

- Nous avons porté un gros effort ces derniers temps pour essayer de démontrer une approche de caractérisation non-destructive par hyperfréquence pour le contrôle de l'eau dans le sol. Nous avons mis au point un scanner, des outils de modélisation et d'inversion qui ont fait apparaître les verrous qui demeurent et nous empêchent de pouvoir atteindre cet objectif de manière satisfaisante. Mon but est de participer à la définition et l'exploitation d'un nouveau scanner circulaire qui, à plus haute fréquence, et avec un milieu ambiant de permittivité plus basse, permettra une meilleure sensibilité de mesure aux variations de teneur en eau du monolithe. Ce travail s'effectue d'ailleurs actuellement dans le cadre du stage de O. Caratozzolo et d'autres étudiants d'IUT présents dans le groupe Hipe cet été.
- Les premières mesures avec la petite chambre anéchoique installée dans les locaux de l'Institut Fresnel sont toutes récentes. Il va falloir à nouveau se plonger dans une étape de caractérisation du bruit de mesure, ainsi que dans une étape de modélisation spécifique à cette géométrie de mesure. De part la disposition des antennes sur une ligne de mesure, les propriétés spectrales de l'opérateur de radiation seront différentes, il faudra à nouveau définir un protocole robuste de calibrage des mesures. Un large champ d'activités est prévu pour cette chambre, passant de la caractérisation de l'eau dans le proche sous-sol, au contrôle de l'absorption de l'eau par les plantes, à la détection d'objets enfouis, à la caractérisation d'antennes en champ très proche, ...
- Il existe également tout un pan de recherches qui connaît une recrudescence d'activité dans la communauté problèmes inverses par diffraction et qui concerne les systèmes d'imagerie hyperfréquences pour des applications biomédicales. Nous avons ainsi commencé une étude amont en collaboration avec le CEA pour aider à caractériser les

fantômes qu'ils utilisent dans le cadre de l'imagerie IRM. Nous sommes également en train d'étudier l'intérêt d'une approche microonde pour la caractérisation précoce du cancer du sein, avec des partenaires néerlandais et italiens.

Au niveau algorithmique, un certain nombre d'axes s'ouvrent également :

- l'optimisation de configuration est une voie de recherche qui m'intéresse plus particulièrement. Comme expliqué précédemment, le but est de pouvoir définir et réaliser des prototypes d'instruments d'imagerie hyperfréquences qui ont des caractéristiques optimales au vu de l'application visée. Mon intérêt se porte plus particulièrement sur la définition de critères d'optimalité, la prise en compte du caractère non-linéaire des équations de diffraction (les résultats que nous avons obtenu jusqu'à présent ne tiennent pas compte du caractère non-linéaire des équations), le choix du placement des antennes et de leur polarisation en différentiant les antennes d'émission et de de réception, le type d'éclairement voulu, ...
- Tous les algorithmes qui ont été développés dans des configurations bidimensionnelles doivent être maintenant adaptés à des configurations tridimensionnelles. Pour se faire, le code par éléments finis que H. Tortel a mis au point ces dernières années sera grandement mis à profit. Il faut simplement définir correctement l'état adjoint, en faisant attention aux différentes polarisations des champs, ainsi qu'au calcul du gradient. Un gros effort numérique sera également nécessaire afin de réduire les temps de calcul, en essayant par exemple une implémentation sur architecture parallèle. De plus, l'incorporation de maillages conformes provenant d'images obtenues par d'autres systèmes de mesure, comme en particulier les rayons X ou l'IRM dans le cadre des applications biomédicales, s'avèrera indispensable pour augmenter la précision spatiale des images reconstruites.
- Le passage à des matériaux anisotropes se fera alors de manière naturelle. Il sera ainsi intéressant de comparer les champs diffractés simulés aux champs mesurés pour des matériaux composites complexes, en tirant profit de l'expertise de mesure que nous avons avec la grande chambre anéchoique.
- Un couplage étroit entre les processus hydrodynamiques et électromagnétiques mis en jeu dans le cadre du contrôle de l'écoulement de l'eau dans le sol devra être incorporé dans l'algorithme d'inversion. Il est par exemple possible d'incorporer un second terme dans la fonctionnelle à minimiser pour contraindre la solution à suivre les deux phénomènes physiques à la fois.
- Les algorithmes itératifs mis en jeu n'utilisent que le calcul des dérivées premières. Il serait intéressant de trouver des formulations analytiques simples, inspirées de celle du gradient qui utilise l'état adjoint, pour calculer les dérivées secondes. L'obtention du Hessien permettrait alors d'évoluer vers des algorithmes de minimisation itératifs plus efficaces. La problématique que l'on rencontre alors est de ne pas passer plus de temps à calculer les dérivées secondes qu'à faire converger un algorithme n'utilisant que des dérivées premières.
- L'introduction d'information a-priori adaptée aux configurations de mesure continuera d'être un sujet de recherche important. En particulier, avec les prochaines mesures qui sortiront de la nouvelle chambre anéchoique, les configurations stratifiées utilisant des champs mesurés, et non plus simulés, vont susciter un nouvel intérêt. Les fonctions de base utilisant un échantillonnage exponentiel n'ont été pour l'instant exploitées que dans le cadre d'une approche linéarisée. Il serait intéressant de les étendre dans le cas où tout le phénomène de diffraction est mis en place. De même, l'exploitation de champs mesurés par l'algorithme de caractérisation de surface rugueuse que nous avons mis au point est une voie à poursuivre.
- Dans ce manuscrit, aucune méthode qualitative n'a été évoquée. Il existe pourtant tout un pan de la littérature des problèmes inverses portant sur ce genre de techniques. Ci-

tons en particulier la rétroprogation, la décomposition de l'opérateur de retournement temporel, l'algorithme Music, ... Des premiers travaux basés sur ces algorithmes de rétropropagation ont été entrepris dans le cadre de la thèse de R. Lencrerot et se poursuivent actuellement dans le cadre d'un stage de master. Ces méthodes sont également au coeur du sujet de thèse de X. Zhang, encadré par H. Tortel avec qui je collabore également.

– Pour finir, il existe de nombreuses voies de recherche spécifiques au formalisme des fonctions de niveau. Il serait difficile de les lister toutes, on peut néanmoins évoquer le passage aux géométries tridimensionnelles, la reconstruction de surfaces rugueuses de manière quantitative, la détermination de la forme de fissures qui peuvent être disjointes et éventuellement présenter des ramifications multiples.

La liste de ces futurs thèmes de recherches n'est bien sûr pas exhaustive et risque fortement de varier dans les prochaines années en fonction des avancées obtenues dans l'un ou l'autre domaine.

Chapitre 8

Sélection d'articles

Diagraphie différée

Configurations

Information a-priori

Resistivity Modeling of Array Laterolog Tools: An Application in an Offshore Norway Clastic Reservoir

M.T. Galli, M. Gonfalini, SPE, and **M. Mele,** Eni-E&P Div., and **P. Bělík, O. Faivre,** SPE, **L. Jammes,** SPE, and **A. Litman,** Schlumberger S-RPC

Summary

Resistivity logs, while used extensively in the oil industry for the determination of water-saturation profiles and, consequently, for the quantification of hydrocarbon originally in place (HOIP), are strongly affected by environmental effects such as borehole, shoulder-bed resistivity contrasts, mud-filtrate invasion, dipping beds, and electrical anisotropy. It is well known by log interpreters that the combination of the different effects may strongly affect the estimation of hydrocarbon in place and hydrocarbon reserves. This paper highlights the strong reduction of the uncertainties in water-saturation determination and, consequently, the petrophysical characterization of the reservoir achieved by applying the appropriate 2D resistivity-modeling and -inversion techniques to two wells of the Norwegian offshore area. Both wells were drilled in a sandstone reservoir, with some thin-bedded intervals, and affected by the presence of anomalous invasion profiles.

Introduction

Resistivity logs, as directly used for the determination of water-saturation profiles, have always been of focal interest for the oil industry; it is clear that the quality of these measurements, currently used in the net-pay and hydrocarbon-in-place determinations, must be very high. As a consequence, more accurate and flexible resistivity tools have been developed in recent years. We will address the family of array tools, particularly the HRLA,* which makes available a set of five galvanic resistivity measurements at different depths of investigation.

Unfortunately, the most common types of environmental noise (borehole effects, shoulder-bed resistivity contrasts, invasion, the presence of dips, and anisotropy) still alter the measured resistivity, thus affecting the estimation of the true resistivity in hydrocarbon-bearing levels. To remove these alterations, we have developed a 2D resistivity modeling and inversion technique that can correct a number of environmental effects simultaneously.

This paper presents the results obtained in two wells of the same reservoir in the offshore Norway area, where the sandstone bodies are interbedded with deltaic shales. The values of porosity and permeability are generally very high, and a complete set of data [conventional and special core analysis, conventional wireline logs, microresistivity imaging logs, nuclear magnetic resonance (NMR), and sedimentological analysis from core and images] is available. The 2D modeling provides a better definition of the water saturation in the thinner sandstone bodies of the sequence and in the presence of anomalous invasion profiles.

When comparing the resistivity-modeling results with those obtained by standard interpretation techniques, we can see the effectiveness of the developed methodologies (both hardware and software) in improving the reservoir characterization and in maximizing the return of the investments in logging and well-data measurements.

The aim of this paper is two-fold: the authors want to show how complex reservoir studies can benefit from the correct integration of heterogeneous geological data, while addressing at the same time the added value of applying a 2D modeling and inversion numerical technique to resistivity measurements to compute accurate water-saturation profiles.

One of the most important issues of the formation-evaluation process is the correct estimation of all the petrophysical parameters necessary to determine the hydrocarbon content of the reservoir. This implies the need to compute a saturation profile as correct as possible. Because S_w (and, consequently, S_h) strongly depends on resistivity, porosity, and shale volume, it is of the utmost importance that the uncertainty on these measurements be kept very low. In recent years, the accuracy of resistivity tools has been improved greatly by the introduction of array measurements[1,2]; unfortunately, the utter complexity of real formations can often lessen the intrinsic advantages of the available logs. The most common environmental noise sources, as listed in many well-known works,[3–5] are:

- Thin beds and/or dips.
- Deep and/or exotic invasion profiles.
- High resistivity contrasts between mineralized (porous) and tight layers (shoulder effects).
- Electrical anisotropy (usually related to laminations and grain-size variations).

In most cases, their combined effects cannot be removed separately but must be treated as a unique, nonlinear problem. In previous work,[6–9] it has been shown how resistivity modeling and inversion techniques can solve these kinds of problems, provided that an appropriate and fast forward model (2D or 3D) is available for all the acquired tools and that a robust and efficient inversion algorithm can be implemented.

In the following paragraphs, we will show how the integration of different types of data [geological studies, wireline logs, nuclear magnetic resonance (NMR) measurements, core data], together with the most advanced numerical interpretation techniques, can produce accurate and robust results for many formation-evaluation problems, thus reducing the uncertainty of the estimation of the petrophysical parameters that are relevant in reservoir studies. The importance of geological and petrophysical information in defining a correct formation model was also addressed in a recent paper,[10] which shows how this is also useful in constraining the inversion process.

For this reason, we will first describe the geological setting of the reservoir and the available data, highlighting the interpretation process and the problems encountered; we will then focus on the methodology used for the evaluation of the correct water-saturation profile from resistivity measurements, demonstrating how this methodology, based on modeling and inversion techniques, can enhance the robustness of the results, as confirmed by different sources of information. Because the field study has not been yet completed, from the reservoir point of view, the conclusions will not be definitive, and the paper will end with a work-in-progress description of future activities. We will, however, be able to state the advantages of the proposed numerical modeling

* Mark of Schlumberger.

This paper (SPE 89072) was revised for publication from paper SPE 77714, first presented at the 2002 SPE Annual Technical Conference and Exhibition, San Antonio, Texas, 29 September–2 October. Original manuscript received for review 21 August 2002. Revised manuscript received 5 November 2004. Paper peer approved 23 November 2004.

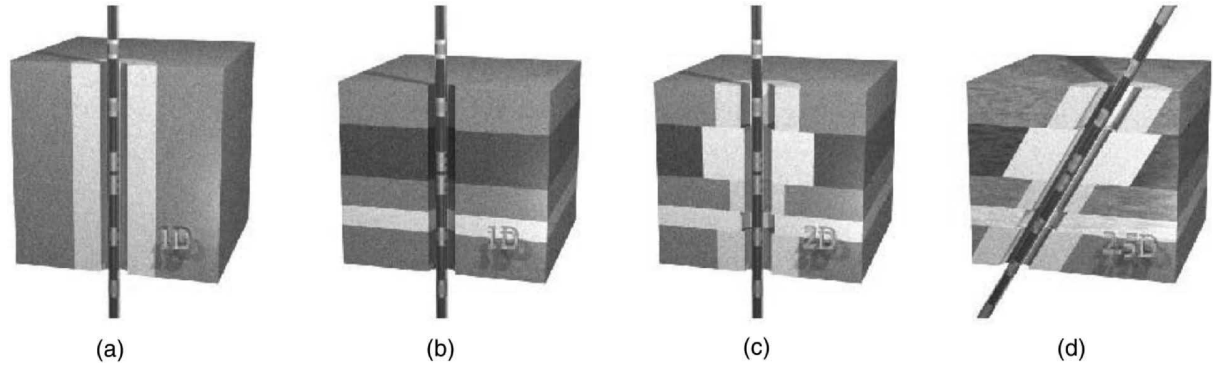

Fig. 1—Formation models: (a) infinitely thick bed with radial variation of resistivity, geometry assumed for borehole and invasion correction (1D radial); (b) geometrical model assumed for shoulder correction (1D vertical); and (c) formation geometry assumed in the 2D and (d) 2D+dip cases.

and inversion technique applied to laterolog array measurements, especially when in the presence of data of different qualities.

Resistivity Modeling and Inversion

Resistivity measurements are used widely for the determination of water-saturation profiles, net pay, and hydrocarbon in place in hydrocarbon-bearing reservoirs, but because of a number of environmental effects (borehole, shoulder beds, invasion, dipping beds, anisotropy), the measured resistivity may differ from the true resistivity, thus affecting the correct estimation of the most important petrophysical parameters.

Two-dimensional resistivity modeling has been developed to provide a robust tool for correcting the different, and often superimposed, environmental effects by iteratively inverting resistivity logs, both wireline and while-drilling. The robustness of the solution is increased by constraining the optimization process with *a priori* information (e.g., some geometrical and/or petrophysical characteristics of the formation).

The application of inversion techniques to resistivity logs has been proposed and effectively described by Mezzatesta *et al.*[7] In 1995, they showed that a simultaneous 2D inversion of galvanic and induction data could significantly improve the estimation of the virgin-zone resistivity.

With the development of more robust minimization algorithms, the availability of fast modeling codes, and more efficient hardware/software environments, inversion techniques have become a usable tool for well-log interpreters.

Jammes *et al.*[6] presented a 2D parametric inversion aimed at improving saturation determination in a thin-bedded environment, carried out with new methodology for the analysis of electrical-tool responses in layered and invaded formations; this methodology was developed by Schlumberger in collaboration with Eni-E&P Div. as a result of a joint R&D project and is now implemented in an integrated software product.

The methodology is based on the modeling and inversion of resistivity measurements in 1D, 2D, and 2D+dip environments **(Fig. 1)** and is divided into three main steps; these steps are iterated **(Fig. 2)** until a proper cost function is optimized:

- Describe the formation model properties (geometry and petrophysics).
- Compute the corresponding synthetic resistivity by way of numerical forward models.
- Modify the values of the formation parameters by minimizing the quadratic distance between the synthetic logs and the actual measurements.

The complete set of properties (geometrical and physical) necessary to describe a layered (or pancake) formation model is shown in **Fig. 3.**

Interesting results have been obtained by applying the methodology in operational environments,[11,12,17] which can assess its state of the art (at least for 2D applications), while new developments toward 3D are due in short time.

Geological Setting and Petrophysical Description of the Reservoir

The reservoir under investigation is characterized by sandstone bodies interbedded with deltaic shales.

The sandstone bodies are characterized by high values of porosity and permeability; the reservoir is oil-bearing, and an oil/water contact (OWC) is evident from log interpretation and is confirmed by pressure analysis.

The formation pressure data indicate the probable presence of a single hydrocarbon column. Three main sedimentological environments have been recognized by the sedimentological facies analysis; these will be discussed in the following sections.

Vegetated, Water-Saturated Flood Plain (Fig. 4). This environment consists of mottled massive to thinly laminated silty shales and very-fine-grained sandstones. Sandstones occur as thin or very thin-bedded alternances or, more commonly, as amalgamated packages in which the bioturbation can be very intensive. The internal structures and the original thin-bedded stratification suggest a deposition from small-volume sand-laden waning currents, probably produced by fluvial overbank floods or crevasse splays.

All of these flood-plain deposits are expected to be characterized by a remarkable lateral continuity.

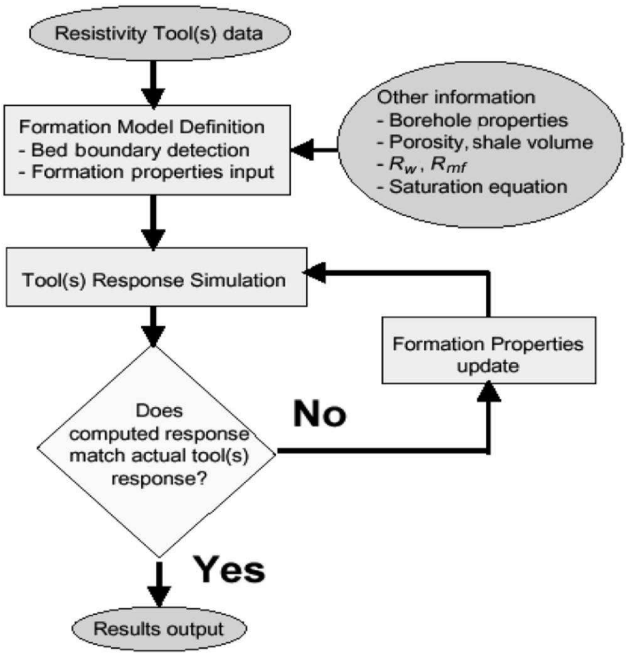

Fig. 2—Measurement-processing flow chart.

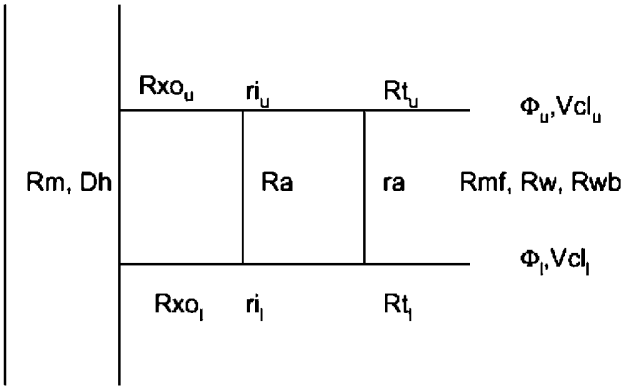

Fig. 3—A bed is described by a set of parameters (i.e., physical and petrophysical properties). In addition to standard resistivity description, the user can choose more complex models in which resistivity and petrophysical properties are linked through a saturation equation (refer to the Nomenclature for property definition—*u* stands for upper, *l* for lower).

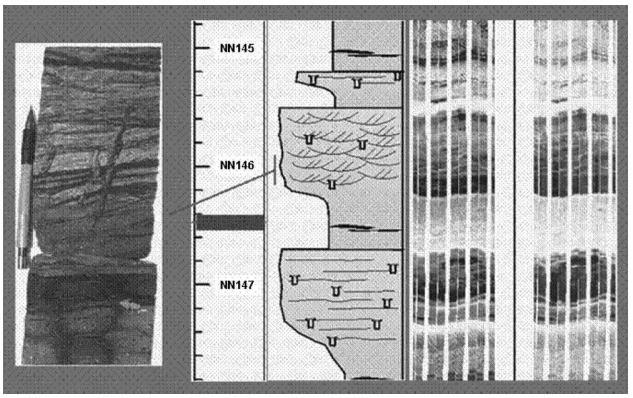

Fig. 4—Overbanks in flood plain.

Porosity. The effective porosity varies between 5 and 8 porosity units (p.u.) in the shaly intervals and up to 30 p.u. in the thin sand layers. In these bodies, the log-measured porosity is always less than that determined on core plugs because of the inadequate vertical resolution of the downhole tool in relation to the thickness of the porous layers.

Pore System. The shaly intervals are dominated by the finest elements and fully saturated with irreducible water, whereas the thin sand bodies are characterized by a poorly sorted pore system with predominating fine elements.

Permeability. The shaly layers may be considered impermeable. The sand layers have permeability values lower than 1 darcy.

Mineralization. S_w values vary between 20% and 40%, although the calculated S_w values are overestimated because of the incorrect value of R_t recorded by the resistivity device.

The value of S_{wirr} calculated from NMR analysis is approximately 20%. It is possible to assume that this value is realistic for the thin sandstone bodies.

Fluvial Distributary Channel (Fig. 5). The channel consists mainly of coarse-grained sandstones. The crossbeddings are of large and medium scale (up to 60 cm in a single foreset), with the individual laminae outlined by grain-size segregations or (more rarely) by coal/plant debris. According to the literature, this type of channel should be characterized by a low sinuosity. Very coarse to microconglomerate sandstone levels are present locally.

Porosity. Porosity varies between 20 and 32 p.u.

Pore System. The system is homogeneous and well sorted, with very low values of irreducible water saturation (always lower than 5%).

Permeability. There is very good estimated permeability, especially in association with higher values of effective porosity (2 to 4 darcies, with peaks at 5 darcies).

Mineralization. S_w values calculated for this system generally match the value of S_{wirr} derived from the NMR device in the oil-bearing levels. The values of S_{wirr} are generally very low (from 5 to 10%).

Tidal-Influenced Fluid Interdistributary or Tidal Channel (Fig. 6). This environment consists of medium- and fine-grained sandstones and silty shales. The sandy levels show internal crossbedding (medium- and small-scale) characterized by occasional bidirectionality. This tidal sandstone package should be characterized by a considerably greater lateral extent than the underlying fluvial distributary.

Porosity. Porosity varies between 22 and 32 p.u.

Pore System. The pore system is poorly sorted, with irreducible water volumes related to the grain size of the sediment.

Permeability. There is very good estimated permeability, especially in association with higher values of effective porosity (always less than 2 darcies).

Mineralization. The S_{wirr} values of this system can vary from 5% (in the best-sorted levels) to 20%, with an average value of 12%.

Operational Information

The data under evaluation were acquired in two vertical wells; the data for the wells can be found in **Table 1.** The sequence of data acquisition is shown in **Table 2.**

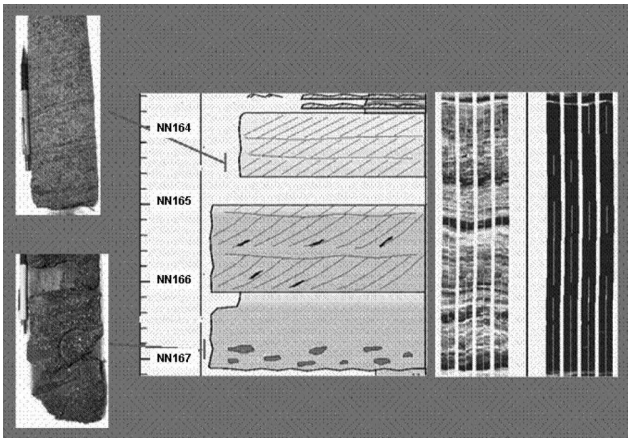

Fig. 5—Fluvial channel.

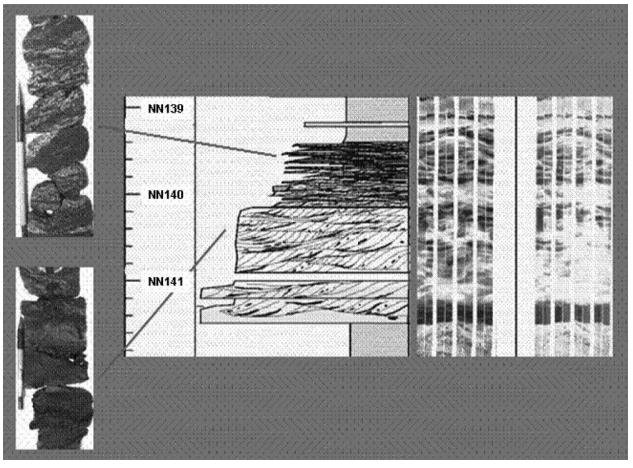

Fig. 6—Tidal-influenced channel.

TABLE 1—WELL DATA

	Well 1	Well 2
Mud type	Formate polymer	K + formate
Mud density	1.31 g/cm^3	1.25 g/cm^3
Mud resistivity at 15°C	0.062 ohm.m	0.078 ohm.m
Mud-filtrate resistivity at 15°C	0.052 ohm.m	0.061 ohm.m
Resistivity devices	HALS*–MCFL*	HRLA*-MCFL
Cores	Yes	Yes
Hole diameter	8.5 in.	12.25 in.

* Mark of Schlumberger.

TABLE 2—DATA-ACQUISITION SEQUENCE

Well 1	
Run 1	PEX*–HALS
Run 2	CMR*–GR
Run 3	FMI*–DSI* (monopole-upper dipole-lower dipole)–GR
Run 4	MDT* sampling
Run 5	MSCT*
Well 2	
Run 1	PEX–HRLA
Run 2	FMI–DSI-(monopole-upper dipole-lower dipole)–GR
Run 3	CMRplus*–APS*–HNGS*
Run 4	MDT sampling
Run 5	Dual CSAT*–GR

* Mark of Schlumberger.

All of the operations were conducted without operational problems, and there were no reports of mud losses during or between the wireline operations. A description of the HALS* and HRLA* laterolog tools can be found in Refs. 13 and 14.

Resistivity Modeling

The analysis of deep-reading electromagnetic measurements is critical to the evaluation of hydrocarbon reserves. However, in thin-bed formations, poor tool vertical resolution and corresponding low sensitivity to hydrocarbon presence makes interpretation in the virgin zone difficult. *A priori* knowledge such as formation geometry or auxiliary petrophysical information is necessary to overcome these difficulties.

The purpose of the proposed methodology[6] is to provide a common environment for the interpretation of electrical tools, wireline or logging while drilling (LWD), in thinly bedded environments:

- To provide tool-interpretation modules with a common interface and inversion-based techniques for better reserve estimations.
- To define a standard processing methodology with progressive refinements, as explained later.
- To validate each step from the analysis of quality-control indicators.
- To propose different levels of user mode: (1) the automatic mode enables R_t to be derived for the whole interval assuming simple invasion profiles, and (2) the expert mode allows local analysis of different resistivity data together with the possible use of petrophysical knowledge to constrain the formation in complex environments.

Methodology. The processing methodology is usually split into three main phases, applied in sequence:

- 1D+1D corrections and validation.
- 2D automatic modeling and inversion.
- 2D expert mode processing.

We will describe in brief the purpose and the outputs of each phase.

1D+1D Corrections and Validation. In many circumstances, environmental effects (such as borehole, shoulder, and invasion effects) can be corrected independently, in sequence. This is often referred to as the 1D (radial)+1D (vertical) sequence of corrections. These so-called 1D environments are characterized by just one noise source (i.e., radial invasion in an infinitely thick layer). This assumption is valid if the corresponding types of environmental noise are independent.

In real cases, if the tool response can be simulated coherently by a 2D forward model given the resistivity distribution (R_t, R_{xo}, D_i) identified after performing the 1D+1D sequence of corrections, we are surely in the presence of independent effects, and no further processing is required. This quality control is referred to as the "validation" phase.

* Mark of Schlumberger.

2D Automatic Modeling and Inversion. Automatic processing (2D and 2D+dip) is an efficient way to model and invert a complex formation (as described in the Introduction); it is based on the capability of the software to describe the formation as a large number of beds, each of which is then modeled and inverted as a step-profile invasion layer. The simplification of the formation modeling guarantees very fast processing but may lead to inaccurate results (e.g., when very complex invasion profiles are present); in this case, the expert-mode inversion is the only solution.

2D Expert-Mode Processing. Expert modeling is based on an accurate description of each formation layer in terms of invasion profile, thickness, dip, and possibly porosity and shale volume. The inversion process optimizes some of the petrophysical parameters, (e.g., resistivity, radius of invasion, and layer thickness) but it can lead to wrong answers in the presence of badly modeled formations. From this point of view, the term "expert" is often related to the petrophysicist's capabilities.

The methodology described has been applied to both wells. In some intervals, the 1D+1D corrections were sufficient to recompute the correct value of R_t. In general, the 2D automatic modeling brought little improvement. The 2D expert mode was needed to optimize the most difficult "local" problems (complex invasion profile, thin beds).

1D+1D Processing and Validation

The first step consisted of running a 1D+1D sequence on both Well 1 and Well 2. Environmental corrections were performed according to the following procedure:

- For HALS data (Well 1): borehole corrections, eccentering corrections, Groningen effect corrections (negligible), shoulder correction, and inversion for invasion to obtain the values of R_t, D_i, and R_{xo} being directly given by the MCFL microresistivity tool.
- For HRLA data (Well 2): borehole corrections, eccentering corrections (obtained by forcing the five readings to overlay in the shale areas), and inversion for invasion to obtain R_t, D_i, and R_{xo}. External R_{xo} from the MCFL microresistivity tool was used here only as a quality-control check.

For both wells, 1D+1D processing provided satisfactory results when the assumption that environmental corrections are independent is valid. This was confirmed by the small reconstruction errors obtained through the validation task in the zones in which bed thickness is relatively large.

For thin beds in which shoulder-bed effects are important, the validation task, with large reconstruction errors, showed the necessity of further processing.

2D Automatic Processing

The second phase of the processing, the 2D automatic mode, has been applied on the full interval for both wells.[1]

This processing first performs a segmentation of the input logs on a relatively fine sampling scale (1 to 3 ft for the HALS, 0.5 to 1.5 ft for the HRLA), taking into account the vertical resolution of the tools. Each bed of the formation is then described as a simple step profile, using 1D+1D processing results to initialize the values of R_t, R_{xo}, and D_i. For the HALS, because of the limited number of available data at each measured depth, the resistivity of the flushed zone has been fixed to the MCFL value. An iterative inversion scheme is then performed to minimize the errors between the measured and simulated logs.

Results in zones in which shoulder effects were important have been improved. This 2D automatic processing provided best results, in a fast and robust manner, for large beds and simple formation models (step invasion profile).

2D Expert-Mode Processing

The last phase of the processing, the 2D expert mode, was performed only in a few selected intervals extracted from both wells.

The interval extracted from Well 1 presents a very interesting characteristic: the presence of a peculiar invasion profile at the bottom of the main sand layers. These layers show very shallow invasion along most of the bed, and then a very deep invasion ramp at the bottom of the body. These profiles are more evident in thick sand beds, and they are mostly caused by high values of both vertical and horizontal permeability.[15] Their detection is also related to the time span between drilling and the beginning of logging operations because such deep invasion needs some time to set.

The second characteristic we want to address is the presence of sequences of thin beds generally related to the overbanks in the flood plain. In these beds, the differences between the calculated S_w from log data and the S_{wi} measured on core plugs are quite large.[16] The reduced thickness of these layers (definitely below the resolution capability of most of the tools used for both resistivity and porosity measurements) suggests the possibility of an incorrect measurement of R_t and Φ, and, consequently, the possibility of an overestimation of S_w.

This problem can be observed in Well 2, where sequences of thin layers at different depths induce a general reduction of the measured-resistivity value.

Deep Invasion. The presence of high vertical permeability-driven anomalous invasion profiles has been described in former work,[15] and it is known to produce alterations in the induction-resistivity measurements. These alterations, which can lead to a misplacement of the OWC, have been observed in the laterolog measurements available for Well 1 and can be summarized as follows **(Fig. 7):**

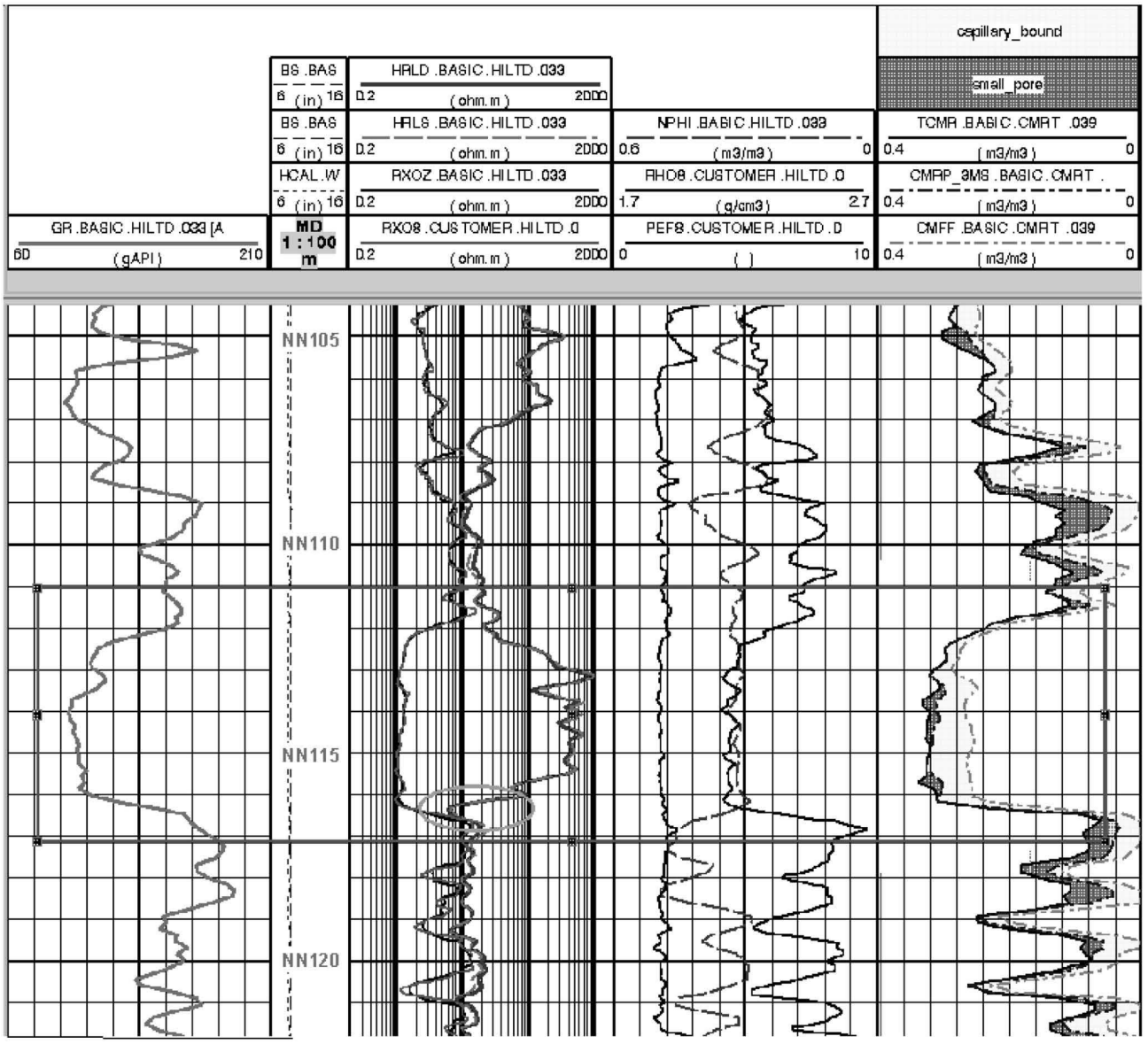

Fig. 7—Well 1: anomalous invasion or OWC?

- Linear reduction of measured R_t at the bottom of the layer.
- Undershooting of R_t at the lower boundary of the layer.
- Problems in defining fluid contacts.

The automatic 2D modeling provided a reasonable solution for R_t and r_i, but when looking at the reconstruction errors, we can see that both petrophysical and geometrical (boundary positions) formation parameters can still be improved. The expert-mode 2D modeling allowed the petrophysicists to correct the misplaced boundary positions and, moreover, to describe a very accurate invasion profile. The thick sand body (more than 4 m) was thus split into three petrophysical zones:

- A main upper layer, characterized by a constant invasion radius.
- A transition layer (more than 1 m), characterized by a linear increasing of the invasion radius.
- A very thin bottom layer (a few inches), where the invasion radius is again constant.

The expert inversion produced a final result where:

- The value of R_t in the transition layer and in the bottom layer is the same as in the upper one.
- The upper layer is characterized by very shallow invasion, while the slim bottom layer is deeply invaded (more than 40 in.).
- The undershooting effect at the bottom has been removed, and the thickness of the bed as a whole has increased.
- The reconstruction errors have been reduced.

These results are summarized in **Fig. 8,** where, in the center column, the final R_t profile (thick squared line) is plotted together with the measured resistivity (thin, continuous lines) and the output of the 2D automatic modeling (dashed line). The final R_t is more accurate and consistent with the MDT pressure data, which gave evidence of a single oil column with a lower OWC.

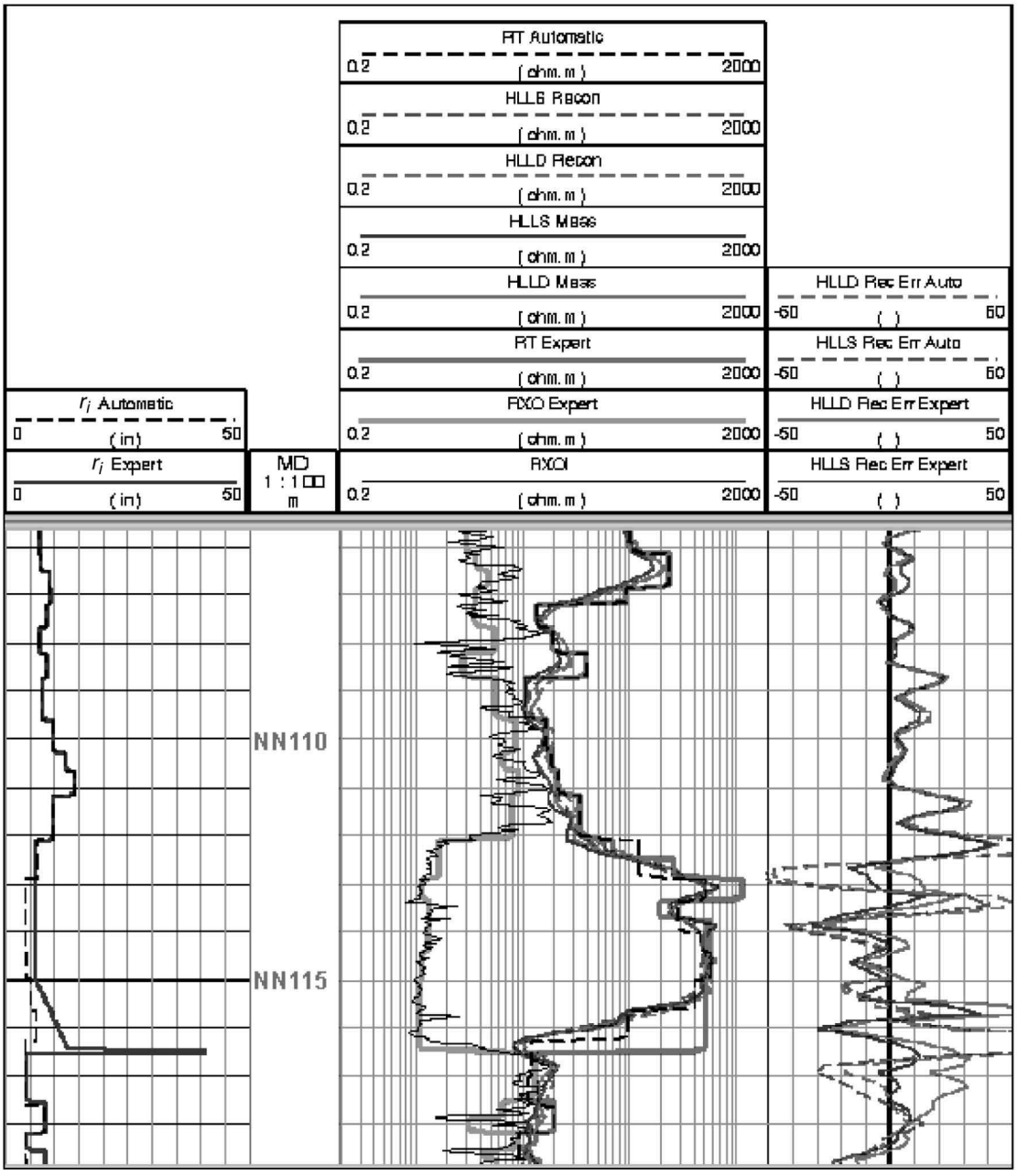

Fig. 8—Well 1: reconstruction of the anomalous invasion profile. The invasion radius (left column, thick line) increases quickly at the bottom of this layer, thus triggering the anomalous R_t profile recorded by the resistivity tool (center column, thin, continuous lines). After the 2D expert-mode processing, the final R_t profile (center column, thick squared line) is consistent along the whole layer.

Sequences of Thin Layers. Sequences of alternating sand-shale thin layers are very common in many sedimentological environments and are present in both Well 1 (**Fig. 9**) and Well 2. The most significant example has been taken from Well 2, where a series of hydrocarbon-bearing layers, each one less than 0.5 m thick, induces a strong reduction in the measured R_t. The 2D automatic modeling, while computing a good R_t profile in thicker beds, still could not recover the correctly enhanced R_t values in the thinner ones, thus suggesting an expert-mode reprocessing of some selected intervals.

Here again, the problem remains the correct evaluation of S_w in thin hydrocarbon-bearing levels[6] and the best estimation of the hydrocarbon potential of the sequence. The 2D expert-mode processing allowed the petrophysicists to compute a more correct R_t for further elaboration.

The initial layering has been driven by a complete sedimentological description of the cores and by FMI data interpretation; R_t was constrained to maintain the same value in all the layers belonging to the sequence. This assumption is supported by the evidence of hydraulic continuity confirmed by formation tests and by the high homogeneity of the textural/sedimentological facies.

The final value of R_t in thin beds has been quite enhanced, with respect to both the field acquisition values and the results of 2D automatic modeling; the reconstruction errors are very low, and the final r_i values are as expected. The final R_t profile, as shown in **Fig. 10** (center column, thick squared line), is the integration of 2D automatic-modeling (in thick beds) and 2D expert-mode-processing (in thin layers) results; reconstruction errors are below 15% for both solutions.

The last step consisted of recomputing the value of S_w according to the new R_t profiles.

The computation of S_w has been performed by using the Indonesia formula; the necessary exponents and coefficients were calibrated against core-analysis data. In **Fig. 11,** a comparison among three different S_w profiles is shown. The first was computed with

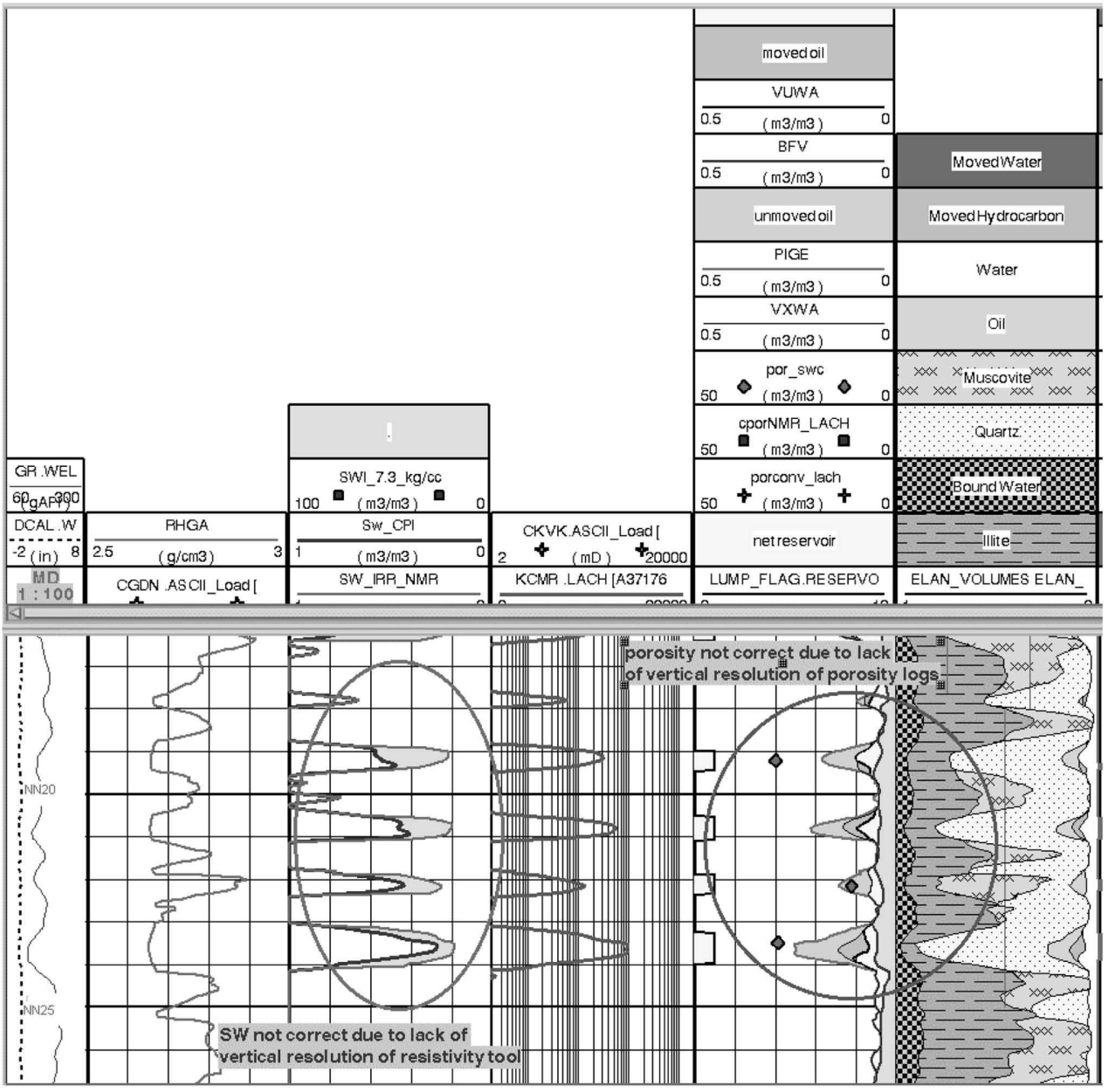

Fig. 9—Well 1—sequence of the thin beds: conventional interpretation. This example shows a conventional interpretation of wireline logs (computer-processed interpretation, or CPI). We can see that the estimated porosity is lower than core measurements (right oval) and that SW_CPI is higher than SW_IRR from NMR (left oval).

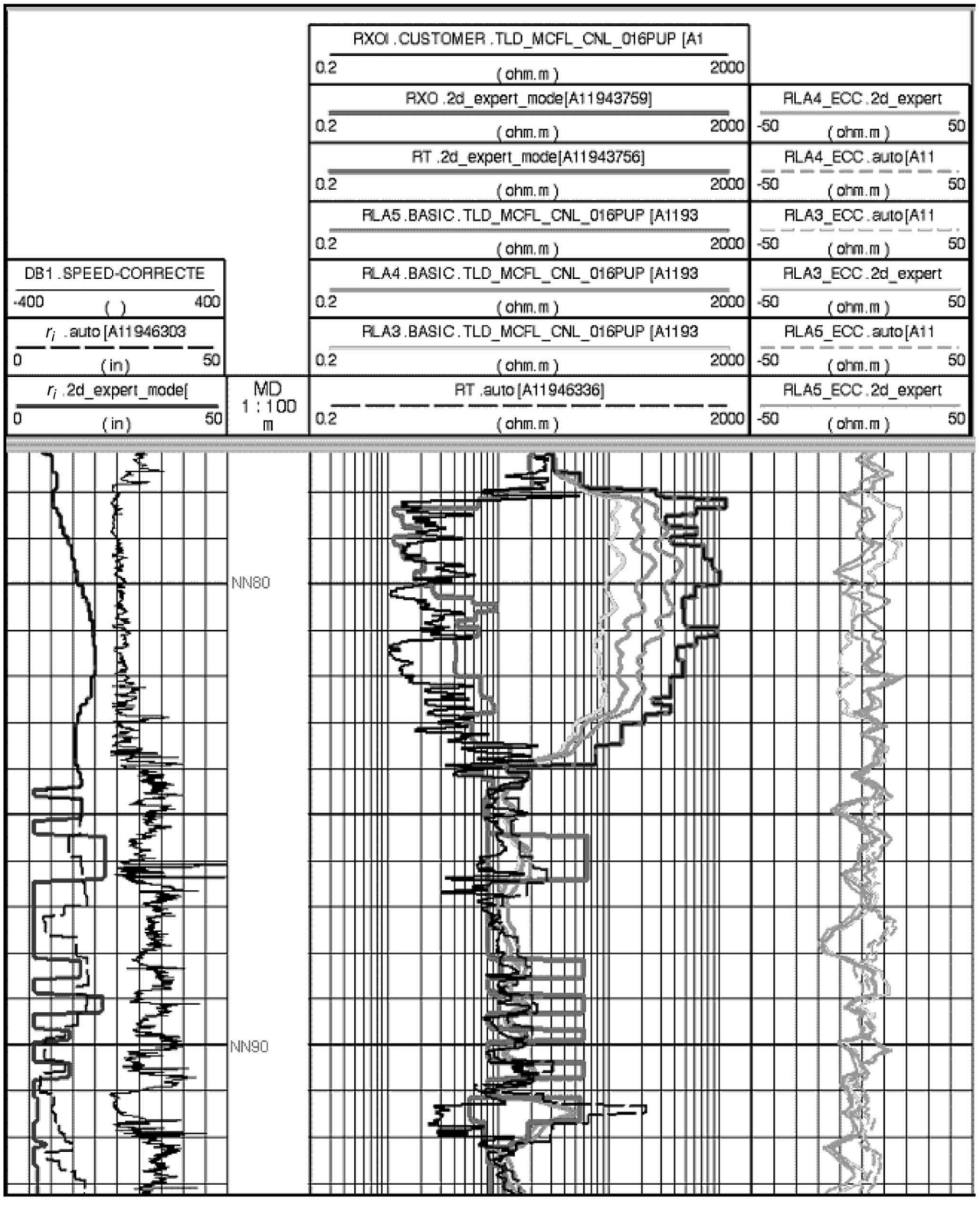

Fig. 10—Well 2—sequence of thin beds: 2D modeling and inversion. The 2D automatic inversion computed a good log reconstruction (right column, dashed lines) but, owing to the low sensitivity of the tool, did not modify the very low resistivities in the thin beds (center column, dashed line). The 2D expert-mode processing did succeed in improving the R_t value in the thin layers (center column, thick squared line) while keeping the reconstruction errors very low.

the field 1D+1D R_t and the density-neutron porosity. The porosity was then modified according to the following criteria:

- The final layering obtained from the resistivity modeling was used to square the porosity curve.
- The porosity was set to 24 p.u. in the levels at which $r_i > 15$ in. to compensate for its underestimation caused by the level thinness. The value of 24 p.u. is consistent with the routine core analysis. The second S_w profile was computed with the field 1D+1D R_t and

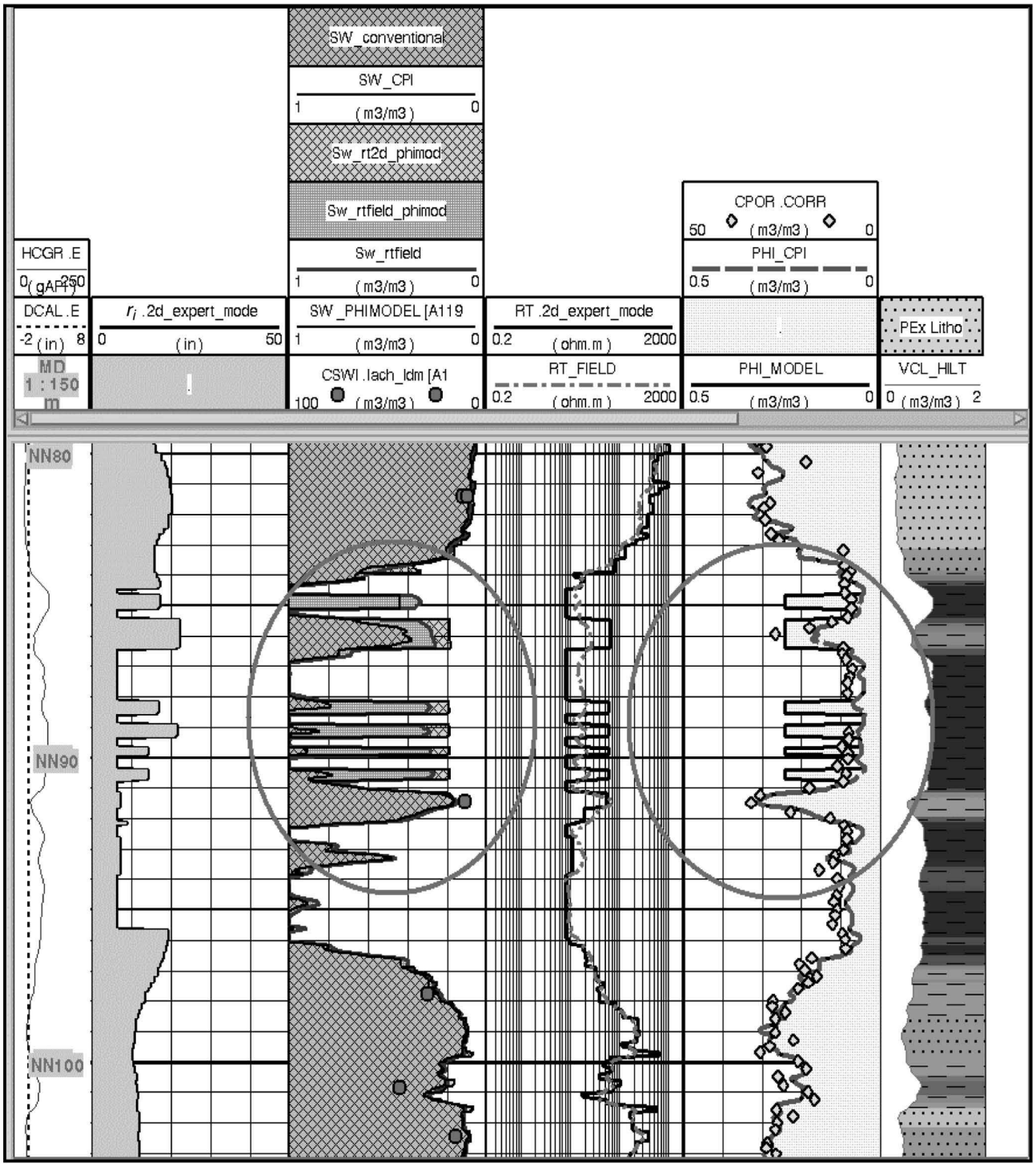

Fig. 11—Well 2: comparison of water-saturation profiles.

the modified porosity; the third S_w was then evaluated with the final 2D R_t (integrated automatic and expert mode) and (again) the modified porosity.

This last S_w profile is more consistent with the field data (single hydrocarbon column) and with core-analysis data (S_{wirr} from NMR and from capillary pressure tests).

Next Steps

The study of the reservoir is still in progress, and the satisfactory results obtained from resistivity modeling in Well 1 and Well 2 will be the start for further analysis, which will include:

- The extension of 2D expert-mode processing to all the intervals with thin sand layers, in both wells.
- The comparison between the traditional petrophysical-analysis data (mainly in terms of S_w) and the new results computed from the 2D modeled resistivity profiles.
- The evaluation of previously unidentified hydrocarbon-bearing zones.
- The evaluation of the differences in the volumes of hydrocarbons in place.

According to the invasion behavior observed in Well 1, the petrophysical interpretation of future wells in this area will check for the presence of anomalous invasion profiles.

Conclusions

A relatively new methodology for 2D resistivity modeling and inversion of laterolog measurements has been applied in operational conditions to reduce the uncertainty on the final water-saturation profile.

The methodology is based on an iterative process split into various phases of increasing complexity, thus allowing the formation-evaluation specialists to take into account all the geological and sedimentological data necessary to obtain petrophysically consistent solutions.

The integration of petrophysical information was helpful to constrain the formation model properties in both the examined wells, where very different R_t estimation problems have been faced and solved.

The final results have been judged of good quality and are quite important, both for the completion of the reservoir study and for future well planning and interpretation.

Nomenclature

k_H = horizontal permeability, md
k_V = vertical permeability, md
D_h = hole diameter, L
D_i = invasion diameter, L
r_i = invasion radius, L
R_m = mud resistivity, ohm.m
R_{mf} = mud-filtrate resistivity, ohm.m
R_t = virgin-zone resistivity, ohm.m
R_w = formation-water resistivity, ohm.m
R_{wb} = bound-water resistivity, ohm.m
R_{xo} = invaded-zone resistivity, ohm.m
S_h = virgin-zone hydrocarbon saturation
S_{xo} = invaded-zone water saturation, %
S_w = virgin-zone water saturation, %
S_{wirr} = virgin-zone irreducible water saturation
V_{cl} = shale volume, %
Φ = porosity, %

Acknowledgments

The authors wish to thank Eni Norge, Phillips, Statoil, Enterprise, and Fortum for permission to publish the data in this paper; Giorgio Maletti and Franco Fonnesu of the Eni-E&P Div. Petrophysics and Sedimentology departments, who contributed to the preparation of this work; Georges Pilot of Schlumbeger S-RPC for his full support on Invasion2; and Jean-Marc Donadille of Schlumberger S-RPC for providing the 1D results for HRLA. A special thanks to Anna Maria Lyne for her important contribution to the work and for the revision of the text.

References

1. Griffiths, R. *et al.:* "Optimal evaluation of formation resistivities using array induction and array laterolog tools," paper BBB presented at the 2000 SPWLA Annual Logging Symposium, Dallas, 4–7 June.
2. Griffiths, R. *et al.:* "Better saturation from new array laterolog," paper DDD presented at the 1999 SPWLA Annual Logging Symposium, Oslo, Norway, 30 May–3 June.
3. Barber, T. *et al.:* "Interpreting multi-array induction logs in difficult environments," paper YY presented at the 1999 SPWLA Annual Logging Symposium, Oslo, Norway, 30 May–3 June.
4. Barber, T. and Rosthal, R.A.: "Using a Multiarray Induction Tool To Achieve High-Resolution Logs With Minimum Environmental Effects," paper SPE 22725 presented at the 1991 SPE Annual Technical Conference and Exhibition, Dallas, 6–9 October.
5. Klein, J.D. *et al.:* "The petrophysics of electrically anisotropic reservoirs," paper HH presented at the 1995 SPWLA Annual Logging Symposium, Paris, 26–29 June.
6. Jammes, L. *et al.:* "Improved Saturation Determination in Thin-Bed Environments Using 2D Parametric Inversion," paper SPE 62907 presented at the 2000 SPE Annual Technical Conference and Exhibition, Dallas, 1–4 October.
7. Mezzatesta, A.G. *et al.:* "Integrated 2D interpretation of resistivity logging measurements by inversion methods," paper E presented at the 1995 SPWLA Annual Logging Symposium, Paris, 26–29 June.
8. Frenkel, M.A. *et al.:* "Minimum and maximum pay estimation using resistivity log data inversion," paper Z presented at the 1998 SPWLA Annual Logging Symposium, Keystone, Colorado, 26–29 May.
9. Warrilow, I.M. *et al.:* "Application of Resistivity Inversion Software to Thin-Bed Evaluation," paper SPE 29263 presented at the 1995 SPE Asia Pacific Oil and Gas Conference, Kuala Lumpur, 20–22 March.
10. Zhang, Z. *et al.:* "Petrophysically constrained inversion of resistivity logging data," *Petrophysics* (March–April 2002) **43,** No. 2.
11. Gonfalini, M. and Galli, M.T.: "Array Induction Measurements in Complex Environments: A Comparison Between AIT and HDIL Responses," paper SPE 71711 presented at the 2001 SPE Annual Technical Conference and Exhibition, New Orleans, 30 September–3 October.
12. Haynes, F.M. *et al.:* "Applications of resistivity modeling in reservoir development: examples from Balder Field, Norwegian North Sea," *Petrophysics* (July–August 2000) **41,** No. 4.
13. Smits, J. *et al.:* "High Resolution From a New Laterolog With Azimuthal Imaging," paper SPE 30584 presented at the 1995 SPE Annual Technical Conference and Exhibition, Dallas, 22–25 October.
14. Smits, J. *et al.:* "Improved Resistivity Interpretation Utilizing a New Array Laterolog Tool and Associated Inversion Processing," paper SPE 49328 prepared for presentation at the 1998 SPE Annual Technical Conference and Exhibition, New Orleans, 27–30 September.
15. Dussan, V. *et al.:* "Estimating vertical permeability from resistivity logs," paper UU presented at the 1994 SPWLA Annual Logging Symposium, Tulsa, 19–22 June.
16. Bona, N. *et al.:* "Use of an Integrated Approach for Estimating Petrophysical Properties in a Complex Fractured Reservoir: A Case History," paper SPE 71741 presented at the 2001 SPE Annual Technical Conference and Exhibition, New Orleans, 30 September–3 October.
17. Gossenberg, P. *et al.:* "Practical applications of resistivity modelling techniques in clastic reservoirs," paper 110 presented at the OMC 2003, Ravenna, Italy, 26–28 March.

SI Metric Conversion Factors

ft × 3.048*	E–01	= m
°F (°F – 32)/1.8		= °C
in. × 2.54*	E+00	= cm
$in.^3$ × 1.638 706	E+01	= cm^3

*Conversion factor is exact.

Maria Teresa Galli joined Eni-E&P Div. in 1998 as a designer and developer of advanced software applications for geosciences, She moved to the Petrophysics Dept. in 2000 and is currently managing the Resistivity Modelling Project. Galli holds a degree in electrical engineering and computer science from the Politecnico of Milan. **Maurizio Mele** joined Eni in 1988; he is currently a senior petrophysicist at Eni-E&P Div. headquarters in Milan and is involved in petrophysical studies of several Eni field projects. He holds a degree in earth science from Parma U. **Mauro Gonfalini** was, for many years, the Senior Professional for Formation Evaluation at Eni-E&P Div. His activities involved both operational and technology innovation programs, but he was mainly dedicated to R&D projects in the area of resistivity measurements, effective use of measurements while drilling, and geosteering technologies. He retired in December 2003. **Pavel Belik** is currently a research associate at the U. of Minnesota. From 2001 to 2002, he was a mathematical simulation and inversion specialist at the Schlumberger-Riboud Product Center. Belik holds a degree in mathematics from Charles U. (Prague) and a PhD degree from the U. of Minnesota. **Ollivier Faivre** graduated at Ecole Polytechnique (France) in 1973 and joined Schlumberger in 1976. After working as a field engineer he moved to interpretation and held various positions as log analyst and interpretation manager. In 1991 he joined the Schlumberger-Riboud Product Center working on new tool in-

Drift correction for scattering measurements

C. Eyraud, J.-M. Geffrin,[a] A. Litman, P. Sabouroux, and H. Giovannini
Institut Fresnel, UMR CNRS 6133, Université de Provence Aix-Marseille I, Université Paul Cézanne Aix-Marseille III, Ecole Généraliste d'Ingénieurs de Marseille, Campus de Saint Jérôme, 13392 Marseille cedex, France

(Received 8 April 2006; accepted 3 November 2006; published online 14 December 2006)

The authors propose a method to correct for drift errors which occur when performing three-dimensional scattering field measurements. This method has the advantages of being fast, without loss of information and with no need of *a priori* information on the scatterer. It is based on the properties of limited spatial bandwidth of the scattered field. © *2006 American Institute of Physics*. [DOI: 10.1063/1.2404978]

Thanks to the success of the two-dimensional scattering field databases that we have measured in the anechoic chamber of the Institut Fresnel and proposed to the inverse problem community,[1–3] we are now extending these studies to three-dimensional (3D) spherical bistatic configurations.[4] This introduces challenges due to the low level of signal as well as its sensitiveness to small disturbances. A careful characterization of the experimental errors is therefore necessary, and as they are mainly responsible for the scattered field variations, we will focus therein on drift errors. The objective is double: improve scattered field measurement accuracy and reduce acquisition time as it can take several hours for one incident illumination for 3D inverse scattering applications. To compensate for this drift error, we propose a fast correction based on a limited spectral bandwidth criterion, with the benefit of no loss of information and no need of *a priori* knowledge on the scatterer. After introducing the measurement setup and describing this correction protocol, we will highlight its influence on the acquisition process.

The configuration of the faradized anechoic chamber of the Institut Fresnel[2] is presented in Fig. 1. Its consists of a vector network analyzer (VNA, Agilent-HP 8510) used in a multisource setup with two synthesizers, two deported mixers, and two wide-band ridged horn antennas (ARA DRG118). The receiving antenna (vertically polarized here) is positioned on an arm rotating around the vertical z axis in the same azimuthal plane ($x0y$) as the target. Due to restrictions coming from the physical existence of the arch, the receiving angular position ϕ_r is varying between −130° and 130°. The transmitting antenna (vertically polarized here) is fixed on the arch in the same azimuthal plane. The object, which can rotate on 360° (z axis) with angular position ϕ_o, is supported by a positioner supposedly transparent in the frequency band (from 2 to 18 GHz with a step of 1 GHz here).

The target scattered field is not directly measured but determined by complex subtraction of two field measurements: the total field E_t^{meas} with the presence of the target and the incident field E_i^{meas} without the object. Calibration is then performed using a metallic sphere as reference target.[5]

The pattern of this scattered field is very different from the measured fields. It has a very low level of magnitude, with up to 20 dB of difference for the dielectric sphere case presented afterwards. It also presents very slow variations along the receiver positions whereas the incident field can vary of 2π in less than 1° at 18 GHz. Thus, measurement accuracy, in particular, on the phase, is primordial and even more drastic for 3D configurations.

The characterization of experimental errors is a mandatory step to improve the measurement accuracy.[5,6] A careful analysis of the different errors has thus been made and it seems that the drift error is predominant in our case. Indeed, the incident and total field measurements are not performed at the same time and require several hours. During this time, the field phase and/or magnitude can be drifted (cable drift and network analyzer drift) due to some factors related to time (as temperature, for example). To show the influence of the drift errors, the scattering of a small dielectric sphere (diam=50.75±0.05 mm, ϵ_r=2.50±0.13) has been studied. The dielectric constant has been measured with the commercial kit EPSIMU.[7]

In Fig. 2, the scattered field E_d^{simu} computed analytically using Mie series,[8] and the measured one E_d^{meas} are plotted at 18 GHz. The discrepancy between these two fields is numerically evaluated by an error criterion defined at each frequency f by

$$\mathcal{F}(f) = \frac{\sum_{\phi_r} |E_d^{\text{simu}} - E_d^{\text{meas}}|^2}{\sum_{\phi_r} |E_d^{\text{simu}}|^2}, \tag{1}$$

which has a value of 0.484 for the case of Fig. 2 at 18 GHz. A minimum tolerance variation of 0.1% in magnitude and 0.017 rad in phase is necessary to maintain an error criterion below 0.001. Unfortunately, we have experimentally noticed

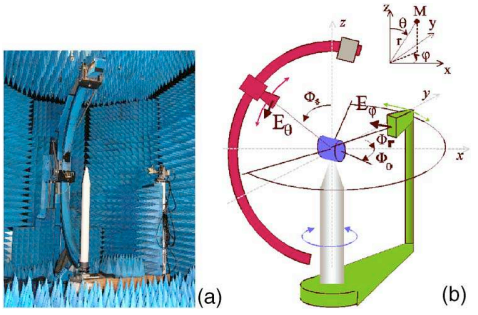

FIG. 1. (Color online) (a) Picture and (b) schematic of the experimental setup.

[a]Author to whom correspondence should be addressed; electronic mail: jean-michel.geffrin@fresnel.fr

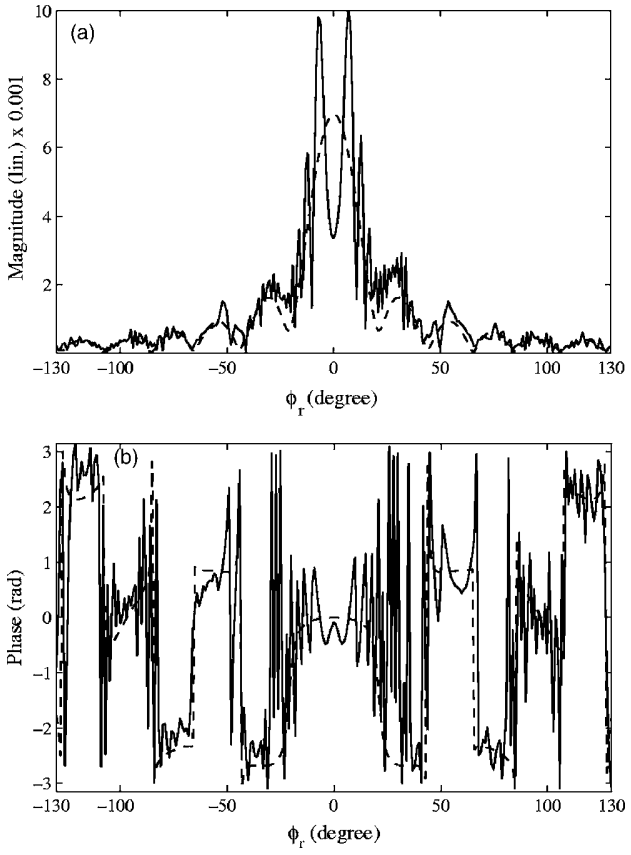

FIG. 2. (a) Scattered field amplitude and (b) phase obtained at 18 GHz [(—) measured and (--) simulated].

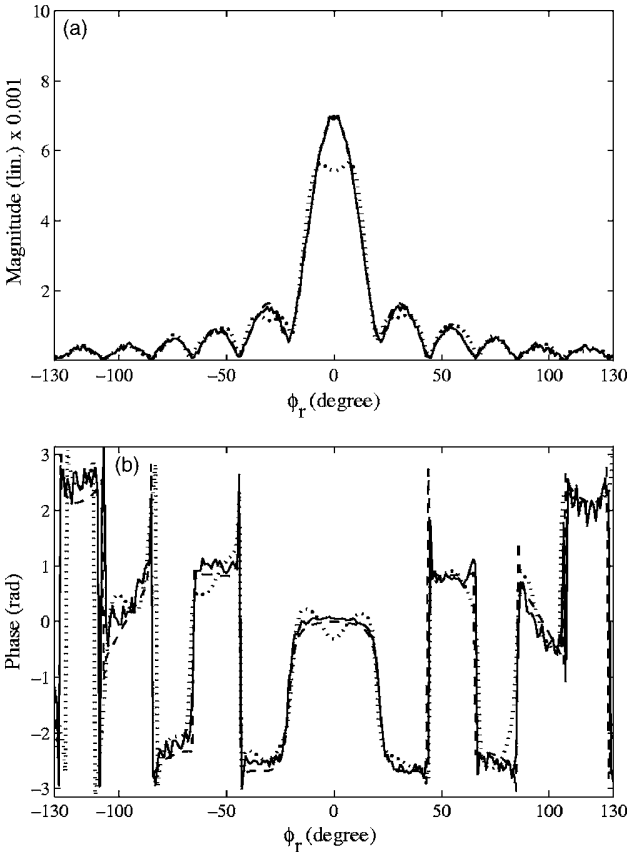

FIG. 4. (a) Scattered field amplitude and (b) phase obtained at 18 GHz [(—) measured and drift corrected, (···) measured and low-pass filtered, and (--) simulated)].

variations around 1% in magnitude and 0.01 rad in phase for 10 h of measurement time. The VNA and the temperature cable drifts[9] are themselves responsible for variations of 0.9% in magnitude and 0.09 rad in phase. Therefore, drift errors have significant effects on the scattered fields.

The goal is to quantify the drift error term for a given source illumination. One solution is to measure several times the same point during total and incident field measurements and deduce the drift coefficients.[10] This method provides good results but is very slow (30% additional measurement time in our configuration). We propose a different approach which is based on the properties of limited spatial bandwidth of the scattered field.

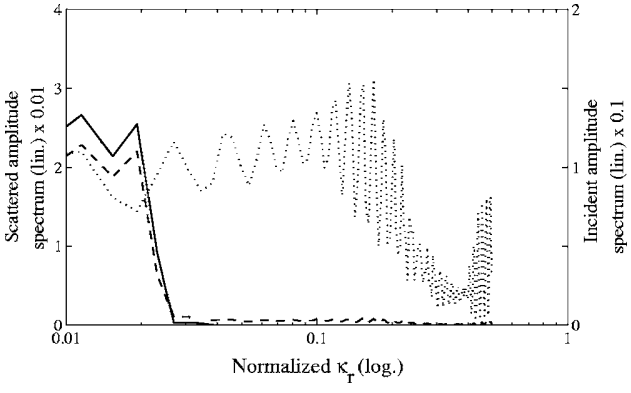

FIG. 3. Spectrum of the (···) incident field, (--) scattered field before correction, and (—) scattered field after correction.

It has been shown[11] that the electromagnetic fields scattered by bounded sources present specific properties when measured on an observation curve Γ described by a proper parametrization $r=r(\xi)$. In particular, the *generalized reduced field*,[12] $F(\xi)=E_d(r(\xi))\ \exp(j\psi(\xi))$, obtained from the measured field by extracting a suitable phase function $\psi(\xi)$ can be approximated by spatially band-limited functions with an error which becomes negligible as the bandwidth governing the sampling representation exceeds a critical value W. In our case, the observation curve Γ is a circle which totally encircles the induced sources, and the phase function $\psi(\xi)$ is nothing but a constant.[12]

All these properties stand for the scattered field but not for the total and incident fields. Therefore, by performing a Fourier transform of the different fields along the receiver positions, as shown in Fig. 3, we can notice that the incident field presents a large spectrum with high frequency components whereas the scattered field has a more compact spectral support. In fact, the spectrum of E_d^{meas} is much broader than expected with high frequency components that are responsible for the large oscillations observed in Fig. 2.

One simple idea would be to low-pass filter the scattered field. This implies to know in advance the cutoff frequency to limit information loss. As the bandwidth W depends only on the scatterer size and shape,[12] this requires *a priori* information on the scatterer.

Here, another approach is proposed. We assume that the drift error between the total and incident fields can be described by a complex coefficient. As the associated acquisi-

tion time on all receiver positions is around 40 min for a given source position and a given target orientation, we neglect the drift and take the complex coefficient as a constant along the receivers for a given incidence. This complex coefficient $ae^{j\gamma}$ is introduced to compute a corrected scattered field E_d^c such that

$$E_d^c = E_t^{\text{meas}}(ae^{j\gamma} - 1) + E_d^{\text{meas}}. \tag{2}$$

The best drift coefficients a^* and γ^* are adjusted by minimizing the bandwidth $B_{E_d^c}$ of the corrected field E_c^d,

$$B_{E_d^c}(a^*, \gamma^*) = \min_{a,\gamma} \frac{\int \kappa_r^2 |\hat{E}_d^c(\kappa_r)|^2 d\kappa_r}{\int |\hat{E}_d^c(\kappa_r)|^2 d\kappa_r}, \tag{3}$$

where $\hat{E}_d^c$ denotes the Fourier transform along ϕ_r and κ_r is the associated Fourier coordinate.

Comparison between the spectral bandwidth minimization effect and a standard low-pass filter is visible in Fig. 4. In one case, the spectrum was corrected with best values $a^*=0.999$ and $\gamma^*=-0.093$ rad (see Fig. 3). In the second case, a rectangular window was used with a cutoff frequency of 0.05. Both approaches remove the high frequency part. But the drift correction term also acts on the low frequency part and maintains the information content. With the proposed drift correction, the scattered fields from Fig. 2 are now considerably improved, as shown in Fig. 4. This is also visible in the error criterion $\mathcal{F}$ which has been divided by 60, from 0.484 to 0.008 (and from 0.600 to 0.009 if averaged on all frequencies), compared to 0.067 obtained with the filtering process.

The drift correction provides interesting features for the measurement time. Indeed, for 3D inverse problem application, both the incident field and the total field are necessary and take a long time to obtain. Without the correction, when using a total field and an incident field measured one month apart, the scattered field was inexploitable. Nowadays, after correction, the scattered field is extracted and thus we can spare one field measurement.

Another way to reduce the acquisition time is to minimize the number of receiver positions.[12] After correction, we can extract the maximum spatial frequency and deduce the corresponding sampling step. For example, by performing this postprocessing protocol, with a sampling step of 5° (10° when possible) instead of 1°, we can gain 40% (50%) of measurement time.

The drift correction presented here has been tested on various objects and measurement configurations with the same very satisfactory results. This method, which takes into account the underlying physics of the electromagnetic fields, is a very useful tool for increasing the measurement accuracy of the 3D database that will soon be available for the scientific community working on the theoretical aspects of scattering.

[1] K. Belkebir and M. Saillard, Inverse Probl. **17**, 1565 (2001).
[2] J.-M. Geffrin, P. Sabouroux, and C. Eyraud, Inverse Probl. **21**, S117 (2005).
[3] K. Belkebir and M. Saillard, Inverse Probl. **21**, S1 (2005).
[4] J.-M. Geffrin, C. Eyraud, P. Sabouroux, P. Chaumet, H. Tortel, and H. Giovannini, Proceedings of the of the IEEE AP-S/URSI International Symposium (2006), p. 2007.
[5] P. van den Berg, M. G. Coté, and R. Kleinman, IEEE Trans. Antennas Propag. **43**, 1389 (1995).
[6] B. A. S. Gustafson, J. Quant. Spectrosc. Radiat. Transf. **55**, 663 (1996).
[7] P. Sabouroux and P. Boschi, Rev. Electr. Electron. **10**, 58 (2005).
[8] J. Jackson, *Classical Electrodynamics* (Wiley, New York, 1975).
[9] Atem 0–40 GHz, Atem Product Catalog (1996), Vol. 39.
[10] D. W. Hess, D. R. Morehead, and S. J. Manning, http://www.mi-technologies.com/literature/mit8.pdf.
[11] O. Bucci and G. Franceschetti, IEEE Trans. Antennas Propag. **35**, 1445 (1987).
[12] M. Bucci, C. Gennarelli, and C. Savarese, IEEE Trans. Antennas Propag. **46**, 351 (1998).

Two-dimensional inverse profiling problem using phaseless data

Amélie Litman and Kamal Belkebir

Institut Fresnel, UMR-CNRS 6133, Campus de Saint Jérôme, case 162, Université de Provence, 13397 Marseille Cedex, France

Received December 19, 2005; revised March 30, 2006; accepted May 9, 2006; posted June 8, 2006 (Doc. ID 66694)

We discuss the characterization of two-dimensional targets based on their diffracted intensity. The target characterization is performed by minimizing an adequate cost functional, combined with a level-set representation if the target is homogeneous. One key issue in this minimization is the choice of an updating direction, which involves the gradient of the cost functional. This gradient can be evaluated using a fictitious field, the solution of an adjoint problem in which receivers act as sources with a specific amplitude. We explore the Born approximation for the adjoint field and compare various approaches for a wide variety of objects. © 2006 Optical Society of America

OCIS codes: 290.3200, 110.6960.

1. INTRODUCTION

In some practical applications, the phase measurement of the scattered fields is too corrupted by noise to be useful, and sometimes there is no phase measurement at all as in, e.g., optical measurement setup. Even if there is some effort nowadays to provide experimental setups that measure all components of the scattered fields,[1,2] our purpose herein is to investigate a method that images samples from the modulus of the scattered field only. Indeed, it has been shown that the scattered intensity could provide useful information on the obstacles.[3]

Instead of extracting some phase information from measurements[4] and then solving the inverse scattering problem from the measured intensity and the preliminary retrieved phase, we directly retrieve the targets under test from the scattered intensity. Following the ideas of Refs. 5 and 6, the approach suggested herein builds up the parameter of interest, namely the contrast of permittivity, iteratively. It is gradually adjusted by minimizing a cost functional properly defined.

This minimization under constraints is reformulated in terms of a Lagrangian functional, whose saddle point leads to the definition of an adjoint problem.[7] By virtue of the reciprocity principle, this adjoint problem is equivalent to a forward-scattering problem where receivers act as sources with correctly defined amplitudes. It will be shown that the only difference between a standard minimization process using modulus-phase data and this algorithm is expressed in these weighting coefficients. This implies that passing from full data to amplitude data requires only one line change in a software program if an adjoint field formalism is used.

This approach is then introduced for two cases of permittivity profiles: a continuous profile and a step profile. The first case is solved with a conjugate-gradient-type algorithm. For the second case, a level-set representation is introduced that fully takes into account prior information stating that the obstacle is homogeneous.[8] Results using modulus-only measurements will then be analyzed in a free-space configuration for those two cases of permittivity profiles. In particular, by using various numerical examples, we highlight the effect on the gradient computation and on the convergence of physical approximations such as the Born approximation for both the forward and adjoint fields. We also introduce a new initial guess based on an appropriate use of a topological derivative, which is no more than the variation of the cost functional due to the inclusions of small dielectric balls.[9]

This paper is organized as follows. In Section 2, a description of the geometry is provided. Section 3 is devoted to the definition of the inverse scattering problem, with the introduction of the cost functional and the associated Lagrangian formulation. Then the gradient expression is provided and several choices of computation are discussed. Section 4 focuses on the application of this gradient computation to the case of heterogeneous obstacles by means of the conjugate-gradient algorithm or to the case of homogeneous obstacles by means of level sets. The method used to obtain the initial guess is also explained in this section. Finally, Section 5 provides numerical examples for both homogeneous and heterogeneous obstacles, with and without noise, showing the effects of a correct gradient computation as well as the appropriate use of *a priori* information on the nature of the scatterers.

2. STATEMENT OF THE PROBLEM

The geometry of the problem studied in this paper is shown in Fig. 1 where a two-dimensional object of arbitrary cross section Ω is confined in a bounded domain D. The embedding medium Ω_b is assumed to be infinite and homogeneous, with permittivity $\varepsilon_b=\varepsilon_0\varepsilon_{br}$, and of permeability $\mu=\mu_0$ (ε_0 and μ_0 being the permittivity and permeability of the vacuum, respectively). The scatterers are assumed to be inhomogeneous cylinders with a permittivity distribution $\varepsilon(\mathbf{r})=\varepsilon_0\varepsilon_r(\mathbf{r})$; the entire configuration is nonmagnetic ($\mu=\mu_0$). A right-handed Cartesian coordinate frame $(O,\mathbf{u_x},\mathbf{u_y},\mathbf{u_z})$ is defined. The origin O can be either

1084-7529/06/112737-10/$15.00

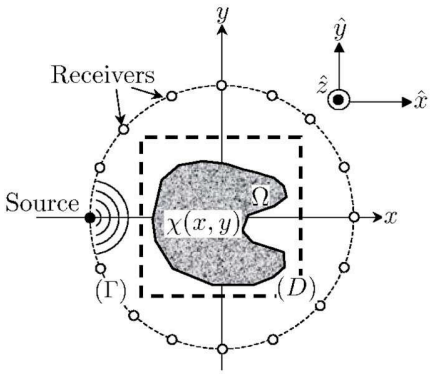

Fig. 1. Geometry of the problem. A two-dimensional cylinder with cross-section Ω and permittivity contrast $\chi(x,y)$ is radiated by an electromagnetic source located on a circle Γ. The scattered intensity is assumed to be available on Γ.

inside or outside the scatterer and the z axis is parallel to the invariance axis of the scatterer. The position vector **OM** can then be written as $\mathbf{OM}=\mathbf{r}+z\mathbf{u_z}$. The sources that generate the electromagnetic excitation are assumed to be lines parallel to the z axis, located at $(\mathbf{r}_l)_{1\leqslant l\leqslant L}$. Taking into account a time factor $\exp(-i\omega t)$, in the transverse magnetic (TM) case, the time-harmonic incident electric field created by the lth line source is given by

$$\mathbf{E}_l^{\mathrm{i}}(\mathbf{r})=E_l^{\mathrm{i}}(\mathbf{r})\mathbf{u}_z=P\frac{\omega\mu_0}{4}H_0^{(1)}(k_b|\mathbf{r}-\mathbf{r}_l|)\mathbf{u}_z, \tag{1}$$

where P is the strength of the electric source, ω the angular frequency, $H_0^{(1)}$ the Hankel function of zero order and of the first kind, and k_b is the wavenumber in the surrounding medium.

For the inverse-scattering problem, we assume that the unknown objects are successively illuminated by L electromagnetic excitations and for each the scattered field is available along a contour Γ at M positions. The direct scattering problem may be formulated as two coupled contrast-source integral relations: the observation equation [Eq.(2)] and the coupling equation [Eq. (3)],

$$E_l^s(\mathbf{r}\in\Gamma)=k_0^2\int_D\chi(\mathbf{r}')E_l(\mathbf{r}')G(\mathbf{r},\mathbf{r}')\mathrm{d}\mathbf{r}', \tag{2}$$

$$E_l(\mathbf{r}\in D)=E_l^{\mathrm{i}}+k_0^2\int_D\chi(\mathbf{r}')E_l(\mathbf{r}')G(\mathbf{r},\mathbf{r}')\mathrm{d}\mathbf{r}', \tag{3}$$

where $\chi(\mathbf{r})=\varepsilon_r(\mathbf{r})-\varepsilon_{br}$ denotes the permittivity contrast that vanishes outside $D\supset\Omega$, $G(\mathbf{r},\mathbf{r}')$ is the two-dimensional free-space Green function, and k_0 represents the vacuum wavenumber. For the sake of simplicity, Eqs. (2) and (3) are rewritten as

$$E_l^s=\mathbf{K}\chi E_l \quad E_l=E_l^{\mathrm{i}}+\mathbf{G}\chi E_l. \tag{4}$$

3. INVERSE SCATTERING PROBLEM

The inverse scattering problem is stated as finding the permittivity distribution in the box D such that the corresponding scattered intensity predicted by the model via the coupling and the observation equation matches the data. We propose an iterative approach to solve this ill-posed and nonlinear problem. The first step is to define a discrepancy criterion between the measured fields and the simulated ones. This criterion depends on the amount of available data, e.g., modulus and phase or modulus only. The derivative of this cost functional must then be explicitly obtained, and it will be shown that it introduces an adjoint state equation where receivers act as sources with amplitude that depends mainly on the expression of the cost functional.

A. Cost Functional Definition

The parameter of interest, namely, the contrast χ, is gradually adjusted by minimizing a cost functional $\mathcal{J}(\chi)=\Sigma_{l=1}^L\mathcal{F}[E_l^s(\chi)]$ suitably defined under the constraints of Eq. (4). If both amplitudes and phase must be matched, the cost functional reads as

$$\mathcal{J}(\chi)=\frac{1}{2}\sum_{l=1}^L w_l\|E_l^{\mathrm{obs}}-E_l^s(\chi)\|_\Gamma^2, \tag{5}$$

where E^{obs} corresponds to the available measurements and w_l to the appropriate weight coefficients, for example, $w_l^{-1}=\|E_l^{\mathrm{obs}}\|_D^2$. If scattered intensity must be matched, the cost functional reads as

$$\mathcal{J}(\chi)=\frac{1}{2}\sum_{l=1}^L w_l\|I_l^{\mathrm{obs}}-|E_l^s(\chi)|^2\|_\Gamma^2, \tag{6}$$

where I^{obs} corresponds to the available intensity measurements and $w_l^{-1}=\|I_l^{\mathrm{obs}}\|_\Gamma^2$.

B. Gradient Expression

This minimization problem under constraints can be reformulated using a Lagrangian functional $\mathcal{L}$ as[7]

$$\mathcal{L}(\chi,E^s,E,U^s,U)=\sum_{l=1}^L\{\mathcal{F}(E_l^s)+\langle U_l^s|E_l^s-\mathbf{K}\chi E_l\rangle_\Gamma + \langle U_l|E_l-E_l^{\mathrm{i}}-\mathbf{G}\chi E_l\rangle_D\}, \tag{7}$$

where χ is the unknown contrast, $\mathcal{F}$ is the cost function to minimize, E^s and E correspond to the simulated scattered and total fields, U^s and U are Lagrange multipliers, $\langle|\rangle_\Gamma$ is the scalar product on Γ ($\langle u|v\rangle_\Gamma=\int_\Gamma u*(\mathbf{r})v(\mathbf{r})\mathrm{d}\mathbf{r}$), and $\langle|\rangle_D$ is the scalar product on D ($\langle u|v\rangle_D=\int_D u*(\mathbf{r})v(\mathbf{r})\mathrm{d}\mathbf{r}$). This Lagrangian is used to express first- and second-order conditions for a local minimizer, which are linked to the existence of a saddle point. This saddle point provides an efficient way to compute the gradient of the cost functional by introducing an adjoint field. The adjoint field, owing to the reciprocity principle, is equivalent to the direct field where receivers act as sources with an amplitude linked to the cost functional expression

$$P_l=P_l^{\mathrm{i}}+\mathbf{G}\chi P_l, \qquad P_l^{\mathrm{i}}=-\mathbf{K}^t\overline{\nabla\mathcal{F}(E_l^s)}. \tag{8}$$

If both amplitude and phase must be matched, the incident adjoint field is given by

$$P_l^{\mathrm{i}} = w_l \mathbf{K}^t (\overline{E_l^{\mathrm{obs}} - E_l^s}). \tag{9}$$

If scattered intensity must be matched, the sources for the adjoint problem read as

$$P_l^{\mathrm{i}} = 2 w_l \mathbf{K}^t \overline{E_l^s} (I_l^{\mathrm{obs}} - |E_l^s|^2). \tag{10}$$

Therefore the adjoint method is a very convenient way for computing derivatives for several types of cost functional.

It can be shown (Subsection 2.A) that the gradient of the cost functional is given by

$$\langle \nabla \mathcal{J}(\chi) | \delta\chi \rangle_D = -\mathrm{Re} \left\langle \sum_{l=1}^{L} \overline{E_l P_l} \middle| \delta\chi \right\rangle_D. \tag{11}$$

In the case of intensity measurements, this gradient shows the ambiguity of the cost functional. On one hand, the cost functional can be reduced if the computed field is close to the measured field. On the other, the cost functional can be reduced if the size of the scatterer is very small, and we can neglect its contribution. In that case, the adjoint field is null as is the gradient.

C. Gradient Approximation

The gradient evaluation requires the computation of two forward problems. The first one computes the direct field E_l as the second one, where the receivers act as sources with a prescribed amplitude, provides the adjoint field P_l. It might be interesting, in order to save some computational time, to perform some approximations such as the Born approximation.

Three cases can be considered: (i) no approximation is done for the direct and adjoint field computation (noted as the FULL–FULL case in the following), (ii) the Born approximation is made only for the adjoint field computation (FULL–BORN), and (iii) finally, the Born approximation is applied for both fields (BORN–BORN). In the last case, the gradient is identical to the one that would be obtained by assuming from the beginning that the Born approximation was valid. As expected, the way the gradient is computed will have an effect on the minimization process, as will be highlighted in Section 5 with some numerical examples.

4. MINIMIZATION SCHEME

Once the discrepancy criterion has been defined and its derivative computed, a minimization algorithm can be applied, which can be specified according to the *a priori* information available. For example, if the permittivity profile of the unknown obstacle is assumed to be continuous, a standard conjugate-gradient-type algorithm can be used. If, on the contrary, one is interested in looking at homogeneous-by-part obstacles, this *a priori* information can be introduced via a level-set formulation in which the cost functional derivative is still needed. In all cases, the initial guess selection is a key point for the convergence of the minimization process.

A. Initial-Guess Selection

The initial-guess computation is based on topological asymptotic expansion results.[9] The topological derivative aims at introducing some small dielectric balls of constant permittivity ε_r into a known background of permittivity $\xi(\mathbf{r})$. These balls induce variations on the electromagnetic fields that are expressed via a topological asymptotic expansion formula. Let us denote by B_ρ a small dielectric ball of size $\rho|B|$ centered at point $\mathbf{r}$ ($|B|$ is the measure of a reference ball B). This means that $\mathbf{r} \in B_\rho \subset B_{\rho'}$ if $0 < \rho < \rho' < 1$. The topological asymptotic expansion of our cost function can then be expressed by[10]

$$\mathcal{J}\{\chi = (\varepsilon_r - \varepsilon_{br}) \mathbb{1}_{B_\rho} (\xi - \varepsilon_{br}) \mathbb{1}_{D \times B_\rho}\} - \mathcal{J}\chi = (\xi - \varepsilon_{br}) \mathbb{1}_D\} = -\rho^2 \mathrm{Re}(\varepsilon_r - \varepsilon_{br}) k_0^2 |B| \left(\sum_{l=1}^{L} E_l P_l \right) + o(\rho^3), \tag{12}$$

where $\mathbb{1}$ is the conventional characteristic function, E_l (resp. P_l) verifies Eq. (3) [resp. Eq. (9)] with $\chi(\mathbf{r}) = \xi(\mathbf{r}) - \varepsilon_{br}$, $\forall \mathbf{r} \in D$. This topological derivative provides, therefore, information on where to place balls such that the cost functional is reduced and is directly linked to the topology of the scatterers. In fact, if we assume that $\xi = \varepsilon_{br}$, this gradient is no more than the first step of the inversion process, as expressed in Eq. (11) assuming that there is no initial guess.

Using this topological derivative, as we do not know the value of ε_r, we construct the initial guess with

$$\chi_0(\mathbf{r}) = \eta \, \mathrm{Re} \sum_{l=1}^{L} E_l(\mathbf{r}) P_l(\mathbf{r}), \tag{13}$$

where η is a constant defined such that $\mathcal{J}(\chi_0)$ is minimal. The fields E_l and P_l are the direct and adjoint fields computed for $\chi(\mathbf{r}) = \xi - \varepsilon_{br}$, $\forall \mathbf{r} \in D$, with ξ very close from ε_{br}. It would have been more natural to use $\chi = 0$ on the entire test domain D (which would have corresponded to $\Omega = 0$) but then, owing to definition of the cost functional for intensity measurements, the adjoint field would have been null as would the topological derivative.

If *a priori* information on the nature of the scatterer is given, such as the obstacle is homogeneous, a truncation at midvalue is performed to obtain a binary image.

B. Retrieval of an Inhomogeneous Profile

If no *a priori* information is available on the nature of the scatterer, a sequence $\{\chi_n\}$ is built up iteratively according to the following relation:

$$\chi_n = \chi_{n-1} + \alpha_n d_n, \tag{14}$$

where d_n is an updating direction and α_n is a weight that is determined at each iteration step by minimizing the cost functional $\mathcal{J}(\chi_n)$ [Eq. (6)]. During the local search for α_n, the field E remains fixed to the value obtained at previous iteration. As a search direction d_n, the authors take a Polak Ribière conjugate direction

$$d_n = g_n + \gamma_n d_{n-1}, \quad \gamma_n = \frac{\langle g_n | g_n - g_{n-1} \rangle_D}{\|g_{n-1}\|_D^2}, \tag{15}$$

where g_n is the gradient of $\mathcal{J}(\chi)$ with respect to χ. As described in Subsection 3.C, this gradient can be exactly computed or approximated.

C. Retrieval of a Binary Profile

As the nonlinear inverse problem stated above is highly ill-posed, all available information is useful for improving the quality of the reconstructions. In some cases, it is possible to assume that the dielectric properties of the obstacle are known and furthermore that this obstacle is homogeneous. The contrast of permittivity will then be a binary function of the following form:

$$\chi(\mathbf{r}) = \varepsilon_r - \varepsilon_{br}(\mathbf{r} \in \Omega), \quad \chi(\mathbf{r}) = 0 \quad (\mathbf{r} \notin \Omega), \tag{16}$$

where ε_r is known and constant. In this approach, which is reduced to a shape optimization problem, the parameter of interest, namely, the shape Ω, is gradually adjusted by minimizing the same cost functional as previously under the constraints of Eqs. (2) and (3). A sequence of shapes $\{\Omega_n\}$ is constructed in order to minimize the cost functional $\mathcal{F}(\Omega_n)$, which requires several elements: (i) the shape representation, (ii) the computation of the derivative of the cost functional according to shape, and (iii) the construction of the iterative sequence. To represent the shape, let us introduce an auxiliary function called a level-set function ϕ such that

$$\Omega = \{\mathbf{r} \in D \text{ such that } \phi(\mathbf{r}) < 0\}. \tag{17}$$

This representation handles naturally all topological changes such as fusion or separation and does not require us to know in advance the number of scatterers and the positions of their centers. The cost functional $\mathcal{J}$, which now depends on ϕ, must then be derived according to this level-set representation to obtain

$$\langle \nabla \mathcal{J}(\phi) | \delta\phi \rangle_D = -\operatorname{Re}(\varepsilon_r - \varepsilon_{br}) \left\langle \delta(\phi) |\nabla \phi| \sum_{l=1}^{L} \overline{E_l P_l} | \delta\phi \right\rangle_D, \tag{18}$$

where $\delta(\phi)$ corresponds to the one-dimensional Dirac delta function concentrated on the interface $\phi=0$, i.e., the interface $\partial\Omega$. As described in Subsection 3.C, this gradient can be exactly computed or approximated. An artificial time variable t is introduced, and the minimization is done by finding the steady state solution of

$$\phi_t = -\nabla \mathcal{J}(\phi), \tag{19}$$

assuming that the $\delta(\phi)$ function is extended everywhere in D with value 1. This equation is solved using the Osher–Sethian numerical scheme described in Ref. 11.

5. NUMERICAL EXPERIMENTS

In this section we report examples of reconstructions of dielectric samples to illustrate the efficiency of the inversion algorithms presented in the previous sections. In all cases, synthetic data are generated thanks to a fast forward solver described in detail in Ref. 12. This forward solver is based on a second-order accurate space discretization that is capable of handling homogeneous as well as inhomogeneous profiles. The convolution-type structure of the integral equation is exploited and solved via a conjugate-gradient fast Fourier transform (CG–FFT) method. Moreover, a special extrapolation procedure is used, by "marching on in" the source position, to generate accurate initial estimates for the CG method to reduce the computation time. In contrast, the inversion solver is based on a standard method of moment without any use of the CG–FFT method.[12] This solver is needed for computing both the internal and adjoint fields. The dielectric permittivity, as well as the electromagnetic field, is interpolated by piecewise-constant basis functions with collocation-point test functions.

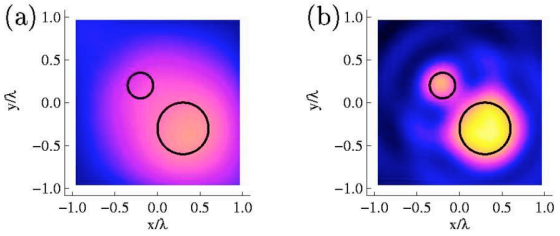

Fig. 2. (Color online) Initial guess using the topological asymptotic expansion results (a) with modulus-only data; (b) with modulus and phase data. The object under test HOMOCYL16 is constituted by two circular cylinders of contrast $\chi=0.6$. Black circles in the images correspond to boundaries of actual cylinders.

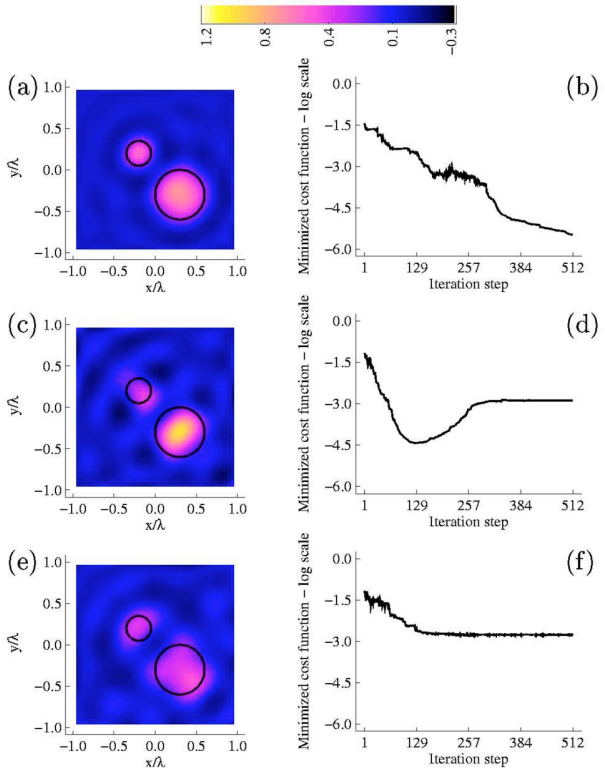

Fig. 3. (Color online) Reconstructed contrast distribution using a conjugate-gradient method, for the HOMOCYL16 object. The updating direction d_n involves a gradient derived from a solution of an adjoint problem. (a) Both the internal field and the adjoint field are computed accurately (FULL–FULL case); (c) same as in (a) but the evaluation of the adjoint field assumes the Born approximation (FULL–BORN case); (e) the Born approximation is assumed for both the internal field and for the adjoint field (BORN–BORN case). Curves (b), (d), and (f) represent the evolution in logarithmic scale of the minimized cost functional with respect to the iteration steps for the reconstructions plotted in (a), (c), and (e), respectively.

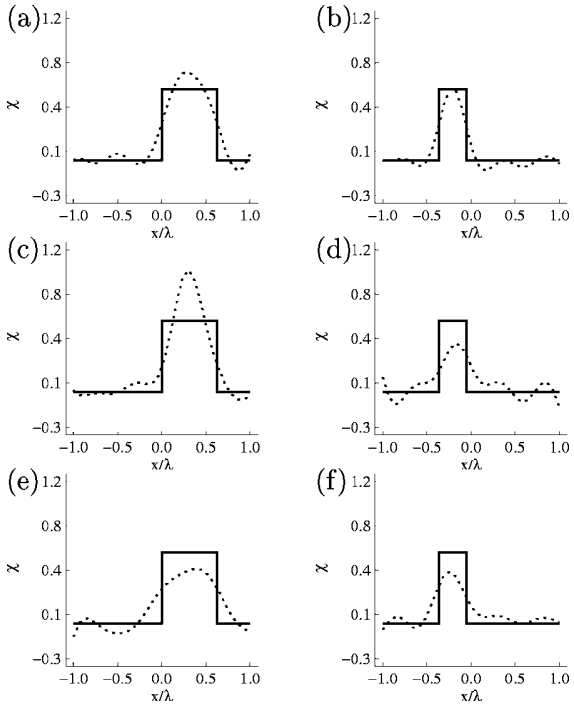

Fig. 4. Comparisons between the reconstructed contrast presented in Fig. 3 and the actual one along the x axis. Left column comparisons are presented along the line $y=-0.3\lambda$, which corresponds to a cut along a diameter of the large cylinder of Fig. 3. The right column presents comparisons along the line $y=0.2\lambda$, which corresponds to a cut along a diameter of the small cylinder of Fig. 3. The solid curves correspond to the actual profiles, while the dotted curves correspond to the reconstructed ones. (a) and (b) correspond to Fig. 3(a). (c) and (d) correspond to Fig. 3(c). (e) and (f) correspond to Fig. 3(e).

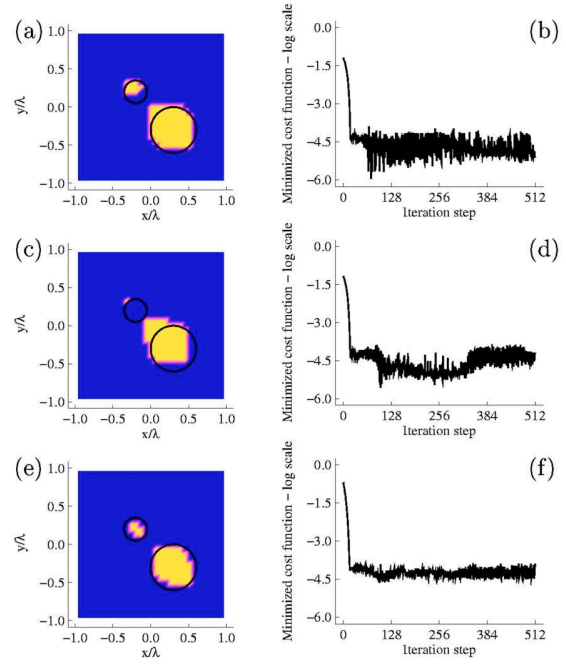

Fig. 5. (Color online) Same as in Fig. 3, but the inversion is performed using the level-set scheme described in Subsection 4.C, where it is assumed that the permittivity contrast of targets under test is known.

The receivers as well as the sources are assumed to be infinite lines located on a circle Γ of radius 1.5λ, λ being the wavelength in the vacuum. In addition, we consider 64 sources and receivers evenly distributed on the measurement circle Γ. The mesh size of the forward solver to generate data is $\lambda/64$. The investigated domain D is a square box with sides of 2λ, subdivided for numerical purposes into 30 square cells, leading thus to a mesh size of $\lambda/15$ for inversion schemes. Consequently, the mesh size used in the inversion is different from the one used to generate data, preventing any "inverse crime." In all the following examples, the initial guess is chosen as described in Subsection 4.C with an initial contrast of $\chi=\xi-\varepsilon_{br}=1.01$. For such contrast value, the Born approximation is applicable. Finally, all iterative schemes have been conducted up to the 512th iteration to ensure that convergence, if any, is achieved. In all cases, the evolution of the cost function is presented. By letting the inversion algorithm run, we then have a good indication of the convergence speed, the discrepancy accuracy, and the trends of the methods. In particular, we can check to see whether we have reached a plateau or whether the algorithm is unstable.

A. Reconstruction of Spatially Homogeneous Profiles

1. HOMOCYL16 Object

First, we consider two circular homogeneous cylinders of radii $a_1=0.15\lambda$ and $a_2=0.3\lambda$ and of relative permittivity $\varepsilon_r=1.6$. The small cylinder is located at $(-0.2\lambda,0.2\lambda)$, while the other cylinder is located at $(-0.3\lambda,-0.3\lambda)$. Henceforth, this object under test is referred as the HOMOCYL16 object.

To emphasize the influence of the phase information, two initial estimates obtained with the same topological expansion method are plotted in Fig. 2 for the HOMOCYL16 object. In Fig. 2(a), only modulus information is used, whereas in Fig. 2(b) modulus and phase are taken into account. It is clear that the phase contains important topological information. Therefore, by using modulus-only data, we are penalized more in the reconstruction process than when using a scattered field.

Figure 3 presents the reconstructed contrast χ within the investigated domain D, using the inversion algorithm described in Subsection 3.B, for various choices of descent direction. Clearly, the best result, Fig. 3(a), is obtained when both the internal and the adjoint fields are computed without assuming the Born approximation (FULL–FULL case). Comparing the reconstructed profiles with the actual one, Fig. 4 shows that not only the shape is well retrieved but also the refractive index. Surprisingly, the other cases, in particular the BORN–BORN case [Fig. 3(e)], lead to relatively accurate reconstructions of the target under test. We emphasize that the object under test has the characteristic dimension about λ and the dielectric contrast of $\chi=0.6$ for which the Born approximation is not valid.

The evolution of the cost functional in the case of FULL–BORN [Fig. 3(d)] exhibits a minimum around iteration 128. Indeed, the corresponding image, not plotted here, is almost as good as Fig. 3(a). After this iteration, the cost functional starts to increase again to reach a plateau

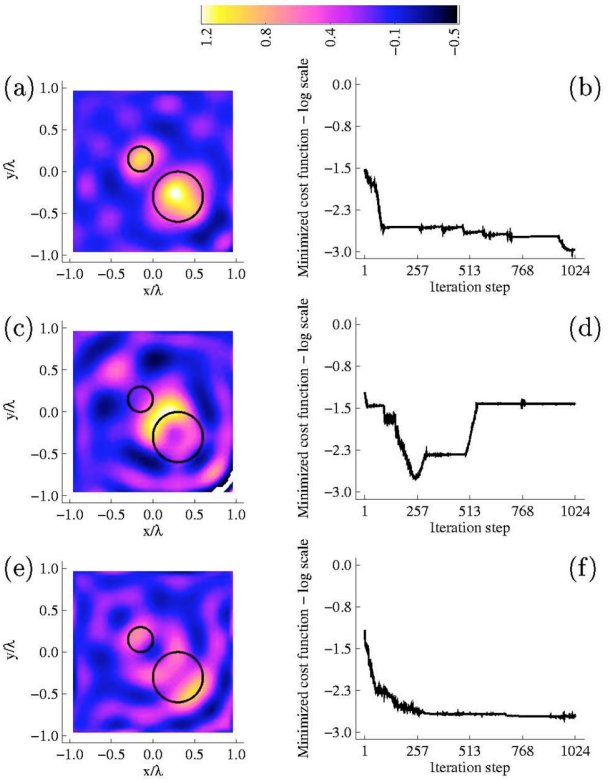

Fig. 6. (Color online) Same as in Fig. 3, but with the object under test HOMOCYL20, which is constituted by circular cylinders of permittivity contrast $\chi=1$.

whose corresponding image is presented in Fig. 3(c). This is because near the minimum, exact gradient computation is of high importance, especially as it is of very small value and numerical noise might cause the divergence of the iterative process. This divergence shows the importance of a correct computation of the gradient. In all cases, such behavior is not observed for the two other schemes, where the computations of the forward and the adjoint fields are consistent.

The same behavior can be observed using *a priori* information on the nature of the scatterers by means of the level-set scheme described in Subsection 4.C. Figure 5 shows the reconstructed images obtained after 512 iterations with different ways of computing the gradient. The initial guess was computed as previously and was truncated at midvalue to obtain a binary image. Again, FULL–FULL and BORN–BORN cases provide very satisfactory results compared with the FULL–BORN case. The oscillations in the cost functional appear when the size of the image changes are of the order of the cell size.

2. HOMOCYL20 Object

Consider the same two cylinders slightly closer and with relative permittivity $\varepsilon_r=2.0$ instead of $\varepsilon_r=1.6$. The small cylinder is now located at $(-0.15\lambda, 0.15\lambda)$. From now on, this object will be referred to as HOMOCYL20. Figure 6 presents results of the reconstructed contrast profile using the conjugate-gradient algorithm for various choices of the gradient. Contrary to the preceding case, the convergence in the case of FULL–FULL [Fig. 6(a)] is slow. The

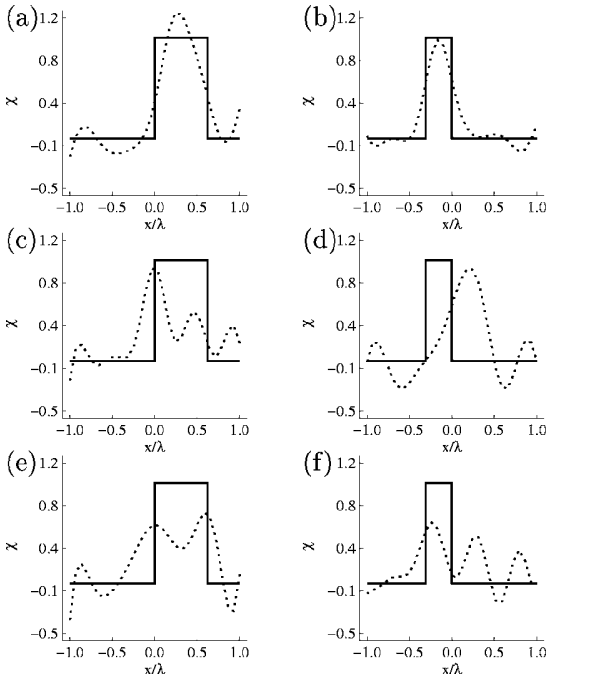

Fig. 7. Comparisons between the reconstructed contrast presented in Fig. 6 and the actual one along the x axis. Left column comparisons are presented along the line $y=-0.3\lambda$, which corresponds to a cut along a diameter of the large cylinder of Fig. 6. The right column presents comparisons along the line $y\approx 0.15\lambda$, which corresponds to a cut along a diameter of the small cylinder of Fig. 6. The solid curves correspond to the actual profiles, while the dotted curves correspond to the reconstructed ones. (a) and (b) correspond to Fig. 6(a); (c) and (d) correspond to Fig. 6(c); (e) and (f) correspond to Fig. 6(e).

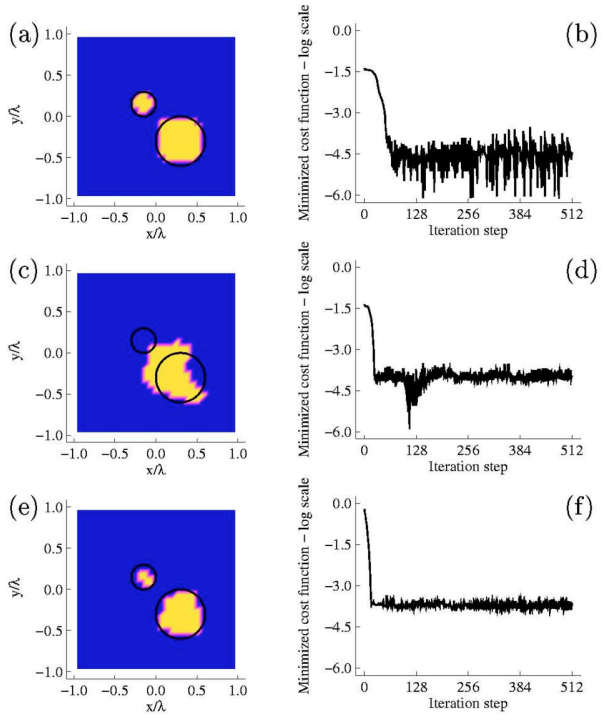

Fig. 8. (Color online) Same as in Fig. 6, but the inversion is performed using the level-set scheme described in Subsection 4.C.

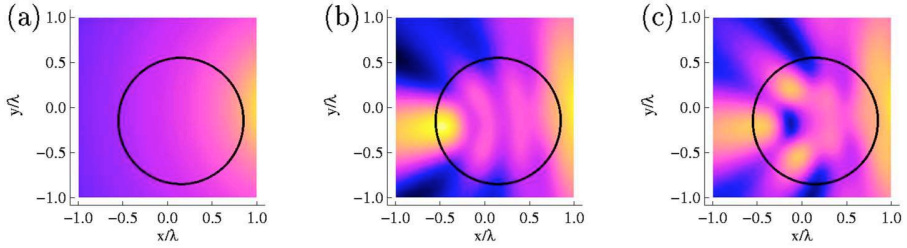

Fig. 9. (Color online) Modulus of electromagnetic fields in the test domain D for a source located at $(1.5\lambda, 0)$. (a) Incident field; (b) internal field of the object LUNEBERG; (c) internal field of the object INHOMOSIN.

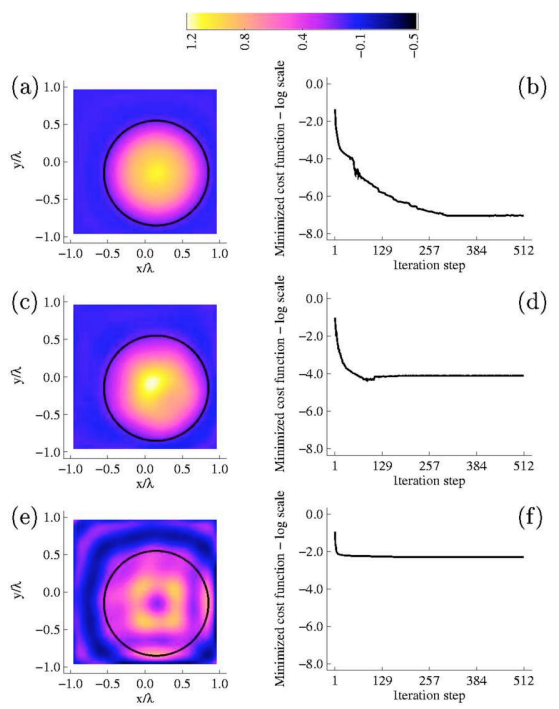

Fig. 10. (Color online) Reconstruction of the inhomogeneous object LUNEBERG from noiseless data, using the conjugate-gradient method described in Subsection 3.B. (a) FULL–FULL case; (c) FULL–BORN case; (e) BORN–BORN case. The second column of the figure presents the evolution in logarithmic scale of the minimized cost functional versus iteration steps that correspond to images plotted in the first column.

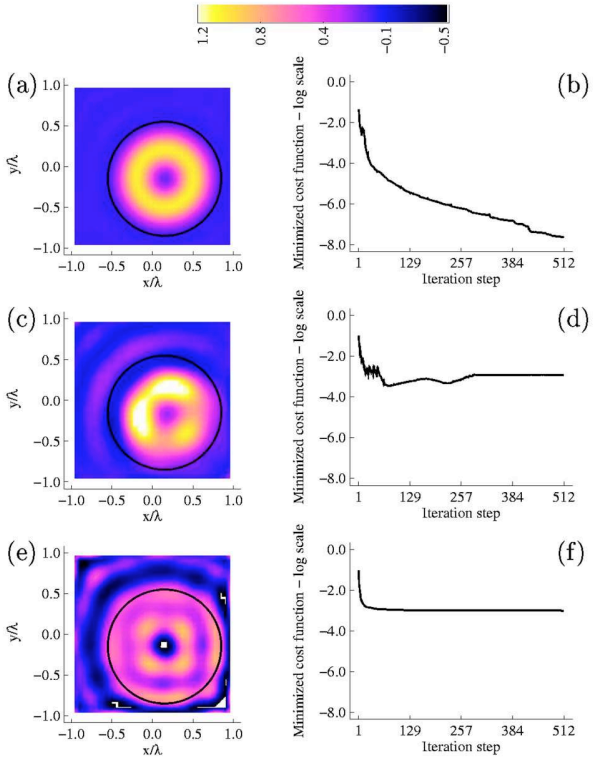

Fig. 11. (Color online) Same as in Fig. 10 but with the object INHOMOSIN.

best result is obtained for the case of FULL–FULL, while for the other cases, FULL–BORN and BORN–BORN, the reconstructed targets are blurred and melded with artifacts. Figure 7 shows quantitative comparisons between reconstructed targets and the actual ones along the diameters of the cylinders.

As the level-set algorithm used is very strong *a priori* on the nature of the scatterer, the reconstructions are improved for this obstacle, and the artifacts disappear as shown in Fig. 8. This effect is also partly due to multiple-scattering effects,[13] which are fully taken into account when using a FULL–FULL approach for the gradient computation and explains how the small scatterer is well reconstructed. Again, the FULL–BORN case provides the worst result and starts to diverge after a while. On the other hand, this case was the first to converge toward an acceptable solution.

From these two examples, one may conclude that the inversion in the FULL–FULL case is more accurate than the two other cases. It requires more computation time than the BORN–BORN case, but it takes into account the multiple-scattering effect. Compared with the FULL–BORN case, the extra computational burden is minimal, as nearly everything has already been computed to obtain the internal field, and the results are more satisfactory.

B. Reconstruction of Spatially Continuous Profiles

We now consider two inhomogeneous profiles, denoted as LUNEBERG and INHOMOSIN. These two profiles consist of an inhomogeneous circular cylinder of radius $a=0.7\lambda$, located at $(0.15\lambda, -0.15\lambda)$. The contrasts within the objects are radially varying. For the profile LUNEBERG, the contrast is of the form $\chi(\rho)=1-(\rho/a)^2$, while for the object INHOMOSIN, the contrast is of the form $\chi(\rho)=\sin^2(\pi\rho/a)$, where ρ denotes the radial coordinate in the frame of the center of the cylinder. These profiles are spatially continu-

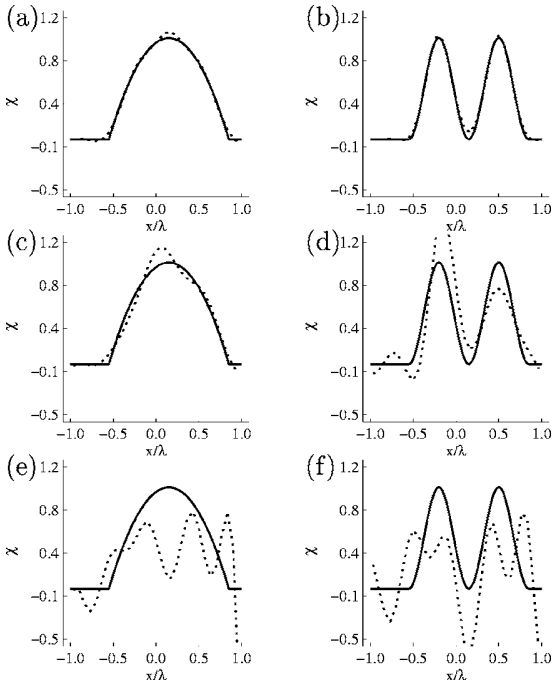

Fig. 12. (Color online) Comparisons between the reconstructed profiles and the actual one along a horizontal line $y \approx -0.15\lambda$ for the LUNEBERG (first column) and INHOMOSIN objects (second column). The solid curves stand for the actual profiles while the dotted curves correspond to the reconstructed ones. (a), (b) FULL–FULL; (c), (d), FULL–BORN; and (e), (f) BORN–BORN.

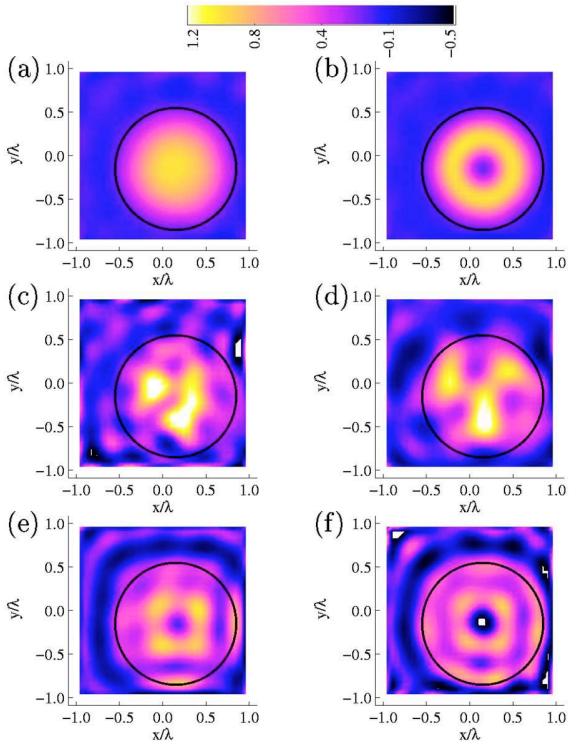

Fig. 13. (Color online) Same as in Figs. 10 and 11 but with 10% additive noise in the data. The first column corresponds to the LUNEBERG object while the second column corresponds to the INHOMOSIN object.

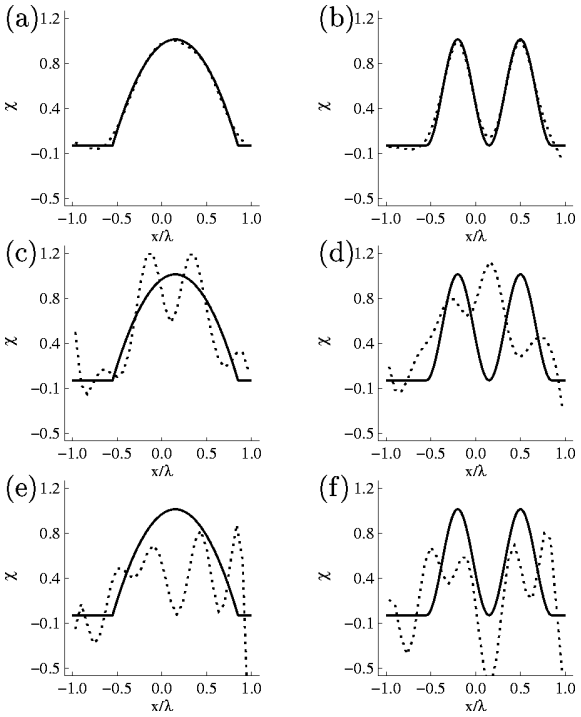

Fig. 14. Same as in Fig. 12 but with 10% additive noise.

ous and cannot be represented by a binary level-set representation nor by the extended one for the representation of multiple constitutive materials as suggested in Ref. 14. In addition, these obstacles present internal fields that are strongly different from the incident fields as shown in Fig. 9. The object LUNEBERG is known as an ideal two-dimensional Luneberg lens. For the object INHOMOSIN, the presence of whispering-gallery modes that propagate along the interior boundary of the cylinder is predicted.[15]

1. Inversion from Noiseless Data

Figures 10 and 11 present results of the reconstruction of the target LUNEBERG and INHOMOSIN, respectively. In all cases, the support of the object under test is well retrieved. However, in the case of the computation under the assumption of the Born approximation for both the internal field and the adjoint field, the reconstructed contrast profile is meaningless as is clearly shown in Fig. 12. A perfect reconstruction is obtained for the FULL–FULL case for both profiles.

2. Inversion from Noisy Data

In this subsection we present results of inversion from noisy data. We restrict ourselves to the case of inhomogeneous targets (LUNEBERG and INHOMOSIN) targets, in view of the fact that no prior information is introduced. The case of homogeneous targets is expected to be more robust against the presence of noise in data. Uniform white noise has been added to the simulated intensity data. Hence, the input data used for the inversion are corrupted according to the following relation:

$$\tilde{I}_l^{\text{obs}}(\mathbf{r}) = (1 + bu) I_l^{\text{obs}}(\mathbf{r}), \tag{20}$$

where $\tilde{I}_l^{\text{obs}}$ denotes the corrupted data, $u \in [-1,1]$ is a random number, and b monitors the level of noise. Figure 13 presents the results of the inversion for the LUNEBERG and the INHOMOSIN targets. For these numerical experiments, the level of noise b is as high as 10%. It is clearly shown (see Fig. 14) that the FULL–FULL scheme is more robust against the presence of noise in the data than the other two inversion schemes (FULL–BORN and BORN–BORN).

6. CONCLUSION

We have examined two configurations of inverse scattering from intensity measurements that are of practical interest. The first one was related to the retrieval of heterogeneous objects, while the second was more specific to homogeneous ones. A cost functional criterion has been defined and minimized to compute the best available estimate. We have shown that the gradient computation is similar to the one that would have been obtained using modulus and phase information. Indeed, this gradient is obtained by combining an internal field and an adjoint field where the receivers act as sources with a prescribed amplitude that differs according to the available data. We have also shown that this gradient can be used as an initial guess, based on topological derivative results.

We have explored the Born approximation for the internal and the adjoint fields, and numerical examples have shown that the inversion in the FULL–FULL case was more accurate than a Born approximation for the adjoint and/or the internal field. This behavior has been observed for both homogeneous and heterogeneous obstacles. Even if the computational burden is slightly higher in the FULL–FULL case, this can be significantly reduced by using fast forward solvers. In addition, the FULL–FULL scheme is more robust against the presence of noise than the other two schemes.

The numerical examples have also shown the influence of *a priori* information, particularly when the obstacles are homogeneous. In those cases, the level-set representation provides final results where the boundaries of the obstacle are better resolved. It would be interesting to see what would be the extension of the inverse scattering problem with intensity measurements with homogeneous-by-parts obstacles using the ideas of Ref. 14.

It has also been shown that the gradient of the cost functional is null if the initial guess is a flat background, a situation that does not appear when modulus and phase data are used. To compute properly the topological asymptotic expansion and use it as an initial guess, it would be interesting to look at the second-order derivatives following the ideas of Ref. 16.

Finally, this work can easily be extended to the case of obstacles placed on a substrate, which is the typical configuration of optical diffraction setups. The main difference will lie in the Green functions, which will have to take into account the interfaces. The next step will be to handle real data sets.

APPENDIX A: GRADIENT COMPUTATION

The parameter of interest, here the contrast χ, must minimize a properly defined cost functional $\mathcal{J}(\chi)$ [see Eq. (5) and Eq. (6)] under the constraints of Eq. (4). Let us assume furthermore that the cost functional is such that, for all δE^s,

$$\mathcal{F}(E^s + \delta E^s) = \mathcal{F}(E^s) + \text{Re}\langle \nabla \mathcal{F}(E^s) | \delta E^s \rangle_\Gamma + o(\|\delta E^s\|_\Gamma).$$

If, for example, amplitude and phase measurements must be matched, this means $\nabla \mathcal{F}(E_l^s) = -w_l(E_l^{\text{obs}} - E_l^s)$. If intensity measurements must be matched, this means $\nabla \mathcal{F}(E_l^s) = -2w_l E^s(I_l^{\text{obs}} - |E_l^s|^2)$.

Let us denote by $\mathcal{L}$ the Lagrangian functional defined in Eq. (7). It can be noticed that if the fields E^s and E both satisfy the forward equations then

$$\mathcal{L}[\chi, E^s(\chi), E(\chi), U^s, U] = \mathcal{J}(\chi), \quad \forall U^s, \forall U.$$

If we differentiate this equation in the $\delta\chi$ direction, we get

$$\begin{aligned}\langle \nabla \mathcal{J}(\chi) | \delta\chi \rangle_D = &\langle \partial_\chi \mathcal{L}(\chi, E^s, E, U^s, U) | \delta\chi \rangle_D \\ &+ \langle \partial_{E^s} \mathcal{L}(\chi, E^s, E, U^s, U) \partial_\chi E^s | \delta\chi \rangle_D \\ &+ \langle \partial_E \mathcal{L}(\chi, E^s, E, U^s, U) \partial_\chi E | \delta\chi \rangle_D.\end{aligned}$$

The quantities U^s and U are chosen in order to eliminate the last terms in the summation, i.e., they must satisfy the adjoint equations

$$\langle \partial_{E^s} \mathcal{L}(\chi, E^s, E, U^s, U) | \delta E^s \rangle_\Gamma = 0, \quad \forall \delta E^s, \tag{A1}$$

$$\langle \partial_E \mathcal{L}(\chi, E^s, E, U^s, U) | \delta E \rangle_D = 0, \quad \forall \delta E. \tag{A2}$$

This implies that the Lagrangian coefficient U_l^s must satisfy the following equation:

$$U_l^s = -\nabla \mathcal{F}(E_l^s).$$

Substituting this into Eq. (A2), combined with the reciprocity principle $\bar{\mathbf{G}}^\dagger = \mathbf{G}$, and using the notation $U_l = \overline{\chi P_l}$ the adjoint state equation is induced:

$$P_l = \mathbf{G}\chi P_l - \mathbf{K}^t \overline{\nabla \mathcal{F}(E_l^s)}.$$

This equation is similar to the forward problem equation where only the incident field has changed. For the adjoint problem, the incident field is due to the receivers that act as sources with an amplitude specified by $\overline{\nabla \mathcal{F}(E_l^s)}$.

Let us go back to the derivation in the $\delta\chi$ direction, computed at the saddle-point position. This means that

$$\begin{aligned}\langle \nabla \mathcal{J}(\chi) | \delta\chi \rangle_D &= \langle \partial\chi \mathcal{L}(\chi, E^s, E, U^s, U) | \delta\chi \rangle_D \\ &= -\text{Re}\left\langle \sum_{l=1}^{L} \overline{E_l P_l} \,\middle|\, \delta\chi \right\rangle_D,\end{aligned}$$

where P_l satisfy the adjoint state equation.

The author's e-mail addresses are kamal.belkebir@fresnel.fr and amelie.litman@fresnel.fr.

REFERENCES

1. V. Lauer, "New approach to optical diffraction tomography yielding a vector equation of diffraction tomography and a novel tomographic microscope," J. Microsc. **205**, 165–176 (2002).
2. N. Destouches, C. A. Guérin, M. Lequime, and H. Giovannini, "Determination of the phase of the diffracted field in the optical domain. Application to the reconstruction of surface profiles," Opt. Commun. **198**, 233–239 (2001).
3. G. Gbur and E. Wolf, "The information content of the scattered intensity in diffraction tomography," Inf. Sci. (N.Y.) **162**, 3–20 (2004).
4. L. Crocco, M. D'Urso, and T. Isernia, "Inverse scattering from phaseless measurements of the total field on a closed curve," J. Opt. Soc. Am. A **21**, 622–631 (2004).
5. T. Takenaka, J. N. Wall, H. Harada, and M. Tanaka, "Reconstruction algorithm of the refractive index of a cylindrical object from the intensity measurements of the total field," Microwave Opt. Technol. Lett. **14**, 182–188 (1997).
6. M. Lambert and D. Lesselier, "Binary-constrained inversion of a buried cylindrical obstacle from complete and phaseless magnetic fields," Inverse Probl. **16**, 563–576 (2000).
7. F. James and M. Sepulveda, "Parameter identification for a model of chromatographic column," Inverse Probl. **10**, 1299–1314 (1994).
8. A. Litman, D. Lesselier, and F. Santosa, "Reconstruction of a two-dimensional binary obstacle by controlled evolution of a level-set," Inverse Probl. **14**, 685–706 (1998).
9. M. Masmoudi, J. Pommier, and B. Samet, "The topological asymptotic expansion for the Maxwell equations and some applications," Inverse Probl. **21**, 547–564 (2005).
10. B. Samet, "L'analyse asymtotique topologique pour les équations de Maxwell et applications," Ph.D. thesis (Université Paul Sabatier, 2004).
11. S. Osher and J. A. Sethian, "Fronts propagating with curvature-dependent speed: algorithms based on Hamilton–Jacobi formulations," J. Comput. Phys. **79**, 12–49 (1988).
12. Z. Q. Peng and A. G. Tijhuis, "Transient scattering by a lossy dielectric cylinder: marching-on-in frequency approach," J. Electromagn. Waves Appl. **7**, 739–763 (1993).
13. K. Belkebir, P. C. Chaumet, and A. Sentenac, "Influence of multiple scattering on three-dimensional imaging with optical diffraction tomography," J. Opt. Soc. Am. A **23**, 586–595 (2006).
14. A. Litman, "Reconstruction by level sets of n-ary scattering obstacles," Inverse Probl. **21**, S131–S152 (2005).
15. A. G. Tijhuis, "Angularly propagating waves in a radially inhomogeneous, lossy dielectric cylinder and their connection with natural modes," IEEE Trans. Antennas Propag.**34**, 813–824 (1986).
16. J. Sokolowski and A. Zochowski, *On Topological Derivative in Shape Optimization*, Tech. Rep. RR-3170 (Institut National de Recherche en Informatique et Automatique, 1997).

Inverse Problems **25** (2009) 065001 (17pp) doi:10.1088/0266-5611/25/6/065001

On embedded microwave imaging systems: retrievable information and design guidelines

Lorenzo Crocco[1] **and Amélie Litman**[2]

[1] CNR—IREA, National Research Council, Institute for Electromagnetic Sensing of the Environment, 328 via Diocleziano, 80124, Napoli, Italy
[2] Institut Fresnel, Aix-Marseille Université, CNRS, Ecole Centrale de Marseille, Campus de Saint-Jerôme, 13397 Marseille Cedex 20, France

E-mail: crocco.l@irea.cnr.it and amelie.litman@fresnel.fr

Received 5 December 2008, in final form 11 February 2009
Published 27 March 2009
Online at stacks.iop.org/IP/25/065001

Abstract
In several applications, microwave imaging systems are enclosed in a dielectric or metallic casing, which is aimed at hosting a matching fluid and/or enabling a 'removal' of the parasitic interactions with the surrounding environment. In order to understand which are the expected results of an imaging process carried out in such a configuration, in this paper we study the spectral properties of the integral radiation operator relative to an imaging system hosted in a circular metallic cavity. The analysis allows us to explain the role of the several parameters coming into play in the design of such a system, as well as their effect on the imaging procedure.

(Some figures in this article are in colour only in the electronic version)

1. Introduction

Microwave imaging techniques have been a topic of active research in recent years. Indeed, researchers from many groups in the world have worked on developing several inversion techniques and providing evidences of their actual feasibility for quantitative imaging purposes. An almost comprehensive overview of these results is, for instance, given in some special sections published by this journal [1–3].

With respect to this context, besides the interest in developing new approaches and algorithms, there is a growing need for making the approaches suited to the practical conditions actually faced in the applications. This is, for instance, the case of subsurface imaging via ground penetrating radar, wherein the modification of the radiation pattern of the antenna is important for the correct setting of the inversion [4].

Another example, which is of interest in biomedical applications and non-destructive testing, is that in which the imaging system is immersed in a matching fluid aimed at improving the coupling between the target under test and the probing wave [5–10]. In such a case, the

overall system is enclosed in a casing, either dielectric or metallic, needed to confine the fluid and helpful in shielding or at least controlling the electromagnetic interactions between the imaging system and the surrounding environment. Of course, the presence of the casing must be properly taken into account in the imaging procedure [5, 11–14], but it is also of importance to understand which constraints on the design of the overall imaging system are introduced by its presence. In addition, it is of interest to understand the effect of the presence of an embedding on the performances of the imaging procedures. It is worth noting that the proper design of such a system is nowadays an issue of extreme relevance, since these kinds of devices are the most considered ones in microwave diagnostics for breast cancer, probably the most promising and challenging context for inverse scattering based microwave imaging methods [8, 10].

Nevertheless, to the best of our knowledge, a systematic study of the factors which arise in this context has not been carried out yet, even in canonical configurations. For instance, it still seems not at all clear if and to what extent the imaging system may benefit from the presence of the casing [11, 14]. With respect to such a framework, the aim of this paper is to study the case of a two-dimensional circular scanning system embedded in a metallic casing. It is worth noting that this configuration corresponds to an actual device, which has been realized and exploited [5, 6, 15].

In order to pursue the above aim, we take advantage of an analysis of the properties of the *radiation* operator that relates the induced contrast sources to the scattered fields. In particular, by computing its singular value decomposition [16], we investigate the number of degrees of freedom (NDF) [17] pertaining to this linear operator. As is well known, the NDF provides a convenient tool to understand those features of the inverse scattering problem which are of interest in the design of the imaging system, that is:

(i) the minimum number of independent measurements needed to correctly perform the experiment,
(ii) the amount of parameters which can be reliably extracted from the inversion of data (in the absence of any other *a priori* information),
(iii) the 'class' of unknown functions which can be reconstructed in the imaging process.

Therefore, a study of the NDF allows us to assess both the *quantity* and the *quality* of the information available in the inverse problem at hand. As will be shown, in the specific case considered, these features are influenced by the various parameters that come into play (e.g., the working frequency, the position of the probes, and the size of the metallic casing and of the targets), so that the provided analysis will give an insight into how to properly choose these quantities with respect to the performance of an imaging procedure carried out in an embedded set-up. It is worth remarking that the study of the NDF of the relevant linear operator has been widely adopted in the literature to address the problem of characterizing the information content of an inverse problem, meant as the number of parameters and the class of functions which can be reliably retrieved. For instance, this tool has been exploited to study the features of the linear inverse scattering problem in the canonical free-space configuration [18–20], in the subsurface or aspect-limited geometries [21, 22], as well as to study the inverse source problem in nonhomogeneous backgrounds or in the presence of unconventional media [23, 24]. It is also worth noting that the information content of the inverse problem at hand could also be instigated by exploiting a statistical framework based on the Fisher information analysis [25, 26].

The paper is organized as follows. In section 2, the scattering problem underlying an imaging system hosted in a perfectly conducting casing is formulated with respect to the two-dimensional scalar case (TM polarization). Section 3 is devoted to briefly recalling the

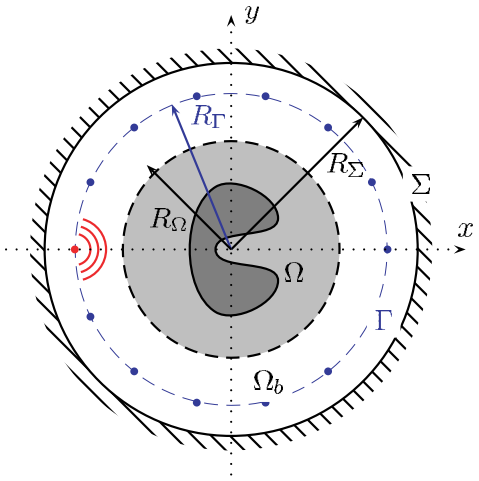

Figure 1. Cross section of the imaging system enclosed in a cavity. The metallic border Σ has a circular cross section of radius R_Σ. The emitters and receivers are placed within the cavity on the circular probing line Γ. The investigation domain Ω is also circular; it is placed at the center of the set-up and encloses the unknown targets that have arbitrary cross sections.

properties of the radiation operator in the canonical idealized situation, in which the system is hosted in an unbounded medium. Section 4 introduces the singular system of the radiation operator as valuated in the presence of the embedding, while section 5 investigates the role of the factors that affect the spectral properties of this latter, in order to address the choice of these parameters in the design of the imaging system. Once these tools have been assessed, the comparison of the expected performances of an embedded imaging system versus those of an 'unbounded' one is discussed in section 6. Concluding remarks follow.

2. Formulation and tools

2.1. Description of the problem

The imaging system configuration which will be considered in the following is depicted in figure 1. The system (made by the scatterer and the probes) is enclosed in a metallic casing of circular cross section Σ having radius R_Σ that is filled with a medium Ω_b having (complex) permittivity $\varepsilon_{rb} = \varepsilon'_{rb} - \mathrm{i}\varepsilon''_{rb}$. All the considered materials are assumed to be non-magnetic; hence the magnetic permeability is everywhere equal to that of vacuum, μ_0. An array of time-harmonic ideal 2D point sources, i.e., filamentary current distributions infinitely extended along the z-axis, is placed on a circle Γ with radius R_Γ and exploited to produce the primary field and measure the scattered field due to a set of non-magnetic targets having arbitrary cross section and of infinite extent along the z direction. These latter are located at the center of the set-up, within a cylindrical volume of circular cross section Ω with radius R_Ω.

By assuming and omitting the time factor $\exp(\mathrm{i}\omega t)$, the propagation problem can be modeled as a scalar one, owing to the invariance properties, and cast as the pair of equations:

$$E^s(\vec{r}) = k_b^2 \int_\Omega G(\vec{r},\vec{r}\,')E^t(\vec{r}\,')\chi(\vec{r}\,')\,\mathrm{d}\vec{r}\,', \qquad \vec{r} \in \Gamma \tag{1}$$

$$E^t(\vec{r}) = E^i(\vec{r}) + k_b^2 \int_\Omega G(\vec{r},\vec{r}\,')E^t(\vec{r}\,')\chi(\vec{r}\,')\,\mathrm{d}\vec{r}\,', \qquad \vec{r} \in \Omega, \tag{2}$$

where $k_b = \omega\sqrt{\varepsilon_{rb}\mu_0}$ is the wavenumber in the host medium Ω_b at the pulsation ω, and E^i, E^t and E^s are the z-components of the field radiated from the primary sources, the total field induced by this latter inside the targets and the field scattered by the objects under test on Γ, respectively. The function,

$$\chi(\vec{r}) = \frac{\varepsilon_r(\vec{r})}{\varepsilon_{rb}} - 1, \tag{3}$$

defines the 'contrast' between the host medium permittivity and that corresponding to the targets embedded in Ω, $\varepsilon_r(\vec{r}) = \varepsilon_r'(\vec{r}) - \mathrm{i}\varepsilon_r''(\vec{r})$.

The kernel $G(\vec{r}, \vec{r}')$ of the integral equations (1), (2) is the Green function of the problem that expresses the field of an elementary source located at $\vec{r}' = (\rho', \theta')$ as observed in the point $\vec{r} = (\rho, \theta)$. In the considered configuration, it has been shown that such a function can be expressed as a single summation of Bessel functions [5, 12] as

$$G(\vec{r}, \vec{r}') = \frac{1}{4}\sum_{n=-\infty}^{+\infty} \frac{J_n(k_b\rho_<)}{J_n(k_bR_\Sigma)}\left[Y_n(k_bR_\Sigma)J_n(k_b\rho_>) - J_n(k_bR_\Sigma)Y_n(k_b\rho_>)\right]\mathrm{e}^{\mathrm{i}n(\theta-\theta')}, \tag{4}$$

where $\rho_< = \min(\rho, \rho')$ and $\rho_> = \max(\rho, \rho')$, and J_n, Y_n denote the first and second kind Bessel functions of order n, respectively.

2.2. *Field properties via spectral analysis*

As long as one is interested in understanding the properties of the fields in the considered configuration, it proves convenient to rewrite (1) in an operator formalism. To this aim, let us denote with $J(\vec{r}) = \chi(\vec{r})E^t(\vec{r})$ the contrast source induced by the incident field in Ω and define the integral operator,

$$\mathcal{A} : J \in L^2(\Omega) \to E^s \in L^2(\Gamma) = k_b^2 \int_\Omega G(\vec{r}, \vec{r}')J(\vec{r}')\,\mathrm{d}\vec{r}', \tag{5}$$

that relates the current induced in the investigated region to the field scattered by the anomalies therein located as evaluated at the receivers locations. Owing to the Green's function properties, the *radiation* operator $\mathcal{A}$ is compact, so that it can be represented through its singular value decomposition (SVD) as [16]

$$\mathcal{A}(J)(\vec{r}) = \sum_{n=-\infty}^{+\infty} \sigma_n \langle J|v_n\rangle_\Omega u_n(\vec{r}), \tag{6}$$

where the scalar product on Ω is defined by

$$\langle f|g\rangle_\Omega = \int_\Omega f(\vec{r})g^*(\vec{r})\,\mathrm{d}\vec{r}, \tag{7}$$

with g^* denoting the complex conjugate of g.

In equation (6), $\{\sigma_n\}$ are the singular values ordered for decreasing magnitude and accumulating to zero for $n \to \infty$, while $\{v_n\}$ and $\{u_n\}$ correspond to the singular functions. In particular, the left-hand singular functions u_n provide a basis for the space of the scattered fields on Γ, while the right-hand ones, v_n, are a basis for the set of the radiating part of the contrast sources defined on Ω.

Now, the properties of the scattered fields can be inferred from the SVD equation (6). As a matter of fact, the decaying behavior of the singular values introduces a spectral cut-off that essentially defines the dimension of the scattered field's space. This, in turn, fixes the NDF of the field [17] that identifies the number of parameters needed to represent the field, within a given accuracy, as well as the number of basis functions that contribute in a meaningful way

to the radiation of the (induced or impressed) sources J. The span of these latter identifies the allowable spatial content for a radiating contrast source, and therefore it is useful in defining the class of retrievable contrast functions in the inversion procedure [19–22].

It is worthwhile to explicitly note that, due to reciprocity and due to the fact that the receiving and transmitting probes are located on the same curve, the study of the singular system of $\mathcal{A}$ also determines the number of independent scattering experiments that can be realized with the imaging system at hand, as well as the kind of incident fields that can be induced by means of the adopted set-up.

3. Field properties in the unbounded medium configuration

For the sake of clarity, we briefly recall in this section the well-known results concerning the radiation operator in the canonical unbounded medium configuration [18–20].

In this configuration, which corresponds to removing the metal casing present in figure 1 and thus considering the medium Ω_b to be unbounded, the singular system is given by [19]

$$v_n^u(\vec{r}') = c_n^u [J_n(k_b \rho')]^* \exp(\mathrm{i}n\theta') \tag{8}$$

$$u_n^u(\vec{r}) = d_n^u H_n^{(2)}(k_b R_\Gamma) \exp(\mathrm{i}n\theta) \tag{9}$$

$$\sigma_n^u = \frac{1}{c_n^u d_n^u}, \tag{10}$$

with $H_n^{(2)}$ being the second kind Hankel function of order n and

$$c_n^u = \left(2\pi \int_0^{R_\Omega} |J_n(k_b \rho')|^2 \rho' \, \mathrm{d}\rho' \right)^{-1/2} \tag{11}$$

$$d_n^u = \left(2\pi R_\Gamma \left| H_n^{(2)}(k_b R_\Gamma) \right|^2 \right)^{-1/2}, \tag{12}$$

where the superscript u is meant to recall that an *unbounded* medium is being considered. Note that, for a fixed position of the observation domain R_Γ, the singular functions u_n^u only depend on the angular variable.

From the analysis of this singular system, the following main observations arise:

- when primary sources and measurement probes are placed at some wavelengths apart from the object under test, the field can be represented, within a given accuracy, with a finite number of parameters [17, 18];
- if the scatterer is in size sufficiently large with respect to the wavelength, such a number only depends on the electrical dimension of the scatterer, whatever the required accuracy [17, 18];
- an increase in the number of parameters (this time depending on the considered accuracy) can be induced by moving the probes, in the 'close proximity' of the scatterer. Such an enlargement can be explained by considering that the higher-spatial-frequency components of the fields are catched by the probes when positioned in the vicinity of the targets [19].

These observations provide some clues to the quantity of information that is associated with the measured field and that can be extracted in the inverse problem. Moreover, the singular functions also provide a characterization of the kind of incident fields that can be realized, as well as of the components of the contrast source that can be reconstructed. When

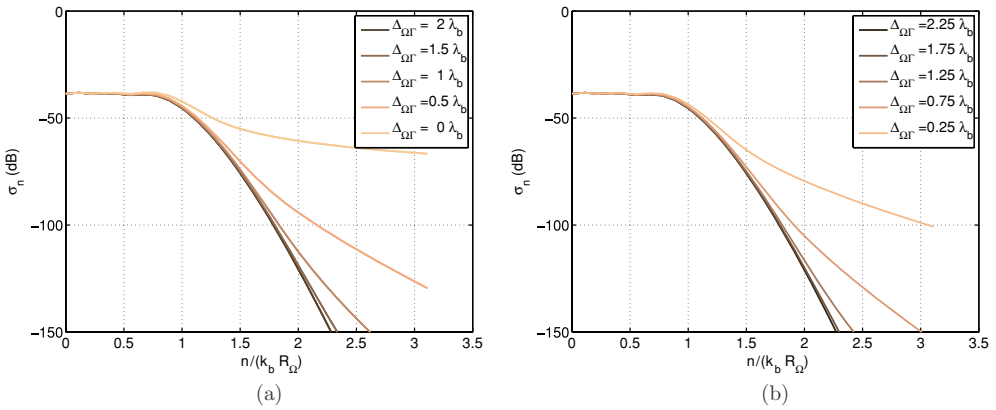

Figure 2. Singular spectrum in the unbounded medium configuration for several values of the distance $\Delta_{\Omega\Gamma}$. The probing line R_Γ is moving (a) with a step of $\lambda_b/2 + p\lambda_b/2$ from $R_\Gamma^{\max}$, (b) with a step of $\lambda_b/4 + p\lambda_b/2$ from $R_\Gamma^{\max}$. The embedding medium Ω_b is lossless.

a linear inverse scattering problem is dealt with, this knowledge directly furnishes a definition of the class of retrievable contrast functions, in both the single-view and multi-view cases [17, 19, 20]. In the general nonlinear case, no general result can be drawn. Nevertheless, the observation of the singular functions still provides some hints on the kind of retrievable functions [19].

In order to give an example of the above observations, let us observe figure 2, where the behavior is reported of the singular values σ_n^u for a source domain $R_\Omega = 1.5\lambda_b$ hosted in a lossless medium, when varying the position of the probes R_Γ between $R_\Gamma^{\min} = R_\Omega$ and $R_\Gamma^{\max} = R_\Omega + 2.5\lambda_b = 4\lambda_b$. The wavelength of the embedding medium λ_b is given by $\lambda_b = 2\pi/k_b$. In particular, in panel (a) R_Γ is decreased with a step of $\lambda_b/2$ from $R_\Gamma^{\max}$, while in panel (b) it is decreased with the same step but starting from $R_\Gamma^{\max} - \lambda_b/4$. As can be observed, for a fixed accuracy, the number of significant singular values depends on the distance $\Delta_{\Omega\Gamma} = |R_\Gamma - R_\Omega|$ [19]. As a matter of fact, when such a distance is larger than $\lambda_b/2$, the singular values have an almost identical decay regardless of the particular value. In particular, with the scatterer not being extremely large, the number of significant singular values slightly depends on the considered accuracy, but it is always larger than $k_b R_\Omega$. On the other hand, when the probes approach the investigation area, the decay becomes slower and strongly depends on the position of the probes. Accordingly, the number of significant singular values strongly depends on the considered accuracy. It is worth noting that, in agreement with the physical intuition, this increase of the NDF does not entail a straightforward improvement of the achievable spatial resolution. As a matter of fact, as shown in [19], owing to the spatial properties of the singular functions associated with the 'extra' above-threshold singular values, the resolution improvement is circumscribed to those parts of the domain under test that are actually in the near-field region of the probes.

In figure 3, we reported the behavior of the singular values σ_n^u in the same conditions as before, but assuming a lossy host medium having a loss tangent of $\tan(\delta) = \varepsilon''_{rb}/\varepsilon'_{rb} = 0.051$. In this case, the background wavelength of the embedding medium is defined as $\lambda_b = 2\pi/\Re(k_b)$. As can be observed, while the presence of losses leaves unaltered both the 'far-field' and 'proximity' features of the singular values' spectrum, it affects the overall spectrum level, which appears to be slightly attenuated when the distance between targets and probes increases.

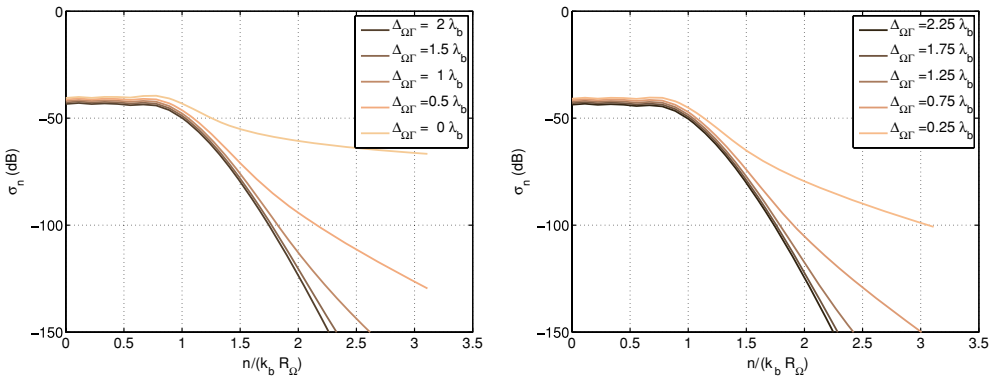

(a) (b)

Figure 3. Singular spectrum in the unbounded medium configuration for several values of the distance $\Delta_{\Omega\Gamma}$. The probing line R_Γ is moving (a) with a step of $\lambda_b/2 + p\lambda_b/2$ from $R_\Gamma^{\max}$, (b) with a step of $\lambda_b/4 + p\lambda_b/2$ from $R_\Gamma^{\max}$. The embedding medium Ω_b is lossy, with a loss tangent of $\tan(\delta) = 0.051$.

4. Field properties in the embedded configuration

Let us now turn to the study of the singular system of the radiation operator $\mathcal{A}$ pertaining to the embedded configuration. By exploiting similar tools as those used to compute the singular system in the unbounded medium case, it is possible to show that the associated singular system is given by (see the appendix)

$$v_n(\vec{r}') = c_n[J_n(k_b\rho')]^* \exp(\mathrm{i}n\theta') \tag{13}$$

$$u_n(\vec{r}) = d_n \left[\frac{Y_n(k_b R_\Sigma) J_n(k_b R_\Gamma) - J_n(k_b R_\Sigma) Y_n(k_b R_\Gamma)}{J_n(k_b R_\Sigma)} \right] \exp(\mathrm{i}n\theta) \tag{14}$$

with

$$c_n = \left(2\pi \int_0^{R_\Omega} |J_n(k_b\rho')|^2 \rho' \, \mathrm{d}\rho' \right)^{-1/2} \tag{15}$$

$$d_n = \left(2\pi R_\Gamma \left| \frac{Y_n(k_b R_\Sigma) J_n(k_b R_\Gamma) - J_n(k_b R_\Sigma) Y_n(k_b R_\Gamma)}{J_n(k_b R_\Sigma)} \right|^2 \right)^{-1/2}, \tag{16}$$

and the singular values are still given by

$$\sigma_n = \frac{1}{c_n d_n}. \tag{17}$$

As can be observed, several analogies and differences hold with respect to the previous case. In particular, as far as the singular functions are concerned, one can immediately note that the right singular functions v_n and v_n^u coincide in the two cases, whereas the left singular ones u_n and u_n^u share the same dependence on the angular variable, consistently with the fact that the observation domain is the same, but are weighted for different factors owing to the different boundary conditions arising in the cases considered. When observing the singular values spectrum, the first analogy which appears is that the factor c_n, which only depends on the electric dimension of the investigated region $k_b R_\Omega$, is exactly coincident with that of the

unbounded medium configuration, c_n^u. As such, it will provide the aforementioned decay of the singular spectrum for $n > k_b R_\Omega$. Such a decay will be exponentially fast in the high-frequency regime (i.e., for $k_b R_\Omega \gg 1$), while it will exhibit a slower rate when considering a region in size comparable or smaller than the wavelength. Therefore, the possible differences in the singular spectrum's properties are related to the term d_n. To analyze this quantity, it is worthwhile to first recall that the considered configuration can be seen, in the absence of the scatterer, as a resonant cavity, which will be therefore characterized by the eigenmodes provided by the solution of the following set of equations:

$$\begin{cases} \Delta E(\vec{r}) + k_b E(\vec{r}) = 0 & \vec{r} \in \Omega_b \cup \Omega \\ E(\vec{r}) = 0 & \vec{r} \in \Sigma. \end{cases} \tag{18}$$

Apart from the trivial null solutions, the eigenmodes for the considered geometry are of the form [27]

$$E_{n,m}(\vec{r}) = a_{n,m} J_n(k_{n,m}\rho) \exp(\mathrm{i}n\theta), \qquad n \geqslant 0, \quad m \geqslant 1 \tag{19}$$

with the condition that

$$k_{n,m} = \frac{j_{n,m}}{R_\Sigma}, \tag{20}$$

where $j_{n,m}$ corresponds to the mth zero of the nth Bessel function J_n.

In particular, for a given size of the embedding $k_b R_\Sigma$, there exist a finite number of pairs n, m such that the condition

$$\frac{j_{n,m}}{k_b} < R_\Sigma \tag{21}$$

is matched. This means that the associated eigenmodes are present in the cavity, since the corresponding Bessel function admits at least a zero inside the embedding. The largest order $n_{\max}$ that can be allowed is given by the condition

$$j_{n_{\max},1} \leqslant k_b R_\Sigma < j_{n_{\max}+1,1}. \tag{22}$$

5. Molding the singular spectrum through eigenmodes excitation

Some interesting observations can be done if the condition

$$\frac{j_{\tilde{n},\tilde{m}}}{k_b} = R_\Sigma \tag{23}$$

holds for some $\tilde{n}$ and $\tilde{m}$, i.e., if, for a given dimension of the empty cavity, a Bessel function of order $\tilde{n}$ exists, whose $\tilde{m}$th zero *exactly* falls on the cavity border. Indeed, if this happens, the excited eigenmode coincides with the $\tilde{n}$th singular function $v_{\tilde{n}}$. Moreover, due to the fact that owing to (23) $J_{\tilde{n}}(k_b R_\Sigma) = 0$ it follows that the corresponding singular value becomes infinite. As a consequence, the spectrum of the operator $\mathcal{A}$ has an abrupt modification with respect to the unbounded medium case depicted in figure 2, as it will only present a very large (infinite, actually) singular value which will dominate all the others, becoming the only significant contribution to the data in the inverse problem.

On the other hand, by observing the expression of d_n in (16), one can understand that this circumstance can be avoided by properly positioning the probing/observation circle R_Γ. Indeed, by choosing this latter in such a way that R_Γ exactly falls on a $\tilde{p}$th zero of $J_{\tilde{n}}$, i.e., $J_{\tilde{n}}(k_b R_\Gamma) = 0$, of course under the constraint $\tilde{p} < \tilde{m}$, i.e., $R_\Gamma < R_\Sigma$, it follows that the

considered eigenmode is still excited, but the corresponding singular value attains a finite value, i.e.,

$$\sigma_{\tilde{n}}^2 = \frac{2\pi R_\Gamma}{c_{\tilde{n}}} \times \left| Y_{\tilde{n}}(k_b R_\Gamma) + Y_{\tilde{n}}(k_b R_\Sigma) \prod_{k=1, k\neq\tilde{m}, k\neq\tilde{p}}^{\infty} \frac{j_{\tilde{n},k}^2 - j_{\tilde{n},\tilde{p}}^2}{j_{\tilde{n},k}^2 - j_{\tilde{n},\tilde{m}}^2} \right|^2 . \tag{24}$$

By doing so, it is possible therefore to *mold* the spectrum of the operator by properly enhancing the contribution of a specific singular function, through the increase of the corresponding singular value. In particular, since the singular values are by definition ordered in a decreasing fashion, this means that the choice of the design parameters of the embedded system (i.e., working frequency, embedding medium, R_Σ and R_Γ) introduces a modification in the ordering of the singular functions with respect to the unbounded configuration, thus actually modifying the class of 'retrievable' functions in the inversion.

The previous considerations were drawn by considering that the size of the embedding was exactly matching a zero of a particular Bessel function and assuming a purely dielectric embedding medium. However, these conditions, especially the latter, are seldom satisfied in the applications, so that it is of interest to understand if and to what extent the above observations apply.

To this aim, note that, when a lossy medium is considered and/or when condition (23) is not met, nevertheless, owing to (21), several eigenmodes will be present in the embedding. In particular, these latter will exactly coincide (in the imaged region) with the singular functions v_n corresponding to the relevant Bessel functions.

Now, by observing the expression of d_n (16), one can understand that the singular values corresponding to these particular singular functions will be more or less enhanced depending on the relative distance of the zero of the pertaining singular function from the cavity border, as this parameter directly influences the denominator of d_n, i.e., $J_n(k_b R_\Sigma)$. As a consequence, even in this case, it is possible to properly act on the spectral content of the singular functions span by means of a convenient ordering of the sequence of the zeros.

However, it must be recalled that R_Σ is not the only quantity that comes into play. As a matter of fact, one must take also into account the effect of the probing line position R_Γ on which the factor d_n depends in a periodic way, with a different periodicity for different values of the index n.

In particular, it is useful to observe the behavior of the amplitude of

$$f_n(R_\Gamma) = \frac{Y_n(k_b R_\Sigma) J_n(k_b R_\Gamma) - J_n(k_b R_\Sigma) Y_n(k_b R_\Gamma)}{J_n(k_b R_\Sigma)}, \tag{25}$$

as a function of the distance $R_\Sigma - R_\Gamma$. For some values of n, a plot of this latter is given, for both the lossless and lossy cases, in figure 4. As can be noted, for all the indices, $f_n(R_\Gamma)$ reaches a maximum of the amplitude for $R_\Sigma - R_\Gamma = \lambda_b/4$ and a minimum amplitude for $R_\Sigma - R_\Gamma = \lambda_b/2$. As a consequence, whatever the choice of the casing size R_Σ (which entails a particular ordering of the singular functions), when the probing line is placed at $R_\Sigma - R_\Gamma = \lambda_b/2$, the singular value spectrum will be lowered. Clearly, this does not happen if $R_\Sigma - R_\Gamma = \lambda_b/4$, so that, provided this condition is fulfilled, it follows that it is still possible to selectively enhance the singular values by fixing the size of the embedding. It is also worth noting that when the distance becomes larger than $\lambda_b/2$, the periodicity of the extremal points of (25) is not the same for all the values of n, so that the effect is not anymore easily predictable. Accordingly, $R_\Sigma - R_\Gamma = \lambda_b/4$ appears as convenient practical choice.

A simple physical explanation of the above findings is that, when considering a source located in the imaged domain Ω, the interaction between this latter and the casing gives raise to different destructive and constructive patterns. Therefore, depending on the observation line's

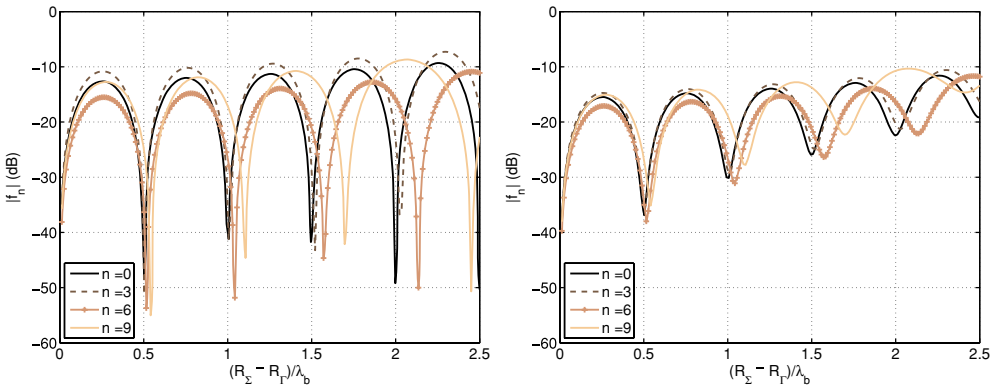

(a) Without loss (b) With loss

Figure 4. Evolution of the amplitude of f_n with respect to the distance between the probing line R_Γ and the metallic casing R_Σ. The external medium is (a) lossless or (b) with a loss tangent of $\tan(\delta) = 0.051$.

position, different field levels can be detected. Exploiting reciprocity arguments, this also suggests that the probing line has to be properly positioned (i.e., in a location corresponding to a constructive interference), in order to provide a meaningful incident field in the imaged region. Of course, such an effect will be generally smoothed when losses are present in the host medium Ω_b.

5.1. A practical example

In order to observe the above-described effects, we have evaluated the singular spectrum in the same cases considered in the unbounded configuration, section 3, assuming that the metallic boundary is located at $R_\Sigma = R_\Gamma^{\max} = 4\lambda_b$. The results obtained for the case in which the host medium Ω_b is lossless are shown in figure 5.

Some comments are now in order:

- First, note that the spectra are ordered according to the indices of the pertaining Bessel function. By so doing, one can indeed appreciate the 'selective enhancement' effect induced by the presence of the casing.
- It can also be noted that, as expected, the spectra are different depending on the relative position of the probing line with respect to the casing. As a matter of fact, for values of n below $k_b R_\Omega$, when the probing line is placed in such a way that $R_\Sigma - R_\Gamma$ is a multiple of $\lambda_b/2$, the amplitude of the 'low-order' singular values is generally lowered, whereas, when $R_\Sigma - R_\Gamma$ is a multiple of $\lambda/4$, this does not happen.
- When $R_\Sigma - R_\Gamma$ is a multiple of $\lambda/2$, the low-order singular values increase when approaching the boundary of the investigated region R_Ω. This is due to the increase of the minima of (25) as well as to the different periodicity of its extremal points; see figure 4.
- Conversely, for values of n above $k_b R_\Omega$, all the spectra exhibit a very similar behavior, since they are basically dominated by the factor c_n, which is independent of the set-up parameters (R_Σ and R_Γ).
- It is worth observing that, for $n > k_b R_\Omega$, an increase or a decrease of some singular values can still be observed, as long as the probes are far from the investigation domain. In the

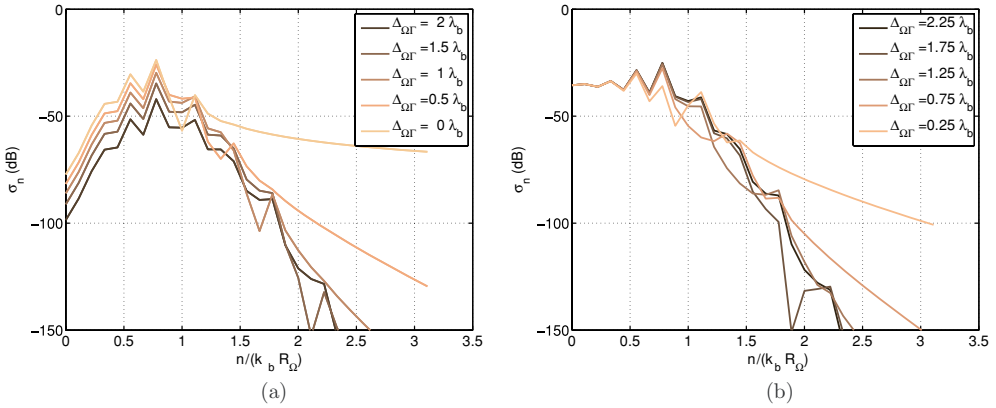

Figure 5. Singular spectrum for the embedded configuration with $R_\Sigma = 4\lambda_b$, $R_\Omega = 1.5\lambda_b$ and different values of $\Delta_{\Omega\Gamma}$. The probing line moves (a) with a step of $\lambda_b/2 + p\lambda_b/2$ from R_Σ or (b) with a step of $\lambda_b/4 + p\lambda_b/2$ from R_Σ. The embedding medium is lossless.

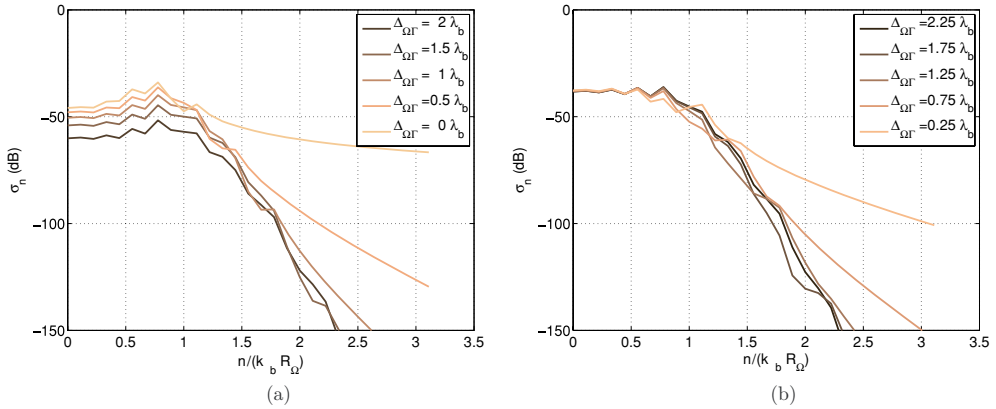

Figure 6. Singular spectrum for the embedded configuration with $R_\Sigma = 4\lambda_b$, $R_\Omega = 1.5\lambda_b$ and different values of $\Delta_{\Omega\Gamma}$. The probing line moves (a) with a step of $\lambda_b/2 + p\lambda_b/2$ from R_Σ or (b) with a step of $\lambda_b/4 + p\lambda_b/2$ from R_Σ. The embedding medium is lossy, with a loss tangent of $\tan(\delta) = 0.051$.

close proximity case (i.e., when $R_\Gamma \to R_\Omega$), no specific singular value is enhanced. This circumstance is due to the fact that probes positioned close to the domain do not intersect the zeros of the high-order Bessel functions (that are relevant to that part of the spectrum), which are indeed located in the vicinity of the metallic casing.

In figure 6, the same situation as before has been considered, but for the presence of losses in the embedding medium Ω_b. As can be noted, despite the obvious smoothing introduced by the attenuation, still similar considerations as those done in the previous case hold true.

For the considered geometry, it is also interesting to observe the displacement of the zeroes of the Bessel functions, since their ordering with respect to their distance from the embedding exactly provides the 'molding' rule for the singular values and functions. This circumstance is shown in figure 7(a), wherein it is reported the position of the zeroes of the first eight eigenmodes that fall close to the boundary. As can be seen by comparing

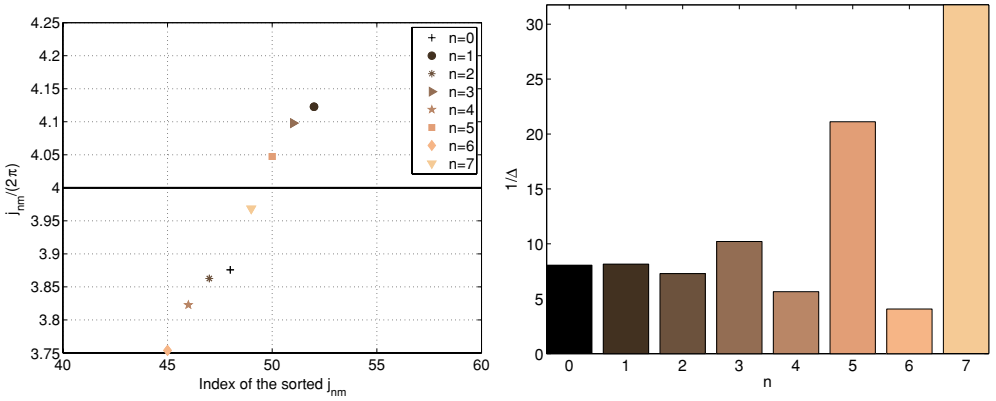

(a) (b)

Figure 7. (a) Position of the zeroes of the first eight eigenmodes which are located in the vicinity of $R_\Sigma = 4\lambda_b$. (b) Ordering of the eigenmodes with respect to $1/\Delta$, where $\Delta = |j_{nm}/(2\pi) - R_\Sigma/\lambda_b|$, with m being the index of the zero of J_n which is closest to R_Σ/λ_b.

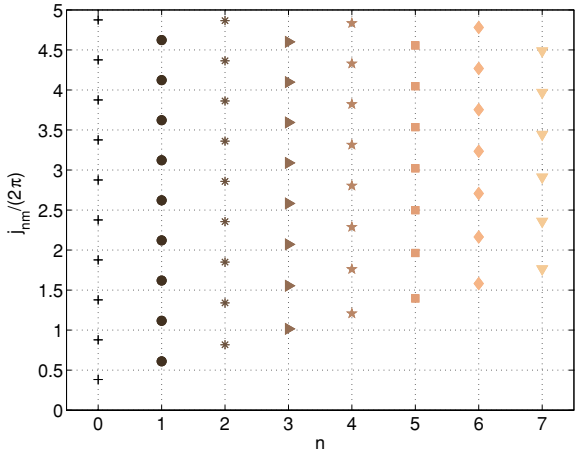

Figure 8. A simple abacus for the design of the embedded imaging system.

figure 7(b) and figure 5(b), the eigemode's zero distance from the border is exactly proportional to the magnitude of the singular values.

5.2. A simple tool to design the imaging set-up

According to the above observations, it follows that a simple and useful tool to design an embedded imaging system like that at hand is constituted by the plot shown in figure 8, wherein the sequence of the zeros of several Bessel functions in normalized coordinates is reported. As a matter of fact, by just entering the ordinate of this plot with a value of R_Σ normalized to the wavelength, it is possible to immediately draw the ordering of the corresponding singular values. So, one can then foresee which are the singular functions u_n (resp. v_n) onto which the most part of the field (resp. the contrast source is projected. Then,

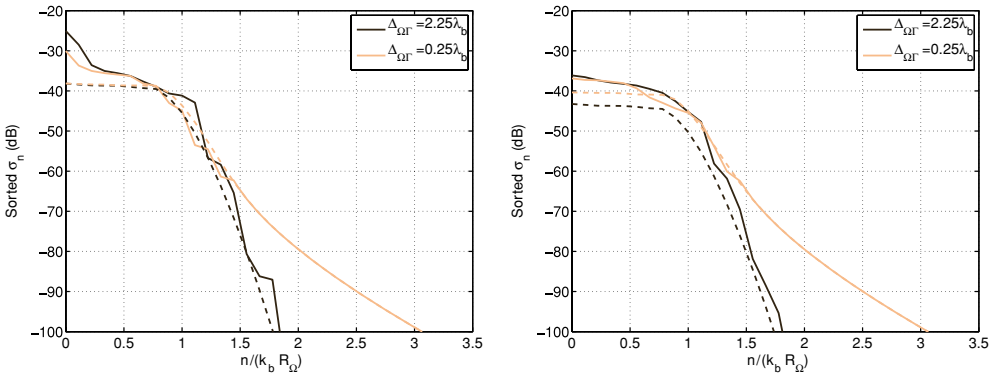

(a) Without loss (b) With loss

Figure 9. Comparisons of the unbounded configuration (dashed line) and the embedded configuration (full line) spectra for two positions of the receiving line. The target is located inside the domain Ω of radius $R_\Omega = 1.5\lambda_b$ and the casing, if present, is located at $R_\Sigma = 4\lambda_b$. The embedding medium is either (a) lossless or (b) with some losses with a loss tangent of $\tan(\delta) = 0.051$.

depending on which of the two conditions (21) or (23) is being fulfilled, the probing line has to be positioned either on a zero of the Bessel function supporting the excited eigenmode or at a distance of $\lambda_b/4$ from the casing.

6. Some considerations on embedded versus unbounded imaging systems

The analysis and the tools described in the previous section can be of help in trying to address a question which naturally comes to mind, i.e., how the presence of the metallic embedding affects the imaging process with respect to the corresponding unbounded situation. To this end, let us again consider the particular set-up described in the example of the previous sections. Although this is, of course, a particular case, it allows us to draw some general conclusions; thanks to the results achieved in section 5.

In figure 9, we have reported the singular values spectra in the two cases (unbounded and embedded), for several positioning of the probing line (away from the targets and in the close proximity) and considering a lossless/lossy host medium Ω_b. Note that, unlike the previous plots, the singular values have been properly ordered in the case of the embedded system, in order to make a fair comparison between the spectra.

A first feature to note is that the general trend of the singular values in either the transition ($n \approx k_b R_\Omega$) and the asymptotic regions is the same for both cases. This outcome, which is not surprising, being dictated by the factor c_n that is common to both σ_n and σ_n^u, entails that the amount of independent information carried by the fields is the same in the two configurations. Hence, *no modification of the quantity of available independent information* is introduced by considering a properly designed embedded imaging system.

Conversely, it appears that a different signal energy pertains to the two cases (i.e., the area subtended by the spectrum curve). As can be observed, when the embedding and probing lines are properly selected, the energy is larger in the presence of the casing, than in the unbounded configuration. This circumstance is physically related to the constructive interactions between the sources (primary or induced) and the casing, and entails that a larger signal-to-noise ratio is expected when the imaging system is properly embedded. As a consequence, the imaging

process in this configuration can be either more stable against the unavoidable uncertainties on the measured data and/or lead to the stable retrieval of a (slightly) larger number of spectral components when considering a fixed-accuracy level. On the other hand, if the design of the embedding is not fulfilling the given criteria concerning the probing line positioning, the spectrum pertaining to the embedded configuration can be lower than the unbounded one.

A further difference can be pointed out recalling that, while the singular value index of the unbounded case corresponds to a singular function containing a Bessel function and a complex exponential of the same order, this is not the case for the embedded system configuration, in which the ordering is dictated by the relative position of the zeroes of the eigenmodes with respect to the casing. For instance, in the lossless case, this could mean that most part of the energy can be associated with large-order Bessel functions, rather than with the low-order ones. This circumstance entails that, even if the *quantity* of information is the same in the two cases, the molding of the spectrum allows for a change in the *quality* of the retrievable information.

As far as the imaging process is concerned, it is worth noting that such a circumstance is not necessarily leading to an improvement, due to the spatially inhomogeneous behavior of the Bessel functions over the imaged domain Ω. As a matter of fact, when the index of the Bessel function (and of the pertaining exponential) grows, the corresponding singular function exhibits increasingly faster angular oscillations confined on the border of Ω. This also means that the corresponding incident field is almost vanishing in the center of the imaged domain. In the simple case in which the Born approximation holds true, wherein the contrast source is linearly related to the incident field as $J(\vec{r}) = \chi(\vec{r})E_{\mathrm{inc}}(\vec{r})$, this entails that when the target support occupies only the center of the imaged region, a weaker, almost negligible, current will be induced on it, thus making it more difficult or even impossible to retrieve. This circumstance explains the finding based on numerical observations done in [14], where a similar kind of target (i.e. concentrated in the center of the imaged area) is better reconstructed when probing it under the unbounded configuration than when using the embedded system. On the other hand, our analysis also suggests that, under the same conditions, a target located on the border of the domain Ω will be more easily and accurately retrieved by adopting the embedded configuration. Examples of such behavior can be found in [28].

In the general case in which the Born approximation does not hold true, the reasoning cannot be as straightforward. However, it can be expected that similar results are found, since the singular functions still provide a basis for the contrast source. Hence, the circumstance under which the projection of the contrast source onto the leading singular functions is almost negligible in some part of the domain can indeed affect the result of the imaging process.

7. Conclusion

Owing to the growing interest toward the embedded microwave imaging system, in this paper we have studied a configuration in which the system is enclosed in a circular metallic casing, with the goal of understanding the expected features of an imaging process performed in such an environment.

By taking advantage of the analysis of the NDF of the relevant radiation operator, we have shown that, with respect to the canonical unbounded medium configuration, there is no change in the *quantity* of available independent information that can be exploited in the inverse problem. Conversely, the *quality* of this information is different, due to the fact that the geometrical parameters of the set-up (i.e., the electric dimension of the embedding and the position of the probing line) may lead to an enhancement of some singular functions with respect to others. Accordingly, we have recognized that by properly designing, by means of

simple tools, the resonances of the embedding, it is possible to modify to some extent the class of retrievable contrast functions. Interestingly, our findings provide an explanation for the numerical observations reported in [14, 28] and appear in agreement with the practical criteria adopted in the actual realization of a system like that considered in [5]. It is worth remarking that the similarities which have been pointed out between the SVD of the radiation operator for the embedded system considered in this paper and that of operator relevant to the canonical unbounded case allows us to easily extend the achieved results to the inverse scattering problem under multiple incidences, taking advantage of the results in [20]. Moreover, it is also interesting to note that the capability of molding the spectrum of the operator that we have observed is in agreement with the considerations reported in the literature concerning the possible radiation enhancement achieved by means of a suitably designed metamaterial's substrate [24].

The present analysis does not deal with another parameter of importance in the solution of the inverse scattering problem, that is the nonlinearity of the relationship between the data and the unknowns. As a matter of fact, it is known that the scenario plays a major role on determining the *degree of nonlinearity* [29, 30] of the inverse scattering problem, so that further differences may arise between the embedded configuration and the unbounded one. As such, future work will be concerned with the evaluation of the nonlinearity of the inverse scattering problem solved in an embedded configuration, along the lines traced in [29, 30].

In addition, the study of systems embedded in non-circular and/or non-metallic casing will be tackled, by exploiting suitable numerical procedures capable of achieving the Green's function that pertains to the considered geometries.

Acknowledgments

This work has been performed while L Crocco was visiting Institut Fresnel, thanks to a visiting researcher grant from Ecole Centrale Marseille. A Litman would also like to acknowledge the support of Agence Nationale pour la Recherche under the 'Jeunes Chercheurs' grant no JCJC06-141021 as well as the support of INTAS through the grant no 06-1000017-8909.

Appendix

When the Green's function is the product of two functions of separate variables in terms of ρ and θ, the singular values are always given by the inverse product of the weighting coefficients c_n and d_n of the singular functions.

In order to show this result, let us assume that the Green's function is of the following form:

$$G(\vec{r},\vec{r}') = \sum_{n=-\infty}^{+\infty} A_n(\rho)\,\mathrm{e}^{\mathrm{i}n\theta}\,B_n(\rho')\,\mathrm{e}^{-\mathrm{i}n\theta'}, \tag{A.1}$$

where the functions A_n and B_n are depending on the configuration at hand, $\vec{r} = (\rho,\theta)$ corresponds to the observation point and $\vec{r}' = (\rho',\theta')$ to the excitation point. The observation equation (1) can be rewritten as

$$E^s(\vec{r}) = \sum_{n=-\infty}^{+\infty} A_n(\rho)\,\mathrm{e}^{\mathrm{i}n\theta} \int_\Omega J(\vec{r}')B_n(\rho')\,\mathrm{e}^{-\mathrm{i}n\theta'}\,\mathrm{d}\vec{r}' \tag{A.2}$$

$$= \sum_{n=-\infty}^{+\infty} A_n(\rho)\,\mathrm{e}^{\mathrm{i}n\theta}\langle J(\vec{r}')|[B_n(\rho')]^*\mathrm{e}^{\mathrm{i}n\theta'}\rangle_\Omega, \tag{A.3}$$

where $J(\vec{r}')$ corresponds to the induced sources distribution inside the investigation domain Ω. By direct identification with (6), and due to the orthogonality properties of the exponential functions, we obtain

$$v_n(\vec{r}') = c_n[B_n(\rho')]^* \, \mathrm{e}^{\mathrm{i}n\theta'} \tag{A.4}$$

$$u_n(\vec{r}) = d_n A_n(\rho) \, \mathrm{e}^{\mathrm{i}n\theta}, \tag{A.5}$$

where c_n and d_n are normalization coefficients in order to obtain a set of orthonormal singular functions. Thus, the coefficients c_n and d_n are given by

$$|c_n|^2 = 2\pi \int_0^{R_\Omega} |B_n(\rho')|^2 \rho' \, \mathrm{d}\rho' \tag{A.6}$$

$$|d_n|^2 = 2\pi \, R_\Gamma |A_n(R_\Gamma)|^2. \tag{A.7}$$

By rewriting A.3 using the singular vectors notation, we obtain

$$E^s(\vec{r}) = \sum_{n=-\infty}^{+\infty} \frac{u_n(\vec{r})}{d_n} \left\langle J \left| \frac{v_n}{c_n} \right\rangle_\Omega . \right. \tag{A.8}$$

By direct identification with (6), it follows that the singular values are given by

$$\sigma_n = \frac{1}{c_n d_n}. \tag{A.9}$$

In the free-space case, the functions A_n and B_n are defined as

$$B_n(\rho') = J_n(k_b \rho'), \qquad A_n(\rho) = H_n^{(2)}(k_b \rho). \tag{A.10}$$

In the casing case, the functions A_n and B_n are defined as

$$B_n(\rho') = J_n(k_b \rho'), \qquad A_n(\rho) = \frac{Y_n(k_b R_\Sigma) J_n(k_b \rho) - J_n(k_b R_\Sigma) Y_n(k_b \rho)}{J_n(k_b R_\Sigma)}. \tag{A.11}$$

References

[1] Belkebir K and Saillard M 2001 Special section: testing inversion algorithms against experimental data *Inverse Problems* **17** 1565–71

[2] Belkebir K and Saillard M 2005 Special section: testing inversion algorithms against experimental data: inhomogeneous targets *Inverse Problems* **21** S1–3

[3] Litman A and Crocco L 2009 Testing inversion algorithms against experimental data: 3d targets *Inverse Problems* **25** 020201 (5pp)

[4] Soldovieri F, Persico R and Leone G 2005 Effect of source and receiver radiation characteristics in subsurface prospecting within the DBA *Radio Sci.* **40** RS3006

[5] Geffrin J-M 1995 Imagerie microonde: etude d'un scanner a 434 MHz pour des applications biomedicales *PhD thesis*, Univ. Paris XI, Orsay, France

[6] Lencrerot R, Litman A, Tortel H and Geffrin J-M 2007 A microwave imaging circular setup for soil moisture information In *IGARSS Conf. Proc.* pp 4394–7

[7] Jofre L, Hawley M S, Broquetas A, Reyes E De Los, Ferrando M and Elias-Fuste A R 1990 Medical imaging with a microwave tomographic scanner *IEEE Trans. Biomed. Eng.* **37** 303–11

[8] Meaney P M, Paulsen K D, Hartov A and Crane R K 1995 An actice microwave imaging system for reconstruction of 2-d electrical property distributions *IEEE Trans. Biomed. Eng.* **42** 1017–25

[9] Broquetas A, Romeu J, Rius J M, Elias-Fuste A R, Cardama A and Jofre L 1991 Cylindrical geometry: a further step in active microwave tomography *IEEE Trans. Microw. Theory Tech.* **39** 836–44

[10] Ybarra G A, Liu Q H, Stang J P and Joines W T 2007 Microwave breast imaging *Emerging Technology in Breast Imaging and Mammography* ed J S Suri, R Rangayyan and S Laxminarayan (USA: American Scientific Publishers)

[11] Franchois A and Tijhuis A G 2003 A quasi-newton reconstruction algorithm for a complex microwave imaging scanner environment *Radio Sci.* **38** 8011
[12] van den Berg P M and Fokkema J T 2003 Removal of undesired wavefields related to the casing of a microwave scanner *IEEE Trans. Microw. Theory Tech.* **51** 187–92
[13] Tijhuis A G and Franchois A 2001 A two-dimensional microwave imaging algorithm for a complex environment: preliminary results In *Proc. URSI Int. Electromagnetic Theory Symp.* pp 445–7
[14] Gilmore C and LoVetri J 2008 Enhancement of microwave tomography through the use of electrically conducting enclosures *Inverse Problems* **24** 035008
[15] Lencrerot R, Litman A, Tortel H and Geffrin J-M 2009 Imposing zernike representation for imaging two-dimensional targets *Inverse Problems* **25** 035012 (18pp)
[16] Bertero M and Boccacci P 1998 *Introduction to Inverse Problems in Imaging* (Bristol, UK: Institute of Physics)
[17] Bucci O M and Isernia T 1997 Electromagnetic inverse scattering: retrievable information and measurement strategies *Radio Sci.* **32** 2123–38
[18] Porter R P and Devaney A J 1982 Generalized holography and computational solutions to inverse source problems *J. Opt. Soc. Am.* **72** 1707–13
[19] Bucci O M, Crocco L and Isernia T 1999 Improving the reconstruction capabilities in inverse scattering problems by exploitation of close-proximity setups *J. Opt. Soc. Am.* A **16** 1788–98
[20] Brancaccio A, Leone G and Pierri R 1998 Information content of born scattered fields: results in the circular cylindrical case *J. Opt. Soc. Am.* A **15** 1909–17
[21] Pierri R, Persico R and Bernini R 1999 Information content of the born field scattered by an embedded slab: multifrequency, multiview, and multifrequency-multiview cases *J. Opt. Soc. Am.* A **16** 2392–9
[22] Bucci O M, Crocco L, Isernia T and Pascazio V 2001 Subsurface inverse scattering problems: quantifying, qualifying, and achieving the available information *IEEE Trans. Geosci. Remote Sens.* **39** 2527–38
[23] Devaney A J, Marengo E A and Li M 2007 Inverse source problem in nonhomogeneous background media *SIAM J. Appl. Math.* **67** 1353–78
[24] Khodja M R and Marengo E A 2008 Radiation enhancement due to metamaterial substrates from an inverse source theory *Phys. Rev.* E **77** 046605
[25] Nordebo S, Gustafsson M and Nilsson B 2007 Fisher information analysis for two-dimensional microwave tomography *Inverse Problems* **23** 859–77
[26] Gustafsson M and Nordebo S 2006 Cramer–Rao lower bounds for inverse scattering problems of multilayer structures *Inverse Problems* **22** 1359–80
[27] Collins R E 1966 *Foundations for Microwave Engineering* (New York: Mc-Graw Hill)
[28] Lencrerot R, Litman A, Tortel H and Geffrin J-M 2009 Measurement strategies for a confined microwave circular scanner *Inv. Probl. Sci. Eng.* DOI: 10.1080/17415970802577012
[29] Bucci O M, Cardace N, Crocco L and Isernia T 2001 Degree of nonlinearity and a new solution procedure in scalar two-dimensional inverse scattering problems *J. Opt. Soc. Am.* A **18** 1832–43
[30] Bucci O M, Cardace N, Crocco L and Isernia T 2000 2D inverse scattering: degree of non-linearity, solution strategies and polarization effects *Proc. SPIE* vol 4123, 185 DOI: 10.1117/12.409269

IOP PUBLISHING INVERSE PROBLEMS

Inverse Problems **25** (2009) 035012 (18pp) doi:10.1088/0266-5611/25/3/035012

Imposing Zernike representation for imaging two-dimensional targets

R Lencrerot, A Litman, H Tortel and J-M Geffrin

Institut Fresnel, Aix-Marseille Université, CNRS, Ecole Centrale de Marseille, Campus de Saint-Jerôme, case 162, 13397 Marseille Cedex 20, France

E-mail: amelie.litman@fresnel.fr

Received 29 July 2008, in final form 8 December 2008
Published 3 February 2009
Online at stacks.iop.org/IP/25/035012

Abstract

To overcome the ill-posedness of the inverse scattering problem, we introduce an appropriate way of representing the unknown permittivity profile which benefits from two *a priori* pieces of information which are commonly encountered. First, the unknown permittivity map has a limited spatial support which can be contained within a circular investigation area. Second, from physical reasoning based on the scattering operator, there is only a limited number of independent parameters that can be retrieved from the measured fields. Both pieces of *a priori* information can be adequately introduced by representing the unknown permittivity profile in terms of a Zernike polynomial expansion, correctly truncated according to the number of independent parameters. To investigate the effectiveness of such a Zernike representation, the reconstructions obtained from experimentally acquired data in the circular microwave scanner developed at the Institut Fresnel are analyzed.

(Some figures in this article are in colour only in the electronic version)

1. Introduction

Probing a medium using waves to detect, localize and characterize objects has many applications. Generally speaking, quantitative inverse problems (i.e. when one is interested in recovering values of the electromagnetic parameters of an unknown scatterer) are recast in optimization problems. An initial estimate representing the unknown object is progressively modified during an iterative process in order to minimize a well-suited quantity. It is well known that this kind of problem is severely ill-posed and the convergence of the process is linked to many parameters. Any piece of *a priori* information is more than welcome in order to improve the reconstruction process. It can rely on the permittivity value of the scatterer if it is known to be homogeneous, on its permittivity range if its constitutive materials are available or on its shape, etc.

Here, we want to use some *a priori* piece of information related to the spatial support of the scatterer, and in particular take into account the fact that most of the considered targets have limited spatial support. Even if the target support is not perfectly known, it is possible to restrain it by means of a pre-processing technique which provides an appropriate support estimation [1] or even better to find the minimum circular envelope of the target [2].

Once the spatial support has been obtained, the permittivity profile is expanded onto a set of suitably chosen basis functions such that their spatial supports all put together cover the investigation domain. The simplest solution is to take as basis functions the set of piecewise-constant functions whose each support is restricted to a single discretization cell. By doing so, the number of unknowns is nothing but the number of discretization cells. This number is usually given by the discretization discrepancy principle which is needed to correctly compute the associated scattered field. When using a finite element mesh, typically for a $\lambda/20$ discretization criterion, it can reach up to 11 000 unknowns for an investigation area having a diameter of approximately 2λ [3]. Even if we drastically increase the number of emitter–receiver pairs, the maximum amount of information about the target that one can extract from the available data is limited due to the low-pass filter behavior of the radiation operator [4, 5]. It is worth introducing in that case a representation of the scatterer where we can adequately control the number of coefficients to retrieve. If a piecewise-constant interpolation representation is still looked for, it can be of interest to look for sub-domain decomposition where a coarser grid is used and slowly transformed into a finer grid in areas where the scatterer has been found [6]. The main difficulty here lies in correctly introducing the refinement strategy at each step of the iterative process.

Another option is to take basis functions such that each of their spatial supports covers the entire investigation domain. Such a global representation will provide a number of unknowns which is not linked to the geometry but to the overall features of the target that one wants to retrieve. With a limited number of unknowns, it is then possible to represent either smooth profiles or rapidly varying ones with spatial variations on the entire investigation area.

Several basis function representations have already been introduced in the inverse scattering literature. The simplest one is of course the orthonormal basis functions set corresponding to the spatial Fourier harmonics [7]. Such a representation is well adapted when there is a lack of *a priori* information on the support of the unknown scatterers as it has an infinite spatial support. Another option is to use B-spline representations of the object and to control the solution by a limited number of knot sequences [8]. The number of knots is linked to the spatial resolution of the reconstructed image and to the amount of available information. The main issue here relies on the deletion of the knots during the iterative process. The same idea of multiscale representation can be performed by means of wavelet-based methods [9] combined with an adapted approach.

As in the considered application the target support is necessarily bounded, global basis functions with compact supports are required. In particular, if the investigation domain is chosen to be squared, Legendre or Tchebycheff polynomials [10] are well adapted. For circular spatial support, Fourier–Bessel or Zernike polynomials are known to correspond to complete basis sets on the radial unit interval.

The Fourier–Bessel functions correspond to the singular vectors of the scattering operator, both in free space [11] and in the casing environment [12], and consist therefore of a suitable basis representation for the induced current inside the scatterer. In the Born approximation, using their orthogonality properties, it is then easy to obtain the permittivity map inside the investigation area. Unfortunately, such an expansion requires a double summation where the ordering of the terms is not straightforward, and renders the thresholding process more difficult. Moreover, they cannot easily represent constant permittivity profiles.

Here, we exploit the duality existing between Zernike polynomials and Bessel functions on the radial unit interval [13]. Indeed, an expansion of suitable functions in terms of Zernike polynomials is simply related to the corresponding Fourier–Bessel series. The nice feature of the Zernike polynomials is the fact that the polynomial order is directly linked to the radial fluctuations of the investigated function. The zero-order term will therefore correspond to a constant permittivity profile. Due to the duality principle between Fourier–Bessel and Zernike basis, the Zernike polynomials also appear as the singular vectors of the Jacobian matrix which infers in the microwave inverse scattering problem [14]. The Zernike polynomials also have a strong relationship with the image moments (gravity center, external radius, etc) [15]. Recent studies have shown that generalized pseudo-Zernike moments are an useful tool for image descriptors [16].

In the present paper, we want to investigate the features of such a representation as a tool for regularizing our ill-posed problem. Indeed, the regularization is introduced by thresholding the Zernike expansion. The first terms in the expansion will provide profiles with low spatial frequency contents, while the higher terms will correspond to rapidly varying profiles. We will also propose an unsupervised way for defining this thresholding criterion based on the rank of the scattering matrix. Finally, such a representation will enable us to define a stopping criterion for the iterative process which ensures that the iterative scheme has reached the best solution in terms of permittivity map.

To investigate this issue, the Zernike representation has been introduced in the imaging scheme associated with the microwave scanner which is currently being developed at the Institut Fresnel. This setup is meant to demonstrate the potentiality of a non-invasive microwave imaging system for soil–water content monitoring. The goal is to provide a complementary non-invasive measurement setup for intermediate scales between remote sensing scales and ground truth measurement scales. The scanner is made of a metallic cylindrical casing enclosing a ring of emitting and transmitting antennas radiating at a fixed frequency. As the goal is to monitor monoliths of reconstructed soils, the target will necessarily be a cylindrical column placed within the setup.

This paper is organized as follows. In section 2, the investigated cylindrical configuration is defined. Section 3 describes the pixel-based inversion technique. In section 4, the introduction of the Zernike polynomials inside the inversion algorithm is detailed. In section 5, the experimental setup is described and the effects of the Zernike polynomials expansion on the reconstructed permittivity maps are analyzed. Reconstructions from experimental and synthetic datasets are presented. Finally, section 6 provides some concluding remarks.

2. Measurement configuration

The investigated measurement configuration consists of a cylindrical cavity entirely filled with a medium Ω_b. It is enclosed by a metal casing Σ at radius R_Σ. The presence of the casing enables us to remove parasitic reflections that would be present otherwise due to surrounding effects. The embedding medium is assumed to be homogeneous with electromagnetic constants ε_{rb} and μ_0, with μ_0 being the permeability of the vacuum. Moreover, all considered materials are assumed to be non-magnetic. This system contains an array of identical antennas acting either as emitters or receivers, working at a fixed frequency (figure 1). These antennas are placed in the same horizontal plane, inside the cavity, on a circle Γ with radius R_Γ. For the time being, they are simply modeled as infinitely long line sources. Two-dimensional targets of arbitrary cross-section Ω are placed in the setup, and their electromagnetic scattered fields are measured for each pair of emitter–receiver set of antennas. At the cross-section of interest,

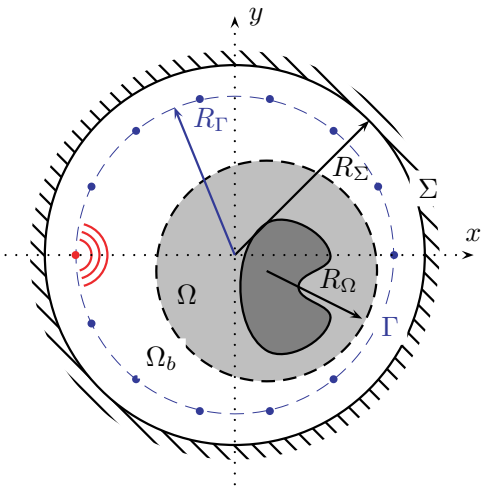

Figure 1. Cross-section of the microwave measurement setup. The emitters and receivers are positioned on the probing line Γ. The investigation domain is known to be contained into the circular part Ω with radius R_Ω. The embedding domain Ω_b is filled with a homogeneous medium of known permittivity ε_{rb}. A metallic casing Σ is enclosing the entire setup.

it is assumed that both the sample and the sources are infinite along the z-axis. Therefore, the propagation problem can be solved as a two-dimensional E scalar field problem (transverse magnetic case). Taking into account a time dependence in $\exp(+i\omega t)$, the z-component of the electric field $\vec{E}^t(\vec{r};\vec{r}_l)$ for a given emitter $\vec{r}_s = (x_s, y_s)$, with strength $J_s(\vec{r}) = \alpha\delta(\vec{r} - \vec{r}_s)$, satisfies the following set of equations:

$$\begin{cases} \Delta E_z^t(\vec{r};\vec{r}_s) + k_0^2\varepsilon_{rb}E_z^t(\vec{r};\vec{r}_s) = -J_s(\vec{r}) & \vec{r} \in \Omega_b \\ \Delta E_z^t(\vec{r};\vec{r}_s) + k_0^2\varepsilon_r(\vec{r})E_z^t(\vec{r};\vec{r}_s) = 0 & \vec{r} \in \Omega \\ E_z^t(\vec{r};\vec{r}_s) \text{ continuous everywhere} & \\ E_z^t(\vec{r};\vec{r}_s) = 0 & \vec{r} \in \Sigma, \end{cases} \tag{1}$$

where k_0 is the vacuum wavenumber, $\alpha = jk_0\sqrt{\mu_0/\varepsilon_0}$, and $\varepsilon_r(\vec{r})$ corresponds to the relative permittivity of the different materials enclosed inside the circular domain Ω. The field E_z^t is traditionally named the 'total field'. Due to the linearity of Maxwell equations, it corresponds to the summation of the incident field E_z^i, which is measured when there is no target inside the cylinder (replacing ε_r by ε_{rb} in (1)), and of the scattered field E_z^d, which corresponds to the field radiated by the currents induced inside the scatterer Ω.

Several algorithms have already been implemented to compute the field inside this specific configuration, all of them being based on the method of moments with various types of Green functions [17–19]. Here, we prefer to use a finite element method (FEM) with conformal meshing adapted to the casing configuration [20]. First, we want to introduce geometrical *a priori* information such as the shape of the target container. Therefore, a conformal mapping technique is appropriate. Second, the presence of the metallic border naturally limits the computational domain and the essential boundary condition for the electric field is very simple to express with finite element methods. Third, the size of the investigation domain has a radius of nearly 3λ, which can be computationally intensive when using the method of moments without the benefit of the convolution structure of the operator. Fourth, for the iterative

inversion schemes as presented in the following sections, the gradient computation is very simple to achieve with a finite element formalism and with limited extra computational burden. Finally, for the envisaged application, it will be helpful in the future to couple electromagnetic modeling with fluid-flow modeling within the soil column.

Our finite element model is applied to the weak form of the Helmholtz equation (1). The electrical field component is expanded onto linear P_1 basis functions [21]. A free unstructured mesh generator Gmsh [22] is used to discretize the whole domain. This step is performed in 33 s on an Intel(R) Core(TM)2 Duo T7100 @ 1.80 GHz, with 2GB of RAM used in a sequential mode. The sparse system is solved thanks to the sequential direct sparse solver SuperLu [23] with a very small computational time. Typically, for a first-order triangular mesh with 45 000 nodes and for 64 emitting antennas, the resolution time of the spare linear system takes 6 s. Comparisons using the method of moments have shown a very good agreement [24].

3. Inversion algorithm

The inverse scattering problem is stated as finding the permittivity distribution inside the microwave cylinder such that the corresponding field predicted by the model via the partial differential equation (1) matches the data. Several inversion techniques have been previously developed for solving such an ill-posed and nonlinear problem in the present configuration. Using the cavity Green function [25], the Newton–Kantorovitch algorithm with additional edge-preserving type of constraints [26] and the modified gradient method [27, 28] were developed and compared. With the de-embedding technique of [18], a quasi-Newton algorithm with an approximate line search was investigated [29].

Due to our finite-element formalism, a specific iterative approach has been developed [3]. The discrepancy criteria are defined by computing the misfit between measured fields and simulated ones

$$\mathcal{J}(\varepsilon_r) = \frac{1}{2}\sum_{s=1}^{N_s} \left\| E_z^{d,\mathrm{obs}}(\cdot;\vec{r}_s) - E_z^{d}(\varepsilon_r)(\cdot;\vec{r}_s) \right\|_{W,\Gamma}^2, \tag{2}$$

where $E_z^{d,\mathrm{obs}}$ corresponds to the scattered field measured by the emitters placed at positions $\vec{r}_s$, $s = 1, \ldots, N_s$, on the probing line Γ. The norm $\| \|_{W,\Gamma}^2$ corresponds to a weighted norm with matrix weight W which may vary from one emitter to the other one. For the present time, W is assumed to be diagonal, neglecting the coupling effects between the receivers.

In order to find a minimizer of $\mathcal{J}(\varepsilon_r)$, a sequence $\varepsilon_r^{(n)}$ is constructed using the following iterative relations:

$$\varepsilon_r^{(n)} = \varepsilon_r^{(n-1)} + \alpha^{(n)} d^{(n)},$$

where the descent direction $d^{(n)}$ is given by the standard Polak–Ribière conjugate gradient direction [30]:

$$d^{(n)} = g^{(n)} + \beta^{(n)} d^{(n-1)} \qquad \text{with} \qquad \beta^{(n)} = \frac{\langle g^{(n)} \mid g^{(n)} - g^{(n-1)} \rangle_\Omega}{\| g^{(n-1)} \|_\Omega^2},$$

where $\langle \cdot | \cdot \rangle_\Omega$ represents the inner product defined on $L^2(\Omega)$ and $g^{(n)}$ is derived from the gradient of the cost functional $\mathcal{J}\left(\varepsilon_r^{(n)}\right)$ given by [31]

$$g^{(n)} = -\nabla_{\varepsilon_r} \mathcal{J}\left(\varepsilon_r^{(n)}\right) = -k_0^2 \sum_{s=1}^{N_s} \left[E_z^{t\,(n)}(\vec{r};\vec{r}_s) P_z^{t\,(n)}(\vec{r};\vec{r}_s) \right]^*.$$

P_z^t is the so-called total adjoint field which also satisfies the Helmholtz equation inside the cavity (3), the receivers acting now as sources and sending back the difference between the simulated and measured fields at the receiver locations,

$$\begin{cases} \Delta P_z^t(\vec{r};\vec{r}_s) + k_0^2 \varepsilon_{rb} P_z^t(\vec{r};\vec{r}_s) = \sum_{r=1}^{N_r} w(\vec{r}_r;\vec{r}_s) & \\ \quad \times \left[E_z^{d,\mathrm{obs}}(\vec{r};\vec{r}_s) - E_z^d(\vec{r};\vec{r}_s)\right]^* \delta(\vec{r}-\vec{r}_r) & \vec{r} \in \Omega_b \\ \Delta P_z^t(\vec{r};\vec{r}_s) + k_0^2 \varepsilon_r(\vec{r}) P_z^t(\vec{r};\vec{r}_s) = 0 & \vec{r} \in \Omega \\ P_z^t(\vec{r};\vec{r}_s) \text{ continuous everywhere} & \\ P_z^t(\vec{r};\vec{r}_s) = 0 & \vec{r} \in \Sigma. \end{cases} \tag{3}$$

The coefficient $\alpha^{(n)}$ is computed using the closed-form solution of the minimum of the following approximated cost functional:

$$\tilde{\mathcal{J}}(\alpha) = \frac{1}{2} \sum_{s=1}^{N_s} \left\| E_z^{\mathrm{obs}}(\cdot;\vec{r}_s) - \left[E_z^{d\,(n-1)}(\cdot;\vec{r}_s) + \alpha \delta E_z^{d\,(n)}(\cdot;\vec{r}_s)\right] \right\|_{W,\Gamma}^2,$$

where $E_z^{d\,(n-1)} + \alpha \delta E_z^{d\,(n)}$ is an approximation at first order of $E_z^{d\,(n)}$ with $\delta E_z^{d\,(n)}$ satisfying the following set of equations:

$$\begin{cases} \Delta \delta E_z^{d\,(n)}(\vec{r};\vec{r}_s) + k_0^2 \varepsilon_{rb} \delta E_z^{d\,(n)}(\vec{r};\vec{r}_s) = 0 & \vec{r} \in \Omega_b \\ \Delta \delta E_z^{d\,(n)}(\vec{r};\vec{r}_s) + k_0^2 \varepsilon_{rb} \delta E_z^{d\,(n)}(\vec{r};\vec{r}_s) = -k_0^2 d^{(n)} E_z^{t\,(n-1)} & \vec{r} \in \Omega \\ \delta E_z^{d\,(n)} \text{ continuous everywhere} & \\ \delta E_z^{d\,(n)} = 0 & \vec{r} \in \Sigma. \end{cases}$$

4. Zernike polynomials representation

As the investigation domain is a circular region with radius R_Ω, the orthonormal basis functions for such a circular parameter domain are analytically known and are called the Zernike polynomials [32]. Let us point out that even if the investigation has a circular shape, it is not necessarily centered with respect to the casing. The Zernike polynomials are defined in cylindrical coordinates $\vec{r} = (\rho, \theta)$, with respect to the center (x_c, y_c) of the investigation domain, by

$$Z_m^l(\vec{r}) = R_m^l\left(\frac{\rho}{R_\Omega}\right) \exp(\mathrm{i}l\theta) \tag{4}$$

where the radial component $R_l^m(\rho)$ is defined by

$$R_m^l(\rho) = \sum_{p=0}^{(m-l)/2} \frac{(-1)^p (m-p)!}{p!\left(\frac{m+l}{2}-p\right)!\left(\frac{m-l}{2}-p\right)!} \rho^{m-2p}, \tag{5}$$

where $m \geqslant 0$, $l \in \mathbb{Z}$ are integers, $m \geqslant |l|$ and $m - |l|$ is even. Choosing a global representation for the permittivity profile implies that the unknowns are now the coefficients $\{a_m^l\}$ such that

$$\varepsilon_r(\vec{r}) = \sum_{l,m} a_m^l Z_m^l(\vec{r}). \tag{6}$$

Using the chain rule derivation principle and the above linear relationship, the derivative of the cost functional according to a_l^m is computed by simply projecting the gradient onto the basis expansion. As the Zernike polynomials form an orthogonal basis, we obtain

$$\nabla_{a_m^l} \mathcal{J} = k_0^2 \left\langle \sum_{s=1}^{N_s} E_z^{t\,(n)}(\cdot;\vec{r}_s) P_z^{t\,(n)}(\cdot;\vec{r}_s) \middle| Z_l^m \right\rangle_\Omega. \tag{7}$$

Therefore, in the previous Polak–Ribière conjugate gradient scheme, the gradient $g^{(n)}$ is now replaced by the following relationship:

$$g^{(n)} = -k_0^2 \sum_{l,m} \left\langle \sum_{s=1}^{N_s} E_z^{t\,(n)}(\cdot;\vec{r}_s) P_z^{t\,(n)}(\cdot;\vec{r}_s) \middle| Z_l^m \right\rangle_{\Omega} Z_l^m. \tag{8}$$

The rest of the iterative scheme remains identical, both for the estimation of $d^{(n)}$ and $\alpha^{(n)}$. Apart from the evaluations of the Zernike radial components, the extra computational burden is rather limited when using such a global representation. The number of coefficients to retrieve is now related to the order of the Zernike representation. The 'order' of the Zernike polynomial expansion is defined as the maximal order achieved by the radial component polynomials, i.e., a representation of order 4 implies that polynomials up to ρ^4 will participate in the summation of (6). The number N_a of associated coefficients a_l^m for a given order N_o is given by

$$N_a = 2\sum_{q=0}^{N_o} \left(\left\lfloor \frac{q}{2} \right\rfloor + 1 \right) = \begin{cases} 2(M_o+1)^2 & \text{if} \quad N_o = 2M_o \\ 2(M_o+1)(M_o+2) & \text{if} \quad N_o = 2M_o + 1. \end{cases} \tag{9}$$

The nth term will provide a combination of polynomials up to $\rho^n \exp(\mathrm{i}n\theta)$. Therefore, when n is small, the radial oscillations as well as the angular oscillations are limited. The first terms in the expansion correspond to smooth profiles, while the higher order ones present profiles with rapidly varying oscillations due to the polynomial terms in ρ. By truncating the Zernike expansion, it is possible to restrain the spatial behavior of the permittivity map and provide a regularized solution of the inverse problem.

5. Numerical results

In this section, we report examples of reconstructions of dielectric samples to illustrate the efficiency of the Zernike polynomials representation. To this hand, we take advantage of the experimental microwave scanner which is presently developed at the Institut Fresnel [17] and which presents the same circular configuration as previously described. The 64 biconical antennas are equally spaced on the circle Γ of radius $R_\Gamma = 27.6$ cm. These biconical antennas have been specifically designed in order to radiate at 434 MHz inside water. A microwave multiplexer/demultiplexer enables us to select one after the other the emitting antenna, while the other antennas sequentially act as receivers. A 64×63 scattering matrix is then obtained, which contains information on the target placed inside the tank. The metallic boundary is placed at $R_\Sigma = 29.5$ cm. The embedding liquid is standard tap water and its permittivity has been measured with a coaxial open-ended probe connected to a network analyzer [33]. A permittivity of $\varepsilon_{rb} = 80.3 - 3.7j$ has been obtained at room temperature. The associated wavelength is $\lambda_b = 7.7$ cm and the overall setup has a diameter of nearly 8λ.

In all the following examples, the initial profile is taken constant throughout the investigation area, with the same permittivity value as the embedding liquid permittivity. In order to evaluate the effectiveness of each process, an error misfit function related to the reconstructed image is defined by

$$\mathcal{F} = \frac{1}{N} \sum_{i=0}^{N} \left| \varepsilon_r^{(n)}(x_i, y_i) - \varepsilon_r^{\text{true}}(x_i, y_i) \right|^2, \tag{10}$$

where N corresponds to the number of discretization cells inside the investigation domain. For an investigation domain with a radius of 10 cm, there are around 11 000 cells. This image cost functional is an indicator of the quality of the reconstructed permittivity profile.

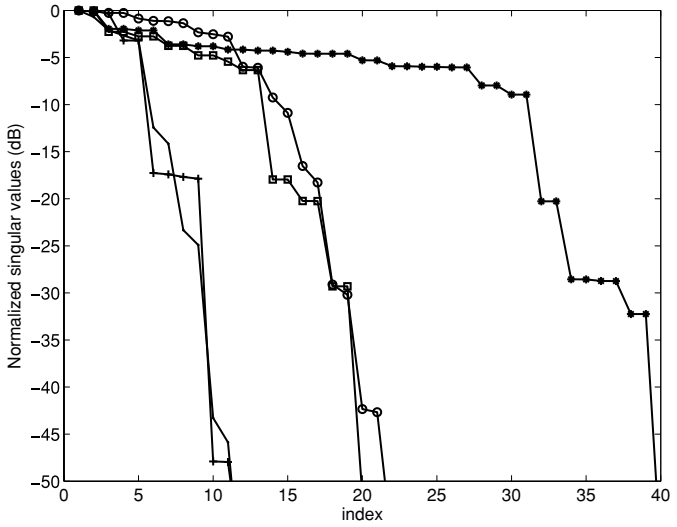

Figure 2. The normalized singular spectrum σ_i/σ_1 plotted in dB scale for a circular target of permittivity $\varepsilon_r = 60 - 5j$ which is placed inside the tank at several locations and with several radii: (——) $r_c = 4.4$ cm and $y_c = 0$ cm, (+) $r_c = 4.4$ cm and $y_c = -8$ cm, (□) $r_c = 10$ cm and $y_c = 0$ cm, (○) $r_c = 10$ cm and $y_c = -10$ cm, (⋆) $r_c = 20$ cm and $y_c = 0$ cm.

5.1. Number of independent data and Zernike polynomial order truncation

It is of interest to investigate at first the amount of independent information available in the present configuration. If we were in a free space configuration, for a circular domain under test and a circular observation domain, it can be proved [34] that the scattered field corresponding to a given incident field can be accurately represented with a number of Fourier harmonics given by $2B_{\text{th}}^{\text{free}}$, where $B_{\text{th}}^{\text{free}}$ is the theoretical bandwidth of the scattered field given by $B_{\text{th}}^{\text{free}} = k_b R_\Omega$ in a free space configuration. From reciprocity, the number of nonsuperdirective independent incident fields impinging on the domain under test is $2B_{\text{th}}^{\text{free}}$ as well. Therefore, in a free space configuration, the scattered field can be accurately represented by a number of samples given by $\left(2B_{\text{th}}^{\text{free}}\right)^2$, where only half of these samples are actually independent [5].

In the scanner configuration, the theoretical bandwidth is of course different and its closed-form expression will be addressed in other work [12]. For the time being, the numerical bandwidth is numerically determined, with the benefit of taking into account the signal-to-noise ratio.

To exactly determine the maximum order of the Zernike polynomial associated with the current configuration, the following numerical experiment is performed. The field scattered by a circular target with a given permittivity of $\varepsilon_r = 60 - 5j$ is computed for several radii r_c and for several eccentricity positions $(0, y_c)$ along the y-axis. Indeed, it can be shown that the amount of relevant information is not depending at first order from the permittivity of the target but only from its shape [34]. The amount of available information is determined by the rank of the scattering matrix K, which is traditionally employed in time reversal techniques [35], and whose elements are defined as $K(s, r) = E_z^d(\vec{r}_s; \vec{r}_r)$, for all emitters positions $\vec{r}_s$ and receivers positions $\vec{r}_s$. The singular value spectra, which have all been normalized with respect to their first singular value, are then plotted in figure 2. As expected, it is clearly visible that the singular values rapidly decrease and that the behavior of the decrease is linked

Table 1. Number of singular values which have some influence on the signal.

r_c (cm)	y_c (cm)	Nb of σ_i	$2B_{\text{th}}^{\text{free}}$
4.4	0	11	8
4.4	−8	11	8
10	0	20	18
10	−10	22	18
20	0	39	34

to the radius of the target but not necessarily to its position inside the tank. The singular value spectra resemble the Bode plot of low-pass filters and this explains why only a limited amount of information can be retrieved from the scattered field. Only the first singular values have influence on the signal subspace (table 1). The behavior of the K matrix spectrum for the casing environment seems to be very similar to the spectrum that would be obtained in a free space environment, as shown by the similarity between the last two columns of table 1. With the singular value spectrum, the numerical bandwidth B_{noise} can be numerically estimated by truncating the spectrum according to the signal-to-noise ratio. Following the free space configuration reasoning, the number of degree of freedom can be computed with

$$\text{DOF}_{\text{noise}} = \frac{(2B_{\text{noise}})^2}{2}. \tag{11}$$

This number of independent data turns out to be much smaller than the number of discretization cells and the problem is heavily under-determined if one is interested in retrieving the permittivity value in each cell. To avoid local minima and numerical instabilities, the reduction of the number of unknowns is of great importance. This can be performed thanks to the Zernike polynomial expansion and by limiting the number of terms in the expansion with the amount of available information.

As the number N_a of Zernike coefficients must be smaller or equal to DOF_{noise}, using equation (9) we get

$$N_o = 2(B_{\text{noise}} - 1). \tag{12}$$

As expected, the bandwidth B_{noise} as well as the maximum order of the Zernike polynomial decrease with the signal-to-noise ratio, meaning that less and less details can be recovered if the noise level is too high. Indeed, the first order terms correspond to smooth features as the higher terms provide refined spatial details on the scatterer.

5.2. Target reconstruction without projection

The following experiment has been performed by placing a cylindrical plastic pipe inside the experimental setup. The pipe is 1 mm thick and is made with PVC, whose permittivity has been measured with the coaxial cell EpsiMu [36]. A lossless permittivity of 2.75 has been found. The pipe was filled with a liquid, which consisted in a mixture of propanediol, water and salt [17]. The permittivity of the liquid has been measured with the coaxial open-ended probe and the obtained value was $\varepsilon_r = 58.4 - 44.5j$. The cylinder has been positioned inside the tank at approximately $x_c = 0$ cm and $y_c = -8$ cm and its radius was 4.4 cm (figure 3). The inversion algorithm described in section 3 has been applied. The scheme has been stopped after 100 iterations and the permittivity maps obtained when using a large and centered investigation area of 20 cm of radius are presented in figure 4.

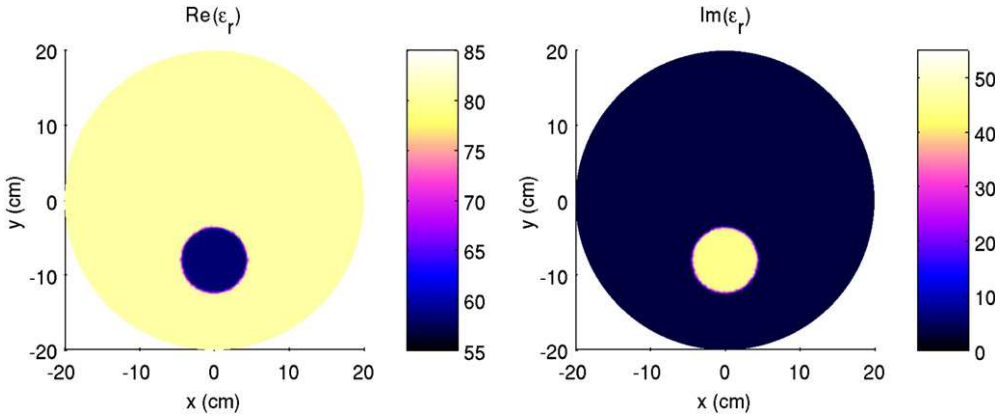

Figure 3. Real part (left) and imaginary part (right) of the exact permittivity map. A cylindrical pipe filled with a liquid of permittivity $(58.4 - 44.5j)$ is placed inside the scanner. The embedding medium is standard tap water.

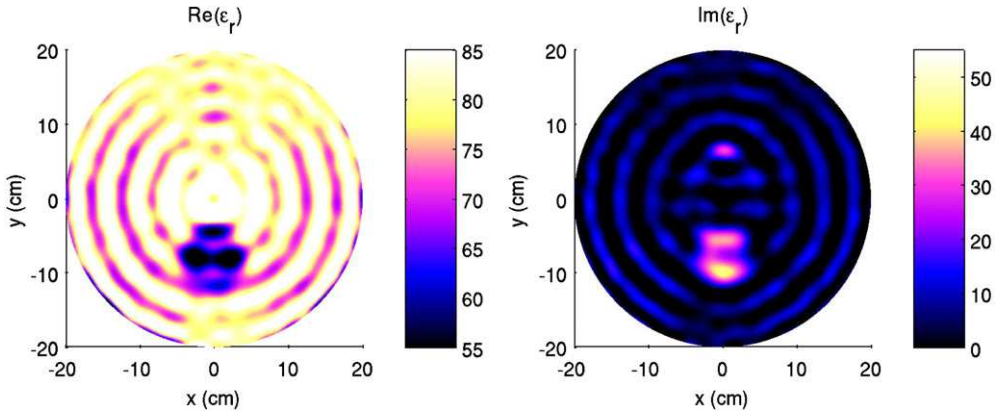

Figure 4. Real part (left) and imaginary part (right) of the permittivity map reconstructed after 100 iterations from a measured scattered field. The value of the permittivity in each discretization cell is taken as an unknown in the inversion scheme. A large centered investigation area of radius 20 cm is taken.

This image allows us to locate the target and to redefine the investigation area in the vicinity of the target. A new excentered investigation area of radius 10 cm is defined, centered at $(0, -10)$ cm. The cost functional $\mathcal{J}$ is plotted in figure 5(a) and it is clearly visible that after a while, this function is no more decreasing. The image cost functional $\mathcal{F}$ is also computed and is plotted in figure 5(b). This image cost functional has a different behavior as it first decreases and after 13 iterations, it increases again. This can be interpreted by the fact that, in the beginning of the inversion process, the main trends of the permittivity map are properly retrieved by fitting the low spatial frequency content of the scattered field. Afterward, the scheme tries to fit the high spatial frequency components which unfortunately are mainly due to the noise. The permittivity map obtained after 100 iterations is plotted in figure 6.

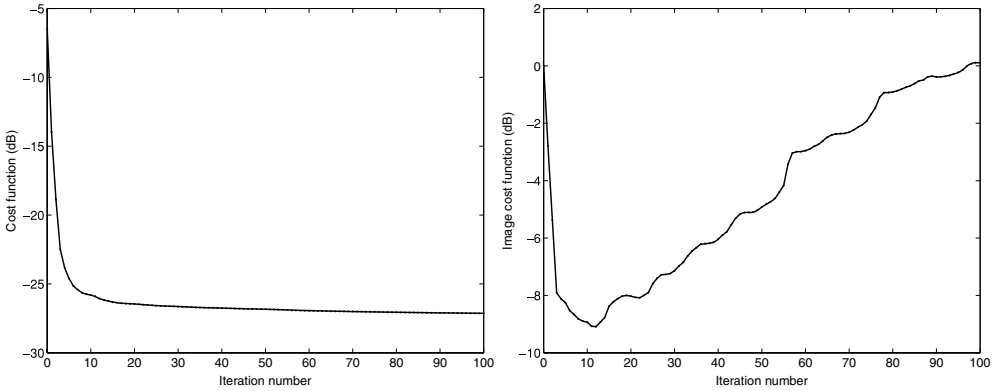

(a) (b)

Figure 5. (a) Cost function $\mathcal{J}$ and (b) image cost function $\mathcal{F}$ evolution along the iterations. The value of the permittivity in each discretization cell is taken as an unknown in the inversion scheme. The initial guess is homogeneous and has the permittivity value of the embedding liquid. The investigation area has been reduced to a circular area of radius 10 cm, centered at $(0, -10)$ cm.

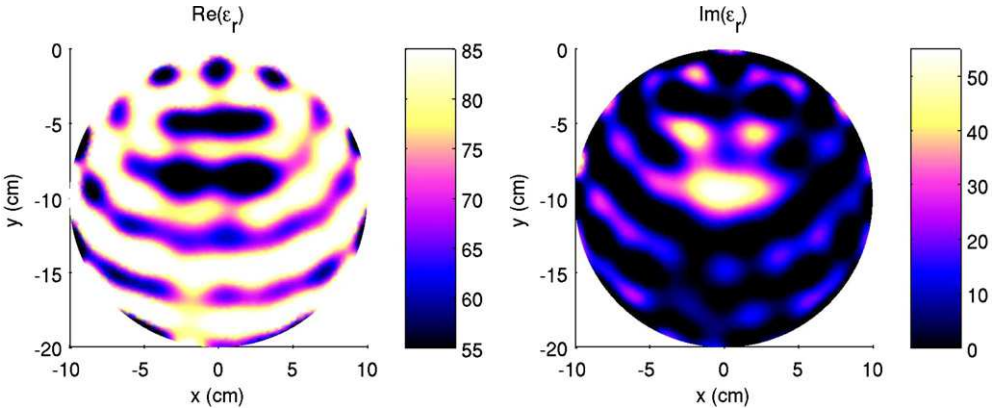

Figure 6. Real part (left) and imaginary part (right) of the permittivity map reconstructed after 100 iterations from a measured scattered field. The value of the permittivity in each discretization cell is taken as an unknown in the inversion scheme. The investigation area of radius 10 cm is centered at $(0, -10)$ cm.

To illustrate the noise effect, the permittivity profiles reconstructed at the iteration 13 and at the iteration 100 are plotted in figure 7, and indeed, the oscillations are much more visible at the end of the iterative process, even if the overall shape of the target has not improved much. The key point in that case is to be able to stop the iterative process at the right iteration in order to avoid these perturbations. Unfortunately, the cost functional $\mathcal{J}$ provides no clue to the correct stopping criterion. One possible solution would be to stop when $\mathcal{J}$ is reaching a plateau but in the present configuration, this would stop the iterative process after reaching the best image solution. Another solution would be to stop the iterative process according to the signal-to-noise ratio. As shown in figure 8, the signal-to-noise ratio is unfortunately low and this would imply stopping the iterations before reaching the best image solution.

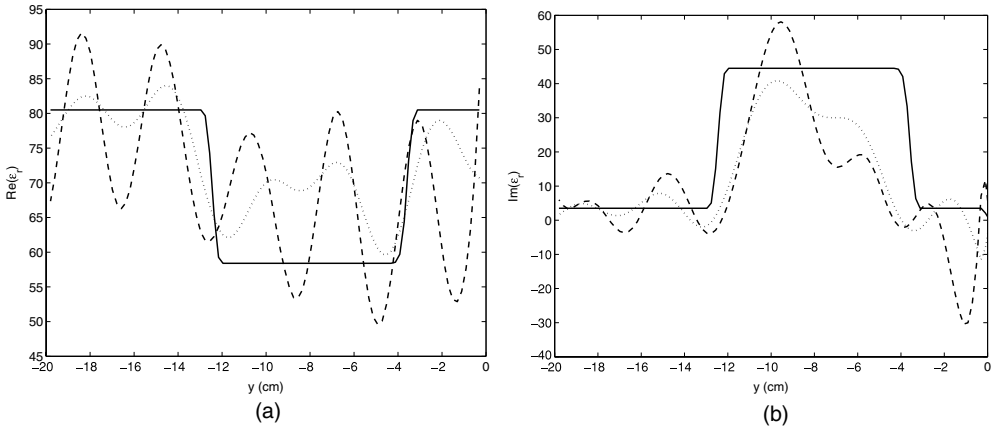

Figure 7. Real part (a) and imaginary part (b) of the permittivity profile reconstructed after 13 iterations (· · · · · ·) and 100 iterations (- - - -). The profile has been obtained along the y-axis at $x = 0$ cm. The exact profile is also plotted (——). In the inversion process, the permittivity value in each discretization cell is taken as an unknown, the investigation area is the excentered disk of radius 10 cm.

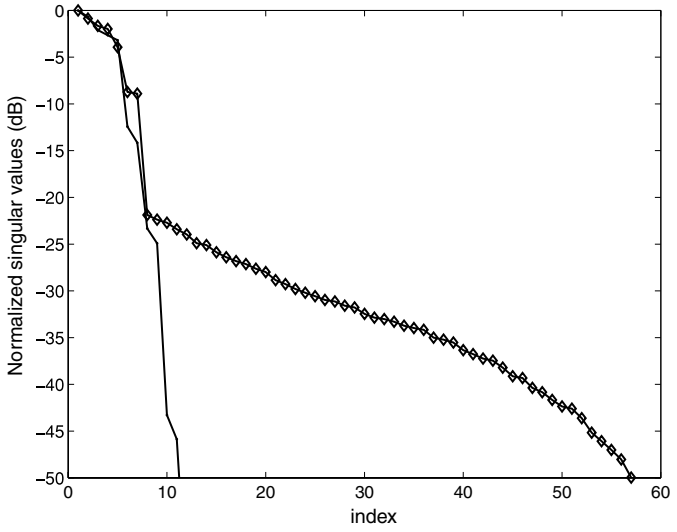

Figure 8. A normalized singular value spectrum in dB scale of the scattering matrix K for a circular target positioned at $(0, -8)$ cm and with radius of 4.4 cm obtained with (——) simulated fields and (◊) measured fields.

5.3. Target reconstruction with Zernike projection

According to the criterion described in section 5.1, the maximum retrievable order of the Zernike polynomials can be estimated for the current setup. Figure 8 shows the comparison between the simulated singular value spectrum and the measured one. As expected, due to the experimental noise level which corrupts the spectrum, there are less amount of information that can be retrieved from the measured signal than from the simulated one. This is visible

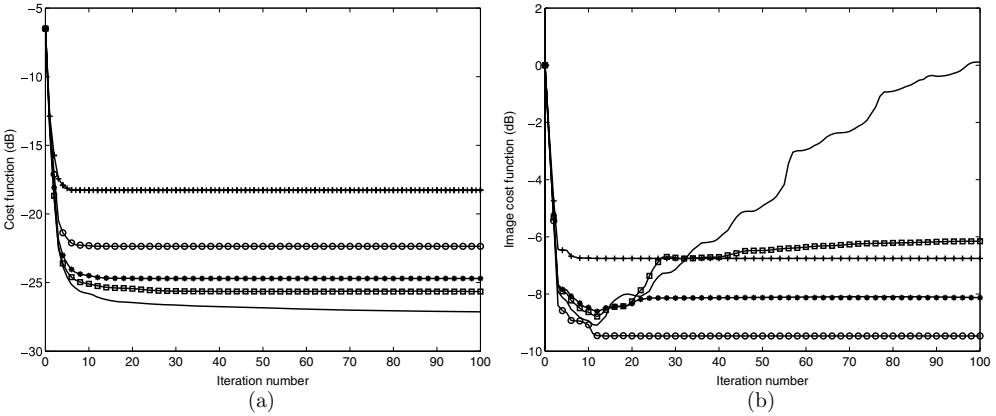

Figure 9. (a) Cost function $\mathcal{J}$ and (b) image cost function $\mathcal{F}$ evolution along the iterations for various order of the Zernike polynomial representation: (+) $N_o = 4$, (○) $N_o = 6$, (∗) $N_o = 8$, (□) $N_o = 10$, (——). No projection as in figure 5.

in the diverging behavior appearing after the 8th singular value. After such a value, there is no way to distinguish the singular values which belong to the signal subspace or to the noise subspace. When the threshold is at 8 and according to (12), the maximum order of the Zernike polynomials is 6. The number of unknowns has been drastically reduced, going from roughly 11 000 to 32. To see the effect of the threshold on the Zernike polynomials order and its adequacy with the prediction from the singular value spectra, several orders of Zernike polynomials have been used in the inversion process, going from 4 to 10.

The cost functionals $\mathcal{J}$ and $\mathcal{F}$ are plotted in figure 9(a) and (b). On one hand, if the Zernike polynomial order is too small ($N_o = 4$), the cost functional $\mathcal{J}$ is reaching a plateau sooner than in the other cases. Indeed, the selected representation does not provide enough description parameters to cope with the spatial variations of the exact permittivity map. On the other hand, if the Zernike polynomial order is too large ($N_o = 10$), the image cost functional $\mathcal{F}$ presents the same behavior than the standard inversion scheme. In that case, there are too many description parameters which allow us to fit the noise contained in the measured scattered field. Finally, as guessed with the singular value spectrum, $N_o = 6$ is the best option because the two cost functionals $\mathcal{F}$ and $\mathcal{J}$ reach a stable value for the entire end of the iterative process. In that case, there is no need to define a suitable stopping criterion as even after 100 iterations, the reconstructed profile will be close to the true profile.

The associated reconstructed permittivity map obtained with $N_o = 6$ is given in figure 10 and the oscillations which were present in figure 4 have been removed when using an appropriate Zernike representation. With $N_o = 10$ (figure 11), the oscillations are present even if the result is still better than without the Zernike representation.

The profile plots of the final reconstructions are presented in figure 12. The small order profile ($N_o = 4$) is nothing but a smooth version of the exact profile, while the large order profile ($N_o = 10$) picks better the imaginary value of the target permittivity, but has higher spatial oscillations on the rest of the investigation area. Finally, selecting ($N_o = 6$) provides a good compromise between the two extreme behaviors. It implies that the degree of freedom computed with (12) is indeed a good indicator for thresholding the Zernike polynomials expansion. Thus, imposing a Zernike expansion combined with the degree of freedom thresholding criterion provides an unsupervised regularization scheme which necessitates

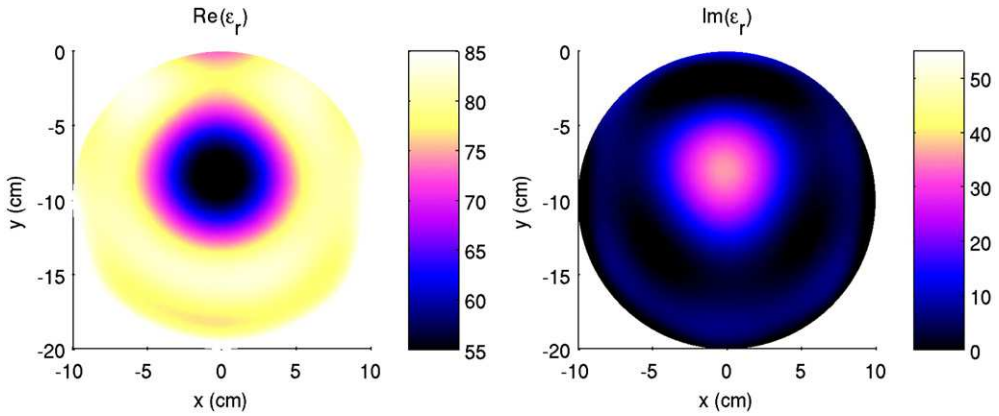

Figure 10. Real part (left) and imaginary part (right) of the permittivity map reconstructed after 100 iterations from a measured scattered field. The permittivity profile has been projected onto the Zernike polynomial basis with $N_o = 6$. The initial guess is again the homogeneous background. A circular investigation area of 10 cm radius centered at $(0, -10)$ cm is used.

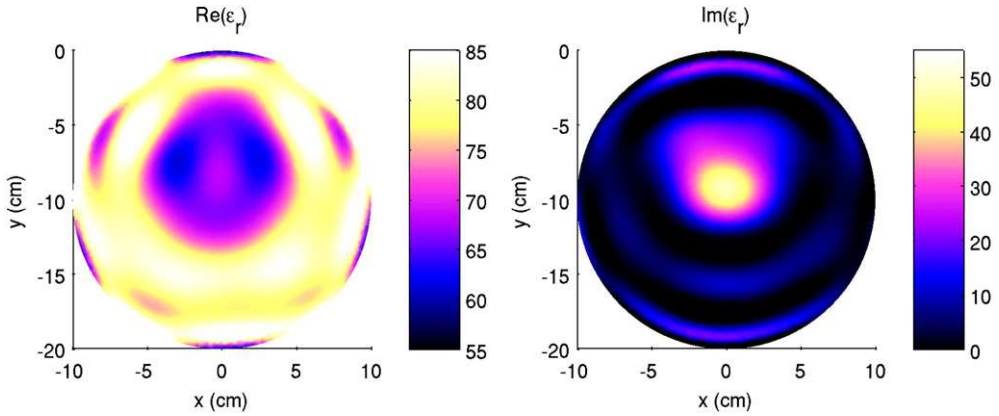

Figure 11. Real part (left) and imaginary part (right) of the permittivity map reconstructed after 100 iterations. The permittivity profile has been projected onto the Zernike polynomial basis with $N_o = 10$. The associated scattered field has been measured in the microwave cylindrical scanner of the Institut Fresnel. The initial guess is again the homogeneous background. A circular investigation area of 10 cm radius centered at $(0, -10)$ cm is used.

very limited *a priori* information. It provides the best solution in terms of the image cost functional and also has the nice feature of being stable throughout the iterative process. As the image cost functional and the data cost functional have the same behavior, it is possible to use the data cost functional to determine a correct stopping criterion. The simplest way is to detect when the data cost functional is reaching a plateau. The nice feature of the Zernike expansion is the fact that now the obtained solution is indeed the best image which can be obtained for the selected threshold.

5.4. Imaging non-circular targets

To highlight the fact that the *a priori* information depend on the shape of the investigation domain, but not on the shape of the scatterers, the following numerical experiment has

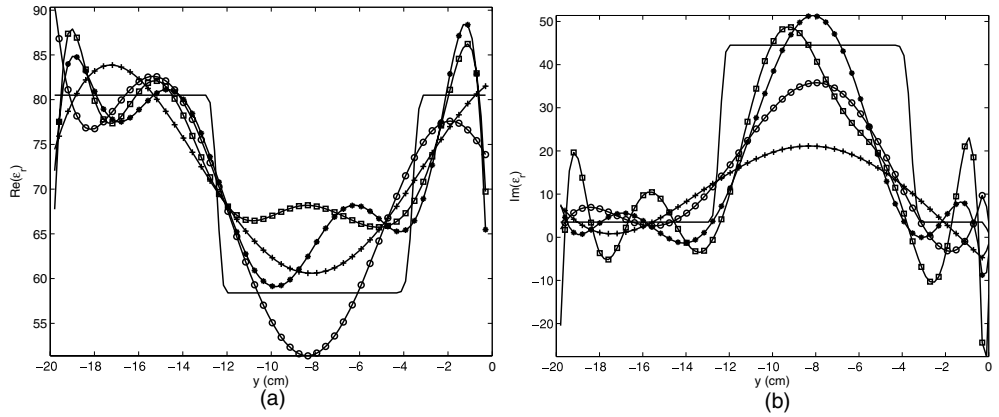

Figure 12. Real part (a) and imaginary part (b) of the permittivity profile reconstructed after 100 iterations. The profile has been obtained along the y-axis at $x = 0$ cm. Several orders of the Zernike polynomial representation have been tested: (+) $N_o = 4$, (○) $N_o = 6$, (∗) $N_o = 8$, (□) $N_o = 10$, (——) exact profile.

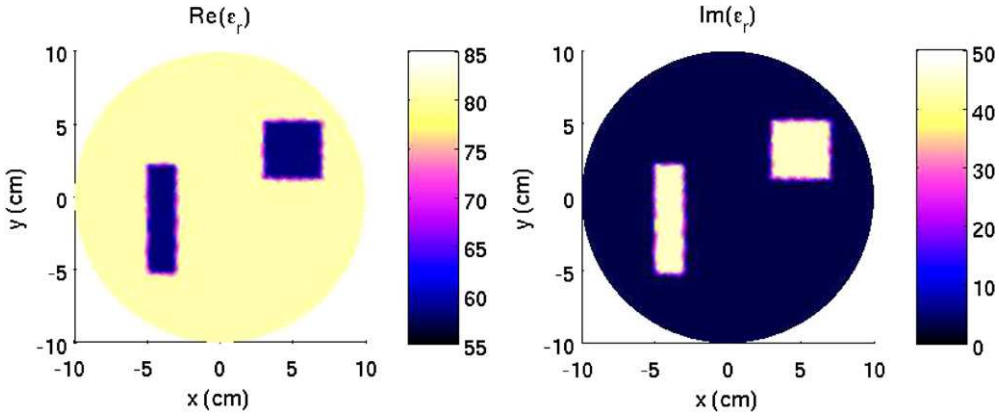

Figure 13. Real part (left) and imaginary part (right) of the exact permittivity map when two rectangles of permittivity $(58.5 - 44.5j)$ have been placed inside the scanner. The embedding medium is standard tap water. The first rectangle with dimensions (2×7) cm is centered at $(-4, 1.5)$ cm. The second rectangle with dimensions (4×4) cm is centered at $(5, 3.25)$ cm.

been performed. Two rectangles, with relative permittivity $\varepsilon_r = 58.5 - 44.5j$, are placed inside the water. The first one is of rectangular form with a length of (2×7) cm and is centered at $(-4, -1.5)$ cm. The second one is a square of length (4×4) cm, centered at $(5, 3.25)$ cm (figure 13). 10 dB of white Gaussian noise has been added to the scattered field and the mesh has been changed between the forward problem and the inverse problem. The rank of the scattering matrix provides a numerical bandwidth of $B_{\text{noise}} = 7$, and a maximal order of 12 for the Zernike expansion. The maps obtained after 100 iterations are presented in figure 14 when the permittivity in each cell is searched for, and in figure 15 when the Zernike expansion is used with the threshold preconized by the scattering matrix rank. As expected, the regularized permittivity map has less oscillations than the un-regularized one. Even if it does not properly recover the square shape, it properly resolves the two targets. More spatial

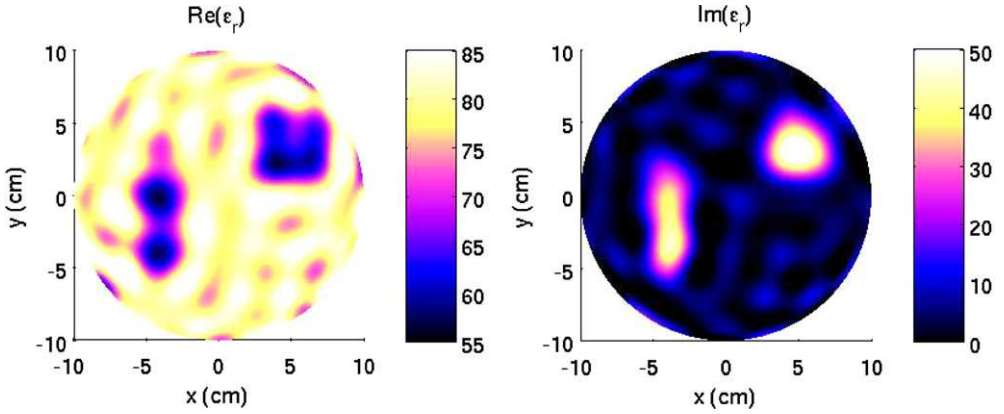

Figure 14. Real part (left) and imaginary part (right) of the permittivity map reconstructed after 100 iterations from a synthetic scattered field. White Gaussian noise with a signal-to-noise ratio of 10 dB has been added to the scattered field. The value of the permittivity in each discretization cell is taken as an unknown in the inversion scheme. The investigation area is a disk of radius 10 cm, centered at (0, 0) cm.

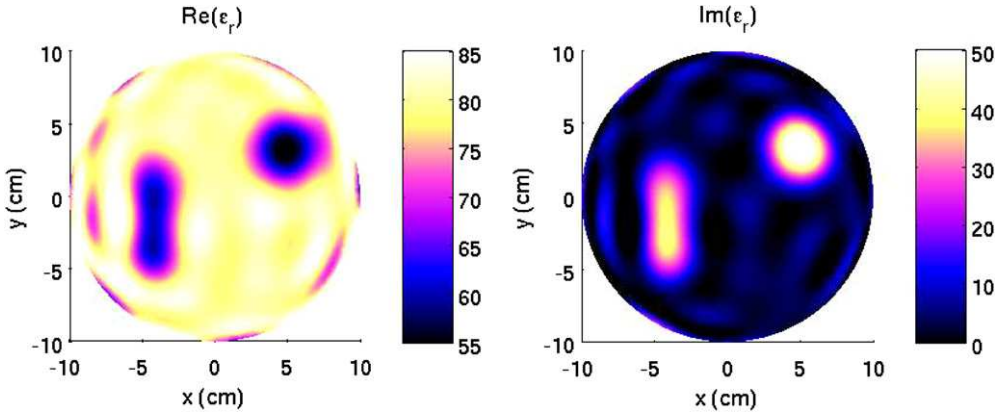

Figure 15. Real part (left) and imaginary part (right) of the permittivity map reconstructed after 100 iterations from a synthetic scattered field. White Gaussian noise with a signal-to-noise ratio of 10 dB has been added to the scattered field. The permittivity profile has been projected onto the Zernike polynomial basis with $N_o = 12$. The initial guess is the homogeneous background. The investigation area is a disk of radius 10 cm, centered at (0, 0) cm.

details can be introduced by adding more terms in the expansion but also by adding more noise in the reconstructed map.

6. Conclusion

In the present paper, we have introduced an appropriate way of representing the unknown permittivity profile which takes benefit of two very simple and not very constraining pieces of *a priori* information: (i) the investigation domain is circular, (ii) there is only a limited number of parameters that can be retrieved from the measured fields. The first piece of information

has been used via a Zernike polynomials expansion. The second piece of information has been used to define a valid criterion for thresholding the expansion and providing therefore an unsupervised regularization scheme. The associated reconstructed permittivity maps are strongly improved, as shown with image cost functional comparisons. Moreover, when using a Zernike representation, the iterative scheme can now easily be stopped when the data misfit cost functional is reaching a plateau and this will correspond for sure to the best reconstructed image. The algorithm has been tested against synthetic data as well as experimental data, which have been measured in the microwave cylindrical scanner currently developed at the Institut Fresnel. The obtained reconstructed images have also shown that the regularization scheme is correctly robust to noise.

Such a Zernike representation is not restricted to the microwave scanner environment described herein but can be applied as long as a circular investigation domain is chosen. This regularization scheme can be combined with other types of *a priori* information. For example, an additional Tikhonov-like constraint term can be added in the cost functional. As well, if the targets are known to be homogeneous by part, this can be incorporated inside the inversion algorithm thanks to a combined Zernike and level-set formalism [37].

As mentioned earlier, the image moments are based on the Zernike polynomials. It could be of interest to investigate the amount of information contained by such moments in the present configuration in order to provide some global trends of the soil moisturizing process, such as, for example, the preferential directions of absorption.

Finally, by reducing the number of unknowns, we can now tackle more easily second-order gradient based iterative schemes, such as Gauss–Newton or Full–Newton algorithms. Indeed, the size of the Hessian matrices will be small enough to be numerically computed and stored.

Acknowledgments

The authors would like to thank Professor L Crocco from IREA-CNR, Napoli, Italy, for very fruitful discussions on the notion of degrees of freedom. They would also like to acknowledge the financial support of the ANR 'Jeunes Chercheurs' grant for the CESAR project no-JCJC06-141021 and INTAS grant no-06-1000017-8909.

References

[1] Catapano I, Crocco L, D'Urso M and Isernia T 2007 On the effect of support estimation and of a new model in 2d inverse scattering problems *IEEE Trans. Antennas Propag.* **55** 1895–9

[2] Bucci O M, Capozzoli A and D'Elia G 2003 A novel approch to scatterers localization problem *IEEE Trans. Antennas Propag.* **51** 2079–90

[3] Lencrerot R, Litman A, Tortel H and Geffrin J-M 2007 A microwave imaging circular setup for soil moisture information *IGARSS Conf. Proc.* pp 4394–7

[4] Bucci O and Isernia T 1997 Electromagnetic inverse scattering: retrievable information and measurement strategies *Radio Sci.* **32** 2123–38

[5] D'Urso M, Belkebir K, Crocco L, Isernia T and Litman A 2008 Phaseless imaging with experimental data: facts and challenges *J. Opt. Soc. Am.* A **25** 271–81

[6] Donelli M, Franceschini D, Massa A, Pastorino M and Zanetti A 2005 Multi-resolution iterative inversion of real inhomogeneous targets *Inverse Problems* **21** S51–63

[7] Isernia T, Pascazio V and Pierri R 2001 On the local minima in a tomographic imaging technique *IEEE Trans. Geosci. Remote Sens.* **39** 1596–607

[8] Baussard A, Miller E L and Premel D 2004 Adaptative b-spline scheme for solving an inverse scattering problem *Inverse Problems* **20** 347–65

[9] Miller E L and Willsky A S 1996 Wavelet-based methods for the nonlinear inverse scattering problem using the extended born approximation *Radio Sci.* **31** 51–66

[10] Bernardi C and Maday Y 1992 *Approximations spectrales de problèmes aux limites elliptiques* (Paris: Springer)

[11] Bucci O M, Crocco L and Isernia T 1999 Improving the reconstruction capabilities in inverse scattering problems by exploitation of close-proximity setups *J. Opt. Soc. Am.* A **16** 1788–98

[12] Crocco L and Litman A 2008 On embedded microwave imaging systems: retrievable information and design guidelines unpublished

[13] Cerjan C 2007 Zernike-bessel representation and its application to Hankel transforms *J. Opt. Soc. Am.* A **24** 1609–16

[14] Fang Q, Meaney P M and Paulsen K D 2006 Singular value analysis of the Jacobian matrix in microwave image reconstruction *IEEE Trans. Antennas Propag.* **54** 2371–80

[15] Teague M R 1980 Image analysis via the general theory of moments *J. Opt. Soc. Am* **70** 920–30

[16] Xia T, Zhu H, Shu H, Haigron P and Luo L 2007 Image description with generalized pseudo-zernike moments *J. Opt. Soc. Am.* A **24** 50–9

[17] Geffrin J-M 1995 Imagerie microonde: Etude d'un scanner a 434 MHz pour applications biomedicales *PhD Thesis* (Univ. Paris XI, Orsay, France)

[18] Tijhuis A G and Franchois A 2001 A two-dimensional microwave imaging algorithm for a complex environment: preliminary results *Proc. URSI Int. Electromagnetic Theory Symp.* pp 445–7

[19] van den Berg P M and Fokkema J T 2003 Removal of undesired wavefields related to the casing of a microwave scanner *IEEE Trans. Microw. Theory Tech.* **51** 187–92

[20] Cmielewski O, Tortel H, Litman A and Saillard M 2007 A two-step procedure for characterizing obstacles under a rough surface from bistatic measurements *IEEE Trans. Geosci. Remote Sens.* **45** 2850–8

[21] Jin J 2002 *finite Element Method in Electromagnetics* (New York: Wiley-Interscience)

[22] Geuzaine C and Remacle J-F 2007 Gmsh reference manual: a three-dimensional finite element mesh generator with built-in pre- and post-processing facilities *Technical Report* (http://www.geuz.org/gmsh)

[23] Demmel J W, Eisenstat S C, Gilbert J R, Li X S and Liu J W H 1999 A supernodal approach to sparse partial pivoting *SIAM J. Matrix Anal. Appl.* **20** 720–55

[24] Lencrerot R 2008 Outils de modélisation et d'imagerie pour un scanner micro-onde: Application au contrôle de la teneur en eau d'une colonne de sol *PhD Thesis* (Univ. Paul Cezanne, Marseille, France)

[25] Tyras G 1970 *Radiation and Propagation of Electromagnetic Waves* (New York: Academic)

[26] Elissalt J M 1995 Imagerie microonde: Reconstruction quantitative bidimensionnelle—Applications au domaine biomédical *PhD Thesis* (Univ. Paris XI, Orsay, France)

[27] Joisel A, Geffrin J M, Elissalt J M, Belkebir K, Joachimowicz N and Bolomey J C 1995 Iterative 2D reconstruction algorithms for microwave active imaging systems *IEE Colloquium Appl. Microwaves Medecine* **28** 9/1–4

[28] Pichot Ch, Lobel P, Blanc-Féraud L, Barlaud M, Belkebir K, Elissalt J M and Geffrin J M 1997 Gradient and Newton–Kantorovitch methods for microwave tomography *Inverse Problems in Medical Imaging and Nondesctructive Testing* ed H Engl, A Louis and W Rundell (New-York: Springer)

[29] Franchois A and Tijhuis A G 2003 A quasi-Newton reconstruction algorithm for a complex microwave imaging scanner environment *Radio Sci.* **38** 8011

[30] Nocedal J and Wright S J 2006 *Numerical Optimization* (New York: Springer)

[31] Litman A and Belkebir K 2006 Two-dimensional inverse profiling problem using phaseless data *J. Opt. Soc. Am.* A **23** 2737–46

[32] Born M and Wolf E 1959 *Principles of Optics* (New York: Pergamon)

[33] Pichot C, Franchois A, Joisel A and Bolomey J-C 1998 Quantitative microwave imaging with a 2.45-GHz planar microwave antenna *IEEE Trans. Med. Imag.* **17** 550–61

[34] Bucci O, Gennarelli C and Savarese C 1998 Representation of electromagnetic fields over arbitrary surfaces by a finite and nonredundant number of samples *IEEE Trans. Antennas Propag.* **46** 351–9

[35] Micolau H, Tortel H and Saillard M 1999 Decomposition of the time reversal operator for electromagnetic scattering *J. Electromagn. Waves Appl.* **13** 687–719

[36] Sabouroux P and Boschi P 2005 Epsimu: a new microwave materials measurement kit *Revue de l'Electricité et de l'Electronique* **10** 58–62

[37] Litman A, Lencrerot R, Tortel H and Geffrin J-M 2008 Level-set imaging in a metallic cylindrical cavity configuration *Inverse Problems: Modeling and Simulation Conf. (Fethiye, Turkey)* pp 114–5

A Two-Step Procedure for Characterizing Obstacles Under a Rough Surface From Bistatic Measurements

Octavien Cmielewski, Hervé Tortel, Amélie Litman, *Member, IEEE*, and Marc Saillard, *Member, IEEE*

***Abstract*—A two-step electromagnetic detection procedure is proposed to characterize a dielectric obstacle buried at low depth under a rough surface from single-frequency and multistatic data. First, we have developed, in the framework of the small perturbation theory, a correlation procedure of the scattered field, which enables us to recover an estimation of the roughness profile. This method is tested for various cases with synthetic data provided by a rigorous boundary integral solver. Second, the obtained surface profile is introduced into the numerical simulation thanks to a finite-element code. An iterative process is then used, based on a level-set formulation, to obtain the shape of the buried target. The influence of the prior step on the accuracy of the reconstruction of the target is studied *via* various criteria and for different configurations.**

***Index Terms*—Correlation, electromagnetic scattering, inverse problems, rough surfaces, shape optimization.**

I. Introduction

THE PROBLEM of detecting, localizing, and characterizing buried objects in natural environments using electromagnetic waves has received great interest over the past decades. In this context, one of the most challenging problems is the clearance of antipersonal land mines shallowly buried in natural soils.

The associated electromagnetic problem in this context is very challenging since we are more specifically faced to: 1) aspect limited data (in general, the scattered field is measured along a line of finite length above the ground); 2) near-field scattering from the irregularly shaped interface (roughness of the air–soil interface); and 3) obstacle shallowly buried (which is typically the case for antipersonal land mines). This last point increases the difficulty of detecting and characterizing properly the obstacle. Indeed, the field scattered by the ground is then polluted by the roughness contribution. The surface is generally seen as clutter, which must be rejected in order to exhibit the target signature, but unfortunately, the roughness profile of the interface separating the air from the ground is unknown. Two main approaches for clutter rejection have been investigated.

Manuscript received December 14, 2006; revised April 10, 2007.

O. Cmielewski was with Institut Fresnel, UMR 6133 Centre National de la Recherche Scientifique–Universités Aix Marseille, 13397 Marseille, France. He is now with Saint Denis, La Réunion.

H. Tortel and A. Litman are with Institut Fresnel, UMR 6133 Centre National de la Recherche Scientifique–Universités Aix Marseille, 13397 Marseille, France.

M. Saillard is with Laboratoire de Sondages Electromagnetiques de l'Environnement Terrestre, Université du Sud Toulon Var, 83957 La Garde, France.

Digital Object Identifier 10.1109/TGRS.2007.902289

On the one hand, the clutter is seen as an additive noise to the scattered field. Statistical approaches are then implemented [1]–[5]. In this context, the clutter is estimated via full-wave Monte Carlo simulations with random realizations leading to the design of an optimal detector. This approach has been applied to various classes of rough surfaces and has shown significant improvements of the detection process compared to the standard matched filter, which was designed for a flat surface response. One can notice that this kind of approach, which is mainly used for detection, has also been applied for classifying unexploded ordnances (UXO) [6]–[8]. In this case, the late time response of the scattered field is used in order to recover the resonant frequencies of the UXO; the targets are then discriminated with a model-based Bayesian approach.

On the other hand, the surface profile is considered as a supplemental unknown that has to be retrieved during the inversion procedure, and there are two ways to tackle this problem. The first option is to reconstruct simultaneously the surface profile and the obstacle. This approach has been developed in [9] and [10] with the help of a domain integral formalism or in [11] with the help of a semianalytical mode matching method. This implies an increase in the associated computational burden as well as in the ill-posedness of the problem. The second option is to recover the roughness and the object separately. Several algorithms are available for reconstructing surface profile. For example, the roughness profile can be found by combining the time gating of the scattered field and physical optics considerations [12]. Then, the stratified geometry of the problem is taken into account in the Green's function of the structure in order to characterize the target. Approaches based on Born and Rytov approximations of the scattered field [13], [14] have also been explored, yielding a simplified inversion algorithm. Recently, nonlinear inversion of the exact wave equation has been performed in 3-D [15], with a reduced computational burden due to a fast multipole technique.

In this paper, we present a new approach for determining directly from the measurement data an estimation of the surface profile. Generally speaking, a nonlinear inverse problem is classically recasted into an optimization problem in which the difference between the field scattered by the object and the field scattered by an estimation is minimized using a gradientlike method. We propose instead to take advantage of a specific correlation technique of the scattered field to gain information on the roughness profile. This technique has been inspired by a novel detection method for buried object into the ground [16], [17]. Thanks to the physical insight gain by the small perturbation theory, we show that the correlation of multistatic data provides information content on the surface roughness.

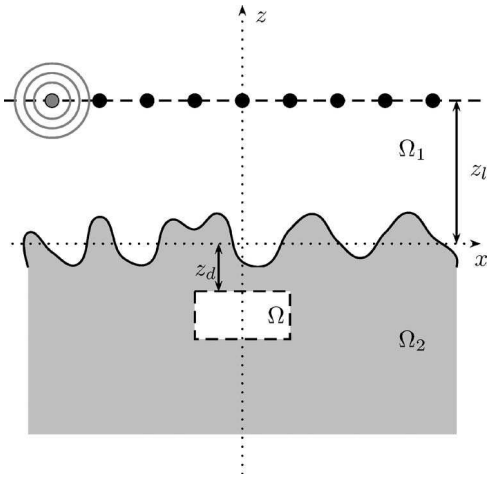

Fig. 1. Configuration of the problem. A dielectric target is buried under a rough interface at depth z_d. Transmitting and receiving antennas are positioned on a probing line located at elevation z_l from the interface.

This approach is validated through various numerical examples using scattered fields computed with rigorous surface integral equations. Once the interface has been recovered, instead of computing the associated Green's function, we choose to discretize it into a finite-element code that is specifically built up for this application.

The next step concerns the characterization of the obstacle that was placed underneath. We assume therefore that the detection part has already been performed. There are numerous techniques for solving this inverse problem. Here, as we want to restrict our study to geometrical problems, such as profile and shape reconstruction, we are using a level-set algorithm to retrieve information on the obstacle [18], [19]. This implies that the various permittivities are assumed to be known. This choice has necessitated the development of specific numerical tools for solving the evolution of the level set on an unstructured mesh [20]–[23]. Finally, to understand the impact of the supplemental information that was added by estimating the roughness profile, we will compare the different approaches throughout the numerical experiments.

II. Scattering Problem

The geometry of the problem is shown in Fig. 1, where a homogeneous cylindrical object of arbitrary cross section Ω is embedded in a semi-infinite homogeneous medium Ω_2. This medium, with permittivity $\varepsilon_2 = \varepsilon_0\varepsilon_{2r}$ (with ε_0 and k_1 being the permittivity and the wavenumber in vacuum, respectively), is separated from the domain Ω_1 constituted of air by a rough surface $\Gamma = \{r = (x, y)$ s.t. $z = h(x)\}$, with the same direction of invariance as the buried rod. The rough surface is characterized by its statistical parameters, namely, its Gaussian distribution of heights and its correlation function, which is either Gaussian or exponential here. Assuming that the incident field is also independent of y leads to a 2-D problem. The scatterers are assumed to be homogeneous dielectric cylinders with complex permittivity distribution $\varepsilon = \varepsilon_0\varepsilon_r$. The entire configuration is supposed to be nonmagnetic $(\mu = \mu_0)$. Only time-harmonic fields are considered, with $\exp(-i\omega t)$ time dependence.

Let us define by $E_{\rm inc}$ the y-component of the field that would be radiated in free space by an electric dipole of moment p_l that is parallel to the y-axis and located at r_l, i.e.,

$$\Delta E_{\rm inc}(r; r_l) + k_1^2 E_{\rm inc}(r; r_l) = p_l(r)\delta(r - r_l) \qquad \forall r. \quad (1)$$

This field is nothing but the direct contribution from one emitter to a receiver, without taking into account the presence of the interface and of the target.

Let us now consider a set of L electric dipoles p_l above the interface, along a piece of line $z = z_l$ with $r_l = (x_l, z_l)$, with each one playing the role of transmitter and receiver, and all acting with the same E polarization. The y-component of the corresponding measured field $E(r; r_l)$ for a given emitter r_l satisfies the following set of equations:

$$\begin{aligned}
\Delta E(r; r_l) + k_1^2 E(r; r_l) &= p_l(r)\delta(r - r_l) && \forall r \in \Omega_1 \\
\Delta E(r; r_l) + k_1^2 \varepsilon_{2r} E(r; r_l) &= 0 && \forall r \in \Omega_2 \setminus \overline{\Omega} \\
\Delta E(r; r_l) + k_1^2 \varepsilon_r E(r; r_l) &= 0 && \forall r \in \Omega \\
E|_1 &= E|_2 && \forall r \in \Gamma \\
\left.\frac{\partial E}{\partial n}\right|_1 &= \left.\frac{\partial E}{\partial n}\right|_2 && \forall r \in \Gamma \\
E|_+ &= E|_- && \forall r \in \partial\Omega \\
\left.\frac{\partial E}{\partial n}\right|_+ &= \left.\frac{\partial E}{\partial n}\right|_- && \forall r \in \partial\Omega \quad (2)
\end{aligned}$$

where $E|_1$ (respectively $E|_2$) denotes the limit of E from the domain Ω_1 (respectively Ω_2), and $E|_+$ (respectively $E|_-$) denotes the limit of E from the exterior (respectively interior) of Ω. This field contains the contributions from each antenna, from the rough surface, and from the buried target.

Finally, we denote by E_s the scattered field that contains both the contributions from the rough surface and from the buried target, for a given emitting antenna l, i.e.,

$$E(r; r_l) = E_{\rm inc}(r; r_l) + E_s(r; r_l). \quad (3)$$

The scattered field satisfies the Sommerfeld radiation condition

$$\lim_{d\to\infty} \sqrt{d}\left(\frac{\partial E_s}{\partial d} - ikE_s\right) = 0 \quad (4)$$

where $d = |r|$.

III. Estimation of the Surface Profile

Let us first consider a rough surface with no buried target. In this case, scattered field E_s only contains the contribution from rough surface $E_{\rm surf}$. Assuming that the height of the roughness is much smaller than the probing wavelength, the calculations can be performed in the framework of the small perturbation method. At first order in height, for an incident field created by

a line source of strength p_l that is placed in $r_l = (x_l, z_l)$, the scattered field measured in $r = (x, z)$ is given by

$$E_{\text{surf}}(r; r_l) = E^{(0)}_{\text{surf}}(r; r_l) + E^{(1)}_{\text{surf}}(r; r_l) + \cdots \tag{5}$$

where $E^{(0)}_{\text{surf}}$ corresponds to the field that would be reflected by a plane interface at $z = 0$, and $E^{(1)}_{\text{surf}}$ is the contribution of the surface roughness at first order. These fields are expressed by [24]

$$E^{(0)}_{\text{surf}}(r; r_l) = \int A_i(\alpha_l, r_l) R(\alpha_l) e^{i(\alpha_l x + \beta_{1,l} z)} d\alpha_l$$

$$E^{(1)}_{\text{surf}}(r; r_l) = \iint A_i(\alpha_l, r_l) \hat{h}(\alpha - \alpha_l) \times B_1(\alpha, \alpha_l) e^{i(\alpha x + \beta_1 z)} d\alpha \, d\alpha_l$$

where $R(\alpha_l)$ denotes Fresnel's reflection coefficient, A_i contains all information about the antenna, α and α_l denote the horizontal components of the wave vectors of the scattered and incident plane wave decompositions, respectively, and $\beta^2_{j,l} = k^2_j - \alpha^2_l$, $j = 1, 2$. $B_1(\alpha, \alpha_l)$ is derived from the boundary conditions

$$R(\alpha_l) = \frac{\beta_{1,l} - \beta_{2,l}}{\beta_{1,l} + \beta_{2,l}} \tag{6}$$

$$A_i(\alpha_l, r_l) = \frac{p_l}{4i\pi\beta_{1,l}} e^{i(-\alpha_l x_l + \beta_{1,l} z_l)} \tag{7}$$

$$B_1(\alpha, \alpha_l) = -2i\beta_1 \frac{\beta_{1,l} - \beta_{2,l}}{\beta_1 + \beta_2}. \tag{8}$$

When measurements are performed along a horizontal line from minus to plus infinity at an elevation z_l, previous results [16] have shown that the correlation of the scattered fields measured at two different locations $r_+ = (X + x, z_l)$ and $r_- = (X - x, z_l)$ can provide useful information on the location of the scatterer. In that case, the following quantity was considered:

$$\iint E_{\text{surf}}(r_+; r_l) E^*_{\text{surf}}(r_-; r_l) dx \, dx_l. \tag{9}$$

Similar analysis can be performed for retrieving the surface profile. Here, the interesting quantity consists in

$$\iint E_{\text{surf}}(r_+; r_l) E^{(0)*}_{\text{surf}}(r_-; r_l) dx \, dx_l. \tag{10}$$

Indeed, the zero-order correlation term is easily computed and turns out to be purely real and constant, i.e.,

$$\iint E^{(0)}_{\text{surf}}(r_+; r_l) E^{(0)*}_{\text{surf}}(r_-; r_l) dx \, dx_l = \frac{|R(0)|^2 |p_l|^2}{4k^2_1} \tag{11}$$

using the fact that

$$\int A_i(\alpha_l, r_l) A^*_i(\alpha'_l, r_l) dx_l = \frac{|p_l|^2}{4\beta_{1,l}\beta'^*_{1,l}} \delta(\alpha_l - \alpha'_l). \tag{12}$$

The first-order correlation term with respect to roughness height is given by

$$\begin{aligned} &\iint E^{(1)}_{\text{surf}}(r_+; r_l) E^{(0)*}_{\text{surf}}(r_-, r_l) dx \, dx_l \\ &\quad = \int \frac{i}{2\beta^*_{1,l}} |R(\alpha_l)|^2 |p_l|^2 \hat{h}(2\alpha_l) e^{2i\alpha_l X} e^{2i(\beta_{1,l} - \beta^*_{1,l}) z_l} d\alpha_l \\ &\quad = h(X) * (g_{\text{prop}}(X) + g_{\text{eva}}(X, z_l)) \end{aligned} \tag{13}$$

with

$$g_{\text{prop}}(X) = \frac{i}{2} \int_{|\alpha_l| \le k_1} \frac{|R(\alpha_l)|^2 |p_l|^2}{\beta_{1,l}} e^{2i\alpha_l X} d\alpha_l \tag{14}$$

$$g_{\text{eva}}(X, z_l) = -\frac{1}{2} \int_{|\alpha_l| > k_1} \frac{|R(\alpha_l)|^2 |p_l|^2}{\text{Im}(\beta_{1,l})} \times e^{-4\text{Im}(\beta_{1,l}) z_l} e^{2i\alpha_l X} d\alpha_l. \tag{15}$$

For evanescent waves, the convolution function g_{eva} is purely real. For propagative waves, it is to be noticed that, for typical soil permittivities, since $|\beta_{1,l}| \ll |\beta_{2,l}|$, R is hardly varying, and a rough approximation of the coefficient in the integral of g_{prop}, up to a real normalization constant, is $i/\beta_{1,l}$. Therefore, the imaginary part of (10) is the convolution product of the surface profile with a function that is very close to a Bessel function, i.e.,

$$\text{Im} \iint E_s(r_+; r_l) E^{(0)*}_{\text{surf}}(r_-; r_l) dx \, dx_l \approx h(X) * 2\pi |R(0)|^2 |p_l|^2 \frac{J_0(2k_1 X)}{4}. \tag{16}$$

Noticing that $(J_0(2k_1 X)/4) = \text{Im}(G(2k_1 X))$, where G denotes free-space Green's function, it is thus found that this technique leads, for a rough surface, to the same result as those established for pointlike scatterers in other contexts. Indeed, the image resulting from autocorrelation of the backscattered field along a line surrounding the scatterer can also be written as $\text{Im}(G(2k_1 r))$, as well as the image derived from backpropagation techniques, such as time reversal. In three dimensions, the Bessel function in (16) just becomes $\text{sinc}(2k_1 X)$.

From prior knowledge of the permittivity of the soil, one can precompute $E^{(0)}_{\text{surf}}$. This quantity is then used in conjuction with the measured scattered field in an equation inspired from (16) to obtain an estimation $\widetilde{h}(X)$ of the surface profile, approximating the Bessel function by a Dirac function, i.e.,

$$C \times \widetilde{h}(X) = \text{Im} \iint E_s(r_+; r_l) E^{(0)*}_{\text{surf}}(r_-; r_l) dx \, dx_l. \tag{17}$$

Since this coefficient C depends on the frequency, permittivity, and length of the line of antennas, a calibration procedure is required. For instance, one can derive C from measurements over a known surface profile, which is used as a reference, or perform two measurements for the same surface for two different elevations of the antennas.

If a target is located below the rough surface, it contributes to both the real and imaginary parts of this correlation function. Considering that the real part only allows one to reject surface clutter and such data processing is thus well suited for target detection [16]. On the other hand, its contribution to the imaginary part creates some noise if one aims at reconstructing the profile of the surface, which results in a local perturbation above the position of the target. This provides nevertheless a good approximation of the surface if the characteristic size of the target is small compared to the wavelength, as will be shown with some numerical results.

IV. Estimation of the Target

After determining the surface, one is interested in finding and characterizing the target. Let us assume that the detection part has already been performed by means of the correlation techniques described previously. The inversion scattering problem is now stated as characterizing the scatterer in a test domain $D \subset \Omega_2$, such that the corresponding scattered field predicted by the Maxwell equations matches the measured data. Additional *a priori* information is introduced as we assume that the dielectric properties of the obstacles are known and that they are constant. Therefore, the inverse scattering problem is reduced to a shape optimization problem where the support of the scatterer is looked for.

Herein, an iterative approach is proposed to solve this ill-posed and nonlinear problem. We first define the discrepancy criteria between the measured fields and the simulated ones by

$$\mathcal{J}(\Omega) = \sum_{l=1}^{L} w_l \left\| E_s^{\text{meas}}(\cdot; r_l) - E_s(\Omega)(\cdot; r_l) \right\|^2 \tag{18}$$

where L is the number of available illuminations, Ω is the unknown support of the buried rod, and $\|\cdot\|$ corresponds to the L_2 norm on the receiver line. w_l is an appropriate weighting factor, and we assume that

$$w_l = \frac{1}{\|E_s^{\text{meas}}(\cdot, r_l)\|^2}. \tag{19}$$

One can notice that E_s^{meas} is the field scattered by the buried object in the presence of the rough surface (only the direct radiation E_{inc} from the emitter to the receiver in vacuum is subtracted to the measured total field E^{meas}).

Significant work now exists on the retrieval of binary obstacles. The level-set representation has proved to be one of the most suitable representations for binary objects when no additional topological information is available, such as connexity for example. This level-set approach has now been widely used in various domains of inverse problem or shape optimization [18], [19], [25]–[29].

For a homogeneous obstacle Ω, the associated level-set function $\phi(r)$ is defined by

$$\Omega = \{ r \in D | \phi(r) < 0 \}. \tag{20}$$

With this representation, the definition of the contour is implicit and made in a geometrical fashion. This level-set representation requires the computation of the shape derivative of the cost functional. It can be shown that this derivative is of the following form:

$$\nabla \mathcal{J}(\phi) = -\text{Re}(\varepsilon_r - \varepsilon_{2r}) \delta(\phi) |\nabla \phi| \sum_{l=1}^{L} \overline{E(r; r_l) P_l(r)} \tag{21}$$

where $\delta(\phi)$ corresponds to the 1-D Dirac delta function concentrated on the interface $\partial\Omega$, $E(r; r_l)$ denotes the total field in the test domain for an incidence l, and $P_l(r)$ is the associated adjoint state where all receivers act as sources with an amplitude linked to the discrepancy criteria of (18). As done in [29], a simple gradient method is used to solve the minimization problem. Therefore, the level-set function is updated by solving the following equation:

$$\phi_t(r) = -\nabla \mathcal{J}(\phi) \tag{22}$$

where t is a fictitious time parameter, and the Dirac delta function is extended everywhere in D with value 1. This equation is nothing but a Hamilton–Jacobi-type equation [21], [25]. A strong effort has been ported on the resolution of this Hamilton–Jacobi equation. Indeed, in the present application, we are using a finite-element code to compute the electromagnetic field with the aid of an unstructured mesh. This has required an implementation of the Hamilton–Jacobi equation on the same unstructured mesh. More numerical details are provided in the next section.

V. Numerical Results

A. Modeling Codes

Several modeling codes are available to solve the scattering problem described in (2), such as [9], [10], and [30]–[32]. Here, two types of forward solvers are used. The first one provides synthetic data and is described in [33]. It accurately takes into account the scattering from an object buried under a rough interface. The problem is solved with a rigorous integral method leading to a single boundary integral equation. Both the rough surface and the target contour are discretized by piecewise-constant functions to solve numerically the integral equation.

For the inversion process, as we also need to compute at each iteration step the scattered field by an object buried under a rough surface and in order to prevent any "inverse crime," we have chosen to develop a fast numerical solver based on a finite-element method. This finite-element method is applied to the weak form of the Helmhlotz equation for the geometrical and polarization problem described in (2). For 2-D open scattering problems, the component of the electrical field can be expanded onto linear $P1$ basis functions [34]. A free unstructured mesh generator [35] is used to provide discretization of the whole domain (air, surface, and ground) truncated by uniaxial perfect matched layers. The obtained mesh is then conformal to the surface profile, either the true profile, the reconstructed one, or any other flat surface if needed. The sparse system is then solved using a frontal method [36].

Methods based on domain equation are best suited for level-set algorithms, but it can be noticed that most of the level-set

algorithms developed so far in inverse scattering have been done on a regular mesh. This is mainly because almost all discretization schemes for the Hamilton–Jacobi equation are based on finite-difference discretization. Here, an unstructured mesh has been used, and a strong effort has been devoted to the development of specific numerical tools as it is not desirable to map quantities from one unstructured grid to a regular one. Among the different schemes proposed in the literature to discretize in a convenient way the Hamilton–Jacobi equation of (22) on an unstructured mesh (see [21] and references therein), we have followed the ideas proposed by Abgrall [20], where it has been proved that this kind of numerical Hamiltonian yields a stable and convergent scheme.

B. Description of the Configuration

Our aim is not to give statistical results here, but various samples of rough surfaces and permittivities of the soil have been considered, and relevant trends have been noticed when comparing inversion based on scattered field with assumed plane interface, with reconstructed rough interface, or with exact rough interface. A rectangular cross-sectional dielectric target of permittivity $\varepsilon_r = 2$ is buried at a depth of $z_d = 5$ cm (the distance is measured from the average plane interface to the top of the target). The dimension of the target under test along the x- and z-directions are $l_x = 7.5$ cm and $l_z = 5$ cm, respectively. The measurement line of length 120 cm is located in the air at a distance of $z_l = 10$ cm and contains $L = 41$ transmitting and receiving antennas that are evenly distributed. The working frequency is equal to 800 MHz. In the following, three types of soils are considered.

- Test case 1 (TC1): a lossless soil with permittivity $\varepsilon_{2r} = 5$ and a surface profile with Gaussian correlation function of correlation length $l_c = 8$ cm and root mean square height $h_{\mathrm{rms}} = 1$ cm.
- Test case 2 (TC2): a lossy soil $(\varepsilon_{2r} = 5 + i)$ and an exponential correlation function with the same correlation length and the same rms height.
- Test case 3 (TC3): same as TC1, except that $\varepsilon_{2r} = 7.5 + 1.2i$.

C. Evaluation Criteria

In order to check the effectiveness of the different approaches, various criteria are used. The first one is based on the evolution of cost function (18), which should decrease while iterating. However, since this cost function contains some mismatch information about the reconstruction of both the surface profile and the target, a second criterion is used. The latter directly compares the shape of the reconstructed target with that of the true one. It would also be possible to focus on the various geometrical or topological properties (barycenter position, perimeter, area, Euler number, etc.) [37]. Here, the two shapes are compared through the number of misclassified pixels, which can be considered as the L_1 distance function between the indicator functions of the reconstructed and exact shapes. We think that this distance is better suited than the Hausdorff distance function [38], [39], which is too sensitive to noise and to isolated pixels. The L_1 distance is thus used as an *a posteriori* criterion in order to check and compare the various reconstructed objects as well as the stability of their shape during the iterative process.

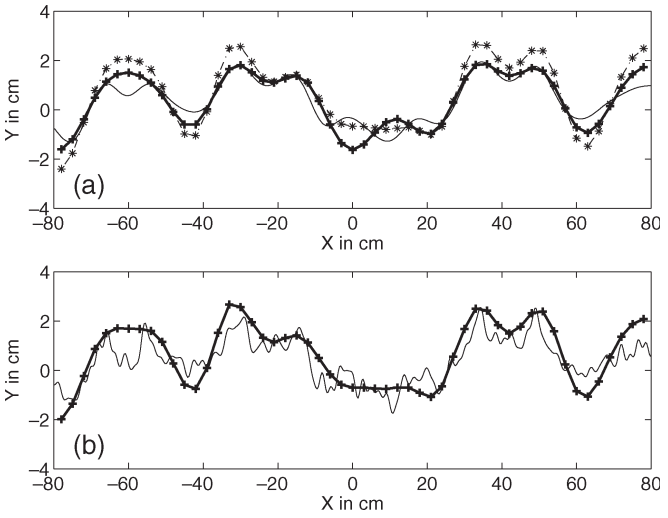

Fig. 2. Reconstructed surface profiles for the three test cases. (a) Gaussian surface profile corresponding to (line with stars) TC1 and (thick line with crosses) TC3. (b) Exponential surface profile corresponding to (thick line with crosses) TC2. The (thin lines) true profiles are also displayed.

D. Surface Profile Reconstructions

In Fig. 2(a), the reconstructed profile obtained from the method described in Section III is presented for the TC1 and TC3 test cases and compared to the true profile. It is clearly seen that, even though the method is based on a small perturbation approach, it works fine even when the scatterer has a characteristic size of $\lambda/2$ in the soil. We can also notice that the embedded scatterer does not really influence the reconstructed profile. There is only a slight variation of the reconstructed profile when the permittivity varies from $\varepsilon_{2r} = 5$ to $\varepsilon_{2r} = 7.5 + 1.2i$.

In Fig. 2(b), we have plotted the reconstructed profile for test case TC2. The exponential correlation function introduces higher frequency components in the surface profile, which cannot be reconstructed beyond some limit, which is related to the operating frequency and to the present scheme. Indeed, the correlation length l_c is on the order of $\lambda/4$, and this explains why only the slow variations of the profile are properly recovered.

Finally, to show the robustness of the proposed approach against noise, additive white Gaussian noise has been added to the data. The obtained reconstructed profiles are all very close from the true profile (Fig. 3), and this seems to be an intrinsic property of the correlation functions to reject uncorrelated noise.

E. Obstacle Reconstruction

We have then applied the iterative level-set algorithm described in Section IV. In all cases, the test domain is a circle with a radius of 8 cm and a center located at $(-10, 0)$ cm below

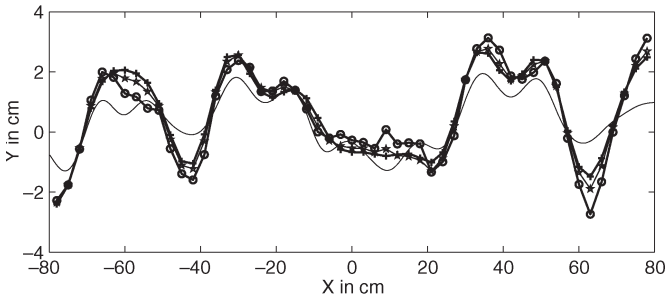

Fig. 3. Reconstructed surface profiles for test case TC1 with (line with crosses) no noise, (line with stars) 10% additive white Gaussian noise, and (line with dots) 30% additive white Gaussian noise. The (thin line) true profile is also displayed.

the interface. The initial guess is always chosen as a circular cylinder centered at $(-11, 0)$ cm and with a radius of 3 cm. The iterative processes have been stopped when the L_1 distance has reached a plateau, which is symptomatic of a stable solution.

Our aim is to understand the influence of the rough surface on the inversion results, particularly, to which extent the rough surface must be recovered in order to obtain a correct image of the target. Therefore, three types of reconstructions have been performed with various types of air–soil interface:

1) a plane interface positioned at average height;
2) the reconstructed surface profile;
3) the true rough surface.

In Fig. 4, the final profile estimate is presented for each test case and for each type of air–soil interface. As expected, for the TC1, TC2, and TC3 test cases, the best reconstructed shape is found out when the exact rough surface is taken into account in the inversion procedure. This is noticed also in Figs. 5 and 6, where we have represented the evolution of the corresponding cost functions as well as the associated L_1 distances. Indeed, in these figures, the values obtained with the exact rough surface are always the lowest ones. On the contrary, for the TC1, TC2, and TC3 test cases, the worst reconstruction is obtained when a plane interface is assumed. Indeed, clutter from surface scattering is thus considered as noise and, as expected, leads to worse results than considering the reconstructed or the true surface profile.

For test case TC1 (lossless background), the convergence of the algorithm is very rapid, as can be shown in both the cost function [see Fig. 5(a)] and the L_1 distance [see Fig. 6(a)]. Let us define by r_{ts}^{rp} (respectively r_{ts}^{pi}) the ratio between the number of misplaced pixels with the reconstructed profile (respectively with the plane interface) and the number of misplaced pixels with the true surface. At the end of the iterative process, we have $r_{ts}^{rp} = 1.6$ and $r_{ts}^{pi} = 2.1$, and a look at Fig. 4(a) shows indeed that the object obtained with the reconstructed profile is less distorted than the one obtained with the plane interface.

For test case TC2, even though the cost function is very quickly reaching a plateau, the number of misplaced pixels is still evolving [see Fig. 6(b)]. This means that the cost function is not sufficiently sensitive to translate the evolution of the shape of the target. Despite of the rough surface being not very well recovered in that case, the improvement of the final estimate is significant since we get $r_{ts}^{rp} = 1.7$, as compared to $r_{ts}^{pi} = 2.8$.

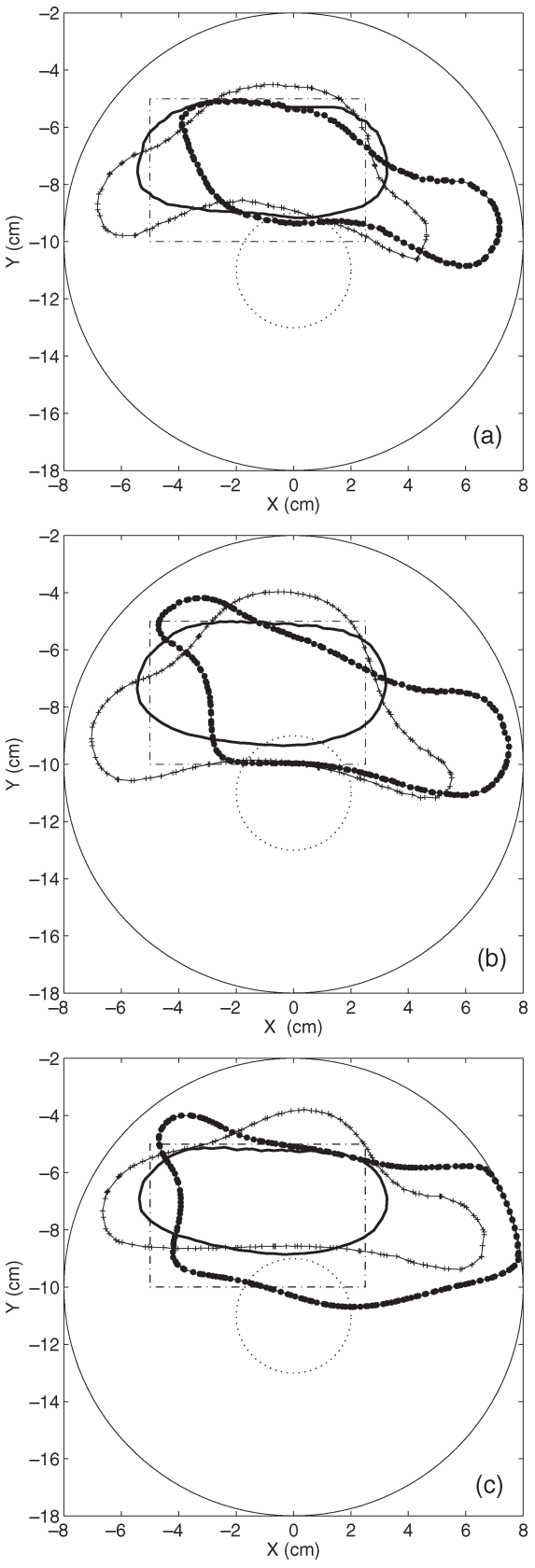

Fig. 4. Estimated shapes at the end of the iterative process for each test case. (a) TC1, (b) TC2, and (c) TC3. Three different types of interfaces are used. (Thick line) the true profile, (line with crosses) the reconstructed profile, and (line with black circles) the plane interface. The (dotted line) initial guess and the (thin line) true object are also displayed.

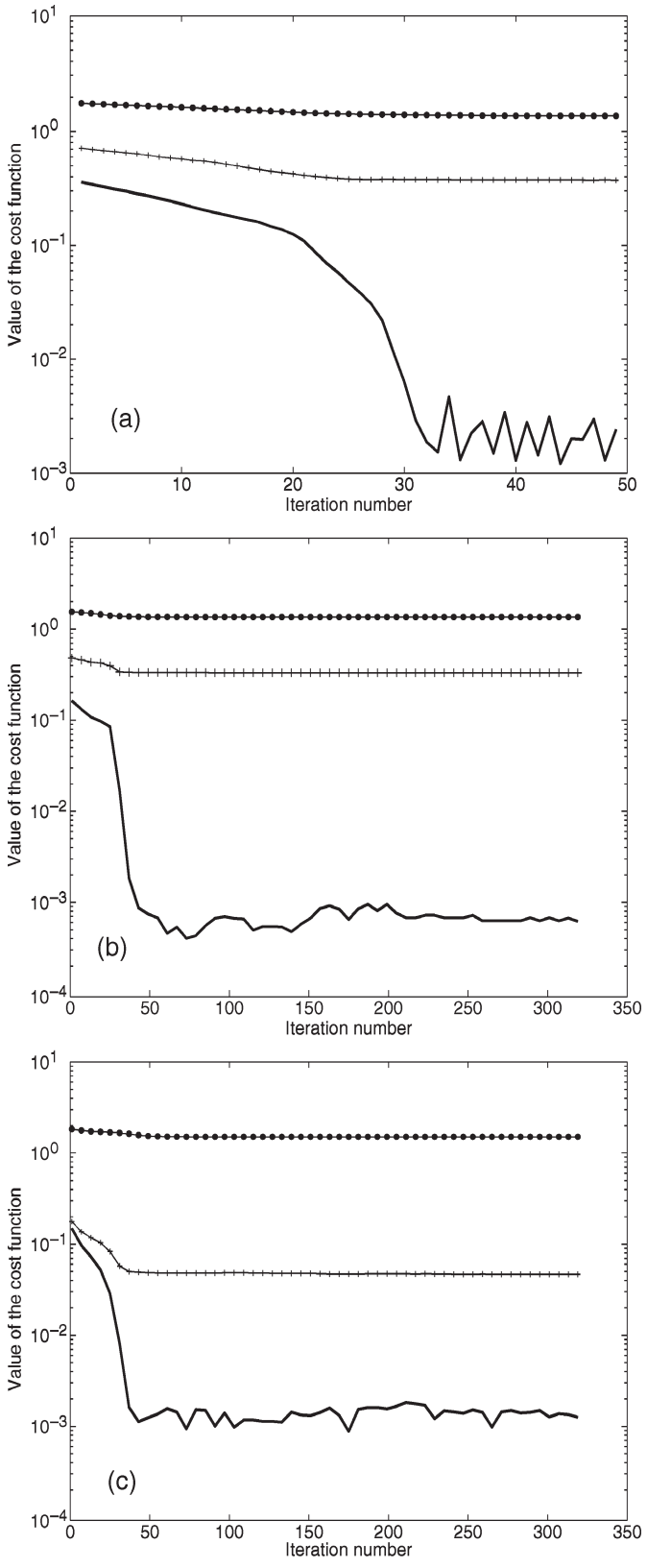

Fig. 5. Evolution of the cost function with respect to the iteration number for each test case and each surface profile. The numbering and the type of lines are the same as those in Fig. 4.

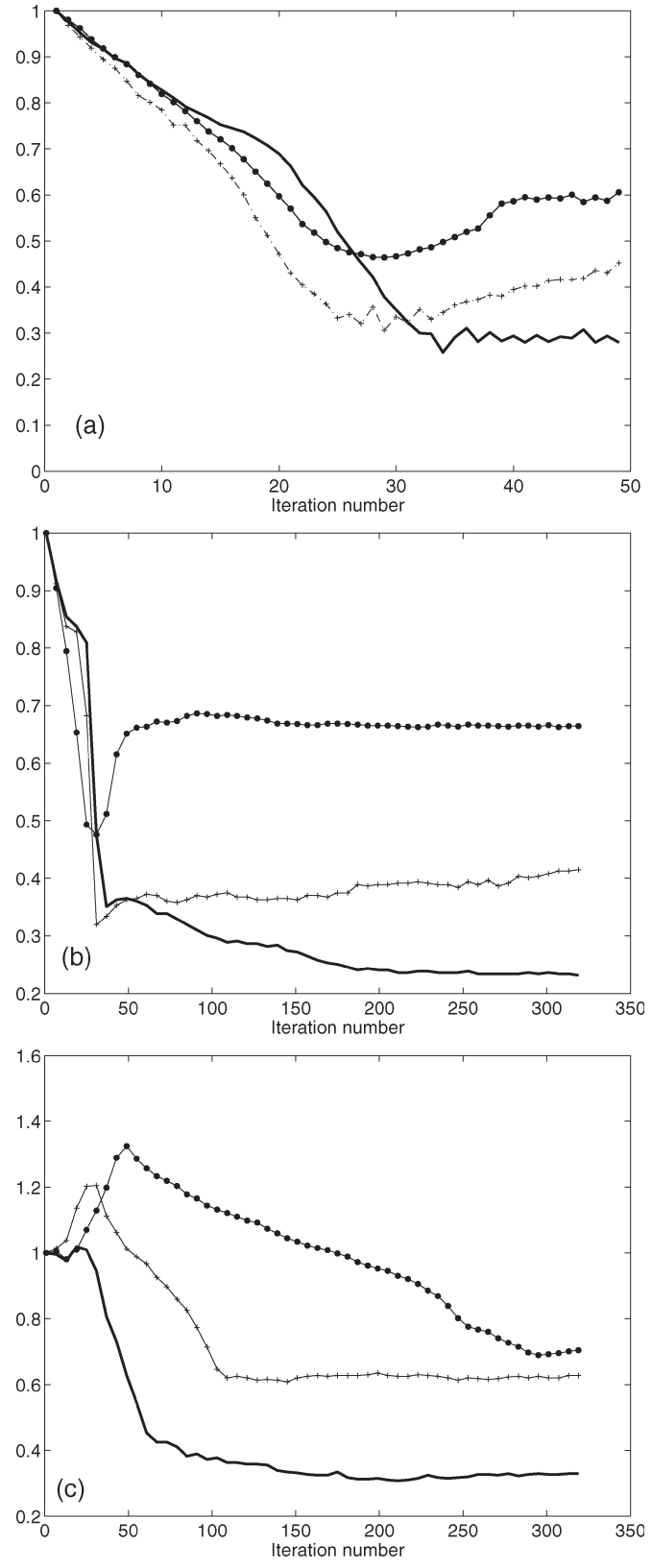

Fig. 6. Evolution of the number of misclassified pixels with respect to the iteration number for each test case and each surface profile. The numbering and the type of lines are the same as those in Fig. 4.

Finally, for test case TC3, we have tested the influence of the permittivity of the background on the reconstruction procedure. Reducing the background wavelength does not improve the resolution here ($r_{ts}^{rp} = 1.8$ and $r_{ts}^{pi} = 2.0$), and the reconstructed objects are more distorted with respect to the true object.

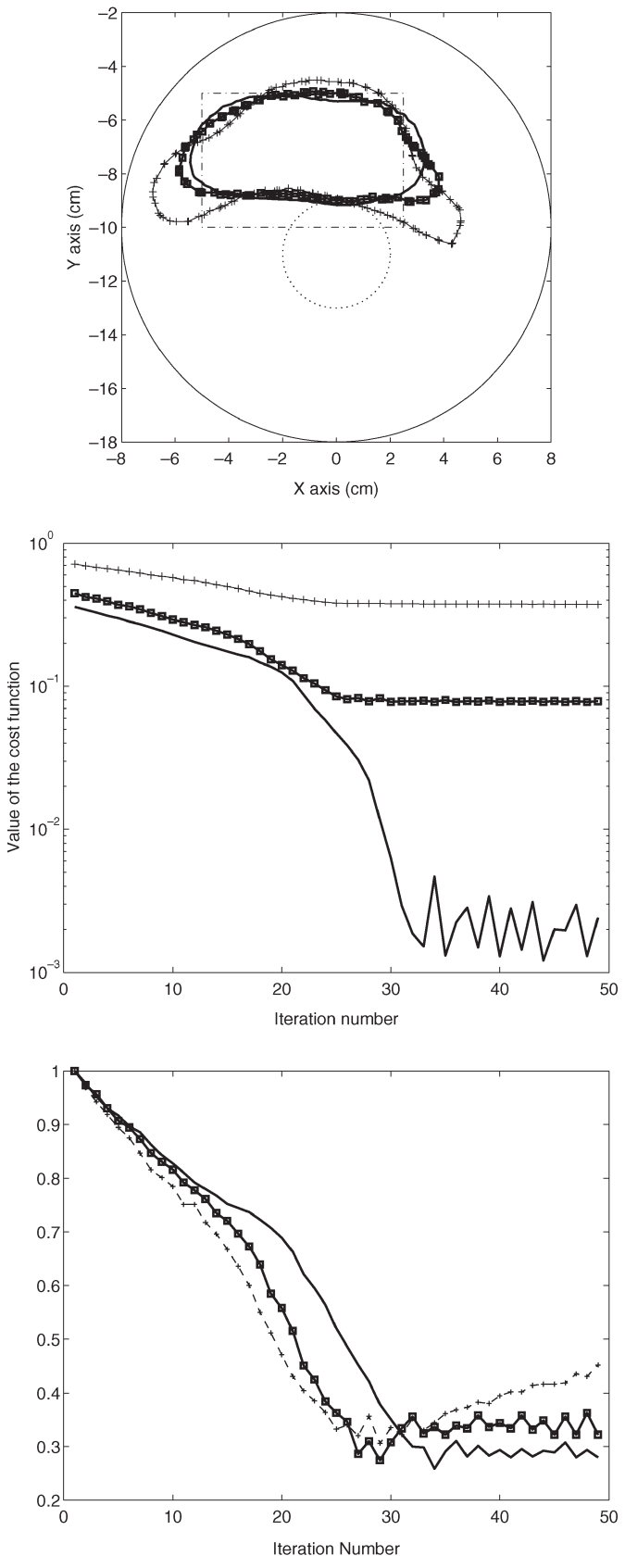

Fig. 7. Comparison of the results obtained in the TC1 case with (thick line) the true surface profile without noise, (thick line with squares) the true surface profile and 4% Gaussian additive noise in the scattered field, and (line with crosses) the reconstructed profile without noise in the scattered field. (Top to bottom) The final estimation found, the evolution of the cost function, and the number of misclassified pixels.

We have also estimated the noise level induced in the scattered field when using the reconstructed surface instead of the true surface, for test case TC1. This noise is on the order of 4% in magnitude. In order to show that this kind of correlated clutter has a strong impact, we have plotted (see Fig. 7) a comparison between the results obtained with the reconstructed profile and the ones obtained when 4% of Gaussian additive white noise is added to the scattered field associated with the true surface profile. As it can be clearly seen, in the case of additive white noise, the results are only slightly modified when compared to the case without noise, while the difference is much more significant when using the reconstructed surface profile.

VI. Conclusion

A two-step procedure for the characterization of a buried target under a rough surface is presented in this paper. It is based on the properties of the correlation function of the scattered field, in order to extract an estimation of the surface profile. Due to a finite-element code, we are able to take into account this reconstructed profile into the inversion process and then focus on the characterization of the buried object.

The algorithm presented therein is restricted to homogeneous scatterers with known properties, but it could easily be extended to inhomogeneous ones, either by means of multiple level-set representations if they are homogeneous by parts [29] or by using standard gradient-type minimization techniques.

In this paper, the correlation of the scattered field has only been used to recover the surface profile. In a previous work, we have shown that it was also a good indicator for detecting and recovering the buried target [17]. It would be interesting to combine both approaches and introduce also this correlation function in the cost function of the minimization process.

Finally, only single-frequency data have been used, and we have seen that, if the correlation length is lower than the wavelength, the high-frequency components of the surface roughness are not recovered. It would be interesting to study the influence of multiple-frequency data in this two-step reconstruction procedure.

References

[1] T. Dogaru and L. Carin, "Time-domain sensing of targets buried under a rough air–ground interface," *IEEE Trans. Antennas Propag.*, vol. 46, no. 3, pp. 360–372, Mar. 1998.

[2] T. Dogaru, L. Collins, and L. Carin, "Optimal time-domain detection of a deterministic target buried under a randomly rough interface," *IEEE Trans. Antennas Propag.*, vol. 49, no. 3, pp. 313–326, Mar. 2001.

[3] T. Dogaru and L. Carin, "Time-domain sensing of targets buried under a Gaussian, exponential, or fractal rough interface," *IEEE Trans. Geosci. Remote Sens.*, vol. 39, no. 8, pp. 1807–1819, Jun. 2001.

[4] P. D. Gader, M. Mystkowski, and Y. Zhao, "Landmine detection with ground penetrating radar using hidden Markov models," *IEEE Trans. Geosci. Remote Sens.*, vol. 39, no. 6, pp. 1231–1244, Jun. 2001.

[5] L. Carin, Ed., "Foreword—Special issue on new advances in subsurface sensing: Systems modeling, and signal processing," *IEEE Trans. Geosci. Remote Sens.*, vol. 39, no. 6, p. 1107, Jun. 2001.

[6] S. Vitebskiy, K. Sturgess, and L. Carin, "Short-pulse plane-wave scattering from buried perfectly conducting bodies of revolution," *IEEE Trans. Antennas Propag.*, vol. 44, no. 2, pp. 143–151, Feb. 1996.

[7] S. Vitebskiy and L. Carin, "Resonances of perfectly conducting wires and bodies of revolution buried in a lossy dispersive half-space," *IEEE Trans. Antennas Propag.*, vol. 44, no. 12, pp. 1575–1583, Dec. 1996.

[8] C. Chen and L. Peters, "Buried unexploded ordnance identification via complex natural resonances," *IEEE Trans. Antennas Propag.*, vol. 45, no. 11, pp. 1645–1654, Nov. 1997.
[9] V. Galdi, D. Castanon, and L. Felsen, "Multifrequency reconstruction of moderately rough interfaces via quasi-ray Gaussian beams," *IEEE Trans. Geosci. Remote Sens.*, vol. 40, no. 2, pp. 453–460, Feb. 2002.
[10] I. Catapano, L. Crocco, and T. Isernia, "A simple two-dimensional inversion technique for imaging homogeneous targets in stratified media," *Radio Sci.*, vol. 39, no. 1, RS1012, Feb. 2004.
[11] R. Firoozabadi, E. Miller, C. Rappaport, and A. Morgenthaler, "Subsurface sensing of buried objects under a randomly rough surface using scattered electromagnetic field data," *IEEE Trans. Geosci. Remote Sens.*, vol. 45, no. 1, pp. 104–117, Jan. 2007.
[12] V. Galdi, H. Feng, D. A. Castanon, W. C. Carl, and L. B. Felsen, "Moderately rough surface underground imaging via short-pulse quasi-ray Gaussian beams," *IEEE Trans. Antennas Propag.*, vol. 51, no. 9, pp. 2304–2318, Sep. 2003.
[13] A. Schatzberg and A. J. Devananey, "Rough surface inverse scattering within the Rytov approximation," *J. Opt. Soc. Amer. A, Opt. Image Sci.*, vol. 10, no. 5, pp. 942–950, May 1993.
[14] R. J. Wonbell and J. A. DeSanto, "Reconstruction of rough-surface profiles with the Kirchhoff approximation," *J. Opt. Soc. Amer. A, Opt. Image Sci.*, vol. 8, no. 12, pp. 1892–1897, Dec. 1991.
[15] M. El-Shenawee and E. Miller, "Multi-incidence and multifrequency for profile reconstruction of random rough surfaces using the 3-D electromagnetic fast multipole model," *IEEE Trans. Geosci. Remote Sens.*, vol. 42, no. 11, pp. 2499–2510, Nov. 2004.
[16] O. Cmielewski, M. Saillard, and H. Tortel, "Detection of buried objects beneath a rough surface," *Waves Random Complex Media*, vol. 16, no. 4, pp. 417–431, Nov. 2006.
[17] O. Cmielewski, K. Belkebir, M. Saillard, and H. Tortel, "On the characterization of buried targets under a rough surface using Wigner–Ville transformation," *IEEE Geosci. Remote Sens. Lett.*, vol. 3, no. 4, pp. 442–446, Oct. 2006.
[18] A. Litman, D. Lesselier, and F. Santosa, "Reconstruction of a two-dimensional binary obstacle by controlled evolution of a level-set," *Inv. Probl.*, vol. 14, no. 3, pp. 685–706, 1998.
[19] O. Dorn and D. Lesselier, "Level set methods for inverse scattering," *Inv. Probl.*, vol. 22, no. 4, pp. R67–R131, Aug. 2006.
[20] R. Abgrall, "Numerical discretization of the first-order Hamilton Jacobi equations on triangular meshes," *Commun. Pure Appl. Math.*, vol. 49, no. 12, pp. 1339–1373, 1996.
[21] J. Sethian, *Level Set Methods and Fast Marching Methods*, ser. Cambridge Monographs on Applied and Computational Mathematics. Cambridge, U.K.: Cambridge Univ. Press, 1999.
[22] X. Li, W. Yan, and C. Chan, "Numerical schemes for Hamilton–Jacobi equations on unstructured meshes," *Numer. Math.*, vol. 94, no. 2, pp. 315–331, 2003.
[23] X. Li and C. Chan, "High order schemes for Hamilton–Jacobi equations on triangular meshes," *J. Comput. Appl. Math.*, vol. 167, no. 1, pp. 227–241, 2004.
[24] S. O. Rice, "Reflection of electromagnetic waves by slightly rough surfaces," in *The Theory of Electromagnetic Waves*, M. Kline, Ed. New York: Interscience, 1963.
[25] F. Santosa, "A level-set approach for inverse problems involving obstacles," *ESAIM: COCV*, vol. 1, pp. 17–33, 1996.
[26] O. Dorn, E. L. Miller, and C. M. Rappaport, "A shape reconstruction method for electromagnetic tomography using adjoint fields and level sets," *Inv. Probl.*, vol. 16, no. 5, pp. 1119–1156, 2000.
[27] C. Ramananjaona, M. Lambert, D. Lesselier, and J. Zolésio, "Shape reconstruction of buried obstacles by controlled evolution of a level set: From a min–max formulation to numerical experimentation," *Inv. Probl.*, vol. 17, no. 4, pp. 1087–1111, 2001.
[28] M. Burger, "Levenberg–Marquardt level set methods for inverse obstacle problems," *Inv. Probl.*, vol. 20, no. 1, pp. 259–282, Feb. 2004.
[29] A. Litman, "Reconstruction by level sets of n-ary scattering obstacles," *Inv. Probl.*, vol. 21, no. 6, pp. 131–152, Dec. 2005.
[30] Y. Altuncu, A. Yapar, and I. Akduman, "On the scattering of electromagnetic waves by bodies buried in a half-space with locally rough interface," *IEEE Trans. Geosci. Remote Sens.*, vol. 44, no. 6, pp. 1435–1443, Jun. 2006.
[31] D. Lawrence and K. Sarabandi, "Electromagnetic scattering from a dielectric cylinder buried beneath a slightly rough surface," *IEEE Trans. Antennas Propag.*, vol. 50, no. 10, pp. 1368–1376, Oct. 2002.
[32] A. Morgenthaler and C. Rappaport, "Scattering from lossy dielectric objects buried beneath randomly rough ground: Validating the semi-analytical mode matching algorithm with 2-D FDFD," *IEEE Trans. Geosci. Remote Sens.*, vol. 39, no. 11, pp. 2421–2428, Nov. 2001.
[33] M. Saillard and G. Toso, "Electromagnetic scattering from bounded or infinite subsurface bodies," *Radio Sci.*, vol. 32, no. 4, pp. 1347–1360, 1997.
[34] J. Jin, *The Finite Element Method in Electromagnetics*. Hoboken, NJ: Wiley, 2002.
[35] C. Geuzaine and J. Remacle, *Gmsh: A Three Dimensional Finite Element Mesh Generator*. [Online]. Available: http://www.geuz.org/gmsh/
[36] P. R. Amestoy, I. S. Duff, and J.-Y. L'Excellent, "Multifrontal parallel distributed symmetric and unsymmetric solvers," *Comput. Methods Appl. Mech. Eng.,* vol. 184, no. 2, pp. 501–520, Apr. 2000. See also http://graal.ens-lyon.fr/MUMPS.
[37] D. Forsyth and J. Ponce, *Computer Vision—A Modern Approach*. Englewood Cliffs, NJ: Prentice-Hall, 2002.
[38] W. Rucklidge, *Efficient Visual Recognition Using the Hausdorff Distance*, ser. Lecture Notes in Computer Science, vol. 1173. New York: Springer-Verlag, 1996.
[39] H. B. Ameur, M. Burger, and B. Hackl, "Level set methods for geometric inverse problems in linear elasticity," *Inv. Probl.*, vol. 20, no. 3, pp. 673–696, Jun. 2004.

Octavien Cmielewski received the degree from the Ecole Normale Supérieure de Cachan, Paris, France, in 2002 and the Ph.D. degree in physics from the University of Provence, Marseille, France, in 2005. During his thesis, which was carried out at Institut Fresnel, he worked on the electromagnetic detection of buried objects beneath a rough surface.

He is currently a prep school teacher in Saint Denis, La Réunion.

Hervé Tortel was born in France in 1970. He received the M.S. and Ph.D. degrees from the University of Provence, Marseille, France, in 1995.

In 1996, he joined Institut Fresnel, UMR 6133 Centre National de la Recherche Scientifique–Universités Aix Marseille, Marseille, as an Assistant Professor. His research interests include direct and inverse scattering problems in electromagnetism.

Amélie Litman (M'06) was born in France in 1972. She received the Ph.D. degree in applied mathematics from the University of Paris XI, Paris, France, in 1997.

During 1997–1998, she was with the Eindhoven University of Technology, Eindhoven, The Netherlands, working in a postdoctoral position. From 1998 to 2002, she was with Schlumberger, France, where she worked on the development of inversion algorithms for oil prospection. In October 2002, she joined Institut Fresnel, UMR 6133 Centre National de la Recherche Scientifique–Universités Aix Marseille, Marseille, France, as an Assistant Professor. Her research interests include forward and inverse scattering techniques.

Marc Saillard (A'01–M'03) was born in Marseille, France, in 1961. He received the "Agrégation" degree in physics and the Ph.D. degree in physics from the University of Marseille, Marseille, in 1985 and 1990, respectively.

From 1990 to 1997, he was an Assistant Researcher in the Electromagnetic Optics Laboratory, National Center for Scientific Research. In 1997, he joined the University of Marseille, as a Professor and ran the Remote Sensing Group of Institut Fresnel. In 2003, he joined the Université du Sud Toulon Var, La Garde, France, as a Professor, where he joined the Remote Sensing Laboratory (Laboratoire de Sondages Electromagnetiques de l'Environnement Terrestre). His professional interests include surface and volume scattering, inverse scattering, and remote sensing.

INSTITUTE OF PHYSICS PUBLISHING INVERSE PROBLEMS

Inverse Problems **21** (2005) S131–S152 doi:10.1088/0266-5611/21/6/S10

Reconstruction by level sets of *n*-ary scattering obstacles

A Litman

Institut Fresnel UMR-CNRSTIC 6133, Université de Provence, Aix-Marseille I, Université Paul Cézanne, Aix-Marseille III, Ecole Généraliste d'Ingénieurs de Marseille, Campus de Saint-Jerôme, case 162, 13397 Marseille Cedex 20, France

E-mail: amelie.litman@fresnel.fr

Received 5 April 2005, in final form 5 July 2005
Published 25 November 2005
Online at stacks.iop.org/IP/21/S131

Abstract

Some extensions of the level set representation are analysed for the reconstruction of the unknown cross-section of multiple phase material obstacles embedded in a homogeneous medium and illuminated by time-harmonic electromagnetic line sources. The *a priori* information assumed therein is that the scatterers are homogeneous by parts and of known characteristics. Two types of approaches are discussed with their pros and cons. In the first approach, a single level set is used to represent the different material phases. In the second approach, the material properties are coded on a binary basis and several level sets are combined, one for each bit of binary coding. Theoretical and numerical details are provided for both approaches, using synthetic and experimental measurements obtained in the anechoic chamber of Institut Fresnel.

(Some figures in this article are in colour only in the electronic version)

1. Introduction

In inverse scattering problems, the goal is to retrieve constitutive parameters of unknown scatterers from their electromagnetic signature. As this problem is highly nonlinear and ill-posed, all *a priori* information is of importance to reduce ill-posedness and therefore the range of plausible solutions.

We restrict ourselves to a two-dimensional transmission problem where the unknown scatterers are embedded in an homogeneous background such as air. Measurements of the scattered fields at several sensor locations around the obstacle and for several locations and/or frequencies of time-harmonic E-polarized sources placed nearby are available. In particular, an experimental database has been obtained in the anechoic chamber of Institut Fresnel for several obstacles.

Additional *a priori* information is introduced as we assume that the dielectric properties of the obstacles are known and that they are constant by parts. Therefore, this inverse scattering problem is reduced to a shape optimization problem where the contour of the different scatterers is looked for. No further assumptions on the connexity or the size of the objects are introduced. This configuration is an extension of the so-called *binary* obstacle case to *n-ary* obstacles, where the obstacles are made of different types of known material phases.

Significant work now exists on the retrieval of binary obstacles. Some of them include this information by discretizing the test domain into black and white pixels (Souriau *et al* 1996). Others are interested in the contour of the obstacle and its representative coefficients (Rozier *et al* 1997, Bonnard *et al* 1998) and provide iterative schemes which perturb the contour. Finally, the level set representation has proved to be one of the most suitable representations for binary objects when no additional topological information is available, such as connexity for example. This level set approach has now been widely used in various domains of inverse problem (Santosa 1996, Litman *et al* 1998, Dorn *et al* 2000, Ramananjaona *et al* 2001, Burger 2004) or shape optimization (Allaire *et al* 2004). This level set representation requires the computation of the shape derivative of the cost functional which links the difference between the measured and simulated scattered field. Shape derivative and topological derivative can also be mixed in order to accelerate the appearance of inclusions in the iterative process (Burger *et al* 2004).

The purpose of this paper is to benefit from the advantages of the level set representation and applying them to *n*-ary obstacles. These advantages consist, for example, in keeping a fixed mesh during the entire iterative process, in handling in a natural way merging and splitting of the obstacles. Several ways of representing *n*-ary obstacles by means of level sets have already been used, for example in contour recognition for image analysis (Zhao *et al* 1996, Samson *et al* 2000, Osher and Paragios 2003). The two extensions analysed therein are of the same nature as those described in Tai and Chan (2004) which provide a survey about the use of multiple level set methods for identifying piecewise constant or piecewise smooth functions. The specificity of this paper comes from the application of the multiple level sets formalism to the Helmholtz equation configuration, and in particular the treatment of experimental datasets.

The first idea is to use a single level set to represent all the obstacles. A smooth level set is cut-off at several levels, each cut-off defining an obstacle area. This method is different from that presented in Lie *et al* (2003) for image segmentation applications, where they use a single piecewise constant level set combined with specific basis functions. The proposed definition is less general, as it does not cover the entire range of possible solutions, but simpler to implement. Indeed, the computational changes introduced by this *n*-ary aspect are minimal compared to the binary case.

The second idea is to use several level sets (Tai and Chan 2004). One could attach a level set to each material phase as done in Zhao *et al* (1996). Overlapping areas then become an issue as they are not physically possible. Instead of introducing a penalty term to prevent those overlapping areas, as done in Samson *et al* (2000), Osher and Paragios (2003), we prefer to follow the ideas of Vese and Chan (2002). The material phases are coded on a binary basis and a level set is attached to each coding bit. The computational changes are more complex in that case but the results are improved as will be shown in the following numerical examples. Another approach would have been to follow the ideas of Lie *et al* (2004) where several level sets are also associated with each coding bit but they are taken to be discontinuous at convergence, instead of continuous as in Vese and Chan (2002).

The paper is organized as follows. In section 2, the formulation of the problem is introduced. In section 3, we discuss different ways of representing an obstacle by means of

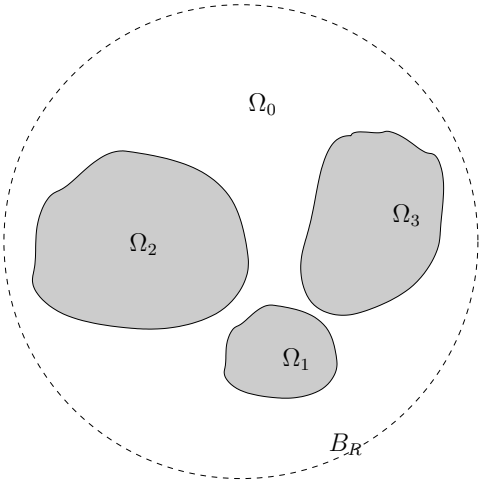

Figure 1. Several scattering obstacles.

level sets, taking into account that the obstacle is homogeneous by parts. These representations can rely on a single level set or on several which are combined in a suitable way in order to fully represent the obstacle. In section 4, the minimization scheme based on a single level set representation is presented in detail. In section 5, a second scheme based on a 'colour' level set evolution is proposed and analysed. Numerical results based on a synthetic configuration are presented in section 6. Reconstructions from the new database measurements of Institut Fresnel are shown in section 7. In section 8 concluding remarks are made. In the appendices, complementary elements are introduced, in particular the adjoint field computation for the single level set representation and the 'colour' level set one.

2. Transmission problem

The model is the following: a set of z-oriented cylindrical obstacles, of cross-section Ω_i, $i = 1, \ldots, n$, is embedded in a homogeneous space denoted by $\Omega_0 = \mathbb{R}^2 \backslash \overline{\bigcup_{i=1}^{n} \Omega_i}$ (figure 1). Each obstacle is assumed to be linear, isotropic, non-magnetic and penetrable and to have a sufficiently smooth boundary Γ_i. Each obstacle is characterized by a unique material property $(\varepsilon_i, \sigma_i, \mu_0)$ and is homogeneous. The set Θ of all those obstacles defined below is therefore homogeneous by parts:

$$\Theta = \bigcup_{i=1}^{n} \Omega_i \qquad \text{and} \qquad \Omega_i \bigcap_{i \neq j} \Omega_j = \emptyset. \tag{1}$$

Each exterior normal to the boundary Γ_i is denoted by $\vec{n}_i$. The wave numbers $k_i(\omega)$ $(\mathrm{Im}(k_i(\omega)) \geqslant 0)$ of the different materials are assumed to be known for each frequency ω and to be independent of the position (the time dependence $\exp(-\mathrm{j}\omega t)$ is chosen and dropped out from now on). An incident wave u^i of the same cylindrical dependence (line source) illuminates the obstacle. We restrict ourselves to a transverse magnetic (TM) or E-polarization configuration. The total field u satisfies the following set of equations:

$$\Delta u + k_i^2 u = 0 \qquad \text{in} \quad \Omega_i, \quad \forall\, i = 0, \ldots, n \tag{2a}$$

$$u^- = u^+ \qquad \text{on} \quad \Gamma_i, \quad \forall\, i = 1, \ldots, n \tag{2b}$$

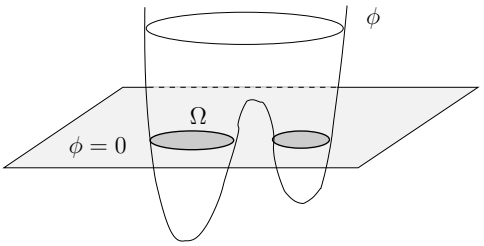

Figure 2. Level set function for a binary obstacle.

$$\frac{\partial u^+}{\partial \vec{n}_i} = \frac{\partial u^-}{\partial \vec{n}_i} \qquad \text{on} \quad \Gamma_i, \quad \forall\, i = 1, \ldots, n \tag{2c}$$

where u^+ (u^-) denotes the limit of u from the exterior (interior) of Ω_i. The scattered field $u^s = u - u^i$ satisfies the Sommerfeld radiation condition

$$\lim_{r\to\infty} \sqrt{r}\left(\frac{\partial u^s}{\partial r} - \mathrm{j}k_0 u^s\right) = 0 \tag{3}$$

where $r = |x|$ and $\mathrm{j}^2 = -1$. It has been shown that this transmission problem has a unique solution $u \in H^1_{\mathrm{loc}}(\mathbb{R}^2)$ for a given set Θ.

The inverse problem consists in finding the shapes $\Omega_i, i = 1, \ldots, n$, corresponding to each material phase, which minimize the error in the data fit. If we denote by $L^2(M)$ the set of the measured scattered fields, where M is the probing line, the cost functional to minimize is of the following form:

$$\mathcal{J}(\Theta) = \tfrac{1}{2}\|u^s(\Theta) - g\|^2_{L^2(M)} \tag{4}$$

where g corresponds to the data and Θ is our collection of shapes of known properties. The inverse problem can then be written as

$$\text{Find } \Theta^* \text{ such that } \mathcal{J}(\Theta^*) = \min_{\Theta} \tfrac{1}{2}\|u^s(\Theta) - g\|^2_{L^2(M)}. \tag{5}$$

3. Shape representation

As stated above, the problem to tackle is reduced to a shape optimization problem. One of the main issues now is to correctly represent the shapes.

In the case of binary obstacles, one of the most suitable representations is via the use of a level set function (Santosa 1996). Indeed, when using such a representation, no *a priori* information is needed on the number of obstacles or the position of their centres. Furthermore, topological changes such as merging or splitting are easily handled.

In the case of n-ary obstacles, the representation is less obvious. In the following, we will focus on two types of representations, both of them being based on the level set functions in order to keep the advantages of such an implicit description. A survey of the different ways of using multiple level sets to identify piecewise constant functions can be found in Tai and Chan (2004).

3.1. Unique level set representation

For a single homogeneous obstacle Ω, the associated level set function $\phi \in C^1(B_R)$ is defined by (figure 2):

$$\Gamma = \{x \in B_R \mid \phi(x) = 0\} \tag{6}$$

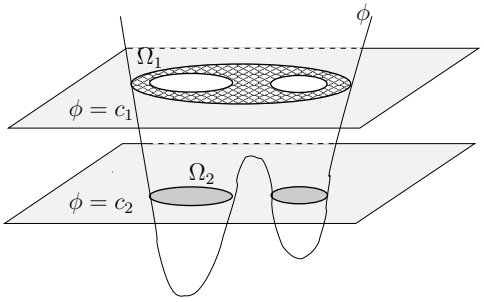

Figure 3. Single level set function for n-ary obstacles.

$$\Omega = \{x \in B_R \mid \phi(x) < 0\}. \tag{7}$$

With this representation, the definition of the contour is implicit and made in a geometrical fashion.

Let us therefore assume that we have several obstacles Ω_i of known characteristics, all of them being homogeneous. The idea is to simply extend the previous level set function to the n-ary case with ϕ defined by (figure 3)

$$\Gamma_i = \{x \in B_R \mid \phi(x) = c_i\} \tag{8}$$
$$\Omega_i = \{x \in B_R \mid c_{i+1} < \phi(x) < c_i\} \tag{9}$$

where the values c_i are predefined level values. Therefore, each truncation plane at the prescribed height c_i will correspond to a contour Γ_i. This representation is very simple and again implicit for each obstacle. The whole structural body Θ will then be partitioned by

$$\Theta = \bigcup_{i=1}^{n} \{x \in B_R \mid c_{i+1} < \phi(x) < c_i\} \tag{10}$$

and such a partition will keep the properties that $\Omega_i \bigcap \Omega_j = \emptyset, i \neq j$.

To simplify the notation, let us introduce the one-dimensional Heaviside function H such that

$$H(x, c) = \begin{cases} 1 & \text{if} \quad x < c \\ 0 & \text{if} \quad x > c. \end{cases} \tag{11}$$

The characteristic function of an obstacle Ω_i is then described by

$$\chi_{\Omega_i}(x) = H(\phi(x), c_{i+1}) - H(\phi(x), c_i) \tag{12}$$

where the limit levels are set to $c_0 = +\infty$ and $c_{n+1} = -\infty$.

Unfortunately this approach suffers from some topological constraints, in particular there might not exist a level set function that satisfies both (8), (9) for general cases. This approach has nevertheless been studied, as described in section 4, as the minimization process for a single phase obstacle (Litman *et al* 1998) can easily be extended to several phases with this description.

3.2. Vector level set representations

Due to the limitations of the previous approach, it might be interesting to look for another description.

3.2.1. Vector level set. Another idea is to provide a level set description for each material phase (Zhao *et al* 1996), i.e.,

$$\Gamma_i = \{x \in B_R \mid \phi_i(x) = 0\} \tag{13}$$
$$\Omega_i = \{x \in B_R \mid \phi_i(x) < 0\} \tag{14}$$

where the level set functions ϕ_i are all defined on $C^1(B_R)$.

This will necessitate in the minimization process to evolve each level set simultaneously and the extension from a single to a multi-phase object is not that obvious. Moreover, it can happen that the level sets overlap during the iterative process, defining therefore a region of multiple values which is not physically possible. This means that the property of (1) is not preserved by this level set representation. Usually, an additional constraint is introduced in the cost function with a Lagrange multiplier in order to minimize the overlap area (Zhao *et al* 1996, Samson *et al* 2000, Osher and Paragios 2003) but this constraint is difficult to maintain accurately. Moreover, the complexity of the algorithms increases drastically with the number of material phases.

3.2.2. 'Colour' level set. A different approach has been proposed in Vese and Chan (2002), Wang and Wang (2004) and Chan and Tai (2003). Here, multiple level sets are still being used. The main difference is the way the association is done from the material phases Ω_i to the level sets. In order to reduce the need for a mixing phase procedure, they have introduced m level set functions to represent a structure of $(n+1) = 2^m$ different material phases, in a principle similar to combining colours from primary colours.

Suppose that we have n different types of material phases and each phase index is denoted by i. The idea is to code those indices in a binary fashion. For n phases, there will be $m = \log_2(n+1)$ coding bits and therefore m associated level sets. The level set ϕ_b associated with the bit b is such that

$$\gamma_b = \{x \in B_R \mid \phi_b(x) = 0\} \tag{15}$$
$$\omega_b = \{x \in B_R \mid \phi_b(x) < 0\}. \tag{16}$$

The domain ω_b will then define the places where the b bit of the phase indices i is nonzero.

To simplify the notation, let us again use the Heaviside function notation. Let B_i^b be a function which provides the b bit of index i. Let us introduce the functions R_i:

$$R_i(\phi_b) = \begin{cases} H(\phi_b, 0) & \text{if} \quad B_i^b = 1 \\ 1 - H(\phi_b, 0) & \text{if} \quad B_i^b = 0. \end{cases} \tag{17}$$

With this notation, an obstacle Ω_i has a characteristic function defined by

$$\chi_{\Omega_i}(x) = \prod_{b=1}^{m} R_i(\phi_b(x)). \tag{18}$$

Let us illustrate this on an example with three different material phases apart from air, which means four different wave numbers $\{k_0, k_1, k_2, k_3\}$. Only $m = 2$ coding bits and associated level set functions are required (figure 4) and the characteristics functions are described by

$$\chi_{\Omega_0} = R_0(\phi_1)R_0(\phi_2) = (1 - H(\phi_1, 0))(1 - H(\phi_2, 0)) \tag{19}$$
$$\chi_{\Omega_1} = R_1(\phi_1)R_1(\phi_2) = H(\phi_1, 0)(1 - H(\phi_2, 0)) \tag{20}$$
$$\chi_{\Omega_2} = R_2(\phi_1)R_2(\phi_2) = (1 - H(\phi_1, 0))H(\phi_2, 0) \tag{21}$$
$$\chi_{\Omega_3} = R_3(\phi_1)R_3(\phi_3) = H(\phi_1, 0)H(\phi_2, 0). \tag{22}$$

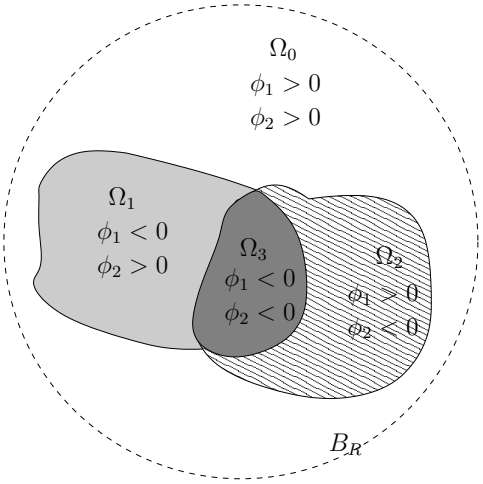

Figure 4. Multiple level set functions for n-ary obstacles.

This representation enables us to reduce drastically the number of level sets that will evolve during the minimization process. Furthermore, the mixing parts are avoided and no extra constraint terms in the cost function are needed. Section 5 will provide the insights of the velocity computations for each level set and some numerical examples.

4. Evolution of a unique level set

The inverse problem of finding the set Θ^* of material phases Ω_i which satisfy (4) is solved with an iterative scheme. A family of shapes $\Theta_t = \bigcup_{i=1}^n \Omega_{i,t}$ is constructed by perturbing an initial shape $\Theta_0 = \bigcup_{i=1}^n \Omega_{i,0}$, for $0 \leqslant t \leqslant T$, where t is a fictitious parameter which describes the iterative process. The deformations are done in order to reduce the following cost function $J(t) = \mathcal{J}(\Theta_t)$ at each step.

In the case of a representation by a unique level set, this iterative scheme is reduced to the deformation of the single level set $\phi(t, x)$.

4.1. The Hamilton–Jacobi equation

The first question is to describe the deformation process for this specific level set. If we derive, according to t, one level contour c_i which corresponds to $\Gamma_{i,t}$, we get (Santosa 1996):

$$\frac{\partial}{\partial t}\phi(t, x) + \vec{V}(t, x) \cdot \vec{n}(t, x)|\nabla\phi(t, x)| = 0 \tag{23}$$

as $\partial x/\partial t = \vec{V}(t, x)$ and $\vec{n} = \nabla\phi/|\nabla\phi|$. Indeed, the level contour value c_i does not evolve with time. Therefore, for each level c_i, the evolution of the level set will be governed by the same equation. This equation is a Hamilton–Jacobi-type equation, where the velocity $\vec{V}$ plays an important role (Osher and Sethian 1988, Sethian 1999).

By using a unique level set representation of the obstacles, the evolution of the level set does not change from the case of a single material phase.

4.2. Cost function derivation

The next point consists in computing the derivative of the cost function for a given deformation of the obstacle Θ_t. It can be shown (see appendix A) (Chan and Tai 2003, Tai and Chan 2004) that the derivative of the cost function $J(t) = \mathcal{J}(\Theta_t)$ for a given velocity field $\vec{V}(t,x)$ can be expressed by

$$\frac{\mathrm{d}J}{\mathrm{d}t} = -\mathrm{Re}\sum_{i=0}^{n} k_i^2 \int_{B_R} [\delta(\phi, c_{i+1}) - \delta(\phi, c_i)] u(t,x)\, p(t,x)\, \vec{V}(t,x)\cdot\vec{n}(t,x)|\nabla\phi(t,x)|\,\mathrm{d}x \quad (24)$$

where $\delta(x, c_i)$ is a Dirac delta function concentrated on the interface $\Gamma_{i,t}$, $u(t,x)$ is the direct total field solution of (2*a*)–(2*c*) at iteration t and $p(t,x)$ is the adjoint field defined by

$$\Delta p + k_i^2 p = -\overline{(u^s - g)}\delta_M \qquad \text{in} \quad \Omega_{i,t}, \quad \forall\, i = 0,\ldots,n \qquad (25a)$$

$$p^- = p^+ \qquad \text{on} \quad \Gamma_{i,t}, \quad \forall\, i = 1,\ldots,n \qquad (25b)$$

$$\frac{\partial p^+}{\partial \vec{n}} = \frac{\partial p^-}{\partial \vec{n}} \qquad \text{on} \quad \Gamma_{i,t}, \quad \forall\, i = 1,\ldots,n \qquad (25c)$$

where δ_M denotes the Kronecker symbol on the probing line M. The adjoint problem is equivalent to the direct problem where emitter and receiver positions are exchanged. This comes from the reciprocity principle satisfied by the electromagnetic fields in this configuration. Both direct and adjoint problems will be solved numerically by a method of moments based on a domain integral representation of the fields.

4.3. Velocity choice

The velocity controls the evolution of the scheme and an appropriate choice is thus essential in order to provide a decrease of the cost functional. Since both the derivative (24) and the Hamilton–Jacobi equation (23) only require the normal component of the velocity, we restrict ourselves to velocities which are in the normal direction:

$$\vec{V}(t,x) = V(t,x)\vec{n}(t,x). \quad (26)$$

As done in Litman *et al* (1998) and Chan and Tai (2003), a simple gradient method is used to solve the minimization problem. Therefore, the level set function is updated by solving (23) with a velocity amplitude defined by

$$V(t,x) = \mathrm{Re}\sum_{i=0}^{n} k_i^2 [\delta(\phi, c_{i+1}) - \delta(\phi, c_i)] u(t,x)\, p(t,x) \qquad \forall\, x \in B_R. \quad (27)$$

Higher-order schemes such as Levenberg–Marquardt level set methods could also have been applied here, as described in Burger (2004), to update the level set function.

4.4. Initialization of the level set

Once the evolution of the level set is described, the next step is a correct definition of a starting point. Usually, when considering a single material phase obstacle, the level set is initialized as the signed distance function once an initial obstacle Ω is given.

$$\phi(0,x) = \begin{cases} -\mathrm{dist}(x, \partial\Omega) & \text{if} \quad x \in \Omega \\ +\mathrm{dist}(x, \partial\Omega) & \text{if} \quad x \notin \Omega. \end{cases} \quad (28)$$

In the case of n-ary obstacles, this type of initialization is no longer possible as there is no way to construct a unique level set which is a distance function for all Ω_i. On the other

hand, the level set representation does not require that only a signed distance function must be used, especially as the Hamilton–Jacobi equation does not preserve this property (Gomez and Faugeras 2000).

Three initialization procedures have been investigated:

- Backpropagation scheme (Kleinman and van den Berg 1992). By applying such a scheme on the data, one can get an estimation of the current density in the investigation area. The backpropagation image is then taken directly as the level set function.
- Topological asymptotic expansion (Guillaume and SidIdris 2002, Burger *et al* 2004). The topological asymptotic expansion corresponds to a first step of a level set procedure by using as an initial guess no object at all. In that case, the velocity computed by means of (27) provides the same type of result and gives a good indication of the topologies. This velocity is then taken directly as the level set function.
- N-ary image. An n-ary image is provided by the end-user. As mentioned above, there is no way to compute a distance function on that image. Nevertheless, a blurring process based on a convolution filter with a Gaussian kernel can be applied to provide a level set function which will have the same topology as the initial image. Unfortunately, by doing this type of blurring, the exact positions of the boundaries are lost. This might be troublesome when performing frequency hopping reconstructions.

Once the initial level set is obtained, the cut-off levels c_i are simply computed by performing an equipartition in height of the level set:

$$c_i = \max(\phi) - (\max(\phi) - \min(\phi))\frac{i}{n}. \tag{29}$$

The first and last levels are set respectively to $+\infty$ and $-\infty$ in order to cover the entire range of values.

5. 'Colour' level set

By using a 'colour' level set representation for n multiple phase materials, we need to change the iterative scheme. Indeed, instead of deforming a unique level set with time, the deformation must be done on a full set of level sets $\phi_b(t, x)$, one for each coding bit as described previously. This implies that the velocity for each level set must be defined carefully.

5.1. The Hamilton–Jacobi equation

For each level set ϕ_b, the deformation process is still governed by a Hamilton–Jacobi-type equation of the following form:

$$\frac{\partial}{\partial t}\phi_b(t, x) + \vec{V}_b(t, x) \cdot \vec{n}_b(t, x)|\nabla\phi_b(t, x)| = 0 \qquad \forall\, b = 1, \ldots, m \tag{30}$$

where $\partial x/\partial t = \vec{V}_b(t, x)$ and $\vec{n}_b = \nabla\phi_b/|\nabla\phi_b|$ and $m = \log_2(n + 1)$ is the number of coding bits required. Each level set evolution will then be performed separately for each specific velocity field on the same fixed grid. The time step is chosen in order to satisfy the CFL condition for all level set functions.

5.2. Cost function derivation

As the representation of the obstacles has changed, it can be shown (see appendix B) (Tai and Chan 2004, Chan and Tai 2003) that the derivative of the cost function $J(t) = \mathcal{J}(\Theta_t)$ from

(4), for a given set of velocity fields $\vec{V}_b$, can be expressed by

$$\frac{\mathrm{d}J}{\mathrm{d}t} = -\mathrm{Re}\sum_{i=0}^{n} k_i^2 \sum_{b=1}^{m} \int_{B_R} \left(\prod_{j=1, j\neq b}^{m} R_i(\phi_j) \right) \times u(t,x)\, p(t,x) \tilde{\delta}_i(\phi_b) \vec{V}_b(t,x) \cdot \vec{n}_b(t,x) |\nabla \phi_b(t,x)|\, \mathrm{d}x \tag{31}$$

where the adjoint state $p(t,x)$ is still defined by (25*a*)–(25*c*) and $\tilde{\delta}_i(\phi_b)$ is a Dirac delta function concentrated on the 0-level of ϕ_b with a positive or negative sign according to B_i^b.

5.3. Velocity choice

A simple gradient-type method is used again to evolve the level sets, by defining velocities along the normal directions only, and with amplitudes given by

$$V_b(t,x) = \mathrm{Re}\sum_{i=0}^{n} k_i^2 \left(\prod_{j=1, j\neq b}^{m} R_i(\phi_j) \right) \tilde{\delta}_i(\phi_b) u(t,x)\, p(t,x) \tag{32}$$

for each level set function ϕ_b associated with the bit b.

6. Numerical results from synthetic data

The two algorithms have been tested in various configurations. A detailed analysis based on synthetic scattered fields is first provided in order to test the influence of the initial guess and to show the pros and cons of each approach.

6.1. Description of the synthetic configuration

The homogeneous background in which the obstacles are located is air ($\varepsilon_0, \sigma_0 = 0, \mu_0$). The area in which the obstacles can be found is a square test domain of length side $d = 2\lambda$ and centred at $(0,0)$. Only one frequency is used, 10 GHz ($\lambda = 3$ cm). The receivers and the sources are equally spaced on a circle of radius 3λ and centred at $(0,0)$. The numbers of receivers and emitters are identical, i.e., 36. The obstacles under study consist of two discs (figure 5). The first one is of radius $\lambda/4$, centred at $(\lambda/4, \lambda/4)$ made of ($\varepsilon_1 = 1.5\varepsilon_0, \sigma_1 = 0, \mu_0$). The second one is of radius $\lambda/4$, centred at $(-\lambda/2, -\lambda/2)$ made of ($\varepsilon_2 = 2\varepsilon_0, \sigma_2 = 0, \mu_0$). The colour association is done such that white corresponds to air ($n = 0$), grey to the material ($n = 1$) made of ($\varepsilon_1 = 1.5\varepsilon_0, \sigma_1 = 0, \mu_0$) and black to the last material ($n = 2$).

6.2. Numerical considerations

The scattering phenomenon is modelled by a method of moments for the direct and inverse problems. The test domain is divided into square cells. The number of cells varies between the direct problem (43×43) and the inverse one (21×21) in order to prevent us from committing an inverse crime. In both cases, the size of the cells is sufficiently small according to the method of moments criteria.

The Hamilton–Jacobi equation is solved on a fixed Cartesian grid using a stable and entropy satisfying scheme developed by Osher and Sethian (1988) and Sethian (1999). The time step is automatically selected in order to satisfy the CFL condition and will be taken as $\Delta t = 0.5\Delta t_{\mathrm{CFL}}$ in order to assure a slow but smooth convergence.

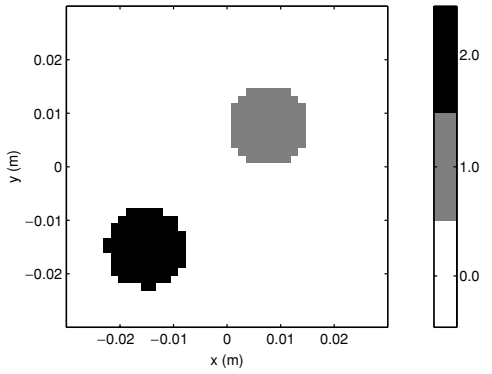

Figure 5. Synthetic obstacle configuration

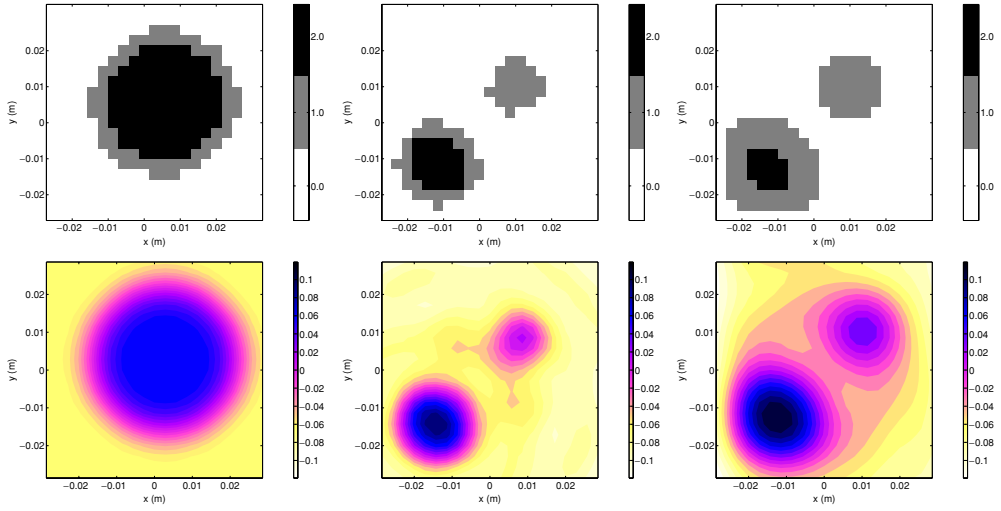

(a) Circle (b) Backpropagation (c) Velocity

Figure 6. Three initialization processes for a single level set representation. Top, image; bottom, level set.

The Heaviside function and its derivate are approximated by the following functions as in Vese and Chan (2002):

$$H(\phi, c) = 1 - \frac{1}{2}\left(1 + \frac{2}{\pi}\arctan\left(\frac{\phi - c}{0.1}\right)\right) \qquad \delta(\phi, c) = -\frac{1}{\pi}\frac{0.01}{0.01 + (\phi - c)^2}. \tag{33}$$

The iteration process is stopped if the cost function is low enough (<0.3) or if the number of iterations has reached 100. The cost function corresponds to the difference between the measured and simulated scattered fields normalized by the measured scattered fields.

6.3. Single level set evolution

6.3.1. Initialization. Three different types of initial level set functions have been investigated: (i) an initial circle made of ($\varepsilon = 1.5\varepsilon_0, \sigma = 0, \mu_0$), centred and of radius $2\lambda/3$ blurred by a convolution with a Gaussian filter (figure 6(a)), (ii) the backpropagation result (figure 6(b)),

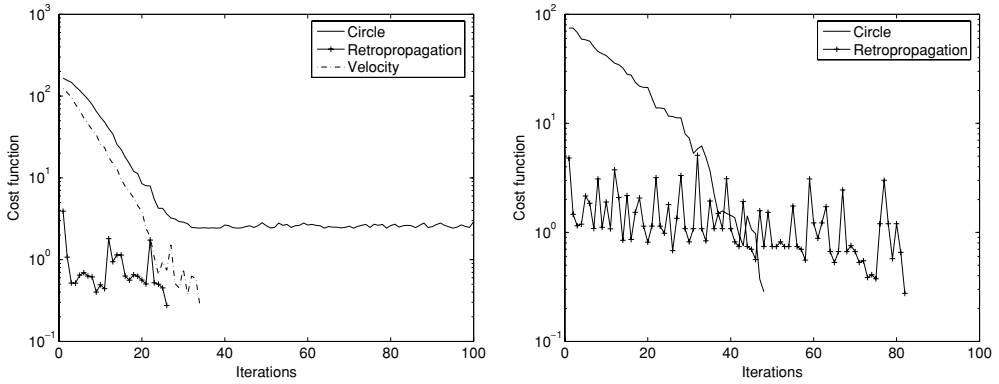

(a) Single level set (b) Colour level set

Figure 7. Cost function for different initial guesses. (——) circle, (+) backpropagation, (— · —) velocity.

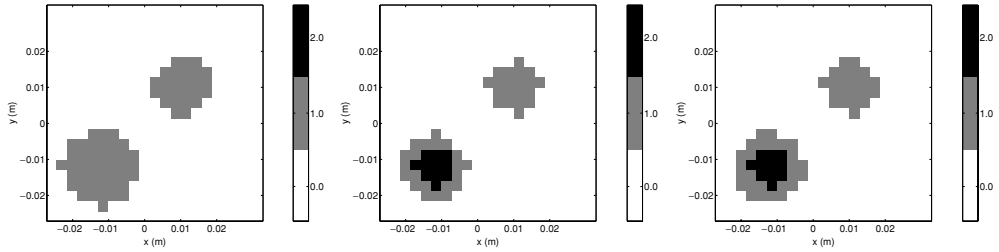

(a) Circle, it. 100 (b) Backprop., it. 25 (c) Velocity, it. 34

Figure 8. Resulting images with a single level set representation for different initial guesses.

(iii) the velocity field obtained with a null initial guess (figure 6(c)). The last two provide a good estimation of the positions of the scatterers as well as their contrasts.

6.3.2. Cost function. The cost function evolution is presented in figure 7(a) for different initialization procedures. It is obvious that the initialization process has some effect on the convergence and in particular, the value of the cost function at final iterations is more important when using a single centred circle as the initial guess. Let us specify that the oscillations in the cost function are due to oscillations of the solution which evolves in a non-smooth way when looking at small scale changes compared to the pixel size.

6.3.3. Image and level set evolution. When initializing with a centred circle, the algorithm does not converge towards the actual profile (figure 8(a)). The positions of the objects are correctly found but the shape and the value of associated permittivity are different. Indeed, by having more material properties available, the number of degrees of freedom has increased and the solution obtained is an equivalent one where the scatterer of largest permittivity is replaced by a scatterer of larger area with reduced permittivity. Figure 9 shows the evolution of the associated level set function, when the initialization is done with a circle, and one can see the decrease of the amplitude of the level set and its spread.

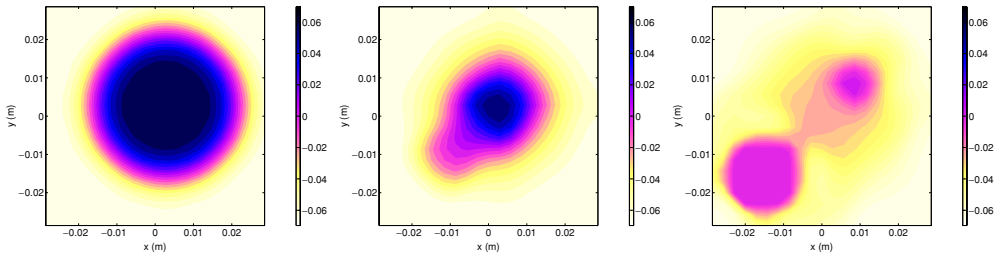

(a) Iteration 0 (b) Iteration 10 (c) Iteration 100

Figure 9. Single level set evolution with a circle as initial guess.

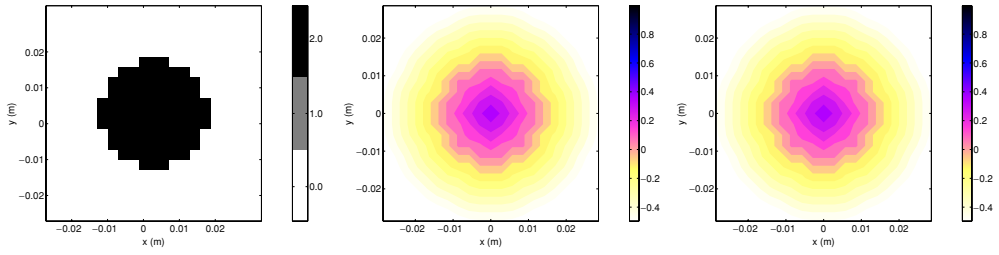

(a) Circle

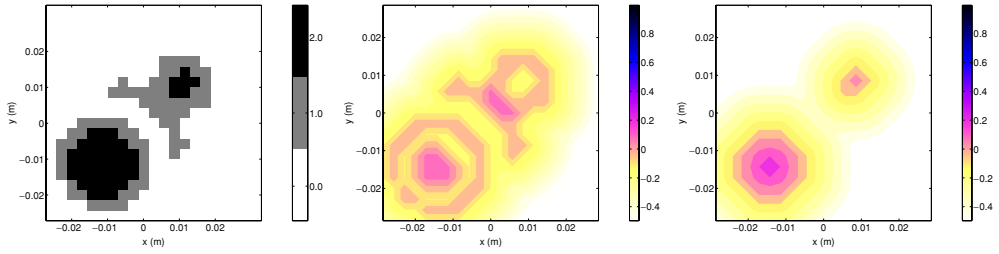

(b) Backpropagation

Figure 10. Two initialization processes for a 'colour' level set representation: left, image; middle, level set for first bit; right, level set for second bit.

If more *a priori* information is introduced in the initial guess, as is done with the other two initialization processes, the resulting image is very close to the 'exact' one (figures 8(b) and (c)). Nevertheless, fast transitions from one material to another are not handled by a single level set representation. This is a severe drawback of such a representation which can be slightly reduced with a more refined mesh but will still be present.

6.4. 'Colour' level set evolution

6.4.1. Initialization. Due to the presence of three different material phases, two level set functions are necessary to represent the coding bits. Two types of initialization process have been investigated: (i) an initial circle made of ($\varepsilon = 2\varepsilon_0, \sigma = 0, \mu_0$), centred and of radius $\lambda/2$ which provides two level sets which are identical (figure 10(a)), (ii) the backpropagation result truncated into two layers to initialize the two level set functions (figure 10(b)).

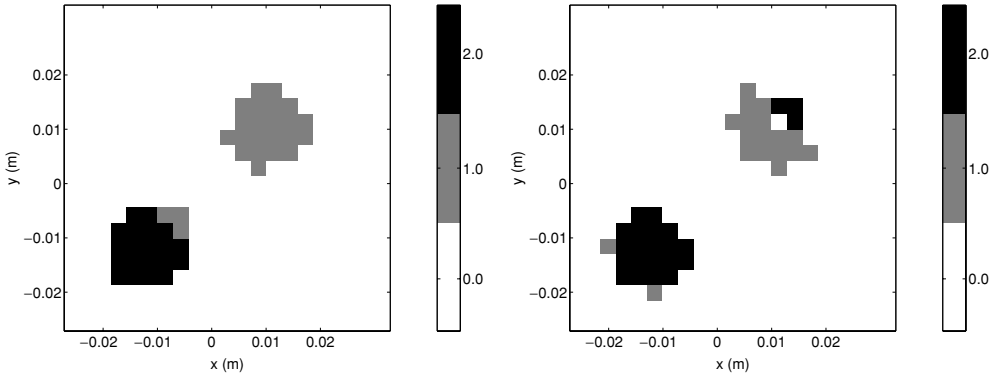

(a) Circle, it. 48 (b) Backprop., it. 82

Figure 11. Resulting images for different initial guesses with a colour level set representation.

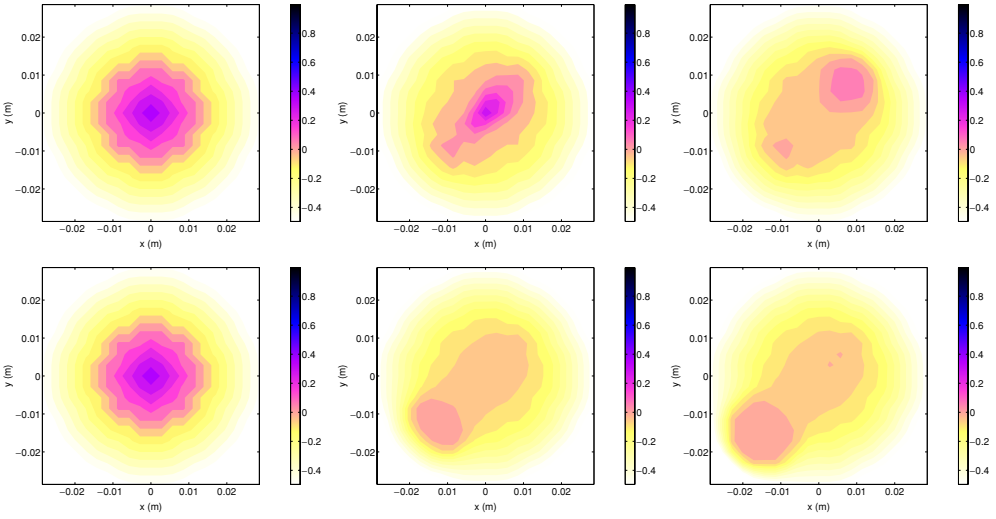

(a) Iteration 0 (b) Iteration 24 (c) Iteration 48

Figure 12. 'Colour' level sets evolution with a circle as initial guess. Top, level set for first coding bit; bottom, level set for second coding bit.

6.4.2. Cost function. Figure 7(b) shows the evolution of the cost function for different initial guesses. Here, the initialization with a circle provides faster convergence, but this can change from one configuration to another.

6.4.3. Image and level set evolution. Figure 11 shows the resulting image for the different initial guesses. The reconstruction is very satisfactory with this type of approach and one can distinctly recognize the two scatterers made of different material. The evolution of the associated level set functions is presented in figure 12. One can easily see the bit association that results in the n-ary images of figure 11.

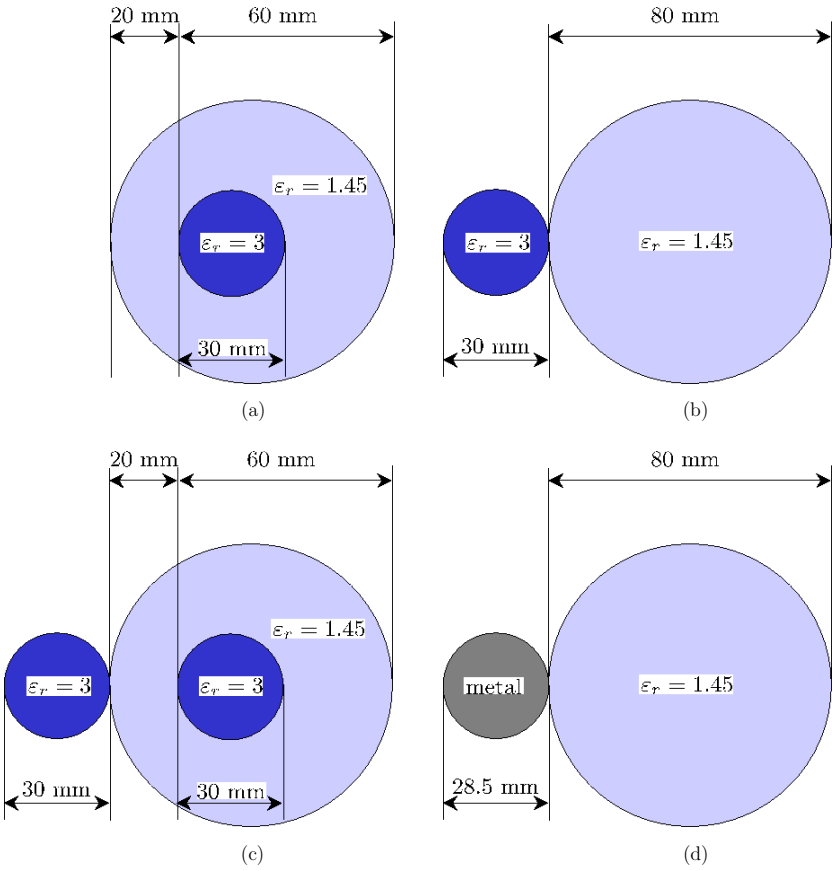

Figure 13. Target database description. (a) FoamDielInt, (b) FoamDielExt, (c) FoamTwinDiel, (d) FoamMetExt.

7. Numerical results from experimental data

The anechoic chamber of Institut Fresnel was used to measure the scattered fields from various objects illuminated at different angles and frequencies. In this paper, only the transverse magnetic measurement is analysed but the same algorithm can be extended to the transverse electric case with a suitable definition of the adjoint fields (Ramananjaona *et al* 2001).

7.1. Experimental setup description

A full description of the experimental setup is provided in Geffrin *et al*. Only some parts are presented here, which are relevant for the inversion process.

The new experimental database consists in measured scattered fields from four obstacles of inhomogeneous properties: FoamDielInt, FoamDielExt, FoamTwinDiel and FoamMetExt (figure 13). All obstacles are assumed to be long in one direction such that a two-dimensional assumption can be made. Every target can be included in a 0.15×0.15 m^2 square centred at the centre of the receiver circle. These new targets consist of a combination of foam ($\varepsilon_r \approx 1.45$), plastic ($\varepsilon_r \approx 3$) and copper tubes.

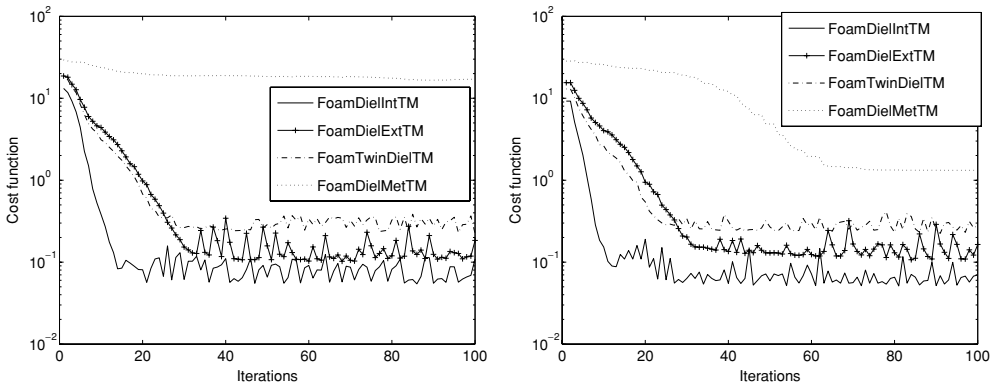

(a) Single level set (b) Colour level set

Figure 14. Cost function for the different experimental configurations. (——) FoamDielInt, (+) FoamDielExt, (— · —) FoamTwinDiel, (· · · · · ·) FoamMetExt.

Receivers and emitters are horn-antennas positioned on a circle of radius $d_e = 1.67$ m. Measurements have been made for several angles of incidence: from 0° to 315° with a spacing of 45° for FoamDielInt and FoamDielExt; from 0° to 340° with a spacing of 20° for FoamTwinDiel and FoamMetExt. Receiving positions have been taken every 1° from 60° to 300°. For all the targets, except for FoamMetExt, the frequencies are taken from 2 to 10 GHz with a step of 1 GHz, the last one being measured up to 18 GHz.

For the inversion process, all incidence and receiver measurements have been used. The scattered fields have been normalized as explained in Tijhuis *et al* (2001) by defining a complex coefficient which assumes that the point opposite to the antenna is measuring an incident field which is equivalent to the field radiated by a line source.

7.2. Numerical considerations

As previously, a method of moments is used for modelling the electromagnetic phenomenon. The number of cells is taken as (31×31) and the test domain corresponds to a centred square box of (0.2×0.2) m^2. The Hamilton–Jacobi equation is solved as previously with the same Δt condition and the same Heaviside function as in (33). The iteration process stops when the cost function is low enough or after 30 iterations. All reconstructions are presented with the same initial guess, corresponding to a circle, centred, of radius 0.05 m. The red circles shown in the pictures correspond to the *a priori* positions of the scatterers as provided by the experimentalist team. The colour association is done such that ($n = 0$, blank) corresponds to air, ($n = 1$, grey) corresponds to the dielectric of permittivity $\varepsilon_r = 1.45$ and ($n = 2$, black) corresponds either to the dielectric of permittivity $\varepsilon_r = 3$ or to the metal part. When the obstacle is metallic, its permittivity is taken as $\varepsilon_r = 1$ and its conductivity is taken as $\sigma = 1$ S m^{-1} to be sure that the cell size is larger than the skin depth.

7.3. Cost functions

For all configurations, the cost functions are presented with the same initial guess in figure 14. In the dielectric cases, the convergence is again very rapid and oscillations appear when the size of the image changes is of the order of the cell size. When there are metallic parts, the

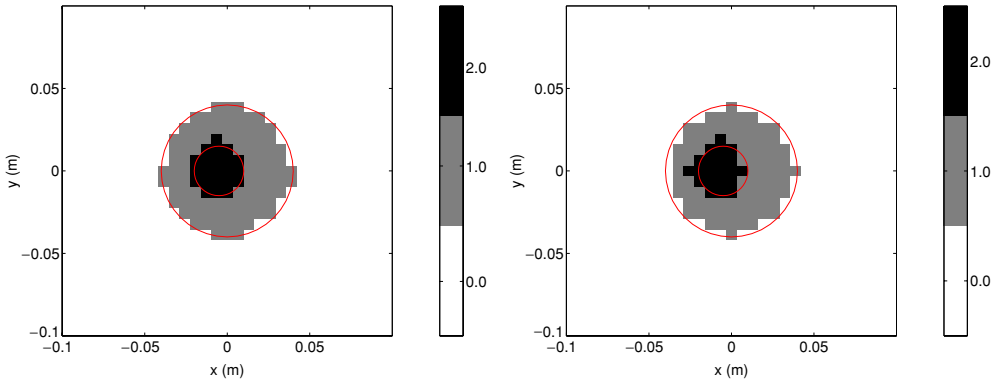

(a) Single level set (b) Colour level set

Figure 15. Resulting images for the FoamDielInt case.

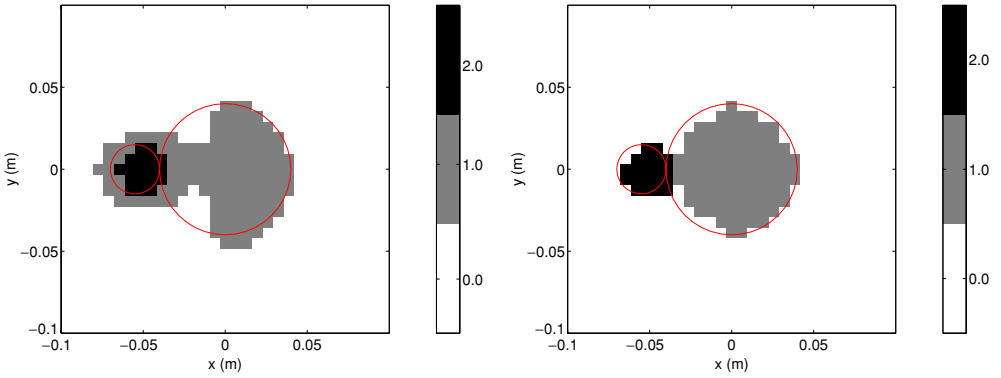

(a) Single level set (b) Colour level set

Figure 16. Resulting images for the FoamDielExt case.

convergence process is slower and in fact does not converge when using a single level set representation.

7.4. Reconstructions at 2 GHz

Reconstructions obtained after 30 iterations for the different dielectric configurations are presented in figure 15 for the FoamDielInt case, in figure 16 for the FoamDielExt case and in figure 17 for the FoamTwinDiel case. All reconstructions are very satisfactory even when using a single frequency. This highlights the importance of *a priori* information introduced into the inversion algorithm.

Reconstructions obtained after 100 iterations for the FoamMetExt case are presented in figure 18. The single level set representation did not converge as the 'colour' level set representation did. Indeed, when there are metallic parts, the convergence is more difficult to achieve as the velocity computation requires the value of the total field inside the object. If the object is metallic, the field will be close to zero and the associated velocity will be null inside. This means that the inner points will not be removed even if needed and this will prevent proper convergence.

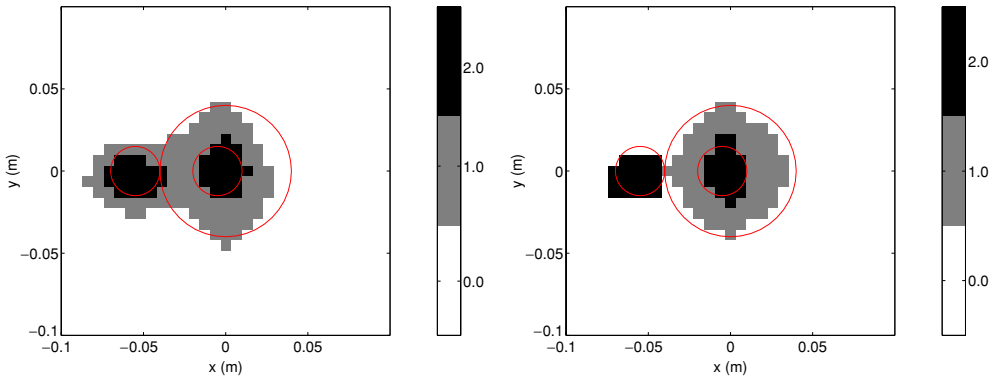

(a) Single level set (b) Colour level set

Figure 17. Resulting images for the FoamTwinDiel case.

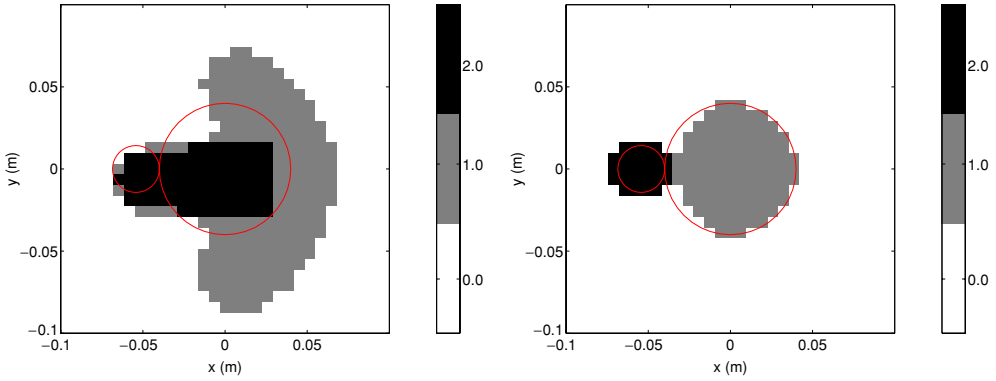

(a) Single level set (b) Colour level set

Figure 18. Resulting images for the FoamMetExt case.

7.5. Reconstructions at higher frequency

Unfortunately, due to the way the initialization process is done with the single level set representation, it is not possible to perform a frequency-hopping approach as in Tijhuis *et al* (2001). Indeed, the initial guess does not fully preserve the topology obtained at previous frequencies as some blurring procedure is applied to the n-ary image in order to create an artificial level set function.

Therefore only frequency-hopping results are presented for the 'colour' level set approach in figure 19 for the FoamTwinDiel case. In order to provide a discretization grid which respects for all frequencies the method of moments ratio of $\lambda/7$, the number of cells has been increased to 41×41. Three frequencies have been used at 2, 4 and 6 GHz. The last iteration, i.e., iteration 100, is used as an initial guess for the next frequency. In fact, as the reconstructions are already of a very good quality at 2 GHz, the higher frequencies do not provide much further information.

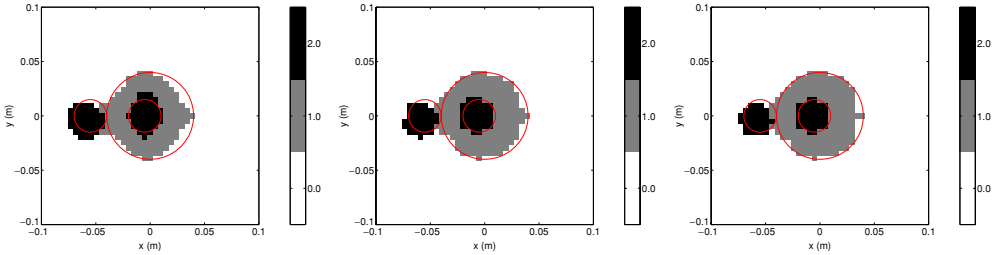

(a) 2 GHz, it. 100 (b) 4 GHz, it. 100 (c) 6 GHz, it. 100

Figure 19. Frequency hopping for the FoamTwinDiel case.

8. Conclusion

We have analysed here two types of approaches for representing n-ary obstacles by means of level set. The first approach is based on a single level set representation and is simpler to implement than the second one which uses several level sets, one for each coding bit necessary to code the material phases on a binary basis.

As we have seen in the numerical examples, the two approaches react differently to initial guess selection. The first one is more sensitive than the 'colour' level set representation. Furthermore, the first approach is not really appropriate when there are sharp transitions, from material ($n = 0$) to material ($n = 2$) for example. In fact, there might not exist a single level set that can represent all obstacles in general cases. This is why 'colour' level sets have been introduced. Another approach would have been to follow the work from Lie *et al* (2003) where a single discontinuous level set is used, combined with specific basis functions. Finally, the single level set approach fails to converge in some situation, for example when there is a metallic part inside the scatterers, as the 'colour' level set does not.

In any case, the 'colour' level set provides very satisfactory results even when using a single low frequency, as can be seen on the reconstructions obtained from the experimental fields measured in the anechoic chamber of Institut Fresnel. This proves the importance of a proper introduction of *a priori* information into the inversion process.

Acknowledgments

The author would like to thank the microwave experimental team of Institut Fresnel for providing the data, as well as K Belkebir and M Saillard for organizing this second special section on 'Testing inversion algorithms against experimental data'. The author gratefully acknowledge helpful discussions with H Tortel. The author also thanks the anonymous referees for their valuable comments and help.

Appendix A. Cost function derivation for a single level set

A.1. Weak formulation of the transmission problem

The objective function to minimize is of the following form:

$$J(t) = \mathcal{J}(\Theta_t) = \tfrac{1}{2}\|u^s(\Theta_t) - g\|^2_{L^2(M)} \tag{A.1}$$

under the constraints that the total field u satisfies equations (2*a*)–(2*c*) or in a weak sense (Hettlich 1995):

$$\int_{B_R} (\nabla u \nabla \bar{v} - \kappa^2 u \bar{v})\,\mathrm{d}x - \langle Lu, v\rangle = (f, v)_{H^1(B_R)} \tag{A.2}$$

for all $v \in H^1(B_R)$, where B_R is a ball of radius $R > 0$, where L is the Dirichlet-to-Neumann map: $H^{1/2}(\partial B_R) \to H^{-1/2}(\partial B_R)$ and $f \in H^1(B_R)$ is a linear functional linked to the incident field. The contrast κ^2 is defined by

$$\kappa^2(t, x) = \sum_{i=0}^{n} k_i^2 \chi_{\Omega_{i,t}}(x) \tag{A.3}$$

where k_i^2 corresponds to the wave number of the obstacle $\Omega_{i,t}$.

A.2. Lagrangian formulation

Let us introduce the Lagrangian functional $\mathcal{L}$ defined by

$$\mathcal{L}(u, v, t) = J(t) + \mathrm{Re}\left(\int_{B_R} (\nabla u \nabla \bar{v} - \kappa^2 u \bar{v})\,\mathrm{d}x - \langle Lu, v\rangle - (f, v)_{H^1(B_R)}\right) \tag{A.4}$$

for a family of shapes $\{\Theta_t\}$. The saddle point of this Lagrangian enables us to find the minimum of the cost function (Ramananjaona *et al* 2001). The partial derivative $\partial\mathcal{L}(u, v, t)/\partial v$ provides the weak formulation (A.2) for the total field u. The partial derivative $\partial\mathcal{L}(u, v, t)/\partial u$ provides the following weak formulation for the adjoint field $p = \bar{v}$:

$$\int_{B_R} (\nabla w \nabla \bar{v} - \kappa^2 w \bar{v})\,\mathrm{d}x = -\int_M \overline{(u^s - g)}(y) w(y)\,\mathrm{d}y \qquad \forall\, w \in H^1(B_R), \tag{A.5}$$

where the receivers act as sources with a prescribed amplitude.

A.3. Cost function derivation

The next step is to derive the objective functional according to a given shape deformation of the obstacle Θ_t under a given velocity field $\vec{V}(t, x)$. We have

$$\frac{\mathrm{d}J}{\mathrm{d}t} = \frac{\partial\mathcal{L}}{\partial t}(u, v, t) \tag{A.6}$$

where u is the total field defined by (A.2) and $p = \bar{v}$ is the adjoint field defined by (A.5). This leads to

$$\frac{\partial\mathcal{L}}{\partial t}(u, v, t) = -\mathrm{Re}\int_{B_R} \frac{\partial\kappa^2(t, x)}{\partial t} u(t, x)\bar{v}(t, x)\,\mathrm{d}x. \tag{A.7}$$

In fact, the shape information is contained in the level set representation and with a single level set representation, this wave number is defined by

$$\kappa^2(t, x) = \sum_{i=0}^{n} k_i^2 [H(\phi(t, x), c_{i+1}) - H(\phi(t, x), c_i)] \tag{A.8}$$

where H is the one-dimensional Heaviside function and $\phi(t, x)$ is the level set at time t. For a given velocity field $\vec{V}(t, x)$ which represents the perturbation vector field, the derivative is given by

$$\frac{\partial\kappa^2(t, x)}{\partial t} = \sum_{i=0}^{n} k_i^2 \left[\frac{\partial H}{\partial\phi}(\phi, c_{i+1}) - \frac{\partial H}{\partial\phi}(\phi, c_i)\right] \frac{\partial\phi}{\partial t} \tag{A.9}$$

$$= \sum_{i=0}^{n} k_i^2 [\delta(\phi, c_{i+1}) - \delta(\phi, c_i)] \vec{V}(t, x) \cdot \vec{n}(t, x) |\nabla\phi(t, x)| \tag{A.10}$$

as ϕ follows the Hamilton–Jacobi equation (23). The function $\delta(\phi, c_i)$ corresponds to the Dirac delta function concentrated on the interface c_i (Osher and Paragios 2003). For c_0 and c_{n+1}, this Dirac delta function has a null support and therefore does not interfere in the computations.

The derivative of the cost function is then given by

$$\frac{\mathrm{d}J}{\mathrm{d}t} = -\mathrm{Re}\sum_{i=0}^{n} k_i^2 \int_{B_R} [\delta(\phi, c_{i+1}) - \delta(\phi, c_i)] u(t,x) p(t,x) \vec{V}(t,x) \cdot \vec{n}(t,x) |\nabla\phi(t,x)| \,\mathrm{d}x. \tag{A.11}$$

Appendix B. Cost function derivation for a 'colour' level set

B.1. Weak formulation and Lagrangian

The cost function to minimize, as well as the Lagrangian formulation or the adjoint state are identical to those described in appendix A. As the main difference relies in the representation of the obstacles, the derivative according to time of the objective functional will be different.

B.2. Cost functional derivation

Let us again express the wave number κ^2 in terms of the level set description. Here we have $m = \log_2(n+1)$ level set functions, each for each coding bit of material phases. Following the definitions of (17) and (18), the wave number is given by

$$\kappa^2(t,x) = \sum_{i=0}^{n} k_i^2 \left(\prod_{b=1}^{m} R_i(\phi_b(t,x)) \right). \tag{B.1}$$

For a given set of velocity fields $V_b(t,x)$ for each level set function $\phi_b(t,x)$, the derivative of the wave number is

$$\frac{\partial \kappa^2}{\partial t} = \sum_{i=0}^{n} k_i^2 \frac{\partial}{\partial t} \left(\prod_{b=1}^{m} R_i(\phi_b) \right) \tag{B.2}$$

$$= \sum_{i=0}^{n} k_i^2 \sum_{b=1}^{m} \left(\prod_{j=1, j\neq b}^{m} R_i(\phi_j) \right) \tilde{\delta}_i(\phi_b) \frac{\partial \phi_b}{\partial t} \tag{B.3}$$

$$= \sum_{i=0}^{n} k_i^2 \sum_{b=1}^{m} \left(\prod_{j=1, j\neq b}^{m} R_i(\phi_j) \right) \tilde{\delta}_i(\phi_b) V_b |\nabla\phi_b| \tag{B.4}$$

where $\tilde{\delta}_i(\phi_b)$ is the Dirac delta function concentrated on the interface of the level set ϕ_b with a positive (resp. negative) sign if the associated bit B_i^j is 1 (resp. 0).

The derivative of the cost function is then given by

$$\frac{\mathrm{d}J}{\mathrm{d}t} = -\mathrm{Re}\sum_{i=0}^{n} k_i^2 \sum_{b=1}^{m} \int_{B_R} \left(\prod_{j=1, j\neq b}^{m} R_i(\phi_j(t,x)) \right) \times u(t,x) p(t,x) \tilde{\delta}_i(\phi_b(t,x)) \vec{V}_b(t,x) \cdot \vec{n}(t,x) |\nabla\phi_b(t,x)| \,\mathrm{d}x. \tag{B.5}$$

References

Allaire G, Jouve F and Toader A M 2004 Structural optimization using sensitivity analysis and a level-set method *J. Comput. Phys.* **194** 363–93

Bonnard S, Vincent P and Saillard M 1998 Cross-borehole inverse scattering using a boundary finite-element method *Inverse Problems* **14** 521–34

Burger M 2004 Levenberg–Marquardt level set methods for inverse obstacle problems *Inverse Problems* **20** 259–82

Burger M, Hackl B and Ring W 2004 Incorporating topological derivative into level set methods *J. Comput. Phys.* **194** 344–62

Chan T and Tai X 2003 Level set and total variation regularization for elliptic inverse problems with discontinuous coefficients *J. Comput. Phys.* **193** 40–66

Dorn O, Miller E L and Rappaport C M 2000 A shape reconstruction method for electromagnetic tomography using adjoint fields and level sets *Inverse Problems* **16** 1119–56

Geffrin J M, Sabouroux P and Eyraud C 2005 Free space experimental scattering database continuation: experimental setup and measurement precision *Inverse Problems* **21** S117–30

Gomez J and Faugeras O 2000 Reconciling distance functions and level sets *J. Vis. Commun. Image Represent.* **11** 209–23

Guillaume P and SidIdris K 2002 The topological asymptotic expansion for the Dirichlet problem *SIAM J. Control. Optim.* **41** 1042–72

Hettlich F 1995 Fréchet derivative in inverse obstacles scattering *Inverse Problems* **11** 371–82

Kleinman R and van den Berg P 1992 A modified gradient method for two-dimensional problems in tomography *J. Comput. Appl. Math.* **42** 17–35

Lie J, Lysaker M and Tai X 2003 A variant of the level set method and applications to image segmentation *CAM Report* **03-50** UCLA

Lie J, Lysaker M and Tai X 2004 A binary level set model and some applications to Mumford–Shah image segmentation. *CAM Report* **04-31** UCLA

Litman A, Lesselier D and Santosa F 1998 Reconstruction of a two-dimensional binary obstacle by controlled evolution of a level-set *Inverse Problems* **14** 685–706

Osher S and Paragios N 2003 *Geometric Level Set Methods in Imaging, Vision and Graphics* (Telos: Springer)

Osher S and Sethian J A 1988 Fronts propagating with curvature-dependent speed: algorithms based on Hamilton–Jacobi formulations *J. Comput. Phys.* **79** 12–49

Ramananjaona C, Lambert M, Lesselier D and Zolésio J 2001 Shape reconstruction of buried obstacles by controlled evolution of a level set: from a min–max formulation to numerical experimentation *Inverse Problems* **17** 1087–111

Rozier C, Lesselier D, Angell T and Kleinmann R E 1997 Shape retreival of an obstacle immersed in shallow water from a single frequency fields using a complete family method *Inverse Problems* **13** 487–508

Samson C, Blanc-Feraud L, Aubert G and Zerubia J 2000 A level set model for image classification *Int. J. Comput. Vis.* **40** 187–98

Santosa F 1996 A level-set approach for inverse problems involving obstacles *ESAIM: COCV* **1** 17–33

Sethian J 1999 *Level Set Methods and Fast Marching Methods (Cambridge Monographs on Applied and Computational Mathematics)* (New York: Cambridge University Press)

Souriau L, Duchene B, Lesselier D and Kleinmann R E 1996 A modified gradient approach to inverse scattering for binary objects in stratified media *Inverse Problems* **12** 463–81

Tai X and Chan T 2004 A survey on multiple level set methods with applications for identifying piecewise constant functions *Int. J. Numer. Anal. Model.* **1** 25–47

Tijhuis A, Belkebir K, Litman A and de Hon B 2001 Multiple-frequency distorted-wave Born approach to 2D inverse profiling *Inverse Problems* **17** 1635–44

Vese L and Chan T 2002 A multiphase level set framework for image segmentation using the Mumford and Shah model *Int. J. Comput. Vis.* **50** 271–93

Wang M and Wang X 2004 'Color' level sets: a multi-phase method for structural topology optimization with multiple materials *Comput. Methods Appl. Mech. Eng.* **193** 469–96

Zhao H, Chan T, Merriman B and Osher S 1996 A variational level set approach to multiphase motion *J. Comput. Phys.* **127** 179–95